

AD-A263 095



WL-TR-92-4104

MICROSTRUCTURAL EFFECTS ON THE
DEFORMATION AND FRACTURE OF THE ALLOY
TI-25AL-10NB-3B-1MO



CAPTAIN CHARLES H. WARD, JR.

MATERIALS DEVELOPMENT BRANCH (WL/MLLM)
METALS AND CERAMICS DIVISION
MATERIALS DIRECTORATE
WPAFB, OH 45433-6533

DEC 1992

FINAL REPORT FOR 07/01/88-12/15/92

DTIC
ELECTE
APR 20 1993
S C D

APPROVED FOR PUBLIC RELEASE; DISTRIBUTION IS UNLIMITED.

MATERIALS DIRECTORATE
WRIGHT LABORATORY
AIR FORCE MATERIEL COMMAND
WRIGHT PATTERSON AFB OH 45433-6533

93-08134

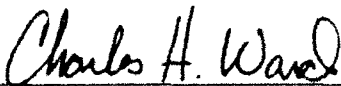


211pt

NOTICE

WHEN GOVERNMENT DRAWINGS, SPECIFICATIONS, OR OTHER DATA ARE USED FOR ANY PURPOSE OTHER THAN IN CONNECTION WITH A DEFINITELY GOVERNMENT-RELATED PROCUREMENT, THE UNITED STATES GOVERNMENT INCURS NO RESPONSIBILITY OR ANY OBLIGATION WHATSOEVER. THE FACT THAT THE GOVERNMENT MAY HAVE FORMULATED OR IN ANY WAY SUPPLIED THE SAID DRAWINGS, SPECIFICATIONS, OR OTHER DATA, IS NOT TO BE REGARDED BY IMPLICATION, OR OTHERWISE IN ANY MANNER CONSTRUED, AS LICENSING THE HOLDER, OR ANY OTHER PERSON OR CORPORATION; OR AS CONVEYING ANY RIGHTS OR PERMISSION TO MANUFACTURE, USE, OR SELL ANY PATENTED INVENTION THAT MAY IN ANY WAY BE RELATED THERETO.

THIS TECHNICAL REPORT HAS BEEN REVIEWED AND IS APPROVED FOR PUBLICATION.

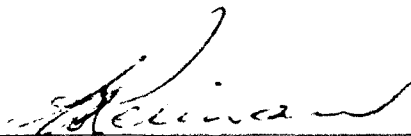


CHARLES H. WARD, Capt, USAF
Materials Engineer
Metals and Ceramics Division



GERALD J. PETRAK
Technical Area Manager
Metals and Ceramics Division

FOR THE COMMANDER



WALTER H. REIMANN
Chief, Materials Development Branch
Metals and Ceramics Division

IF YOUR ADDRESS HAS CHANGED, IF YOU WISH TO BE REMOVED FROM OUR MAILING LIST, OR IF THE ADDRESSEE IS NO LONGER EMPLOYED BY YOUR ORGANIZATION PLEASE NOTIFY WL/MLLM Bldg 655, 2230 TENTH ST STE 1, WRIGHT-PATTERSON AFB, OH 45433-7817 TO HELP MAINTAIN A CURRENT MAILING LIST.

COPIES OF THIS REPORT SHOULD NOT BE RETURNED UNLESS RETURN IS REQUIRED BY SECURITY CONSIDERATIONS, CONTRACTUAL OBLIGATIONS, OR NOTICE ON A SPECIFIC DOCUMENT.

TABLE OF CONTENTS

1. INTRODUCTION.....	1
2. BACKGROUND.....	3
2.1 Physical Metallurgy.....	3
2.1.1 " β " phase.....	7
2.1.2 ω phase.....	9
2.1.3 α_2 phase.....	10
2.1.4 Ordered Orthorhombic Phase.....	17
2.1.5 Martensitic Reaction.....	19
2.2 Slip Behavior.....	25
2.2.1 Experimental Observations.....	25
2.2.1.1 $\langle a \rangle$ Type Dislocations in α_2	27
2.2.1.2 $[c]$ Component Dislocations in α_2	30
2.2.1.3 Slip Behavior in the " β " phase.....	32
2.2.1.4 Two Phase Dislocation Behavior.....	33
2.2.1.5 Interstitial Effects on Slip.....	34
2.2.2 Discussion.....	35
2.3 Correlation of Microstructure to Tensile Properties and Fracture.....	38
2.3.1 Strengthening Effects.....	39
2.3.2 Temperature Dependence of Strength.....	41
2.3.3 Ductility Effects.....	42
2.3.4 Temperature Dependence of Ductility.....	47
2.3.5 Fracture Toughness.....	53
2.5 Research Objectives.....	57
2.5.1 Ductility at room temperature.....	58

2.5.2 Ductility at intermediate temperatures ($25^{\circ}\text{C} < T < 540^{\circ}\text{C}$).....	59
2.5.3 Ductility Loss and Failure at elevated temperature, $\geq 540^{\circ}\text{C}$	59
2.5.4 Fracture Toughness Testing	60
3. EXPERIMENTAL PROCEDURE	62
3.1 Material Processing	62
3.2 Mechanical Testing	63
3.3 Microscopy	71
3.4 X-ray Diffraction	71
4. RESULTS	72
4.1 Microstructural Characterization	72
4.2 Mechanical Testing	79
4.2.1 Room Temperature Tensile Testing.....	79
4.2.2 Elevated Temperature Tensile Testing in Vacuum	84
4.2.3 Elevated Temperature Tensile Testing in Air	103
4.2.4 Room Temperature Fracture Toughness Testing.....	105
4.2.5 Elevated Temperature Fracture Toughness Testing.....	105
4.3 Fractography.....	114
4.3.1 Room Temperature Tensile Specimens.....	114
4.3.2 Elevated Temperature Tensile Specimens Tested in Vacuum.....	124
4.3.3 Room Temperature Fracture Toughness Specimens.....	140
4.3.4 Elevated Temperature Fracture Toughness Specimens.....	140
5. DISCUSSION	149
5.1 Room Temperature Deformation and Fracture.....	149
5.1.1 Tensile Behavior	149
5.1.2 Fracture Toughness.....	158
5.2 Elevated Temperature Deformation and Fracture	160
5.2.1 Work Hardening and Strengthening.....	160

5.2.2	Tensile Failure.....	162
5.2.2.1	Behavior in the Range 450°C - 600°C.....	163
5.2.2.2	Behavior in the Range 650°C - 750°C.....	169
5.2.3	Environmental Effects.....	175
5.2.4	Elevated Temperature Toughness.....	177
6.	SUMMARY AND CONCLUSIONS	180
7.	RECOMMENDATIONS FOR FUTURE RESEARCH	184
8.	REFERENCES	187

DTIC QUALITY INSPECTED 4

Accession For	
NTIS CRA&I	<input checked="" type="checkbox"/>
DTIC TAB	<input type="checkbox"/>
Unannounced	<input type="checkbox"/>
Justification	
By	
Distribution /	
Availability Codes	
Dist	Avail and/or Special
A-1	

LIST OF TABLES

Table 2.1	Slip systems of the hexagonal crystal.....	26
Table 2.2	Prediction of slip system activity in the α_2 phase (after Court et al. 70).....	38
Table 3.1	Work piece forging temperatures.....	62
Table 3.2	Anneal and age treatments for microstructures 25/C, 10/C and 0/C.....	63
Table 3.3	Chemical analysis of the heat under study.....	63
Table 4.1	Analysis of final microstructures.....	73
Table 4.2	Room temperature tensile test results.	80
Table 4.3	Work hardening exponents at room temperature.	81
Table 4.4	Elevated temperature tensile properties from round specimens tested in vacuum.	86
Table 4.5	Elevated temperature tensile properties for flat specimens.....	87
Table 4.6	Strain rate hardening exponents for round tensile specimens.....	99
Table 4.7	Elevated temperature tensile properties of microstructure 0/F tested in air.....	103
Table 4.8	Room temperature fracture toughness values.....	105
Table 4.9	Raw data from elevated temperature J testing.....	107
Table 4.10	Elevated temperature J_{Ic} data.....	108
Table 4.11	Estimates of three point bend bar crack propagation rate	108
Table 5.1	Physical values for fine secondary α_2 microstructures.....	168

LIST OF FIGURES

Figure 2.1	The Ti-Al phase diagram (after Refs. 11 and 12).....	5
Figure 2.2	Proposed Ti-Al-Nb ternary phase diagram at 900°C.....	6
Figure 2.3	Temperature-composition diagram for Ti-25Al-10Nb-3V-1Mo. Samples were isothermally aged for 168 hours after a 2 hour b solution heat treatment. Arrow indicates the nominal alloy composition.....	7
Figure 2.4	Depiction of interfacial misfit dislocation structure between α_2 and b (after Ref. 33).....	12
Figure 2.5	(a) AEM micrograph of primary α_2 grains in a recovered and quenched B2 matrix. (b) Light micrograph showing primary α_2 grains pinning recrystallized B2 grains, sample was quenched from high in the α_2 + B2 phase field (after Ref. 28).....	13
Figure 2.6	(a) Microstructure produced by hot-die forging at 1107°C and direct salt-bath age at 815°C for 30 minutes. YS: 942 MPa, UTS: 1097 MPa, Elongation: 2.7%. (b) Microstructure produced by hot-die forging at 1107°C followed by an oil quench. The forging was then annealed at 1107°C for 1 hour and given a direct salt-bath age at 815°C for 30 minutes. YS: 759 MPa, UTS: 963 MPa, Elongation: 2.6% (after Ref. 28).....	14
Figure 2.7	(a) SEM micrograph showing differences in scale of secondary α_2 across the prior b grain boundary. (b) SEM micrograph exhibiting the crystallographic nature of growth of the cellular reaction (after Ref. 30).....	16
Figure 2.8	(a) AEM micrograph of cellular reaction formed by synchronous growth of α_2 +B2 behind a common interface. (b) AEM micrograph of cellular reaction formed by growth of α_2 "fingers" into the fine scaled matrix (after Ref. 30).....	17
Figure 2.9	Comparison of the (0001) $_{\alpha_2}$ and (001) $_O$ planes.....	18
Figure 2.10	Ti-24-11 α_2' plate showing APD growth from the midrib (after Ref. 12).....	22
Figure 2.11	Proposed time-temperature-transformation curve for Ti-25-10-3-1 (after Ref. 13).....	24
Figure 2.12	Plot showing the dependence of yield strength on the inverse of interlath spacing, l , for Ti-25-10-3-1 with a volume fraction of primary α_2 in the range of 0.15-0.40.	40
Figure 2.13	Tensile properties of Ti-25-10-3-1 as a function of temperature, testing performed in air. Material was α_2 +b forged at 1085°C and direct salt bath aged at 815°C for 30 min (after Ref. 85).....	42

Figure 2.14	Microstructure with an aligned "packet" morphology of secondary α_2 laths. YS: 745 MPa, UTS: 907 MPa, Elongation: 1.1% (after Ref. 28).	44
Figure 2.15	(a) Room temperature tensile specimen cross-section showing the cleavage of primary α_2 grains. Microstructure contains fine Widmanstätten α_2 laths. (b) SEM of the fracture surface of sample in (a) showing area near the failure initiation site, note the cleaved primary α_2 grains (after Ref. 86).	45
Figure 2.16	Tensile elongation and reduction of area for α_2 +b forged Ti-25-10-3-1 with fine and coarse Widmanstätten microstructures as a function of temperature. Testing performed in vacuum (after Ref. 86).	48
Figure 2.17	(a) Light micrograph of a cross-sectioned tensile sample, tested at 425°C. Microstructure contains fine Widmanstätten α_2 laths. (b) SEM micrograph of the fracture surface at a location near the initiation site at a prior b grain boundary (after Ref. 86).	49
Figure 2.18	Fracture toughness, from valid K_{Ic} tests, plotted to 540°C from Blackburn and Smith and DeLuca and Cowles. Microstructure was b processed with fine secondary α_2 laths (after Refs. 4 and 95).	50
Figure 2.19	(a) Light micrograph of a cross-sectioned tensile sample, tested at 540°C. Microstructure contains fine Widmanstätten α_2 laths. Note the alignment of α_2 laths. (b) SEM micrograph of the fracture surface of the same test in (a) (after Ref. 86).	51
Figure 2.20	Fracture stress and yield strength for both a fine and coarse Widmanstätten microstructure as a function of temperature (after Ref. 86).	51
Figure 2.21	(a) Light micrograph of a cross-sectioned tensile sample, tested at 650°C. Microstructure contains coarse α_2 laths. Note the alignment of α_2 laths. (b) SEM micrograph the fracture surface of the same test in (a) (after Ref. 86).	52
Figure 3.1	Locations where specimens were machined from the forgings.	68
Figure 3.2	Axisymmetric round tensile bar. All dimensions are in millimeters.	69
Figure 3.3	Flat tensile bar. All dimensions are listed in millimeters.	69
Figure 3.4	Three-point bend bar used for elevated temperature J-testing. All dimensions are listed in millimeters.	69
Figure 3.5	Compact tension specimen used for room temperature fracture toughness. All dimensions are listed in millimeters.	70
Figure 4.1	Microstructure 25/C. (a) Light micrograph (b) SEM micrograph.	74
Figure 4.2	Microstructure 25/F. (a) Light micrograph (b) SEM micrograph.	74

Figure 4.3	Microstructure 10/C. (a) Light micrograph (b) SEM micrograph.	75
Figure 4.4	Microstructure 10/F. (a) Light micrograph (b) SEM micrograph.....	75
Figure 4.5	Microstructure 0/C. (a) Light micrograph (b) SEM micrograph.....	76
Figure 4.6	Microstructure 0/F. (a) Light micrograph (b) SEM micrograph.	76
Figure 4.7	(a) AEM micrograph of microstructure in microstructure 0/F. (b) Microdiffraction pattern showing the $[001]_{B2}$ zone.....	77
Figure 4.8	X-ray plot of microstructure 10/F. Peaks corresponding to the α_2 , B2 and ordered orthorhombic phases are evident.....	77
Figure 4.9	X-ray plot of microstructure 0/C. Peaks corresponding to the α_2 , and the B2 phases are evident.	78
Figure 4.10	X-ray plot of microstructure 0/F. Peaks corresponding to the α_2 , B2 and ordered orthorhombic phases are evident.....	78
Figure 4.11	Engineering stress-strain and AE RMS voltage-strain curves for room temperature tensile tests of the fine and coarse secondary α_2 microstructures.....	82
Figure 4.12	Data from round tensile specimens of microstructure 10/F tested in vacuum. (a) Plastic elongation and reduction of area at failure as a function of temperature. (b) Yield strength and ultimate tensile strength as a function of temperature.	88
Figure 4.13	Data from round tensile specimens of microstructure 0/C tested in vacuum. (a) Plastic elongation and reduction of area at failure as a function of temperature. (b) Yield strength and ultimate tensile strength as a function of temperature.	89
Figure 4.14	Data from round tensile specimens of microstructure 0/F tested in vacuum. (a) Plastic elongation and reduction of area at failure as a function of temperature. (b) Yield strength and ultimate tensile strength as a function of temperature.	90
Figure 4.15	(a) Representative engineering stress-strain plots of microstructure 10/F in vacuum.....	91
	(b) Representative true stress-true strain plots of microstructure 10/F in vacuum at a strain rate of 10^{-2} s^{-1}	92
Figure 4.16	(a) Representative engineering stress-strain plots of microstructure 0/C in vacuum.....	93
	(b) Representative true stress-true strain plots of microstructure 0/C in vacuum at a strain rate of 10^{-2} s^{-1}	94
Figure 4.17	(a) Representative engineering stress-strain plots of microstructure 0/F in vacuum.....	95

	(b) Representative true stress-true strain plots of microstructure 0/F in vacuum at a strain rate of 10^{-2} s^{-1}	96
Figure 4.18	True fracture stress and strain for microstructure 10/F plotted as a function of temperature.....	97
Figure 4.19	True fracture stress and strain for microstructure 0/C plotted as a function of temperature.....	97
Figure 4.20	True fracture stress and strain for microstructure 0/F plotted as a function of temperature.....	98
Figure 4.21	Strain hardening exponent, n , plotted as a function of temperature for (a) $0.01 < \epsilon < 0.10$ (b) $\epsilon > \epsilon_u$ for microstructure 10/F.....	100
Figure 4.22	Strain hardening exponent, n , plotted as a function of temperature for (a) $0.01 < \epsilon < 0.10$ (b) $\epsilon > \epsilon_u$ for microstructure 0/C.....	101
Figure 4.23	Strain hardening exponent, n , plotted as a function of temperature for (a) $0.01 < \epsilon < 0.10$ (b) $\epsilon > \epsilon_u$ for microstructure 0/F.....	102
Figure 4.24	Light macrograph of tensile specimens of microstructure 0/F tested in air at 650°C . (a) Strain rate of $2 \times 10^{-3} \text{ s}^{-1}$. (b) Strain rate of $1 \times 10^{-1} \text{ s}^{-1}$	104
Figure 4.25	J vs. Δa plot for microstructure 10/F, 450°C	109
Figure 4.26	J vs. Δa plot for microstructure 10/F, 550°C	109
Figure 4.27	J vs. Δa plot for microstructure 10/F, 650°C	110
Figure 4.28	J vs. Δa plot for microstructure 0/C, 450°C	110
Figure 4.29	J vs. Δa plot for microstructure 0/C, 550°C	111
Figure 4.30	J vs. Δa plot for microstructure 0/C, 650°C	111
Figure 4.31	J vs. Δa plot for microstructure 0/F, 450°C	112
Figure 4.32	J vs. Δa plot for microstructure 0/F, 550°C	112
Figure 4.33	J vs. Δa plot for microstructure 0/F, 650°C	113
Figure 4.34	Combined fracture toughness data for all three microstructures.....	113
Figure 4.35	Room tensile fracture surface of microstructure 10/C.....	117
Figure 4.36	Initiation region in sample shown in Figure 4.35.....	117
Figure 4.37	Magnification of Figure 4.36.....	117
Figure 4.38	Fracture surface of a room temperature tensile specimen from microstructure 10/F.....	117

Figure 4.39	Surface of the strained flat tensile specimen from microstructure 25/F.....	118
Figure 4.40	Flat tensile specimen surface from microstructure 0/C. Crack nucleation occurring at slip band intersections.	118
Figure 4.41	Flat tensile specimen surface from microstructure 0/C. Cracking across adjoining prior β grain boundaries.	118
Figure 4.42	Flat tensile specimen surface from microstructure 10/C. Matrix slip band intersection with a failed primary α_2 grain.	118
Figure 4.43	Flat tensile specimen surface from microstructure 25/F. Crack nucleation along slip bands in primary α_2 grain.	119
Figure 4.44	Flat tensile specimen surface from microstructure 25/F. Crack nucleation at interface of primary α_2 grain and matrix.	119
Figure 4.45	Flat tensile specimen surface from microstructure 10/F. Slip band intersections with the α_2 /matrix interface.	119
Figure 4.46	Flat tensile specimen surface from microstructure 25/F. Crack nucleation normal to tensile axis within a primary α_2 grain.	119
Figure 4.47	Sectioned tensile specimen from microstructure 10/C.....	122
Figure 4.48	Sectioned tensile specimen from microstructure 0/C.	122
Figure 4.49	Sectioned tensile specimen from microstructure 10/C. Crack nucleation within primary α_2 grains and at primary α_2 /matrix interfaces.....	122
Figure 4.50	Sectioned tensile specimen from microstructure 10/C. Crack nucleation at primary α_2 /matrix interfaces and extension into the matrix.....	122
Figure 4.51	Sectioned tensile specimen from microstructure 10/C. Enlargement of crack tip from Figure 4.50.....	123
Figure 4.52	Sectioned tensile specimen from microstructure 0/C. Crack nucleation associated with the prior β grain boundary.	123
Figure 4.53	Sectioned tensile specimen from microstructure 0/C. Enlargement of crack tip region in Figure 4.52.....	123
Figure 4.54	Round tensile specimen from microstructure 10/F tested at 450°C.	129
Figure 4.55	Tensile specimen from microstructure 10/F tested at 450°C. Near apparent initiation site at prior β grain boundary.....	129
Figure 4.56	Enlargement of the prior β grain boundary area in Figure 4.55 showing fine dimples associated with the initiation site.....	129

Figure 4.57	Center of a round tensile specimen from microstructure 10/F tested at 450°C with a duplex distribution of fracture features.	129
Figure 4.58	Tensile specimen from microstructure 10/F tested at 650°C showing a more ductile appearing fracture surface.	130
Figure 4.59	Tensile specimen from microstructure 10/F tested at 650°C with larger dimples.	130
Figure 4.60	Tensile specimen from microstructure 10/F tested at 750°C. Fracture surface has even larger and more uniformly spaced dimples.	130
Figure 4.61	Enlargement of the dimple structure in Figure 4.60. Dimples exhibit a textured appearance along their walls.	130
Figure 4.62	Tensile specimen from microstructure 0/F tested at 650°C. Region on fracture surface exhibiting failure along an inclined prior β grain boundary.	131
Figure 4.63	Tensile specimen from microstructure 0/F tested at 650°C. Fracture surface now exhibits larger dimples mixed with the finer ones seen at lower temperature.	131
Figure 4.64	Tensile specimen from microstructure 0/F tested at 750°C. Dimple size was about half that in microstructure 10/F at the same temperature.	131
Figure 4.65	Tensile bar from microstructure 0/C tested at 450°C. Near the failure initiation site on fracture surface, showing aligned secondary α_2 structure.	131
Figure 4.66	Tensile bar from microstructure 0/C tested at 700°C. Fracture surface reveals primarily intergranular failure along the prior β grain boundaries.	132
Figure 4.67	Tensile bar from microstructure 10/F tested at 450°C. Primary α_2 was elongated in direction of the tensile axis, with voids nucleating at ends.	132
Figure 4.68	Tensile bar from microstructure 10/F tested at 500°C. Primary α_2 grains are observed to fail by cracking along a plane inclined to the tensile stress.	132
Figure 4.69	Tensile bar from microstructure 10/F tested at 650°C. The fraction of voids has increased dramatically compared to lower test temperatures.	132
Figure 4.70	Tensile bar from microstructure 10/F tested at 650°C. A number of voids are observed to have coalesced below the fracture surface.	133
Figure 4.71	Tensile bar from microstructure 10/F tested at 750°C. The volume fraction of voids has continued to rise from 650°C.	133

Figure 4.72	Tensile bar from microstructure 0/F tested at 650°C. A large number of voids has nucleated below the fracture surface.....	133
Figure 4.73	Tensile bar from microstructure 0/F tested at 750°C. A much larger volume fraction of voids was present as compared to 650°C.....	133
Figure 4.74	Tensile bar from microstructure 0/C tested at 550°C. Cracks nucleated at a prior β grain boundary.....	134
Figure 4.75	Enlargement of cracks in microstructure 0/C tested at 550°C showing that they appear to nucleate at the α_2 /B2 interfaces.....	134
Figure 4.76	Tensile bar from microstructure 0/C tested at 650°C. Cracks nucleate at prior β grain boundaries which are normal to the tensile axis.....	134
Figure 4.77	Enlargement of cracked region in microstructure 0/C tested at 650°C showing separation of the grain boundary α_2 and B2 interface.....	134
Figure 4.78	Tensile bar from microstructure 0/C tested at 700°C showing separation of the prior β grain boundaries.....	135
Figure 4.79	Surface of a flat tensile bar from microstructure 10/F at 650°C. Fine slip bands intersect with primary α_2 grains.....	135
Figure 4.80	Surface of flat tensile bar from microstructure 0/F. Slip band intersections at a prior β grain boundary.....	135
Figure 4.81	Surface of flat tensile bar from microstructure 0/C. Slip band intersections at a prior β grain boundary.....	135
Figure 4.82	True strain to tensile failure and true strain measured in the primary α_2 particles in microstructure 10/F as a function of temperature.....	136
Figure 4.83	(a) True fracture stress and void nucleation stress, and (b) True fracture strain and void nucleation strain plotted as a function of temperature for microstructure 10/F.....	137
Figure 4.84	(a) True fracture stress and void nucleation stress, and (b) True fracture strain and void nucleation strain plotted as a function of temperature for microstructure 0/C.....	138
Figure 4.85	(a) True fracture stress and void nucleation stress, and (b) True fracture strain and void nucleation strain plotted as a function of temperature for microstructure 0/F.....	139
Figure 4.86	Metallographic section of K_{Ic} specimen from microstructure 10/F tested at room temperature. Fracture path was flat.....	143
Figure 4.87	Metallographic section of K_{Ic} specimen from microstructure 0/C tested at room temperature. Fracture path was still relatively flat.....	143
Figure 4.88	Enlargement of sectioned crack path from microstructure 10/C showing limited secondary cracking.....	143

Figure 4.89	Light macrograph of broken J bend bar from microstructure 10/F tested at 450°C.....	143
Figure 4.90	Light macrograph of broken J bend bar from microstructure 10/F tested at 550°C.....	144
Figure 4.91	Light macrograph of broken J bend bar from microstructure 10/F tested at 650°C.....	144
Figure 4.92	Light macrograph of broken J bend bar from microstructure 0/C tested at 650°C.....	144
Figure 4.93	Fracture surface of J bend bar from microstructure 10/F tested at 450°C.....	144
Figure 4.94	Fracture surface of J bend bar from microstructure 0/F tested at 550°C.....	145
Figure 4.95	Enlargement of fracture surface in Figure 4.94.	145
Figure 4.96	SEM macrograph of broken J bend bar from microstructure 10/F tested at 650°C.....	145
Figure 4.97	Enlarged view of Figure 4.96 showing fracture by a brittle mode.....	145
Figure 4.98	Enlarged view of Figure 4.97 showing primary α_2 with river markings.....	146
Figure 4.99	SEM macrograph of broken J bend bar from microstructure 0/F tested at 650°C.....	146
Figure 4.100	SEM macrograph of broken J bend bar from microstructure 0/C tested at 650°C.....	146
Figure 4.101	Metallographic section of J bend bar from microstructure 10/F tested at 450°C.	146
Figure 4.102	Metallographic section of J bend bar from microstructure 0/F tested at 550°C.....	147
Figure 4.103	Metallographic section of J bend bar from microstructure 0/C tested at 550°C.....	147
Figure 4.104	Enlargement of bifurcating crack front in Figure 4.102.....	147
Figure 4.105	Metallographic section of J bend bar from microstructure 10/F tested at 650°C.....	148
Figure 4.106	Enlargement of crack tip region in Figure 4.105.....	148
Figure 4.107	Metallographic section of J bend bar from microstructure 10/F tested at 650°C.....	148

Figure 4.108	Metallographic section of J bend bar from microstructure 0/C tested at 650°C.....	148
Figure 5.1	Depiction of failure in a primary α_2 particle by slip band decohesion. Slip band length corresponds to particle size.	154
Figure 5.2	Schematic of matrix slip band intersecting with a primary α_2 particle. Slip band length corresponds to secondary α_2 packet size.	155
Figure 5.3	Schematic of matrix slip band intersecting with grain boundary α_2 . Slip band length corresponds to secondary α_2 packet size.	155
Figure 5.4	Crack propagation process through secondary α_2 laths.....	156
Figure 5.5	Schematic of crack propagation along a prior β grain boundary depicting the origin of dimples seen on the fracture surface. The dark features represent the β /B2 phase.....	157
Figure 5.6	Stress intensity factor, K, plotted against the ratio of applied true stress over yield strength at 450°C. The horizontal line indicates the measured fracture toughness, and the box denotes the experimentally measured values at failure. Plotted from the values of the fine secondary α_2 microstructures 10/F and 0/F.	169
Figure 7.1	Two different microstructures of the same material with the same volume fraction of ductile phase, but differing distributions of the ductile phase.....	185

ACKNOWLEDGMENT

I am very grateful to both of my thesis advisors, Dr. J.C. Williams of General Electric Aircraft Engines and Professor A.W. Thompson of Carnegie Mellon University, for taking time to guide and encourage me over the past several years. Their technical insight and wisdom were invaluable to me. Furthermore, I acknowledge the many positive interactions I had with Professor D.A. Koss of the Pennsylvania State University and Professor W.M. Garrison of Carnegie Mellon University who were also members of my thesis committee. Each was very helpful throughout my research and offered many valuable suggestions.

Most of the research in this thesis was completed at the Materials Development Branch, Materials Directorate, Wright Laboratory, Wright-Patterson AFB, OH. I owe Mr. G. Petrak of the Materials Development Branch a great deal of thanks for his confidence in me and for providing a wonderful environment in which to work. I am also indebted to both Dr. D. Dimiduk of the Materials Development Branch and Dr. J. Larsen of the Materials Behavior Branch for supplying me with abundant and high quality experimental resources for performing my research. Additionally, many of my thanks go to Dr. M. Peters for graciously hosting my stay at the German Aerospace Research Establishment, Cologne, Germany. Col. J. Gerber and Mrs. J. Messenger were both very generous in their help by organizing this stay, which was under sponsorship of the U.S. Air Force Scientist and Engineering Exchange Program. Additionally, my heartfelt thanks goes to Mr. T. Broderick of the Materials Development Branch whose stimulating discussions on titanium aluminide physical and mechanical metallurgy helped immensely.

This thesis may not have been possible without the generous support of Mr. D. Rosenthal of Textron-Lycoming who provided the material for this research. The large amount of experimental testing in the course of my research was only feasible due to the tireless help I received from many individuals. In particular, Messrs. G. Hartman,

G. Steinlage, P. Stibich, T. Johnson, J. Eschweiler, J. Eblin, J. Ruschau, S. Apt, and A. Kraus were most kind in giving their time and expertise to aid me in my research.

Much credit is due my parents, Charles and Marguerite Ward, who have always supported and encouraged me in all of my decisions, giving me the confidence to reach for the highest goals. I most of all thank my wife, Laura, for her unwavering understanding and patience during the past several years.

1. INTRODUCTION

Alloys based on the titanium aluminide compound Ti_3Al , referred to as α_2 , have been studied for over thirty years. The intent of these efforts has been to increase the high temperature capability of titanium based alloys. Applications originally intended for this intermetallic class were to be propulsion components, but more recently it has also been considered for use in hypersonic airframe structural components.

An initial alloying study by McAndrew and Simcoe in the 1950's concentrated on Ti-Al-Nb alloys and identified niobium as a potential ductilizing and oxidation resistance enhancing addition to higher aluminum containing titanium alloys.¹ One of the alloys examined during their study was Ti-26Al-10Nb (a/o) which exhibited a yield strength of 552 MPa, an ultimate tensile strength of 738 MPa and a tensile elongation of 3% (All alloy compositions in this paper will be represented in atomic percent). Research on α_2 alloys expanded in the 1960's and early 1970's as nickel-based superalloys were maturing and meeting the engine designer's need for an intermediate temperature material (up to $\sim 815^\circ\text{C}$). The oil crisis in the early 1970's spurred a resurgence in the research of these low density alloys in the interest of increased engine efficiency. Nearly twenty years after McAndrew and Simcoe; Blackburn, Ruckle and Bevan identified the alloy we now know as Ti-24Al-11Nb (Ti-24-11) as the most promising from a very large alloying matrix.² Since that time a large number of researchers have attempted to improve the properties of this intermetallic system, particularly tensile ductility, fracture toughness and creep resistance. Blackburn and Smith found that a higher niobium alloy, Ti-25Al-14Nb, had improved ductility and fracture toughness compared to Ti-24-11.³ Based on this alloy they formulated Ti-25Al-10Nb-3V-1Mo (Ti-25-10-3-1).⁴ Vanadium was added as a lower density β -stabilizing alternative to niobium, while molybdenum was added to improve high temperature strength. The goal was to keep the higher volume fraction of the β phase.

While a number of previous reviews have been written, most have concentrated on the mechanical properties and applications of titanium aluminides.^{5,6,7,8,9} The intent of

this overview is to examine the aspects germane to understanding the effects of microstructure on tensile and fracture behavior of the $\alpha_2+\beta$ /B2 titanium aluminides. These aspects first of all must include a thorough understanding of the way in which microstructure develops. Without this knowledge one cannot arrive at the broad range of microstructures available in this system and, more importantly, the equilibrium phases and their stable morphologies. Second, the dislocation behavior of this material should be well characterized as dislocation slip is the fundamental basis for deformation in these alloys. And last, a presentation of the current knowledge in the area of microstructure/property relationships for this material is required to define the critical issues and avoid unnecessary duplication.

2. BACKGROUND

2.1 Physical Metallurgy

After 35 years of research in the Ti₃Al intermetallic system, equilibrium phase constituents and transformation sequences in the Ti-Al-Nb ternary system are still not well understood. The physical metallurgy of this system is extremely complex, with apparently no less than 11 different phases being required to describe this system. Due to the complexities of the reactions in the Ti-25Al-xNb system, it is best to start with a brief definition of the symbols and origins of the phases to be discussed. β refers to the high temperature disordered bcc phase found in these alloys. B2 (sometimes referred to as β_0) is the ordered derivative of the β phase. Ordering of $\beta \rightarrow B2$ occurs near what is usually called the β transus.¹⁰ Above the β transus, only single phase β or B2 exists. This ambiguity is present due to the lack of experimental data on the $\beta \rightarrow B2$ ordering reaction. Below the β transus the α_2 phase is present, α_2 refers to the ordered hexagonal structure of Ti₃Al.¹¹ α' is the disordered hexagonal martensite formed in alloys from 0 to somewhere less than 15 a/o niobium by shearing of the β phase.¹² α' undergoes diffusional ordering and thickening in alloys with less than 12 a/o niobium to become α_2' . Between approximately 12 and 15 a/o niobium, a metastable ordered orthorhombic phase, O', may nucleate at the α' interface and grow into the matrix.¹³ On long term aging, O' decomposes to $\alpha_2 + B2$. At 15 a/o niobium and above, the martensite is formed by the shearing of the ordered B2 phase, resulting in an ordered orthorhombic structure, termed here α_2'' .^{10,12,14} This too nucleates O' at its interface. On aging, the O' phase in this composition range may decompose to O + $\alpha_2 + B2$ or just O + B2. The O phase may also form by nucleation and growth. O is the equilibrium ordered orthorhombic phase. Finally, ω' , ω'' and B8₂ describe the metastable ω -type phases found in a wide compositional range of Ti-25Al-xNb alloys.^{15,16,17}

However, the phase transformation progression from melt to room temperature is reasonably clear in the binary Ti-Al system. At the composition Ti-25Al, the disordered β phase is first to form from the melt. On further cooling, the alloy goes through the $\alpha+\beta$ two phase region and emerges into the narrow single phase α field, enters the $\alpha+\alpha_2$ two phase region, and finally ends in the single phase α_2 region which persists to room temperature.¹⁸ The most current binary phase diagram proposed is shown in Figure 2.1.^{19,20} A number of phase diagrams for the Ti-Al-Nb ternary system have been proposed, although there remains considerable debate over its construction. A representative diagram is shown here to aid the reader in envisioning this complex system, Figure 2.2.^{10,21,22} A temperature-composition diagram is presented in Figure 2.3 for the alloy Ti-25-10-3-1.²³ This diagram cannot be considered a true pseudo-binary phase diagram as five alloying elements are being considered, but it is instructional to envision what a slice through the ternary diagram may look like.

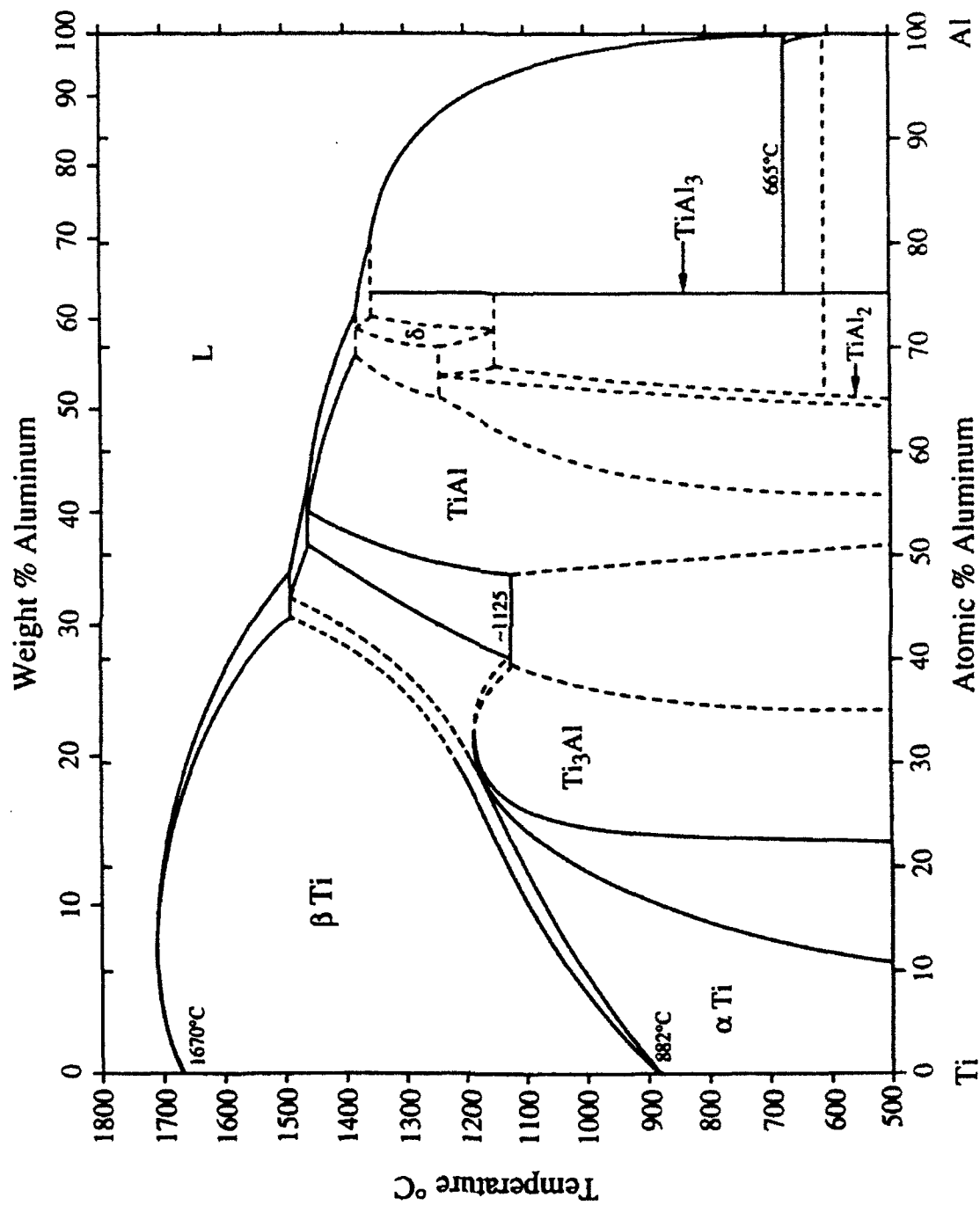


Figure 2.1 The Ti-Al phase diagram (after Refs. 11 and 12).

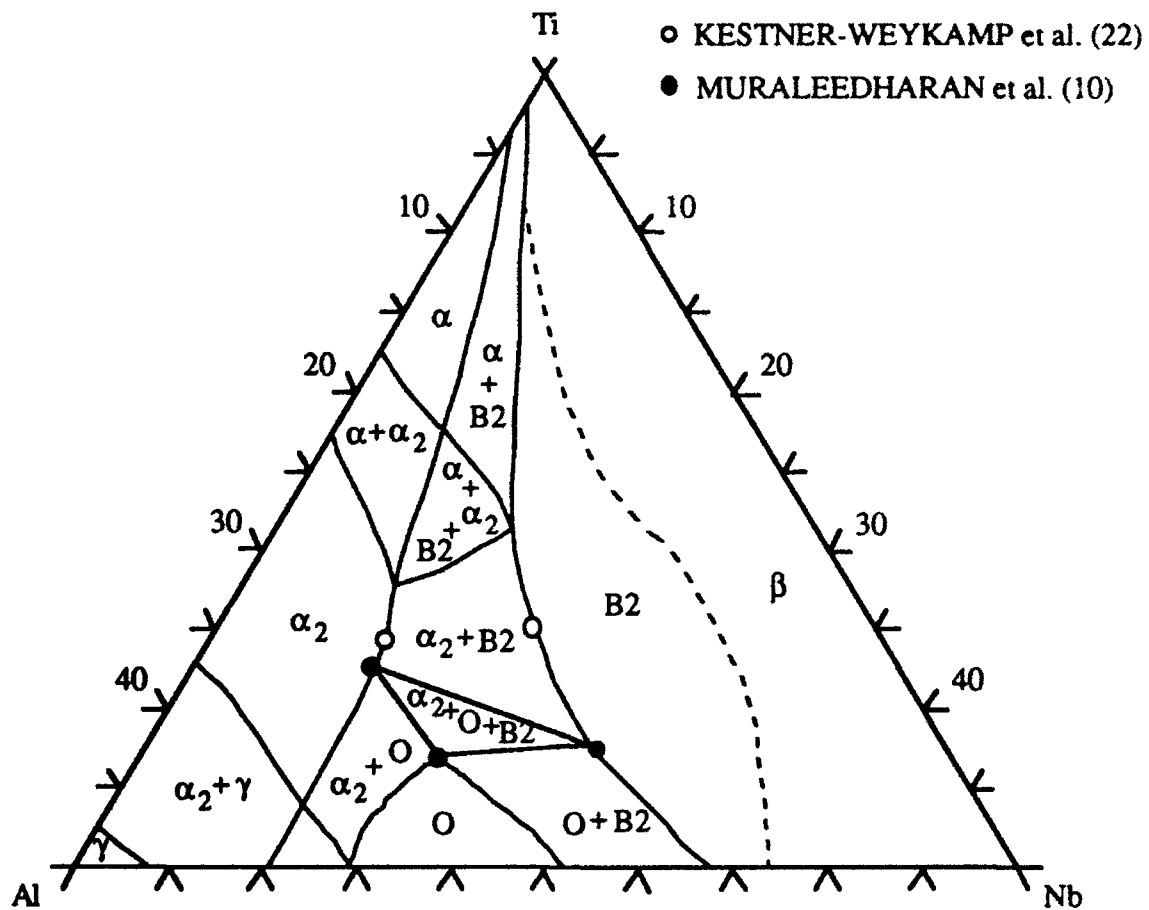


Figure 2.2 Proposed Ti-Al-Nb ternary phase diagram at 900°C
(after Refs. 10, 21 and 22)

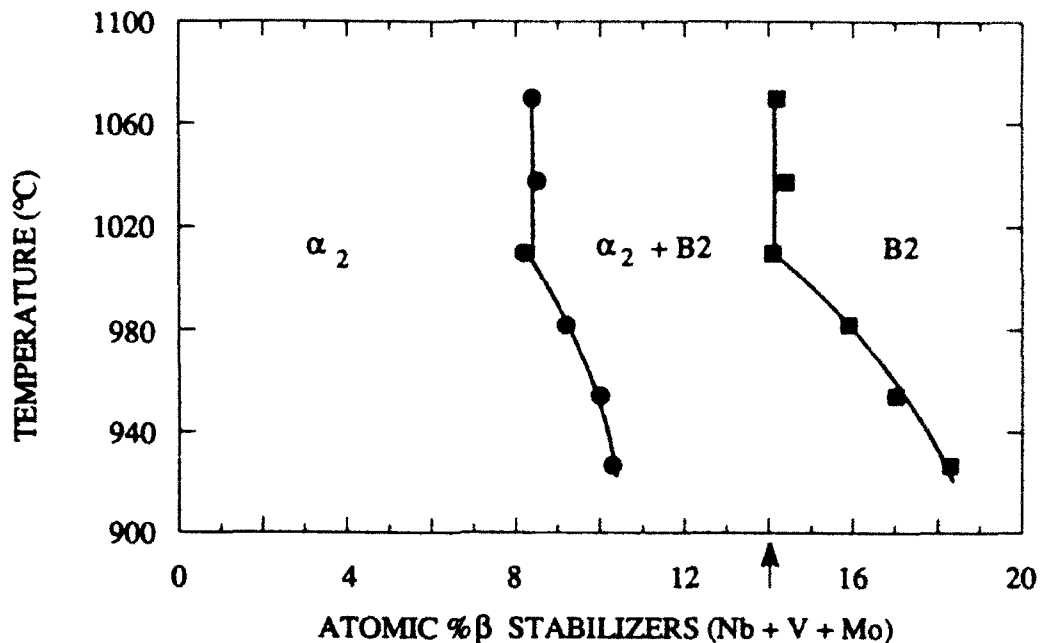


Figure 2.3 Temperature-composition diagram for Ti-25Al-10Nb-3V-1Mo. Samples were isothermally aged for 168 hours after a 2 hour β solution heat treatment. Arrow indicates the nominal alloy composition.

2.1.1 " β " phase

The equilibrium " β " phase has been difficult to characterize in these alloys because of its limited presence at even intermediate temperatures. The ordering of the β phase (A2 crystal structure, $Im\bar{3}m$ space group) to the B2 crystal structure (CsCl crystal structure, $Pm\bar{3}m$ space group) in aluminum rich titanium alloys has been long known, and is found in the Ti-25Al-xNb system as well.^{24,25} However, the critical temperature, T_c , at which β orders has not been accurately determined across the Ti-25Al-xNb system. This is an important parameter that must be known when considering decomposition paths. For Ti-24-11, containing both α_2 and β /B2, analytical electron microscopy has shown in aged and quenched samples that the β phase is ordered at temperatures above 1000°C, but below some T_c .²² At temperatures between 900°C and 1000°C the β is disordered but orders to

the B2 crystal structure during quenching. However, the equilibrium β phase in Ti-24-11 is disordered at temperatures $\leq 800^\circ\text{C}$. Two concurrent compositional changes are occurring with this order to disorder transition; as the B2 phase exhibits more propensity for disordering, its matrix is becoming depleted in aluminum and enriched in niobium. Banerjee *et al.* have shown that in the ordered B2 phase of the Ti-25.6Al-10.1Nb alloy, titanium atoms occupy one sublattice, aluminum atoms the other.²⁶ The remaining sites in the aluminum sublattice are split almost equally between Nb and Ti. Very little Nb, and virtually no Al atoms occupy the titanium sites. As titanium and niobium are known to be isomorphous in a disordered A2 structure, aluminum must be largely responsible for ordering within the B2 phase. However, in the alloy Ti-24.5Al-15Nb, where the T_c for A2 \rightarrow B2 ordering is just higher than the B2/ α_2 +B2 boundary, the B2 phase is found to remain ordered at temperatures down to at least 650°C .¹⁰ In this case, the niobium concentrations in the B2 phase are higher while the aluminum content is similar to that in Ti-24-11. This difference in niobium content appears to be responsible for the retention of order to much lower temperatures. In Ti-25-10-3-1 no evidence of disordered β , either at temperature or on quenching from temperature, has been found at heat treatment temperatures from the β transus down to 815°C .²³

Strychor *et al.* have characterized rapidly quenched alloys lying in the single and two phase region of the pseudo-binary diagram.^{15,16} Much of their work concentrated on analytical electron microscopic (AEM) characterization of the B2 phase, which was formed when niobium bearing alloys were quenched to room temperature. Two independent diffraction effects were identified in the selected area diffraction patterns (SADP's).¹⁶ First was streaking along the $\langle 110 \rangle$ directions in the $[001]_{B2}$ zone, this streaking was not observed along $\langle 110 \rangle$ in the $[011]_{B2}$ zone. A mottled structure, or tweed, in the B2 phase was found to be associated with the $\langle 110 \rangle$ streaking in the SADP's. This tweed contrast was proven to be due to lattice shear strains on $\{110\}$ planes along $\langle 1\bar{1}0 \rangle$ directions. This shear strain configuration is consistent with the absence of streaking along $\langle 110 \rangle$ in the

$[011]_{B2}$ zone as $\mathbf{g} \cdot \boldsymbol{\varepsilon} = 0$, where $\boldsymbol{\varepsilon}$ is the polarization vector.²⁷ The tweed structure has been previously associated with a pre-martensitic reaction in other metallic systems. In addition, these lattice distortion waves lead to small regions of pseudo-hexagonal (2H) structure. The second diffraction effect was characterized by streaking and diffuse intensity along the $\langle 112 \rangle$ directions in the $[011]_{B2}$ zone. Streaking along $\langle 112 \rangle$ is caused by longitudinal planewave atomic displacements along $\langle 111 \rangle$ with a wave vector of $\mathbf{k}_\omega = 2/3\langle 111 \rangle$, or, equivalently, a transverse wave along $\langle 111 \rangle$ with $\mathbf{k}_\omega = 1/3\langle 112 \rangle$. These planewaves are consistent with the formation of an ω -type phase, which will be discussed in greater detail below.

During, or as the result of, thermomechanical processing, the $\beta/B2$ phase may undergo either recrystallization or recovery.²⁸ Both of these processes are able to occur when the material is processed in the $\alpha_2 + \beta/B2$ phase region. While some limited temperatures and strains which define these regions have been identified,²⁹ a comprehensive study has not yet been conducted.

2.1.2 ω phase

Decomposition of β to form a hexagonal ω phase is a well documented process in conventional titanium alloys. As mentioned previously, Strychor and co-workers identified the formation of an ω -like phase in the B2 phase of certain Ti-Al-Nb alloys.¹⁶ This phase, which is formed on rapid quenching from the β phase field and is thus considered athermal, takes on its parent B2 matrix ordering. This process occurs by the collapse of $\{111\}_{B2}$ planes, and can be described by the longitudinal plane wave $\mathbf{k}_\omega = 2/3\langle 111 \rangle$. The collapse of planes results in an ordered ω -type phase, ω' , which has an orientation relationship to the B2 matrix of $\{111\}_{B2} \parallel (0001)_{\omega'}$, $\langle 110 \rangle_{B2} \parallel \langle 11\bar{2}0 \rangle_{\omega'}$. On aging, the athermal ω' phase undergoes a secondary ordering reaction to produce ω'' .^{16,17} Further aging leads to the precipitation of the $B8_2$ phase from ω'' .^{16,17} The sequence of symmetry

transformations has been described by Bendersky *et al.* to progress in the order $Pm\bar{3}m$ (B2) $\rightarrow P\bar{3}m1$ (ω' , ω'') $\rightarrow P6_3/mmc$ (B8₂), where the B8₂ phase is more stable than either ω' or ω'' .¹⁷ An ω -type phase exists in the quenched-in B2 condition in both Ti-24-11 and Ti-25-10-3-1 alloys.^{16,17,30}

While the formation of the low temperature ω -type phase is certainly an interesting metallurgical feature, it is metastable and therefore does not appear to hold much significance with regard to mechanical properties in equilibrium microstructures in the Ti-25Al-xNb system.

2.1.3 α_2 phase

In this section, the structural differences between α_2 and O will be temporarily ignored for simplicity. In most cases, remarks in this section regarding the morphology and distribution of the α_2 phase can also be applied to the O phase. This section addresses the transformations in Ti-24-11 where the O phase does not appear to be present. One should keep in mind that when alloys with 12 at% or greater niobium concentration are discussed, an orthorhombic phase will be involved. The issues regarding the orthorhombic phases will be addressed in the following two sections.

The α_2 phase has the ordered DO₁₉, $P6_3/mmc$, crystal structure where titanium and aluminum occupy separate sublattices. Konitzer *et al.* have determined by channelling enhanced microanalysis that niobium shares the titanium sublattice in α_2 when in solid solution.¹¹ O'Connell and Flinn characterized a splat quenched binary Ti-25Al alloy, cooling rate $\sim 10^6$ °C/sec, by X-ray diffraction (XRD) and found the hexagonal phase to be disordered α .³¹ Upon aging, the α phase ordered to form α_2 by a diffusional process; this was supported by the appearance of ordering peaks in the XRD spectra. Sastry and Lipsitt studied the ordering kinetics in the binary Ti-25Al and ternary Ti-25Al-5Nb alloys by AEM.³² Their results showed that upon water quenching both alloys from the β phase

field the β phase transformed to hexagonal martensite, α' . In the binary alloy the α' underwent an ordering transformation to α_2 during the quench, evidenced by the presence of antiphase boundaries (APB's) and superlattice reflections in selected area diffraction (SAD). They also characterized the activation energy for domain growth in α_2 to be $\sim 2.68 \times 10^5$ J/mole. APB's were not, or could not be, observed in the α' formed in the niobium bearing alloy; nor was the presence of superlattice reflections reported, or referenced. The authors do, however, report that when the ternary alloy was $\alpha + \beta$ heat treated the diffusionally grown α phase retained its disordered state on quenching. This disordered α phase would be richer in aluminum than the nominal alloy composition and thus lie well within the single phase α_2 region at room temperature, suggesting that the ordering reaction was truly suppressed. Kestner-Weykamp *et al.* have shown that in 24-11 APB's could be imaged in α_2 at all cooling rates when formed by a martensitic-like reaction.¹² The majority of evidence shows that the ordering reaction appears to be nearly, if not completely, impossible to suppress.

The α_2 phase has the Burgers orientation relation, $(0001)_{\alpha_2} \parallel \{110\}_{\beta/B2}$, $\langle 11\bar{2}0 \rangle_{\alpha_2} \parallel \langle 1\bar{1}1 \rangle_{\beta/B2}$, with the parent $\beta/B2$ phase whether formed diffusionally or by shear. Rozeveld and Howe have determined the structure of the α_2/β interface in a Ti-16Al-7Mo a/o, $\alpha_2 + \beta$, alloy using high resolution electron microscopy (HREM).³³ The interfacial misfit dislocations were identified as $\vec{b} = 1/3 \langle 11\bar{2}3 \rangle_{\alpha_2}$ with $\hat{u} = \langle 11\bar{2}0 \rangle_{\alpha_2}$ on the $\{1\bar{1}00\}_{\alpha_2}$ planes. The interface between α_2 and β was found to be poorly defined and wavy, being loosely defined by $\{10\bar{1}0\}_{\alpha_2} \parallel \{211\}_{\beta}$, $\langle 11\bar{2}0 \rangle_{\alpha_2} \parallel \langle 1\bar{1}1 \rangle_{\beta}$. This arrangement is depicted in Figure 2.4.

Both research groups of Baeslack/Cieslack and Kestner-Weykamp and co-authors propose that typical nucleation and growth transformations occur only at higher temperatures, $\geq 900^\circ\text{C}$, and for extended periods of time, ≥ 1000 seconds for Ti-24-11.^{12,34,35} At temperatures $\geq 900^\circ\text{C}$ α_2 grows as allotriomorphs at the $\beta/B2$ grain boundaries and as equiaxed or large blocky precipitates in the interior of the B2 grains.

Through thermomechanical processing (TMP), precipitates with these morphologies may undergo recrystallization to become equiaxed grains termed primary, Figure 2.5(a). Texture development may occur in this case resulting in a texturing relationship of the primary α_2 grains to the B2 matrix which is equivalent to the Burgers OR. Also, primary α_2 grains can act to pin B2 grains that have also undergone recrystallization through TMP, Figure 2.5(b).²⁸

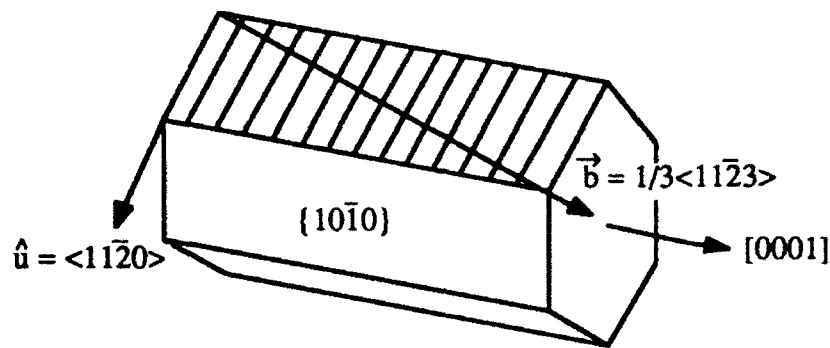


Figure 2.4 Depiction of interfacial misfit dislocation structure between α_2 and β (after Ref. 33)

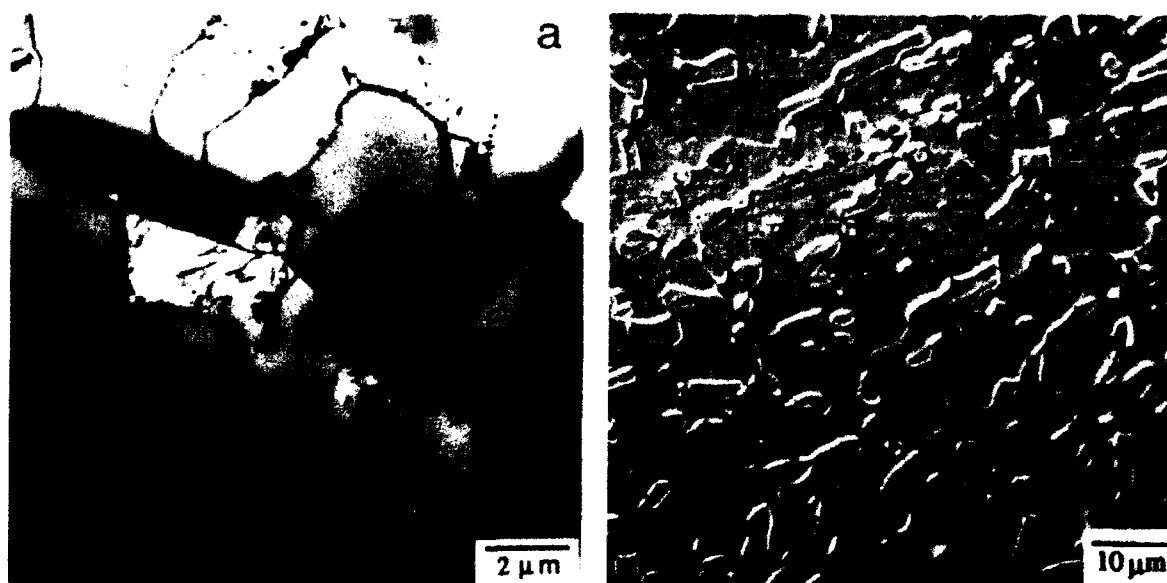


Figure 2.5 (a) AEM micrograph of primary α_2 grains in a recovered and quenched B2 matrix. (b) Light micrograph showing primary α_2 grains pinning recrystallized B2 grains, sample was quenched from high in the $\alpha_2 + \text{B2}$ phase field (after Ref. 28).

Below $\sim 900^\circ\text{C}$ the character of the α_2 phase undergoes a visible change. First, the volume fraction present increases dramatically. This volume fraction change is represented in the "pseudo-binary" phase diagram for Ti-25-10-3-1 in Figure 2.3.²³ Through most of the temperature range for α_2 formation, sideplate growth from the B2 grain boundaries/grain boundary α_2 allotriomorphs is a typical morphology due to heterogeneous, sympathetic nucleation. Second, the α_2 which is formed below this temperature undergoes a morphological change from larger, more equiaxed precipitates, to smaller more elongated laths. The occurrence of grain boundary α_2 allotriomorphs also decreases at lower temperatures as the driving force for intragranular nucleation has increased. The temperature of this morphological change also roughly corresponds to the onset of what appears to be a martensitic-like transformation, discussed further below. This undoubtedly plays a role in this morphological change, but a distinction between lath formation by nucleation and growth and by a shearing transformation has not been provided yet.

Thermomechanical processing may also greatly affect the morphology of secondary α_2 .²⁸ When a billet undergoes a forge and direct age sequence, the secondary α_2 forms as very fine, $<1\mu\text{m}$ for Ti-25-10-3-1, and well distributed Widmanstätten laths, sometimes referred to as a "basketweave" structure. This fine morphology is attributed to the residual dislocation structure within the B2 matrix from forging. From both a diffusional nucleation and growth as well as a shear nucleation standpoint, the large dislocation density leads to a refinement of the secondary α_2 by providing numerous heterogeneous nucleation sites. An example of this morphology is shown in Figure 2.6(a). These nucleation sites are significantly reduced in density if the forged product were subjected to an anneal high in the $\alpha_2+\beta/\text{B2}$ phase field prior to aging, the resulting secondary α_2 would form as coarser, $>1\mu\text{m}$, and more aligned laths, the alignment arising from sympathetic nucleation at grain boundaries. In this case the incidence of grain boundary allotriomorphs rises and in some instances necklacing of α_2 at the prior β grain boundaries may be quite noticeable. This type of microstructure is found in Figure 2.6(b).

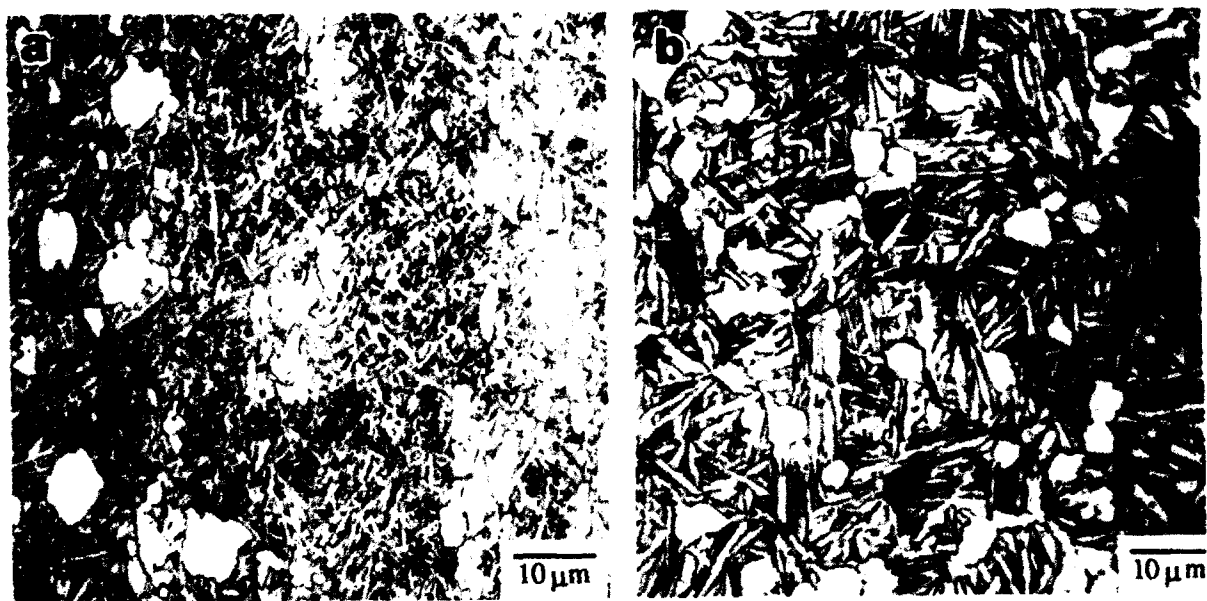


Figure 2.6 (a) Microstructure produced by hot-die forging at 1107°C and direct salt-bath age at 815°C for 30 minutes. YS: 942 MPa, UTS: 1097 MPa, Elongation: 2.7%. (b) Microstructure produced by hot-die forging at 1107°C followed by an oil quench. The forging was then annealed at 1107°C for 1 hour and given a direct salt-bath age at 815°C for 30 minutes. YS: 759 MPa, UTS: 963 MPa, Elongation: 2.6% (after Ref. 28).

In quenched material, where the B2 and ω' phases are present, the precipitation of the α_2 phase on aging may be dramatically affected by the rate at which the material is brought to temperature.³⁰ There are two possible transformation paths which can be conceived. On slow heating in an atmosphere furnace, the ω' phase has time to coarsen to the thermal ω'' or B8₂ phases. Misfit dislocations may form at the B8₂/B2 interface and act as heterogeneous nucleation sites for α_2 precipitation.³⁶ This abundance of finely dispersed nucleation sites results in the extremely fine, <0.5 μm , and blocky α_2 seen in the matrix of Figure 2.7. This precipitation sequence is analogous to that for a metastable β alloy, Ti-10V-2Fe-3Al (w/o), reported by Duerig *et al.*³⁷ The second path would be the result of the intersection of the heating curve with the bottom of the α_2' (or α_2'') C-curve, where driving forces for formation are very high. On more rapid heating in a salt bath, both the ω'' and bottom of the α_2' (or α_2'') C-curves are avoided and the transformation is allowed to occur as though it were occurring isothermally from a higher temperature. The scale of the secondary α_2 laths resulting from a rapid heating rate is similar to that found in Figure 2.6(b).

When Ti-25Al-xNb alloys are subjected to a solution heat treatment and subsequent quench, the system may become unstable and undergo a discontinuous coarsening reaction on aging, Figure 2.7.³⁰ The resulting reaction is analogous to the instability reaction observed in martensitically transformed single phase alloys.^{2,38,39} The coarsening reaction in the two phase alloy is a cellular product consisting of α_2 and B2 lamellae replacing the fine α_2 /B2 matrix. Nucleation of this coarsening reaction occurs at prior β /B2 grain boundaries, likely at the grain boundary α_2 allotriomorphs, and at primary α_2 grains. The driving force for this type of reaction appears to be the reduction of α_2 /B2 interfacial area/energy. This is supported by the micrograph in Figure 2.7(a) showing two prior β /B2 grains having different α_2 plate sizes. The grain on the left exhibits cellular growth into the visibly finer microstructure. This reaction is inhomogeneous between prior β grains. The reason for this inhomogeneity may be due to inhomogeneous deformation.³⁰ However, at

least in Ti-25-10-3-1, an additional driving force comes from the initial formation of the non-equilibrium O' phase on aging.

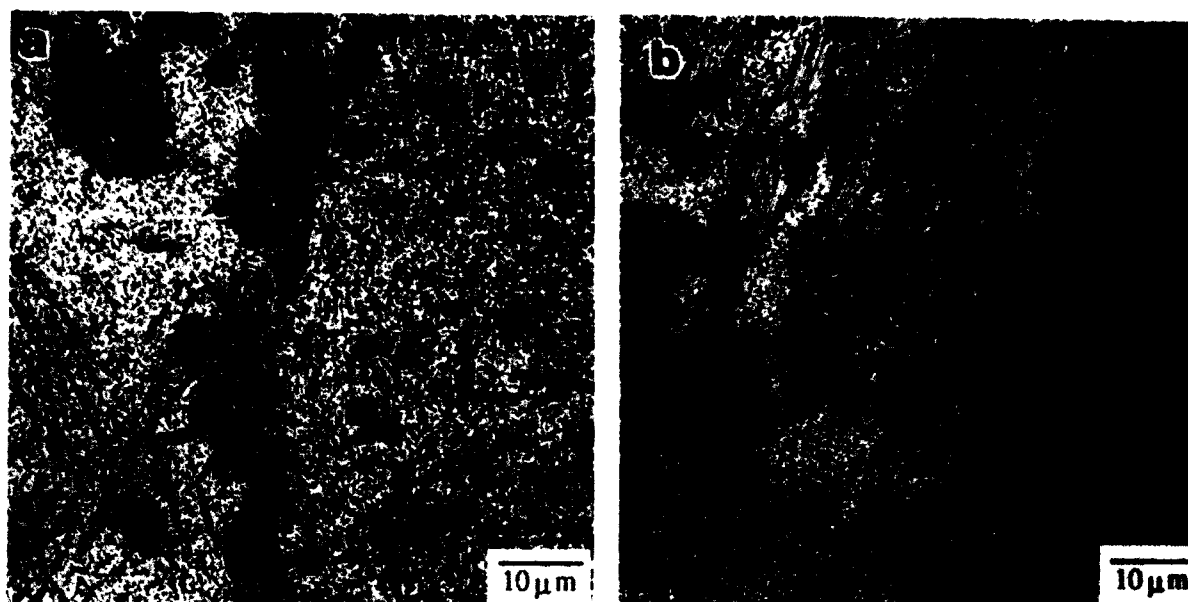


Figure 2.7 (a) SEM micrograph showing differences in scale of secondary α_2 across the prior β grain boundary. (b) SEM micrograph exhibiting the crystallographic nature of growth of the cellular reaction (after Ref. 30).

Figure 2.7(b) shows the crystallographic nature of growth of the cellular reaction product. The character of the cellular product may take on two different morphologies. A typical solid/solid cellular reaction where the cellular reaction occurs by synchronous growth of Burgers related α_2 and B2 phases behind a high angle boundary is observed to the greatest extent, Figure 2.8(a). This is similar to the nucleation and growth mechanism proposed by Aaronson and Aaron, and Tu and Turnbull.^{40,41,42,43} The other nucleation and growth mechanism is best described by Mullins/Sekerka morphological instability.^{44,45} In this case the B2 phase need not undergo nucleation, instead the α_2 interface becomes unstable and begins to bow out leaving behind the B2 phase between the α_2 "fingers," Figure 2.8(b). This mechanism also has the *appearance* of a cellular product

and is found to a much lesser degree than the synchronous growth based mechanism. Both mechanisms exhibit interlamellar spacings of approximately $1\mu\text{m}$.

It is important to note that since the transformation kinetics of Ti-25-10-3-1 are slower than for Ti-24-11; air cooling of a small cross-sectional sample of Ti-25-10-3-1 is equivalent to water quenching a similar sample of Ti-24-11. On reheating this sample to an aging temperature above $\sim 650^\circ\text{C}$ a cellular reaction may occur.

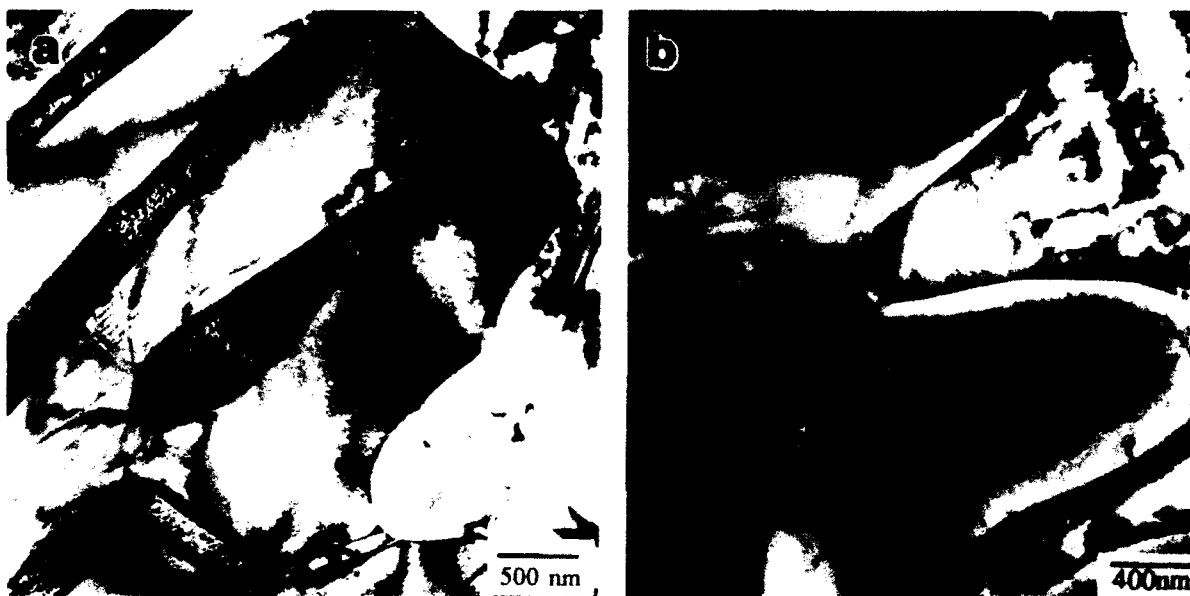


Figure 2.8 (a) AEM micrograph of cellular reaction formed by synchronous growth of α_2 +B2 behind a common interface. (b) AEM micrograph of cellular reaction formed by growth of α_2 "fingers" into the fine scaled matrix (after Ref. 30).

2.1.4 Ordered Orthorhombic Phase

An additional complication to the ternary Ti-Al-Nb alloy system was the discovery by Banerjee and co-workers of an O phase with a Cmc₂m crystal structure in the Ti-25Al-12.5Nb alloy.⁴⁶ The orthorhombic phase can be described by a small distortion of the α_2 phase and a ternary ordering of niobium on particular lattice sites. A comparison of the two 'basal' planes is shown in Figure 2.9. Due to the similarities in structure between α_2 and O, it is not surprising to find that the O phase has a $(001)_O \parallel (110)_{B2}$ and $[110]_O \parallel$

$[1\bar{1}1]_{B2}$ OR to the parent B2 matrix.⁴⁶ Since its discovery, the O phase has been identified in a wide range of compositions, up to and through 30 atomic percent niobium. Kaufman and Kestner-Weykamp *et al.* have reported the lattice parameters for the O phase as a function of alloy composition, and have started to define the temperatures at which the orthorhombic phase is stable.^{47,22} Lattice parameters for the ordered orthorhombic phase appear to be much more sensitive to alloy composition than the $\beta/B2$ and α_2 phases. For Ti-25Al-12Nb the lattice parameters were determined by XRD to be $a=0.590$, $b=0.985$, and $c=0.465$ nm.⁴⁷

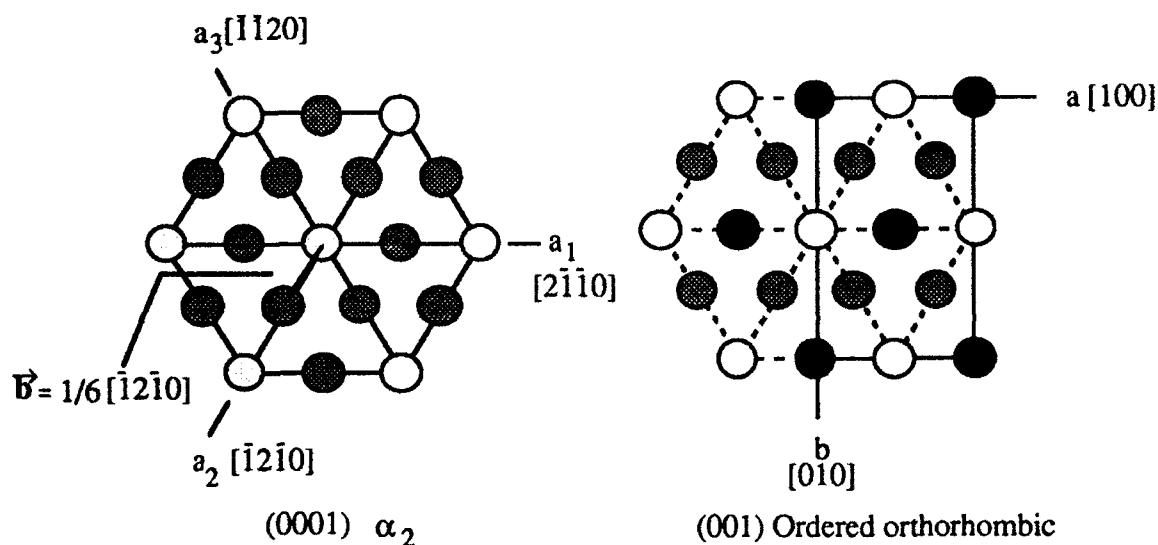


Figure 2.9 Comparison of the $(0001)_{\alpha_2}$ and $(001)_O$ planes.

However, a recent study shows that an orthorhombic phase may be introduced during AEM sample preparation techniques.⁴⁸ In particular, AEM foil preparation by electropolishing may lead to the formation of an orthorhombic phase in the 'rim' of larger α_2 grains. This is in spite of no apparent increase in niobium content in the 'rim', which would be expected if the equilibrium ordered O phase were stabilized. Use of ion milling for AEM foil preparation, to avoid hydrogen charging, results in entire primary α_2 grains exhibiting an orthorhombic phase. Furthermore, acid etching of mechanically polished

samples resulted in the appearance of orthorhombic peaks in XRD. Although it is possible to distinguish between the artifact and O phases by AEM, one must be careful in the analysis. In any case, this result certainly casts doubt on past studies that have used acid etching in XRD to characterize the O phase and were not careful in characterizing an orthorhombic artifact in AEM.

The morphology of the diffusional nucleation and growth O phase has not been discussed at length in this section due to its similarities to the α_2 phase. However, some notable exceptions merit mentioning. Muraleedharan and co-authors have found that on quenching and aging Ti-25-15 from a high solution heat treatment temperature, a massive reaction of O phase overtakes the parent β /B2 matrix.^{10,49} This can also be mixed with an O' martensitic product. The massive O phase decomposes at temperatures as low as 650°C to produce an O + B2 structure.

While O is generally accepted as an equilibrium phase in alloys with greater than ~15 a/o niobium, the O' phase may be a kinetically favorable transition phase in many alloys. This will be considered in the following section.

2.1.5 Martensitic Reaction

Martensitic transformations have long been observed to operate in the single phase α_2 region.^{15,16,32,50} The conclusion of all these early studies was that the martensite start temperature, M_s , was severely depressed by the addition of Nb. Williams and Blackburn showed that at lower niobium contents, Ti-25Al-5Nb, rapid quenching from the β phase field resulted in hexagonal martensite formation, α' , and subsequent diffusional ordering and thickening to α_2' .⁵⁰ They also observed a decreasing plate size as the niobium concentration was increased. At higher niobium contents, ~12 a/o, Strychor *et al.* found that the martensitic transformation did not occur on water quenching to room temperature and instead the B2 phase was formed.¹⁵

Kaufman has also observed the martensitic transformation in Ti-25Al-5Nb.⁴⁷ However, he reported that the martensitic α_2' transformation in this alloy could be suppressed when produced by melt spinning and splat quenching. In melt spun ribbon, with an estimated cooling rate of $10^3 - 10^4$ °C/sec, some α_2' was present in a matrix of retained B2. The splat quenched foil, with an estimated cooling rate of 10^6 °C/sec, only contained the B2 phase. Kaufman found that with higher niobium contents the amount of α_2' phase formed in the melt spun ribbon decreased until at 10 a/o Nb no martensite was observed. These results first suggested that some aspects of the martensitic transformation in niobium enriched α_2 alloys are thermally activated processes and are therefore strongly controlled by cooling rate. Kaufman's observations of a cooling rate dependence of the martensitic reaction are similar to those of Jepson *et al.* in Ti-Nb alloys.⁵¹ At very high cooling rates, $>10^4$ °C/sec, Jepson and coworkers found that the martensitic reaction could be completely suppressed. In addition, they also found that, due to the decreasing diffusion rates in higher niobium bearing alloys, both the cooling rate at which martensite formed and the cooling rate at which it was suppressed decreased. In other words, the range of cooling rates in which a diffusional nucleation and growth product could be formed decreased with increased niobium content.

In fact, the authors of recent papers on the transformation processes in higher niobium alloys, lying within the two phase $\alpha_2 + \beta$ /B2 region, report that they have found a thermally activated shear transformation.^{12,34,35,52,53} Mascarella was the first to refer to a martensitic structure, characterized by light microscopy, in a higher niobium alloy, Ti-24-11, when continuously cooled in the range from 1 to 150°C/sec .⁵² Baeslack *et al.* and Cieslack *et al.* confirmed a martensitic-like structure in 24-11 by AEM and noted that at sufficiently high cooling rates, $>150^\circ\text{C/sec}$, the martensitic reaction could be suppressed and the resulting microstructure would only contain the ordered B2 phase.^{34,35} The martensitic-like reaction that was observed occurred at approximately 893°C , as determined on an instrumented Gleeble system, during continuous cooling and was completed within

about 1 second.³⁵ AEM analysis showed that the microstructure consisted of heavily dislocated and fine acicular α_2 , $<1\mu\text{m}$, with no apparent partitioning of elements and a complete absence of the β phase.^{34,35} A large fraction of the α_2' plates exhibited a midrib. No analysis of the midrib or dislocation structure was presented in either paper. Both papers described chemical partitioning and the appearance of retained β at slower cooling rates, $1^\circ\text{C}/\text{sec}$, with the retention of a midrib structure. They suggest that this occurred by a martensitic reaction followed by tempering. However, this is probably more accurately described by partitioning of the β stabilizing elements as diffusional thickening of the plates occurs. This will become more evident below.

Kestner-Weykamp *et al.* have proposed a transformation sequence based on their observations of an end-quenched Ti-24-11 bar and on the results presented by Moffat and Larbalestier on Ti-Nb alloys.^{12,54} They found that in the most rapidly cooled region of the bar the martensitic-like transformation was largely avoided and the β phase instead underwent an ordering reaction to B2. AEM analysis did show, however, that there was a small number of thin α_2 plates in the B2 matrix lying parallel to the $\{112\}_{\beta/\text{B2}}$ planes. These α_2 plates exhibited very fine APB's indicating that they were the product of diffusional α' ordering. Slower cooling produced a "fully martensitic" structure with no β phase retention and no partitioning of the alloying elements. The plates in this condition were also found to be ordered, with the α_2 antiphase domains (APD's) extending in a columnar fashion from the midribs, Figure 2.10. The midrib was identified by AEM to lie approximately parallel to the $\{10\bar{1}0\}_{\alpha_2}$ plane, which in turn is parallel to the $\{112\}_{\beta/\text{B2}}$ plane, resulting in a Burgers orientation relationship (OR). The $\{10\bar{1}0\}_{\alpha_2}$ and $\{112\}_{\beta/\text{B2}}$ planes are also the planes of best lattice matching and are expected to form a coherent interface.³³ Kestner-Weykamp *et al.* have proposed that the martensitic-like reaction occurs from the disordered β phase and the resulting α' plates form a midrib from which α_2' may grow by an isothermal and compositionally-invariant transformation into the remaining $\beta/\text{B2}$ matrix. Slower cooling rates lead to partitioning of the alloying elements

between the α_2 and $\beta/\text{B2}$ phases during growth. In all cooling rates they observed relatively low dislocation densities, rising slightly in the more slowly cooled sections. Both $[c/2]$ and $\langle a \rangle$ type dislocations were present near the ends of the plates. Dislocation networks were not associated with the midribs. They argue that the formation of the B2 and/or ω' phases precludes the martensitic reaction by making the shearing mechanism unfavorable. The transformation sequence proposed by Kestner-Weykamp *et al.* is very similar to what has been proposed by Okamoto and Oka for the formation of lower bainite with midrib (LBm) in hypereutectoid steels.⁵⁵ In this study, lower bainite was found to nucleate at the interfaces between austenite and thin plates of isothermal martensite (TIM). The resulting bainite contained a midrib that was attributed to the remnants of the thin plate isothermal martensite. In Okamoto and Oka's case, however, the LBm had an OR that was derived from the TIM and was substantially different from that of conventional lower bainite. Unfortunately, in the case of α_2 formation, both the diffusional and martensitic products have the same OR to the parent bcc phase such that no distinction is possible.

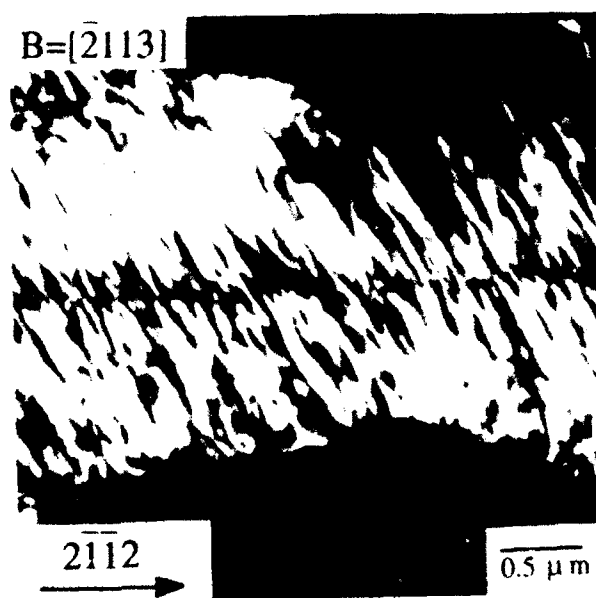


Figure 2.10 Ti-24-11 α_2' plate showing APD growth from the midrib (after Ref. 12)

Since the presence of an ordered orthorhombic phase in the Ti-25Al-xNb alloys was first reported, careful examinations of more highly β stabilized alloys have been conducted. Evidence is now growing that a similar martensitic-like reaction that produces α_2' in Ti-24-11 produces an O' phase in higher niobium alloys. Furthermore, this phase is transitional in some alloys.^{13,14} Based on analysis of defect structure within the lath structure, Bendersky *et al* have proposed that in alloys near 12.5 a/o niobium, orthorhombic formation must have a hexagonal precursor formed by the shearing of the disordered β phase.¹⁴ Thus, isothermal reactions in alloys where there is less than approximately 15 a/o niobium may result in the formation of a thin hexagonal martensitic plate, α' , followed by growth of an O' phase from the midrib. Different defect structures present in the laths of more heavily stabilized alloys, ≥ 15 a/o Nb, led Bendersky and co-workers to propose that the midrib must be an orthorhombic structure, α_2'' , formed by the shearing of the B2 phase. This has been supported by Muraleedharan's results which show that the orthorhombic lath inherits the APB structure from the parent B2 phase of Ti-25-15.⁴⁹ Growth of the O' phase in either case would be expected to be at least kinetically favorable (if not thermodynamically, in higher niobium alloys) since this structure has a higher solubility of niobium and need not wait for the partitioning of slow diffusing elements such as niobium and molybdenum. It has been proposed that such an orthorhombic distortion in these niobium alloys may be related to the formation of orthorhombic martensites in Ti-Nb alloys.^{49,56}

After formation of the O' phase by an isothermal martensitic-like transformation, the O' phase has been found to decompose completely to α_2 +B2 at temperatures as low as 815°C in the following alloys: Ti-25-10-3-1, Ti-24.5Al-10.5Nb-1.5Mo, and Ti-24.5Al-14.5Nb-1.5Mo.¹³ In these cases, the alloys were first solution treated above their respective β transi, and then directly salt bath aged for various times. Characterization of the alloys was accomplished by X-ray diffraction and AEM. A proposed TTT diagram for Ti-25-10-3-1 based on data from Ward *et al.* and Peters and Bassi is presented in Figure

2.11.^{13,57} Bendersky *et al.* have observed that this decomposition of the O' phase to α_2 is quite complex.²¹ Baeslack and Broderick's observation of a martensitic-like transformation behavior in Ti-25-10-3-1 shows that the continuous cooling transformations occur at rates one order of magnitude slower than in Ti-24-11.⁵³ The complex substructure that they observe, in contrast to that of Kestner-Weykamp *et al* in Ti-24-11,¹² may be related to a decomposition of O' to α_2 .

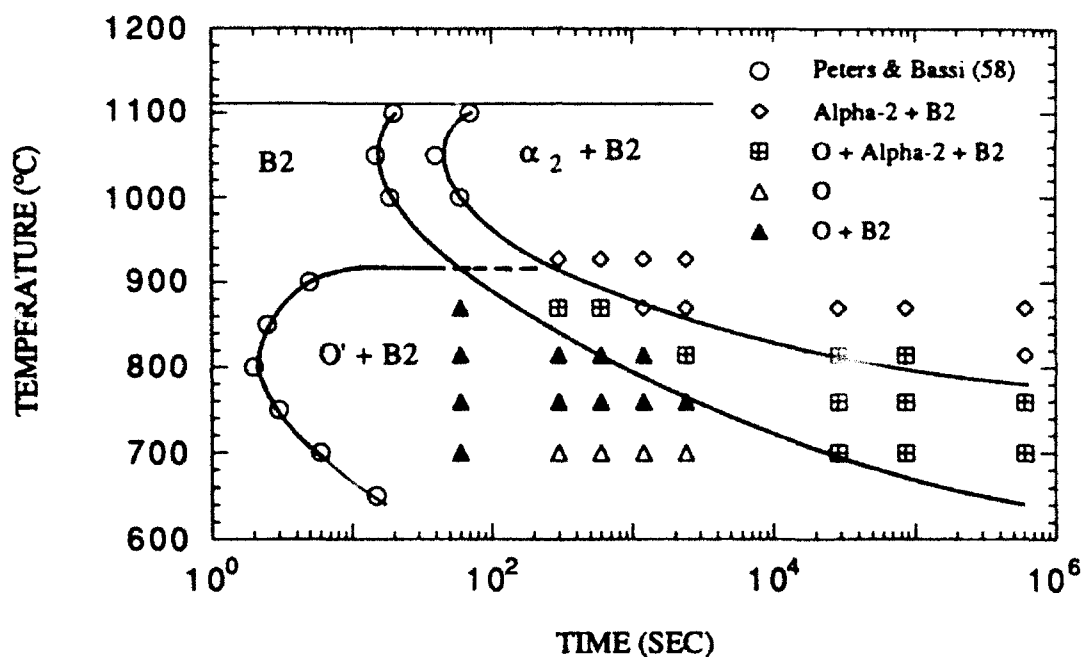


Figure 2.11 Proposed time-temperature-transformation curve for Ti-25-10-3-1 (after Ref. 13).

The ordered orthorhombic phase metastability in the lower niobium alloys referred to above does not seem to be the case in even higher niobium bearing alloys, ≥ 15 Nb. Muraleedharan *et al.* have shown that the O' phase tempers to O + α_2 + B2 phase in Ti-24.5Al-15Nb between 800 and 980°C and O + B2 at lower temperatures.¹⁰ The lower niobium alloys discussed above, namely Ti-24-11, Ti-24.5Al-10.5Nb-1.5Mo and Ti-25-

10-3-1, clearly lie in a two phase field of α_2 +B2 in this temperature range.¹³ However the orthorhombic transformation curve is significantly raised in the Ti-24.5Al-14.5Nb-1.5Mo alloy, similar to Muraleedharan's results.

It appears that a shearing mechanism can play an important role in the formation of both the α_2 and O phases. Furthermore, the formation of α_2' and O' below $\sim 900^\circ\text{C}$ may be similar to that proposed by Okamoto and Oka for the formation of lower bainite with midrib in hypereutectoid steels.⁵⁵ In the case of Ti-25Al-xNb alloys, the phase which subsequently grows from the martensitic midrib is dependent on the niobium concentration. Lower niobium alloys, ≤ 11 a/o Nb, produce α_2' whereas those with higher niobium contents produce an O' phase. In alloys with niobium concentrations above 11 a/o, but below 15, the O' phase appears to be a kinetically favorable transition phase that decomposes to α_2 +B2 on long term aging. From the results cited above for O' stability in molybdenum containing alloys, it is obvious that alloying effects on ordered orthorhombic phase stability are not known. Whether or not the orthorhombic phase is in equilibrium at lower temperatures in these alloys is not clear. At niobium concentrations of approximately 15 and above, the O phase appears to be in equilibrium with the B2 phase at low temperatures.

2.2 Slip Behavior

2.2.1 Experimental Observations

The well known von Mises criteria calls for five independent slip systems within a crystal in order for that crystal to undergo homogeneous deformation.⁵⁸ Groves and Kelly have applied von Mises' criteria to the more complex hexagonal crystal system.⁵⁹ The results of their analysis of hexagonal slip systems are presented in Table 2.1. It is important to note that [c] component slip is essential to providing the fifth required slip

system. Another observation is that slip on plane \hat{n} (the plane normal) with Burgers vector \vec{b} gives rise to equivalent deformation as slip on plane \vec{b} with Burgers vector \hat{n} .

Table 2.1 Slip systems of the hexagonal crystal.

<u>Slip system</u>	<u>Independent systems</u>	<u>Cumulative</u>	<u>Example</u>
$\langle 11\bar{2}0 \rangle \{0001\}$	Two	Two	C(gr)
$\langle 11\bar{2}0 \rangle \{10\bar{1}0\}$	Two	Four	Zr, Te
$\langle 11\bar{2}0 \rangle \{10\bar{1}1\}$	Four	Four	Ti, Zn, Cd
$\langle 11\bar{2}1 \rangle \{11\bar{2}2\}$	Five	Five	Zn, Cd

Before any dislocations in α_2 were ever characterized, or in any other DO_{19} structure, Marcinkowski made some predictions as to the active dislocations in a DO_{19} structure.⁶⁰ His calculations showed that in systems with a c_0/a_0' ratio of less than 0.8165 the $\{10\bar{1}0\}$ prism planes would become more densely packed than the basal planes, thus favoring slip on $\{10\bar{1}0\}$. This is in fact the case in the α_2 phase where $c_0/a_0' = 0.8047$ and prism slip is preferred, as will be discussed below. He also predicted that slip on the basal plane would consist of paired superpartials of $\vec{b} = 1/6\langle 11\bar{2}0 \rangle$ (Marcinkowski expressed this as $1/2a_0'\langle 11\bar{2}0 \rangle$) that further dissociate into four superpartials of $\vec{b} = 1/6\langle 10\bar{1}0 \rangle$ (Marcinkowski expressed this as $1/6a_0'\langle 10\bar{1}0 \rangle$). Thus, dissociation would occur as: $1/3\langle 11\bar{2}0 \rangle \rightarrow 1/6\langle 11\bar{2}0 \rangle + 1/6\langle 11\bar{2}0 \rangle \rightarrow \{1/6\langle 10\bar{1}0 \rangle + 1/6\langle 01\bar{1}0 \rangle\} + \{1/6\langle 10\bar{1}0 \rangle + 1/6\langle 01\bar{1}0 \rangle\}$. This reaction has not been observed in study to date. The lack of dissociation is due to the high APB energy on the basal plane. On the $\{10\bar{1}0\}$ prism planes, Marcinkowski hypothesized, slip of a singular $\vec{b} = 1/6\langle 11\bar{2}0 \rangle$ would leave no first nearest neighbor violations and only a very low, if any, antiphase boundary (APB) energy would result. Thus, no dissociation was to be expected in this case.

2.2.1.1 $\langle a \rangle$ Type Dislocations in α_2

Williams and Blackburn observed that in α_2 alloys compressed to a strain of 3%, straight screw dislocation pairs with $\vec{b} = a/3\langle 11\bar{2}0 \rangle$, referring to the disordered α lattice, were present on the prism $\{10\bar{1}0\}$, pyramidal $\{10\bar{1}1\}$ and basal (0001) planes.⁶¹ The notation used by the authors is probably better expressed as superpartials with $\vec{b} = 1/6\langle 11\bar{2}0 \rangle$, now referring to the ordered lattice for consistency. Appearing in pairs, these superpartials thus formed superdislocations with $\vec{b} = 1/3\langle 11\bar{2}0 \rangle$.

Schafrik was the first to report a ductile to brittle transition at 600°C in a single phase α_2 alloy based on Ti-25Al-5Nb.⁶² Both this composition and the binary have been the basis for most of the dislocation studies of α_2 to date. Sastry and Lipsitt also found straight screw dislocations with $\vec{b} = 1/3\langle 11\bar{2}0 \rangle$ in planar bands in fatigued Ti-26.8Al between 500°C and 700°C.⁶³ It is not clear whether the dislocations that they observed were dissociated or paired. They found that the $\langle a \rangle$ dislocations tended to form braids of screw dislocations along (0001) and $\{10\bar{1}0\}$ and that as the strain amplitude was increased, these braids became closer together. Above 700°C less planar slip was evident as well as slightly increased non-basal slip activity. At 800°C the braid structure and planar slip associated with lower temperature deformation gave way to dislocation knitting, the formation of sub-boundaries and a move away from the screw configuration. It is important to note that the authors did not observe any twinning deformation, as is common in conventional titanium alloys. In tensile deformation at 700°C of Ti-26.8Al and Ti-26.6Al-4.94Nb Sastry and Lipsitt also found similar dislocation configurations as in fatigue.³² In the binary alloy they observed planar arrays of superdislocations, $\vec{b} = 1/3\langle 11\bar{2}0 \rangle$, that were primarily in the screw configuration. Again, dissociation and pairing were not discussed. Slip was observed to be highly planar with pile-ups of $\vec{b} = 1/3\langle 11\bar{2}0 \rangle$ dislocations noticeable. These slip bands were on (0001) and aligned along traces of $\{10\bar{1}0\}$. In the ternary alloy higher ductilities were recorded. The authors argue

that this increase was due to less planar slip and to the increased density of $\langle c+a \rangle$ slip. In a similar study of only binary α_2 , Lipsitt *et al.* found that a significant portion of the 'ductility' observed in the binary alloy above 600°C was in fact due to microcracking normal to the tensile axis.⁶⁴ They determined that the major deformation mode was by $\vec{b} = 1/6\langle 11\bar{2}0 \rangle$ on $\{10\bar{1}0\}$, $\{0001\}$ and $\{10\bar{1}1\}$, with only limited $\langle c+a \rangle$ dislocation densities. Again, they noticed that cross slip of the $\langle a \rangle$ dislocations increased with increasing temperature.

Yang has shown $\langle 11\bar{2}0 \rangle \{10\bar{1}0\}$ to be the primary slip system in binary Ti-25Al. Activation of $\langle 11\bar{2}0 \rangle \{0001\}$ slip is difficult and appears to be sensitive to strain rate, the dislocation density rising in this system with increasing strain rate.⁶⁵

Kerans' study of fatigued Ti-26.8Al between 23°C and 900°C was the first to compare undeformed with deformed samples.⁶⁶ He found that in undeformed material the dislocation density was low and that the dislocations were inhomogeneously arranged and roughly split equally between $\langle a \rangle$ and $\langle c + a \rangle$ or $[c]$ dislocations. Upon testing, grains were observed to be either heavily dislocated or clear of dislocations. Those that were clear were oriented with their $[c]$ axis nearly parallel to the stress axis. This results in a very low resolved shear stress in the $\langle a \rangle$ direction and hence low $\langle a \rangle$ dislocation motion. The little deformation that was found in clear grains appeared near grain triple points where incompatibility stresses are high. Above 500°C dislocation tangles were observed and found to be of the $\langle 11\bar{2}0 \rangle \{10\bar{1}0\}$ type with edge character. As the temperature was increased, the dislocations tended toward screw orientations. Dislocations were observed to lie in persistent slip bands.

Court *et al.* found screw dislocations on the basal planes of a compressed Ti-25Al-5Nb alloy at room temperature and 3% strain.⁶⁷ They determined by tilting experiments that these screw dislocations had a Burgers vector of $\vec{b} = 1/3\langle 11\bar{2}0 \rangle$, which is the unit dislocation in the superlattice structure. No dissociation could be detected, implying a very high APB energy on $\{0001\}$. They also found many apparently unpaired $\vec{b} = 1/6\langle 11\bar{2}0 \rangle$

dislocations, along with $\vec{b} = 1/3\langle 11\bar{2}0 \rangle$ superdislocations, on the $\{10\bar{1}0\}$ planes, in agreement with Marcinkowski's prediction.⁶⁰

In their examination of as-cast Ti-25Al, Thomas *et al.* found that the $\vec{b} = 1/3\langle 11\bar{2}0 \rangle$ superdislocations were dissociated in planes approximately perpendicular to their slip planes, thus implying that these dislocations would be sessile when stressed.⁶⁸ This observation has been corroborated by Court *et al.* in another study.⁶⁹ Court and coworkers also studied the binary and Ti-25Al-4Nb alloys in compression tests. They found that most of the dislocations present were in the form of dipoles made up of dissociated $\vec{b} = 1/3\langle 11\bar{2}0 \rangle$ dislocations. Most of the dissociated dislocations in the dipoles were observed to lie in the same $\{10\bar{1}0\}$ plane as their Burgers vector, implying that these dislocations were glissile. The separation of the superpartials, $\vec{b} = 1/6\langle 11\bar{2}0 \rangle$, on $\{10\bar{1}0\}$ was determined to be $\sim 5\text{-}9$ nm. Since all dislocations could not possibly be shown to dissociate, the authors speculate that perhaps only those dislocations creating second nearest neighbor bond violations have dissociated. This finding contradicts their earlier work showing unpaired dislocations of $\vec{b} = 1/6\langle 11\bar{2}0 \rangle$ on $\{10\bar{1}0\}$. Therefore, it must be assumed that the $\vec{b} = 1/6\langle 11\bar{2}0 \rangle$ superpartial dislocations always travel in pairs.⁶⁷

The most comprehensive study of dislocation behavior to date has been published by Court, Löfvander, Loretto and Fraser.⁷⁰ The authors examined both Ti-25Al and Ti-25Al-4Nb in the undeformed and compressed state; compression was performed at both room temperature and 650°C to 3% strain. In room temperature compression the binary alloy exhibited dissociated dipoles, with $\vec{b} = 1/6\langle 11\bar{2}0 \rangle$, in the screw configuration on $\{10\bar{1}0\}$. These long screws were found to be the result of movement of edge dislocations, $\vec{b} = 1/3\langle 11\bar{2}0 \rangle$, along their lengths. This observation supports the theory that edge dislocations are the most mobile on $\{10\bar{1}0\}$. In addition to the dipoles, paired $\vec{b} = 1/6\langle 11\bar{2}0 \rangle$ dislocations were also observed on $\{10\bar{1}0\}$. The dominant slip system in the binary is $\langle 11\bar{2}0 \rangle \{10\bar{1}0\}$, very little slip occurs on $\langle 11\bar{2}0 \rangle (0001)$. With the addition of niobium, a noticeable change in the slip behavior was observed. Slip on (0001) and

$\{10\bar{1}1\}$ was now significant. Additionally, slip across adjoining α_2 laths on both (0001) and $\{10\bar{1}1\}$ was now occurring.

Compression testing the binary at 650°C showed that similar, though not quite as significant, changes in slip behavior occurred as in the addition of niobium to the binary alloy at room temperature.⁷⁰ Again, superpartial pairs of $\vec{b} = 1/6\langle 11\bar{2}0 \rangle$ on $\{10\bar{1}0\}$ make up the primary slip system. Climb as a means of dislocation motion seems to be very active. In the niobium alloy at 650°C, $\vec{b} = 1/6\langle 11\bar{2}0 \rangle$ slip occurred on $\{10\bar{1}0\}$ as well as on (0001) and $\{10\bar{1}1\}$. They conclude that the addition of niobium has similar effects on dislocation behavior as increases in temperature. A possible explanation will be offered below.

2.2.1.2 [c] Component Dislocations in α_2

Williams and Blackburn observed that as compared to the $\alpha + \alpha_2$ alloys in the same study, the single phase α_2 alloys exhibited very few $a/3\langle 11\bar{2}3 \rangle$ dislocations, again referred to the disordered lattice.⁶¹ They conclude that the lower ductility in the single phase α_2 alloys is due to the planarity of slip of $\langle a \rangle$ dislocations and the lack of $\langle c + a \rangle$ dislocations. Sastry and Lipsitt make mention of small increases in the density of 'non-basal' dislocations in fatigue and tension in both the binary and 5Nb alloys.^{63,32} They noted that the 5Nb alloy exhibits slightly more $\langle c+a \rangle$ slip than the binary.

Yang clearly pointed out that the primitive translation along the pyramidal direction in the $\{10\bar{1}0\}$, $\{2\bar{2}00\}$ and $\{11\bar{2}1\}$ planes is in fact $2[c] + \langle a \rangle$, or $\langle c + a/2 \rangle$.⁶⁵ This translates to a Burgers vector of $\vec{b} = 1/6\langle 11\bar{2}6 \rangle$. He argues that dislocations with Burgers vectors of $\vec{b} = [0001]$ appear active and sensitive to strain rate, only gliding at low strain rates, $<10^{-5} \text{ s}^{-1}$. The only $\langle c + a/2 \rangle$ dislocations observed are attributed to interactions of $[c]$ and $\langle a \rangle$ dislocations. Kerans noticed no difference in either $[c]$ or $\langle c + a/2 \rangle$

dislocation density between the deformed and undeformed samples, even at very high temperatures, 900°C.⁶⁶

Court and coworkers were the first to report significant densities of [c] component dislocations in the ternary 4Nb alloy.⁷¹ These dislocations were not active in significant quantities at compressive strains of 1%; but were observed in dense bands 1-2 mm apart in samples compressed to 3% strain. The dislocations were observed as pairs lying ~50 nm apart on the {11 $\bar{2}$ 1} plane. The Burgers vectors were determined to be parallel to <11 $\bar{2}$ 6> and their line directions were $\hat{u} = <17\bar{8}3>$, which is near-edge in character. The Burgers vector was arrived at by an energy argument. If the Burgers vector were $\vec{b} = 1/3<11\bar{2}6>$, then a Burgers vector of $\vec{b} = 1/3<11\bar{2}3>$ would be expected to be more energetically favorable. Therefore, they concluded that the Burgers vector should be $\vec{b} = 1/6<11\bar{2}6>$, this is in agreement with Yang's predictions.⁶⁵ Court *et al.* did not find this dislocation arrangement in the binary alloy even when compressed to 3% strain at 650°C.⁷¹ They also report no increase in dislocation density or activity for $\vec{b} = [0001]$ for either alloy, at 1% compressive strain. In a later paper Court and coworkers study the same system in greater detail.⁷⁰ In this paper they confirm that dislocations with $\vec{b} = 1/6<11\bar{2}6>$ are generally edge in character, suggesting that screw dislocations are more mobile. They were not able to observe any APB contrast between the $\vec{b} = 1/6<11\bar{2}6>$ superpartial pairs, they attribute this to a very high extinction distance, ~450-650 nm, for this contrast. They also point out that slip on this system only creates second nearest neighbor violations, in this case the APB energy should be small giving rise to the large pair spacings of ~50 nm. Their characterization of $\vec{b} = [0001]$ dislocations, though generally thought to be sessile, determined that it may be glissile on {3 $\bar{4}$ 10} in an edge configuration; but are still observed in only limited amounts.

Thomas *et al.* have characterized [c] slip in the binary alloy under compression to 0.7-1.3% strain at room and elevated temperatures.⁷² They found that the preferred slip plane for $\vec{b} = [0001]$ is {11 $\bar{2}$ 0} and that the dislocations present were of edge character.

This implies that screw configurations are more mobile. They did not find any temperature dependence of $[c]$ slip. Also, they did not notice any significant activity of $\langle c+a/2 \rangle$ slip. This, however, is consistent with other studies where $\langle c+a/2 \rangle$ slip was found to be nearly nonexistent in the binary alloy at strains of around 1%.^{71,73}

In their most recent paper, Court and coworkers clearly show the dependence of $\langle c+a/2 \rangle$ slip on alloy composition, total strain, and temperature.⁷⁰ The incidence of $\langle c+a/2 \rangle$ slip increased with the addition of niobium, increasing strain and increasing temperature.

2.2.1.3 Slip Behavior in the " β " phase

Characterization of the dislocation behavior in the β phase, whether it be ordered or not, is difficult in equilibrium concentrations as it generally appears as a very thin "film" between α_2 constituents. Some attempts have been made to define this behavior in Ti-24-11, but have been only somewhat helpful.^{74,75} The problem with these studies has been that they have looked at slip in the " β " phase quenched from high temperatures, this treatment is meant to leave a larger amount of " β " phase in order to ease characterization. However, this results in B2 phase retention at room temperature; the ordered state is not the room temperature equilibrium condition of β in this alloy.²²

Testing the B2 phase in this condition leads to a number of associated problems. First, being ordered, slip should be comprised of superdislocations as opposed to simple unit dislocations in the disordered matrix. This should inhibit slip and foster planar slip due to the increased difficulty in cross slip. Second, the B2 phase is not of the equilibrium concentration, being enriched in aluminum and lean in niobium. And last, with a much larger slip length in the B2 phase, due to its higher volume fraction, slip behavior observed in the α_2 phase, which is attributed to initiation from slip bands within the B2, may be misleading. This will be discussed further in the next section.

The research group of Banerjee, Gogia and Nandy have characterized slip behavior in the system as just described.^{74,75} They have found slip in the B2 phase to occur on the {112}, {110} and {321} planes with $\vec{b} = 1/2\langle 111 \rangle$. This slip is generally very planar and inhomogeneous in nature. However, they do note that both of these traits are less pronounced as the volume fraction of α_2 is increased. This observation points directly to the problems associated with testing material in this non-equilibrium condition as discussed in the previous paragraph. They have also observed fine slip with $\vec{b} = a\langle 100 \rangle$ at the α_2 /B2 interfaces; they associate this with incompatibilities at the boundary.

2.2.1.4 Two Phase Dislocation Behavior

The first published study on two phase, α_2 + β /B2 dislocation behavior was presented by Marquardt *et al.*⁷⁶ The authors studied a number of alloying additions to a base single phase, niobium bearing α_2 alloy. Alloying additions were added in quantities that maintained a single phase, and also in amounts that stabilized the β /B2 phase at room temperature. The alloys were compressed to 2% strain at temperatures ranging from room to 500°C. They observed $\langle c+a/2 \rangle$ slip in all α_2 grains with their [c] axis oriented to within 15° of the stress axis. They observed no significant increase in the density of $\langle c+a/2 \rangle$ dislocations in the single phase alloys with increasing temperature or with different alloying additions. These results may be misleading as strain is limited to 2%, thus limiting the need for $\langle c+a/2 \rangle$ activity. However, they did notice a drop in the $\langle c+a/2 \rangle$ density in the two phase alloys with increasing temperature. They surmise that the β /B2 phase is carrying most of the deformation at these small strains at 500°C. Of significance, they noticed that even in the heavily alloyed α_2 phase strained at elevated temperatures, slip was still largely planar. In fact, slip is transmitted across and through the α_2 and β /B2 phases from $\langle 11\bar{2}0 \rangle \{0001\}$ to $\langle 110 \rangle \{111\}$. They conclude that the β /B2 phase is offering a mechanism for absorbing strain incompatibilities stemming from the limited slip in the α_2

phase. The increase in ductility in the two phase alloys is attributed to a reduction in strain incompatibility.

As mentioned in the previous section, the research group of Banerjee, Gogia and Nandy have characterized dislocation behavior in the two phase mixture.^{74,75} Also cited above are the problems associated with their analysis as applied to an equilibrium condition. The authors found that slip within the α_2 was predominantly $\langle a \rangle$ in character. They do find, however, the incidence of $\langle c+a/2 \rangle$ slip initiated by intersecting slip bands from the B2 phase.

2.2.1.5 Interstitial Effects on Slip

Blackburn and Smith have performed one of the first, and only, studies to examine the effects of interstitials on α_2 alloys.³ Their results have shown that in alloys based on Ti-25Al-14Nb, oxygen is an extremely potent strengthening and embrittling interstitial. The range of oxygen levels studied was between approximately 300 wppm and 1000 wppm. With a decrease of about 500 wppm oxygen, very significant decreases in yield strength (~140-210 MPa) and increases in ductility (~2-3 times) to 6% elongation were observed. However, oxygen is also a potent α_2 stabilizer and may effect phase content of the alloy and thus its strength.

Löfvander and coworkers added 0.4Er to Ti-25Al in order to getter oxygen from the α_2 matrix.⁷⁷ When compressed to 3% strain, incidence of $\langle a \rangle$ slip on (0001) was significantly increased over a non-Er doped alloy. The observed dislocations consisted of undissociated $\vec{b} = 1/3\langle 11\bar{2}0 \rangle$ superdislocations in screw orientation, implying that edge dislocations are more glissile. The undissociated nature of these dislocations confirms the belief that the APB energy on (0001) is larger than that on $\{10\bar{1}0\}$. Superdislocations of paired $\vec{b} = 1/6\langle 11\bar{2}0 \rangle$ lying on $\{10\bar{1}0\}$ were also prevalent in their observations. In this case the superpartials had a spacing of ~10 nm, close to other observations.⁶⁹

2.2.2 Discussion

Summarizing the experimental observations to date, many studies have been performed and, with few exceptions, there is general agreement on the slip systems operating in the α_2 , DO₁₉, phase. Dominant slip in the single phase binary alloy consists of paired superpartials of $\vec{b} = 1/6\langle 11\bar{2}0 \rangle$ gliding on $\{10\bar{1}0\}$ in an edge configuration. It is fairly certain now that additions of niobium do promote the activation of additional $\langle a \rangle$ component slip systems in α_2 . Superdislocation activity of $\vec{b} = 1/3\langle 11\bar{2}0 \rangle$ is increased on both the (0001) and $\{10\bar{1}1\}$ planes with niobium additions. The superdislocations do not appear to dissociate on the basal plane due to its high APB energy. Slip on (0001) is believed to be more mobile when in the edge configuration. The character of dislocations observed on the $\{10\bar{1}1\}$ has not been clearly presented in any study to date.

Certain alloying additions, particularly niobium, to the α_2 phase do enhance activity of the all important $\langle c+a/2 \rangle$ slip.⁷⁰ This slip has been observed as paired superpartials with $\vec{b} = 1/6\langle 11\bar{2}6 \rangle$ gliding on the $\{11\bar{2}1\}$ planes. The more glissile configuration appears to be screw. Although $[c]$ dislocations have been observed in limited amounts, and may in fact be glissile, they do not significantly contribute to homogeneous deformation as they add no additional independent slip system.

The benefit of the presence of a ductile second phase, $\beta/B2$, appears to be the relief of strain incompatibilities formerly occurring at the α_2/α_2 lath interfaces in single phase compositions. The $\beta/B2$ phase is also capable of transferring slip from one α_2 lath to another, this attribute is not considered to be necessarily beneficial if effective slip lengths are to be minimized. One point to note in the two phase alloys is that the propensity for planar slip behavior does not appear to be reduced by the higher alloying concentration in the α_2 phase.

Oxygen, and likely other interstitials, appear to play a large role in the slip behavior of these alloys. This is the case in conventional titanium alloys as well, where large concentrations of oxygen, >2000 wppm, can alter slip behavior. In the conventional titanium α phase, slip changes from a homogeneous, or 'wavy', mode to a planar mode.⁷⁸ In the case of its intermetallic cousin α_2 , the slip mode observed is already planar at room temperature, with four times less oxygen. By comparison, a decreasing oxygen content appears to promote not a transition in slip mode, but rather an activation of additional slip systems in α_2 . The activation of additional slip systems may well account for the increase in ductility at lower oxygen levels. Whether or not the activation of an additional slip system by lowering oxygen contents is the result of a change in covalent bond structure, as proposed by Löfvander *et al.*, is an issue for debate.⁷⁷ A similar result might be expected from lattice strain relaxation, as interstitials are known to be very potent strengtheners in other, albeit more metallically bonded, alloy systems; however, current models of interstitial interaction do not support this explanation for this system.

In γ alloys based on TiAl, Greenberg *et al.* have described the slip behavior observed in this structure based on charge density distributions associated with an intermetallic compound.⁷⁹ They estimate that there is a large anisotropy between electron populations in the bonds of titanium atoms in the $\langle 110 \rangle$ and $\langle 001 \rangle$ directions. This leads to strong covalent bonding between the titanium atoms in the close packed directions. The strong covalent bonding among titanium atoms suggests that when the dislocation line direction lies perpendicular to planes containing all titanium atoms, the dislocation will fall into a deep Peierls valley. Glide of the dislocation in this instance would be difficult as many of the very strong $\langle 110 \rangle$ covalent Ti-Ti bonds would need to be severed.

Court *et al.* offer a potential explanation of slip behavior in the binary and ternary single phase α_2 alloys based on this theory.⁷⁰ They have identified the relevant planes in the DO_{19} structure which contain only titanium atoms, namely, $\{10\bar{1}0\}$, $\{11\bar{2}0\}$ and $\{10\bar{1}1\}$. They assume a similar electron density distribution behavior to γ , i.e. covalently

bonded titanium atoms; this assumption is supported through modelling by Hong *et al.*⁸⁰ Thus, dislocation line directions lying perpendicular to these planes could potentially experience deep Peierls valleys, thus making movement very difficult. Their predictions for various dislocations and the effect of covalency on their Peierls valleys are presented in Table 2.2.

From the evidence presented above, it is clear that the dislocation activity predicted by Court *et al.* matches experiment in the binary α_2 alloy.⁷⁰ They continue their argument by proposing that the addition of niobium atoms into the α_2 lattice promotes less covalent bonding between the titanium atoms. As niobium is known to occupy titanium lattice sites when in solution, the planes containing all titanium atoms would be disrupted. With less covalent bonding, they contend, the Peierls valleys would be more shallow for dislocations lying perpendicular to formerly all titanium planes. This would allow the activation of additional slip systems at lower resolved shear stresses. A similar argument is offered for the beneficial effects of elevated temperature. Increased temperature would offer thermal activation energy in making the effective depth of the Peierls valleys less severe. Although experimental evidence does support this argument, whether or not bond covalency controls dislocation slip has not yet been proven. However, for now it does seem to offer an apparently accurate predication of dislocation behavior in α_2 .

Table 2.2 Prediction of slip system activity in the α_2 phase (after Court *et al.*⁷⁰).

<u>Slip System</u>	<u>Character</u>	<u>Line Direction</u>	<u>Covalency Effect</u>
$\langle 11\bar{2}0 \rangle \{ 10\bar{1}0 \}$	Screw	$\langle 11\bar{2}0 \rangle$	Deep Peierls Valley
	Edge	$[0001]$	None
$\langle 11\bar{2}0 \rangle \{ 0001 \}$	Screw	$\langle 11\bar{2}0 \rangle$	Deep Peierls Valley
	Edge	$\langle 1\bar{1}00 \rangle$	Deep Peierls Valley
$\langle 11\bar{2}0 \rangle \{ 10\bar{1}1 \}$	Screw	$\langle 11\bar{2}0 \rangle$	Deep Peierls Valley
	Edge	$\langle 0\bar{1}12 \rangle$	Deep Peierls Valley
$\langle 11\bar{2}6 \rangle \{ 11\bar{2}1 \}$	Screw	$\langle 11\bar{2}6 \rangle$	None
	Edge	$\langle 10\bar{1}0 \rangle$	Deep Peierls Valley
$[0001] \{ 11\bar{2}0 \}$	Screw	$[0001]$	None
	Edge	$\langle 11\bar{2}0 \rangle$	Deep Peierls Valley

2.3 Correlation of Microstructure to Tensile Properties and Fracture

The relationship of microstructure to mechanical properties and fracture is somewhat different in the $\alpha_2 + \beta$ /B2 titanium aluminides from conventional $\alpha + \beta$ titanium alloys. When trying to explain the behavior of the titanium aluminides, it is important to recognize that as opposed to conventional titanium alloys where both the α and β phases are generally ductile, the titanium aluminide system contains at least one brittle constituent, namely α_2 .

Some work has attempted to explain the behavior of this system based on the individual constituent phases.⁸¹ While the results have been very interesting and

informative, this has been a difficult and only partially successful approach. The primary culprits in using this approach being the accuracy of phase compositions, indeed the composition of the β /B2 phase has been shown to be unstable at elevated temperature, and also the extension of bulk mechanical behavior to constrained films with typically less than 200 nm thickness. The descriptions to follow will concentrate on multiphase mechanical behavior.

2.3.1 Strengthening Effects

As compared to conventional titanium alloys, basic strengthening mechanisms in the α_2 + β /B2 alloys are similar. As in conventional titanium alloys, boundary strengthening through microstructural refinement can have the most influence on strength. Little careful work has been conducted to determine the strengthening effects of alloying additions. These studies are indeed difficult in a material system that exhibits such a dependence of microstructure on alloying additions.

Blackburn *et al.* reported that the strength of Ti-24-11 could be altered by varying the cooling rate from above the β transus.² Cooling rate variation controls the α_2 lath size (width) or, equivalently, inter-lath spacing. In Ti-25-10-3-1 it has been shown that yield strength may be increased by 50% through microstructural variation alone.^{28,82} The greatest factor in strengthening was found to be secondary α_2 lath size. In conventional titanium alloys, Hirth and Froes found yield strength to correlate well with α lath size, being proportional to λ^{-1} , where λ is the inter-lath spacing.⁸³ This response is attributed to boundary strengthening, or a Hall-Petch type of effect. This relationship can be extended to α_2 + β /B2 alloys as well, this is demonstrated in Figure 2.12.⁸⁴ Examples of two microstructures containing similar volume fractions of primary α_2 but different secondary α_2 lath sizes, and hence different yield strengths, are shown in Figure 2.6. In an α_2 + β /B2 processed condition a more complex situation arises due to the presence of two

morphological variants of α_2 . These microstructures contain both a coarse, 5-10 μm , globular primary α_2 which remains from the $\alpha_2+\beta/\text{B2}$ processing, and a finer, 0.2-1.5 μm , secondary α_2 lath structure formed on cooling or by an isothermal transformation.

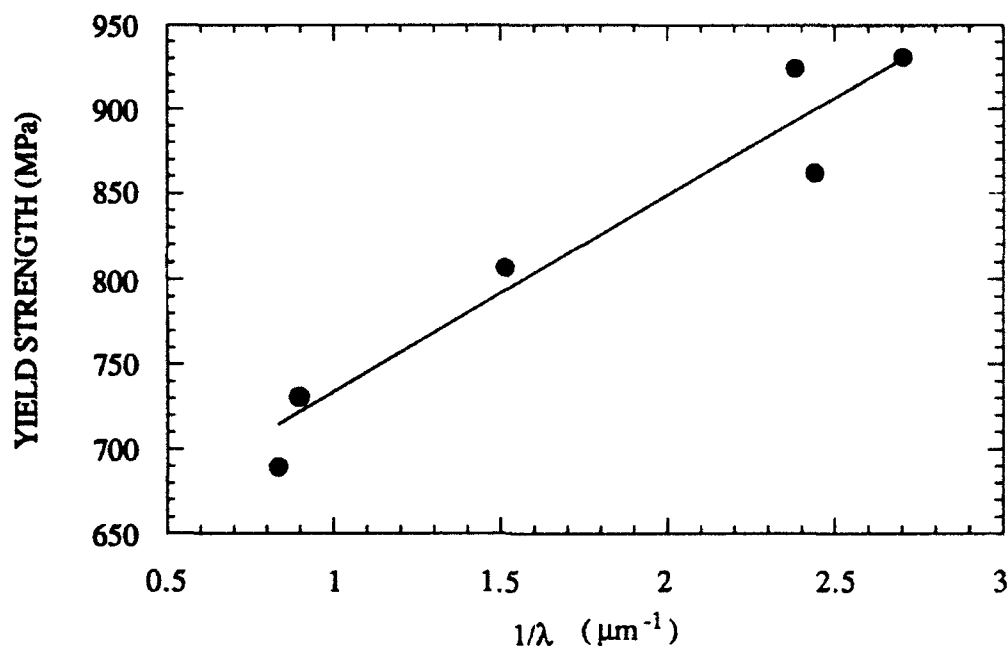


Figure 2.12 Plot showing the dependence of yield strength on the inverse of interlath spacing, λ , for Ti-25-10-3-1 with a volume fraction of primary α_2 in the range of 0.15-0.40.

In general, as the volume fraction of primary α_2 is increased in microstructures containing fine secondary α_2 , the fraction of the boundary strengthened fine secondary α_2 structure is decreased and so the overall yield strength of the material decreases. At approximately 30-40 volume percent primary α_2 this trend is reversed.²⁸ This could be attributed to an increase in the texture strengthening of the primary α_2 , a generally observed decrease in the mean primary α_2 particle size, as well as further refinement of the secondary α_2 structure due to decreased growth rates. In coarser secondary α_2 microstructures the increase in volume fraction of primary α_2 also leads to an increase in

texture strengthening, but more importantly to a decrease in the α_2 inter-lath spacing. Primary α_2 strengthening effects are small below 30-40 volume percent when compared to secondary α_2 interlath spacing. A description of this yield behavior must include the major contributors to strength; namely, the intrinsic strength of the two phase mixture, the volume fraction of primary α_2 , the diameter of the primary α_2 , a texture component, and the α_2 inter-lath spacing.²⁸ Koss *et al.* add other strengthening considerations to form a generalized expression to include substructure strengthening, interstitial and substitutional solid solution hardening, and strengthening due to APB's.⁸

2.3.2 Temperature Dependence of Strength

Tensile testing has shown that the yield strength of Ti-25-10-3-1 falls off from room temperature by approximately 25% at temperatures as low as 205°C and then remains relatively constant to over 650°C, as shown in Figure 2.13.^{85,86} The decrease in yield strength corresponds with a ductile to brittle transition. This implies thermal activation of dislocation motion at relatively low temperatures. The yield strength begins to fall again between 650°C and 760°C.

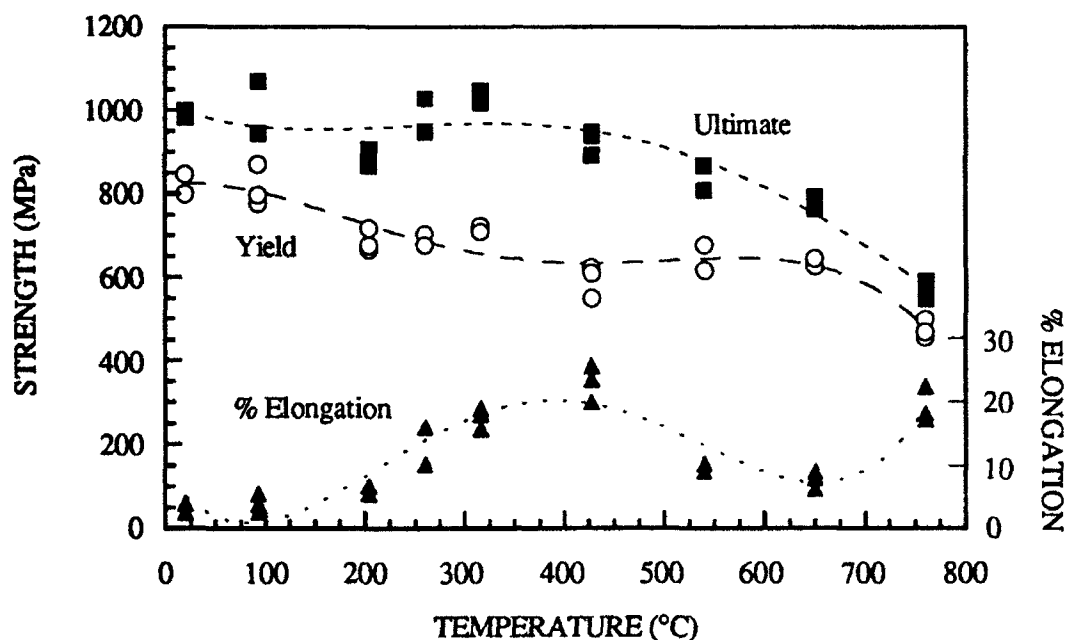


Figure 2.13 Tensile properties of Ti-25-10-3-1 as a function of temperature, testing performed in air. Material was $\alpha_2+\beta$ forged at 1085°C and direct salt bath aged at 815°C for 30 min (after Ref. 85).

2.3.3 *Ductility Effects*

Models developed to describe the ductility behavior of conventional titanium alloys do not generally hold for the $\alpha_2+\beta/\text{B2}$ titanium aluminides at temperatures below approximately 550°C. These models are based on alloys that exhibit equilibrium phases which are ductile. In the case of the titanium aluminides, this is certainly not true at room temperature where α_2 is brittle.

Perhaps it is best to start this discussion with a general picture of the sequence of events that lead to failure at temperatures below 540°C. This picture can be constructed from a recent study on the room temperature tensile behavior of seven different microstructures of Ti-25-10-3-1 using acoustic emission techniques.⁸⁷ Most interestingly, it was found that microcracking did not generally appear in most $\alpha_2+\beta/\text{B2}$ and β processed

microstructures until very late in the work hardening regime of tensile deformation. In fact, six of the microstructures tested exhibited general microcrack nucleation only during the last 0.5% of plastic deformation just prior to failure. Only in a microstructure containing a high volume fraction of primary α_2 , 0.80, was significant microcracking detected during the work hardening regime, and then just after yielding. Microcrack nucleation can be associated with primary α_2 particles in $\alpha_2+\beta/B2$ processed material, or with aligned regions of secondary α_2 laths in either $\alpha_2+\beta/B2$ or β processed material. These results were supported by sectioning and metallographic examination of the failed tensile bars. Thus, microcracking in $\alpha_2+\beta/B2$ alloys is generally restricted to the very last stages of deformation just prior to failure. This suggests that tensile failure of these alloys is by and large a microcrack nucleation controlled event.

The idea that refinement of secondary α_2 lath size will lead to increased ductility is misleading, and may be a totally unnecessary precaution. To date, no conclusive evidence shows that reducing secondary α_2 lath size will increase ductility. Indeed, ductility may decrease when the lath size becomes extremely fine, as the cleavage stress is reached much sooner in features such as primary α_2 due to an increased yield strength. Rather, it is the morphology of the secondary α_2 laths that strongly controls ductility.²⁸ The alignment of these laths results in an effectively larger slip length extending across the region of alignment, or "packet." The larger slip length results in very high stress concentrations at the end of the slip plane due to an increased density of dislocations in the pile-up. This in turn likely leads to Stroh crack nucleation and propagation. Examples of microstructures containing the same volume fraction of primary α_2 and similar secondary α_2 lath size, but variations in lath alignment, are shown in Figures 6(b) and 2.15. Note that the similar lath size results in yield strengths that are very close to each other. However, the ductility is reduced by half in the microstructure in Figure 2.14 due to the alignment of secondary α_2 laths. The lath alignment results in a slip length across the "packet" of approximately 50 mm. Further, the presence of a continuous film of α_2 at the prior β grain boundaries offers

a path for very rapid crack propagation.²⁸ This aids crack growth and leads to premature failure. Thus, slip dispersion is an extremely important factor in determining ductility.



Figure 2.14 Microstructure with an aligned "packet" morphology of secondary α_2 laths. YS: 745 MPa, UTS: 907 MPa, Elongation: 1.1% (after Ref. 28).

As one might expect from their size, primary α_2 particles are also an important consideration in controlling ductility. Gogia *et al.* found that a primary α_2 volume fraction of approximately 0.30 gave the optimum ductility in an $\alpha_2 + \beta$ /B2 solution treated and quenched condition.⁷⁴ This volume fraction struck a balance between failure by slip band decohesion in the B2 phase and failure by extensive amounts of cracking from the cleavage of primary α_2 . However, the B2 matrix was not representative of an equilibrium microstructure, as previously discussed. In a more nearly equilibrium microstructure the effects of primary α_2 grains are not as well defined. Cleavage of primary α_2 grains and cracking at primary α_2 /matrix interfaces have both been observed in stable microstructures and act as nucleation sites for failure, Figure 2.15.^{28,86} It appears that cleavage of α_2 generally occurs along, or very near to, the basal plane.^{74,88} It must be

noted here, however, that in certain instances where a very strong texture has been developed in the primary α_2 through extensive warm working, the favorable alignment of active slip planes and unfavorable orientation of the cleavage plane may help compensate for the brittleness of primary α_2 found in randomly textured microstructures.

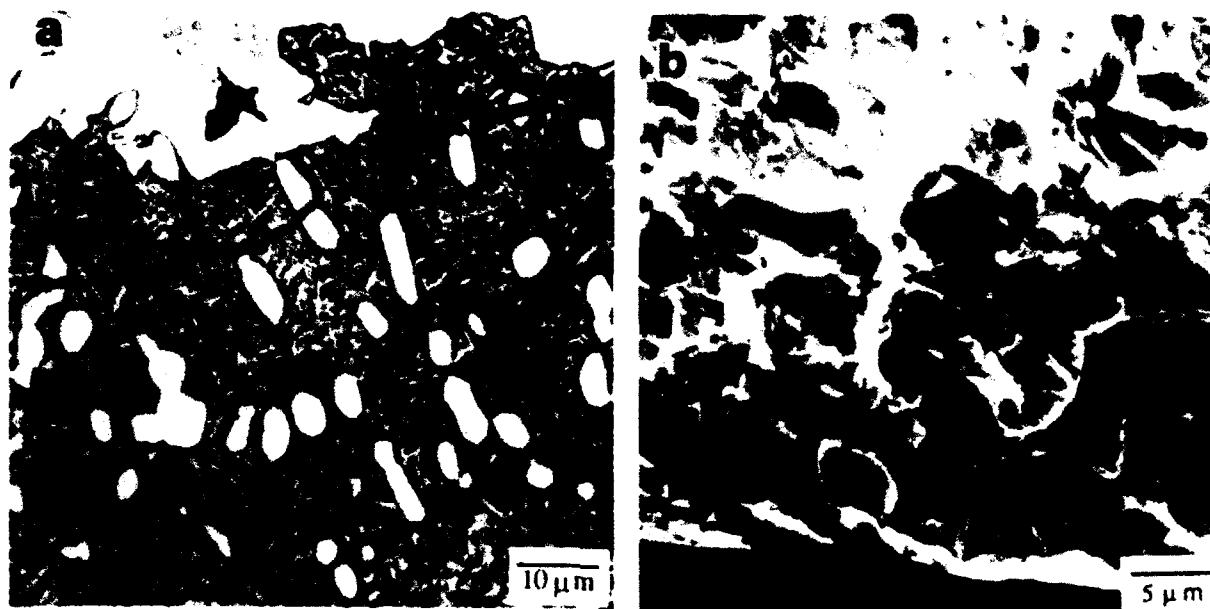


Figure 2.15 (a) Room temperature tensile specimen cross-section showing the cleavage of primary α_2 grains. Microstructure contains fine Widmanstätten α_2 laths. (b) SEM of the fracture surface of sample in (a) showing area near the failure initiation site, note the cleaved primary α_2 grains (after Ref. 86).

Moreover, having limited amounts of primary α_2 in a microstructure may have two very beneficial effects on tensile elongation. Most importantly, primary α_2 grains have been observed to pin recrystallized $\beta/\text{B2}$ grains.²⁸ This may be very helpful in reducing strain incompatibilities across the prior $\beta/\text{B2}$ grain boundaries by reducing the size of the macroscopic microstructural deformation unit, as proposed by Lukasak and discussed below.⁸⁹ Second, the presence of primary α_2 grains can reduce the extent of sideplate formation, through the recrystallization of $\beta/\text{B2}$ grains.

Lukasak and Koss have shown that macroscopic flow occurs anisotropically between prior β grains in a β solution treated and aged condition.⁸⁹ Their tests were

performed in compression from room temperature and 3% strain up to 500°C and 9% strain. Their observations were limited to the pre-polished surface of the specimens. The surfaces of the specimens experience tensile stresses in a circumferential direction during compression testing. They observed that aligned α_2 laths associated with prior β grain boundaries led to strain incompatibilities across the boundaries due to the imposed limitation of slip systems. These incompatibilities led to associated microcrack nucleation, which was only observed to occur near the prior β grain boundaries. The microcracks appeared to be V-shaped and crystallographic in nature. Based on this, Lukasak and Koss propose that the microcracks are formed at the intersections of blocked slip bands extending across large or similarly aligned α_2 plates. However, the reason for slip band blockage has not been resolved. The microcracks, once nucleated, link up and finally result in failure.

Lukasak and Koss conclude that the β /B2 phase may play two roles in enhancing ductility.⁸⁹ First, it may act to bridge microcracks formed in the α_2 and so act to shield the crack tip. And, second, the presence of the β /B2 phase at elevated temperatures may lead to the basketweave morphology of α_2 thus leading to better slip dispersal. While a basketweave morphology may result in better slip dispersal, the presence of an equilibrium β /B2 phase is not essential in providing the basketweave morphology. A similar morphology can be found in single phase α_2 alloys as well. More exactly, the microstructural refinement is caused by the increased concentration of the β stabilizers which leads to sluggish growth kinetics.

Acoustic emission monitoring by Roman and Ward during tensile failure at room temperature suggests that the more important role played by the β /B2 phase for most microstructures is slip accommodation at the α_2 / β /B2 interfaces, as proposed by Marquardt and coworkers.^{87,76} Microcrack nucleation was observed to occur very near the failure point where contributions from bridging in prolonging deformation are negligible. However, β /B2 phase crack bridging may be important in high volume fraction primary α_2

microstructures, thus containing thicker regions of β /B2 presented to the crack front, and at elevated temperatures.

Thus, the optimum microstructure for ductility in α_2 + β /B2 alloys would be one processed in the β phase field and aged in such a way so as to produce and retain a fine recrystallized β /B2 grain structure, minimal grain boundary allotriomorph precipitation, no grain boundary side plate formation and a random Widmanstätten α_2 morphology.

2.3.4 Temperature Dependence of Ductility

Little work to date has been performed to characterize the failure mechanisms in α_2 + β /B2 alloys as a function of temperature. Tensile testing of Ti-25-10-3-1 in air has shown that the tensile elongation begins to rise at approximately 200°C, Figure 2.13.⁸⁵ The rise in elongation continues to 427°C and then takes a steep fall at 540°C, remains low at 650°C, then begins to rise again at 760°C. Microscopic examination of the gage length surface revealed that extensive circumferential cracking occurred. Balsone has observed similar cracking in Ti-24-11 tensile tested in air.⁹⁰ He repeated the tensile testing in vacuum at 550°C and 650°C, finding that the surface cracking disappeared and that the tensile elongation was significantly increased. From this, Balsone deduced that there was a significant effect of the environment, presumably oxygen embrittlement, on tensile properties at temperatures as low as 550°C. Vacuum tensile testing of Ti-25-10-3-1 also results in a significant improvement in the tensile elongation.⁸⁶ Furthermore, the tensile elongation "peak" is shifted from 427°C to 540°C, due to the absence of cracking along the gage length, Figure 2.16. After this peak the elongation again falls steeply at 650°C; however, note that the elongation in vacuum at this temperature is two times larger than in air (Figure 2.13). This ductility deficit will be discussed further below.

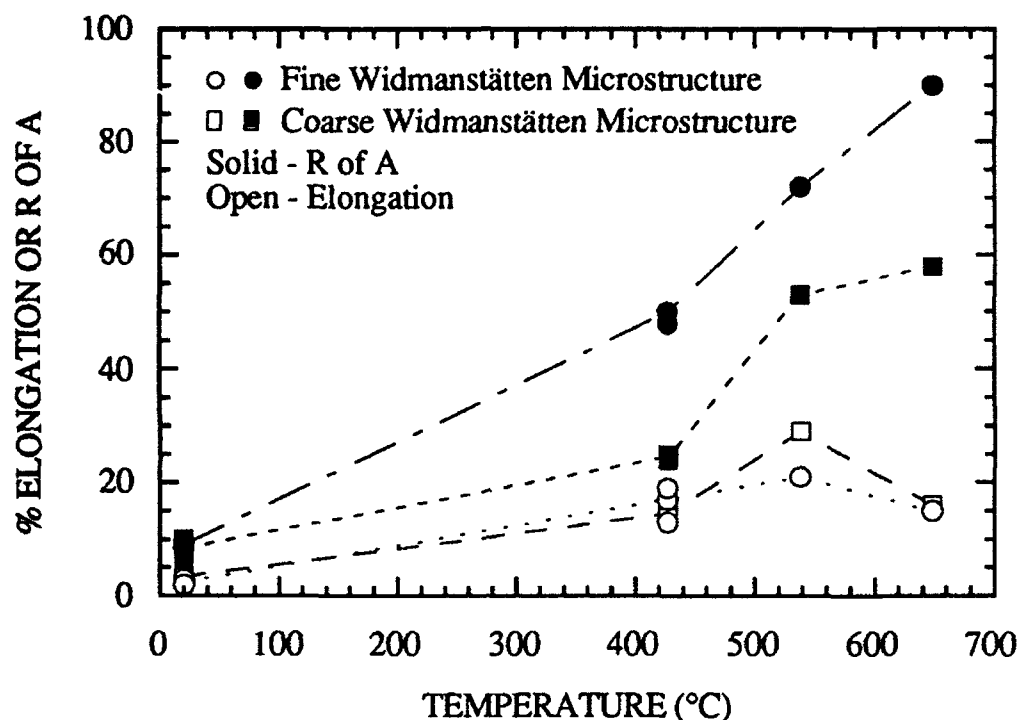


Figure 2.16 Tensile elongation and reduction of area for $\alpha_2+\beta$ forged Ti-25-10-3-1 with fine and coarse Widmanstätten microstructures as a function of temperature. Testing performed in vacuum (after Ref. 86).

Under tensile loading, the dominant failure mechanism generally changes in $\alpha_2+\beta/B2$ processed alloys from initiation by brittle fracture of the primary α_2 particles, at the primary α_2 /transformed matrix interfaces or within regions of aligned secondary α_2 laths at room temperature to ductile void formation at primary α_2 /transformed matrix interfaces at temperatures $\geq 540^\circ\text{C}$.⁸⁵ As the temperature is increased from room temperature to 425°C , the brittle cracks appear to become blunted by the increasingly tougher matrix, Figure 2.17. An increase in tensile elongation with temperature is seen to parallel the increases observed in fracture toughness, Figures 2.16 & 2.18. This is the result of an increased resistance to crack propagation through the transformed matrix following initiation, and agrees well with Chan's model of failure in brittle intermetallics.⁹¹ This is not to say that there is necessarily good correlation between variations in fracture

toughness and ductility at room temperature. The tougher matrix at elevated temperature resists crack propagation and results in higher stress to failure and so higher elongation. At elevated temperatures, 425-540°C, fine microstructures, which have higher yield strengths, have been observed to fail at prior β grain boundaries, despite the presence of numerous failed primary α_2 particles, Figure 2.17. Failure at the prior β grain boundaries in a strong microstructure is consistent with the behavior of $\alpha+\beta$ conventional titanium alloys. This is believed to be the result of faster strain accumulation within the weaker grain boundary α film that is almost always present in some thickness.⁹²

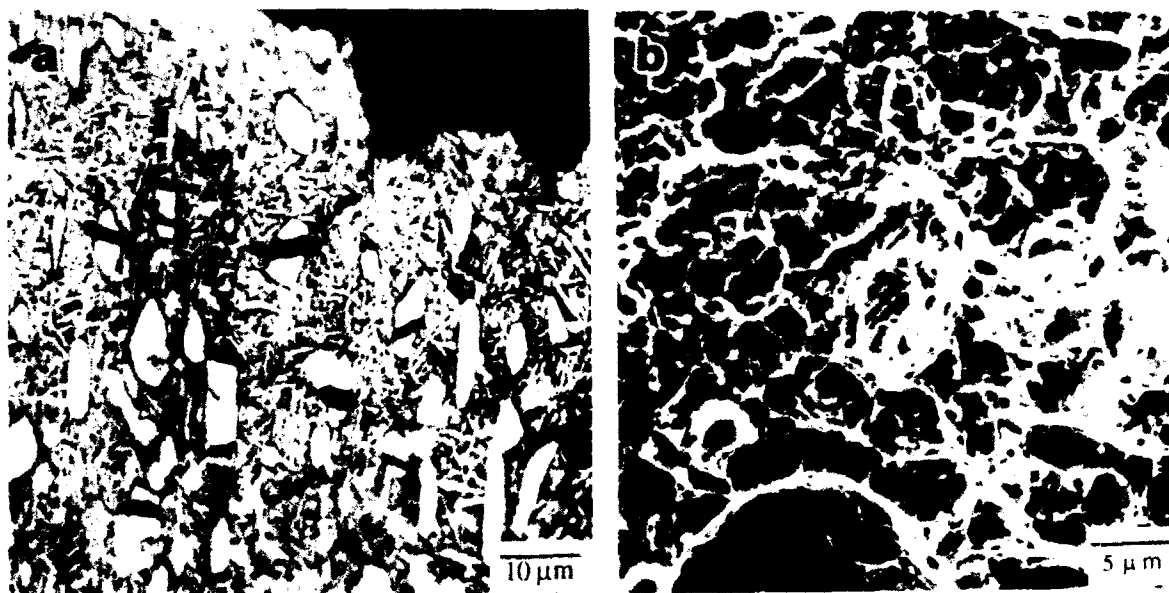


Figure 2.17 (a) Light micrograph of a cross-sectioned tensile sample, tested at 425°C. Microstructure contains fine Widmanstätten α_2 laths. (b) SEM micrograph of the fracture surface at a location near the initiation site at a prior β grain boundary (after Ref. 86).

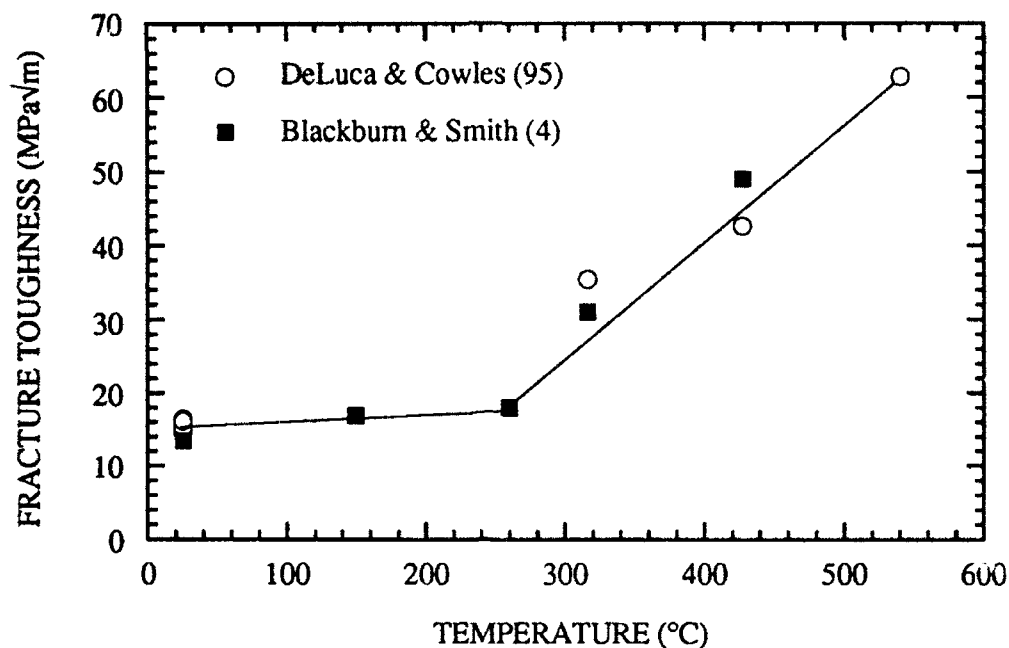


Figure 2.18 Fracture toughness, from valid K_{IC} tests, plotted to 540°C from Blackburn and Smith and DeLuca and Cowles. Microstructure was β processed with fine secondary α_2 laths (after Refs. 4 and 95)

At 540°C there appears to be difficulty in both the nucleation and propagation of cracks through the matrix, Figure 2.19. Also, the first indications of void nucleation and coalescence associated with ductile rupture are noticeable. Both of these failure mechanisms appear to be equally difficult to initiate and thus result in the highest elongation, and highest fracture strength, Figure 2.20, before the elongation minimum. At 650°C failure is clearly dominated by ductile rupture. In this case voids are nucleated at primary α_2 /matrix interfaces and are linked by void sheet coalescence across the secondary α_2 laths, Figure 2.21. Similarly, Lukasak and Koss have observed crack blunting at 500°C in the β processed condition; again, the cracks are associated with the prior β grain boundaries.⁸⁹

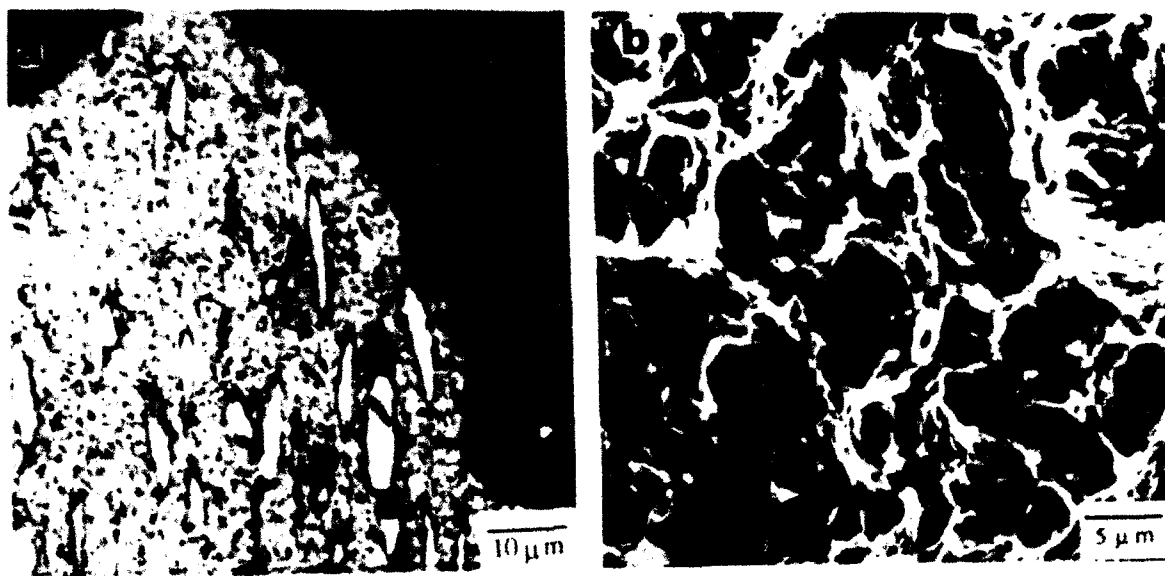


Figure 2.19 (a) Light micrograph of a cross-sectioned tensile sample, tested at 540°C. Microstructure contains fine Widmanstätten α_2 laths. Note the alignment of α_2 laths. (b) SEM micrograph of the fracture surface of the same test in (a) (after Ref. 86).

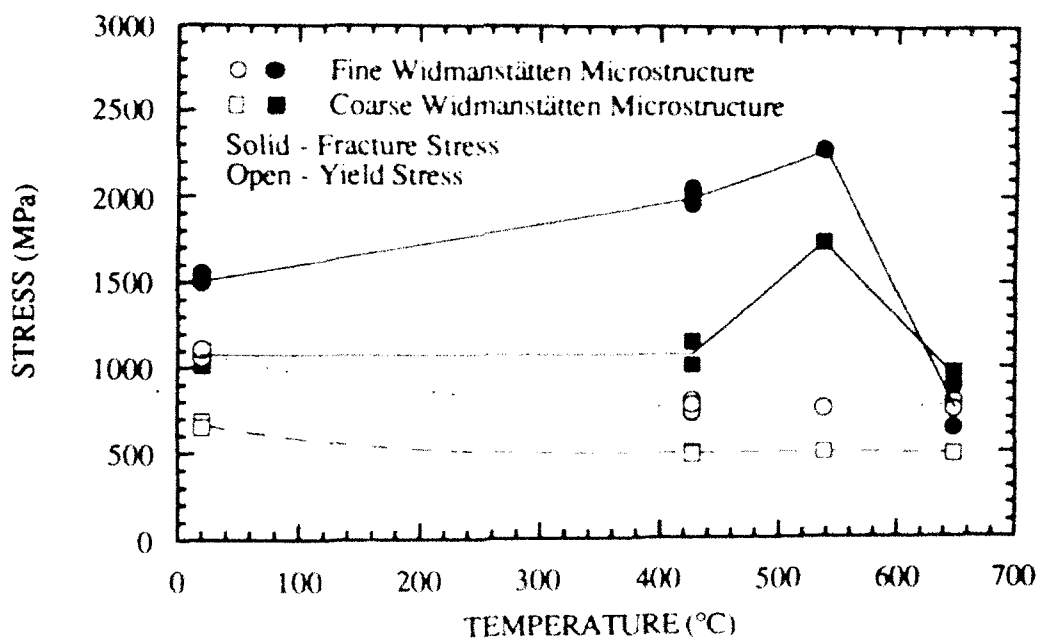


Figure 2.20 Fracture stress and yield strength for both a fine and coarse Widmanstätten microstructure as a function of temperature (after Ref. 86).

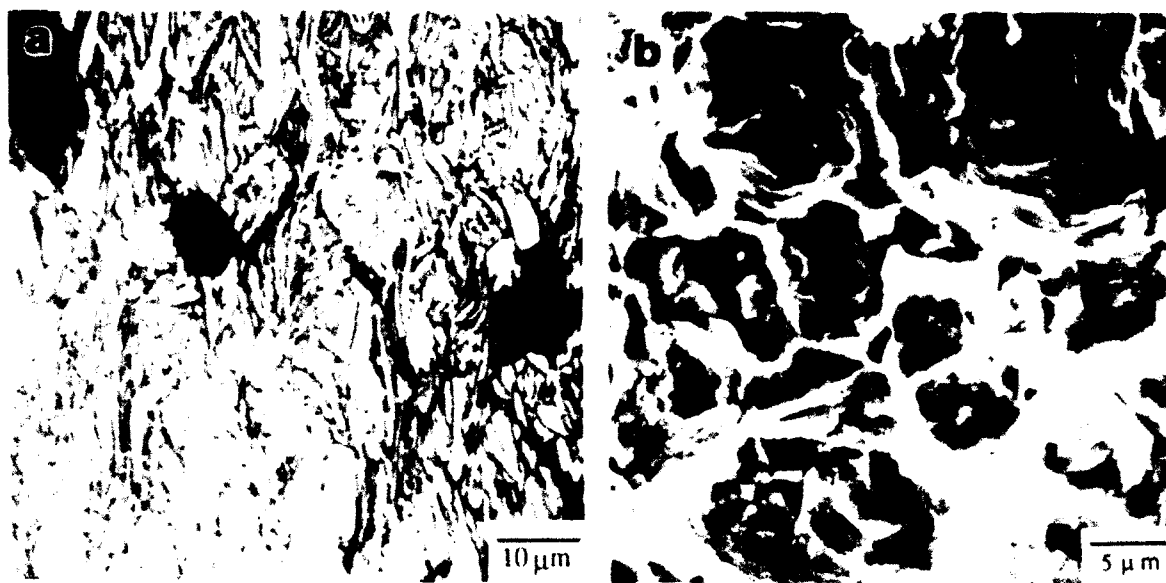


Figure 2.21 (a) Light micrograph of a cross-sectioned tensile sample, tested at 650°C. Microstructure contains coarse α_2 laths. Note the alignment of α_2 laths. (b) SEM micrograph the fracture surface of the same test in (a) (after Ref. 86).

From Figures 2.13 & 2.16 we can conclude that the reason for the observed elongation minimum is not just an environmental issue, but is in fact also an intrinsic property of the material. This decrease in elongation at $\sim 650^\circ\text{C}$ is manifested through localized necking, note that the reductions in area continue to increase with temperature. Santhanam and Reed-Hill have seen a similar elongation minimum at 427°C , the so called "blue brittle" temperature, in CP titanium.⁹³ A reversal in the work hardening response to strain rate, as described by Santhanam and Reed-Hill, could certainly offer an explanation for the minima in $\alpha_2+\beta/\text{B2}$ alloys. However, this is an area requiring further investigation. Interestingly, coarse secondary $\alpha_2/\text{B2}$ transformed matrix appears to be more resistant to this strain localization phenomenon. Perhaps, this may be attributed to a break up of slip band formation by the coarser microstructure.

Let us assume for a moment that the brittle fracture of these multi-component materials can be described by a unique cleavage stress at temperatures below 540°C . Cleavage, as traditionally thought of, should be characterized by a cleavage stress that is

relatively temperature insensitive. Also, cleavage stress is known to increase with decreasing microstructural size for a given material. When the tensile true fracture stress, a measure of the cleavage stress, is plotted against temperature a maximum is reached at the same temperature as the ductility maximum, Figure 2.20. This data distinctly shows the change in failure mode at 540°C. Also of interest is the rise in fracture stress in the fine (strong) microstructure at 425°C. This is consistent with the observation above that fracture was associated with failure along the prior β grain boundaries, and not microcracking of the primary α_2 particles.. The coarser microstructure is apparently still dominated by brittle cleavage fracture below 540°C as no increase in the fracture stress is observed. It is important to keep in mind, as both Chan, and Chu and Thompson point out, that failure of these materials would best be described as a combination of both stress and strain.^{88,94}

2.3.5 Fracture Toughness

There have been several recent studies to understand the fracture toughness behavior of the $\alpha_2+\beta$ /B2 titanium aluminides. Blackburn and Smith, and DeLuca and Cowles have characterized the fracture toughness of Ti-25-10-3-1 in air up to 540°C; their combined data is shown in Figure 2.19.^{4,95} The microstructural condition for both studies was a β processed condition from a forging containing fine Widmanstätten α_2 laths. The data defines a ductile to brittle transition at approximately 250°C. DeLuca and Cowles studied the effect of orientation within the forging, i.e. the effect of prior β grain boundaries, on fracture toughness at room temperature and found no change in properties.⁹⁵

Chu and Thompson have studied the room temperature fracture behavior of Ti-24-11 in a number of microstructural conditions.⁹⁶ The microstructures studied can generally be described as β processed with a basketweave, albeit at times coarse, α_2 lath

morphology. They determined that the fracture strength followed the trends of the yield and ultimate tensile strength which can be directly attributed to the change in microstructure. Further, they found very good correlation between the fracture strength of the material and its fracture toughness. As such, this is the first result showing that fracture toughness increases with microstructural refinement. In their study, they observed that the α_2 plates fail in a brittle manner and act as crack initiation sites while the β phase arrested crack propagation. They conclude that microstructural refinement acts as a barrier to cleavage crack nucleation and propagation, they also report, however, that the finer microstructures contained larger volume fractions of β phase.

Marquardt has presented an extensive experimental study concerning fracture toughness as a function of microstructure at room temperature.⁹⁷ His data shows that fracture toughness in a Ti-24Al-5.5Nb-1Mo alloy can be nearly doubled, from $K_{exp} = 14 \text{ MPa}\sqrt{\text{m}}$, by going from a fine $\alpha_2 + \beta$ processed Widmanstätten microstructure to a colony morphology in the β processed condition. K_{exp} refers to an experimental toughness obtained by a notched bend bar without precracking. This is consistent with toughening trends in conventional $\alpha + \beta$ titanium alloys. The increased toughness is presumably due to an increase in crack tortuosity attributed to greater crack deflection. Marquardt also found trends in fracture toughness which appeared to correlate well with the volume fraction of primary α_2 and microstructural texture.

Chan has examined the temperature dependence of fracture toughness of "as-rolled" Ti-24-11.⁹⁸ The microstructure studied consisted of fully equiaxed α_2 grains, $\sim 8 \mu\text{m}$ in diameter, in a matrix of " β " with a volume fraction of 0.26. More stable volume fractions of the " β " phase are thought to be closer to 0.05 - 0.10 in this alloy. J_{Ic} tests were performed at 25, 316 and 450°C and a J-resistance test on a single edge notched specimen at 600°C. The corresponding initiation toughness, K_{Ic} , values were 20.4, 21.3, 47 and 12.5 $\text{MPa}\sqrt{\text{m}}$, respectively. As the K_{Ic} values in Chan's work were calculated from J_{Ic}

values, they represent the toughness at $\Delta a = 0$, the onset of crack growth, and as such do not include contributions to toughness from crack growth.

These are the first published results showing a decrease in initiation fracture toughness, at $\Delta a = 0$, at elevated temperatures, 600°C. Interestingly, the temperature at which this occurs is also at the point of the elongation minimum for Ti-24-11 and Ti-25-10-3-1. Chan observed substantial crack-tip plasticity in Ti-24-11, and that the crack path is tortuous and characterized by cleavage-like facets. SEM examination showed that there is extensive crack and void nucleation within the process zone, up to 40 μm ahead of the crack tip. Microcrack nucleation in the equiaxed structure was found to occur in both tensile and fracture toughness tests by three mechanisms; (1) along α_2 slip bands, (2) along $\alpha_2/\beta/\text{B}2$ interfaces and (3) within the $\beta/\text{B}2$ phase, perhaps associated with small α_2 precipitates that appear within the $\beta/\text{B}2$ phase. Near-tip strain measurements demonstrated that approximately 5% effective strain was needed to nucleate cracks within α_2 and at $\alpha_2/\beta/\text{B}2$ interfaces, while approximately 40% strain was required to nucleate cracks in the $\beta/\text{B}2$ phase. Chan reports that there is no temperature dependence of these failure strains.⁸⁸ After crack nucleation, and still below K_{IC} , the microcracks are affected by the $\beta/\text{B}2$ phase through bridging and blunting processes. As K is increased, the $\beta/\text{B}2$ ligament breaks and the crack links up with the main crack. Thus, crack extension is a series of microcrack and void nucleation and linkage events. This process is observed to occur in this microstructure up to 600°C. The presence of microcracking ahead of the main crack is attributed with acting to increase the near-tip K through an anti-shielding process, thus tending to lower the observed K_{IC} .

Chan concludes that the observed initiation toughness of Ti-24-11 in the temperature range 25-450°C originates from the $\beta/\text{B}2$ phase.⁹⁸ This increased toughness is imparted by the $\beta/\text{B}2$ phase through two mechanisms: (1) accommodation of strain incompatibility at the interfaces (2) a barrier to crack propagation. This latter mechanism is manifested in the blunting and deflection of cracks on the microscopic level and as a ductile

ligament on the macroscopic level. Both of these mechanisms lead to an increased K_{Ic} by decreasing the near-tip J or K by a shielding process. And in fact, by measuring the near-tip strain field the author concludes that the near-tip K at K_{Ic} remains nearly constant as the temperature is increased. It appears that the measured K_{Ic} is increasing with temperature by the increase in the occurrence of microcrack shielding. However, the reason for an increase in microcracking is not known. At 600°C the author asserts that the observed fracture toughness is decreased due to easy void nucleation and growth and the inability of the now soft $\beta/B2$ phase to offer a crack bridging mechanism. He does, however, note bridging by the α_2 phase at this temperature.

A number of toughening mechanisms, both intrinsic and extrinsic, have been observed to operate in $\alpha_2+\beta/B2$ alloys in combinations with changing microstructure and increasing temperature.^{88,99} These mechanisms include ductile phase blunting and bridging, crack deflection, microcrack shielding, and, most recently, crack ligament shearing.¹⁰⁰ Both Chan and Soboyejo have attempted to sort out the individual contributions to toughness from these mechanisms, a quite complicated task. By modeling the crack tip, both agree that crack tip blunting by the ductile $\beta/B2$ phase can have the largest contribution to initiation toughness in either an equiaxed or basketweave α_2 morphology. Furthermore, both describe the same result of decreased fracture toughness with the presence of discontinuous $\beta/B2$ phase. In this case it was observed that the crack tip was not effectively blunted by the $\beta/B2$ phase, and in some cases did not have to pass through the $\beta/B2$ phase before entering the next α_2 particle. This may be a function of not only discontinuity but thickness of the $\beta/B2$ phase. It is interesting to note, however, that while Soboyejo includes ductile phase bridging in his model for initiation toughness, Chan does not. Perhaps one of the most interesting and certainly highest toughness microstructures, namely a β processed colony microstructure, has not been examined in a quantitative manner.

There is no doubt that the presence of $\beta/\text{B2}$ phase is beneficial for both ductility and toughness. Extremely limited results are available for the behavior of fracture toughness with microstructure and temperature. While some toughness is certainly imparted to the two phase alloys by the presence of a $\beta/\text{B2}$ phase, the large increases in fracture toughness with temperature should include the increase in the intrinsic toughness of the α_2 phase. Indeed, a similar temperature dependence of toughness can be inferred from K_Q values taken from fatigue crack growth curves for single phase Ti-25Al-5Nb.^{2,101} From all of the previously discussed studies, it appears that there is little hope of significantly increasing the fracture toughness of the $\alpha_2+\beta/\text{B2}$ alloys through microstructural manipulation alone, save the β processed colony microstructure. It is apparent that the quantity of the $\beta/\text{B2}$ phase must be increased to have a substantial effect. However, as previous alloy development programs have shown, this is not an easy task and that the higher volume fractions of the O phase may occur instead. However, the presence of the O does not appear to be necessarily a detriment. Research on these relatively new alloys have shown promising fracture toughness values of near 30 MPa $\sqrt{\text{m}}$ or better, with the retention of strength and ductility.⁷

2.5 Research Objectives

There were three primary goals set for this research: (1) Understand the role of microstructure in controlling ductility as a function of temperature. (2) Understand the mechanism by which the material experiences a ductility loss at elevated temperature. (3) Understand the role of microstructure in controlling fracture toughness both at room and elevated temperatures.

Three microstructures were to be studied in detail. Two of the microstructures were β processed and represent the general behavior of a finer basketweave microstructure and a coarse, colony microstructure. The third microstructure was $\alpha_2+\beta$ processed with a

significant volume fraction (~ 0.25) of primary α_2 in a fine basketweave microstructure. The presence of the primary α_2 grains will be important in cleavage crack and void nucleation during failure throughout the temperature range considered. As it is not clear what role primary α_2 grains will have in the fracture process in a coarser microstructure, some limited testing has been added to the study on this microstructure.

2.5.1 Ductility at room temperature

At room temperature, failure occurs by cleavage of the α_2 phase and subsequent microcrack propagation through the matrix. As "tough" microstructures in this material exhibit nil ductility, crack nucleation appears to be the dominant process in tensile failure. However, exactly how the failure process proceeds in $\alpha_2 + \beta$ alloys with the same volume fraction primary α_2 but different transformed matrix strengths, for example, is not clear. In this particular situation there is no appreciable difference in ductilities between the two strength levels, even though failure might be controlled by a maximum normal stress. If this were the case, the lower strength microstructure would be expected to reach a higher ductility, assuming the same work hardening rates for both.

Issues: (1) The α_2 appears to fail by cleavage, what is the contribution of strain to crack nucleation? (2) Is there a difference in deformation character between the fine and coarse basketweave microstructures that leads to the lower fracture stress of the coarse microstructure? (3) How close to fracture does crack nucleation occur, ie. how important is the crack nucleation event?

Approach: (1) Pre-polished flat tension tests to characterize deformation character and crack initiation with respect to the microstructural components. (2) Use a $10\mu\text{m}$ grid on selected specimens to try to characterize local strains to failure using optical and SEM observations. (3) Calculate true (as opposed to engineering) fracture stresses and strains

from data gathered on round tensile bars. (4) Employ acoustic emission techniques to capture the crack nucleation event and associate it with the stress-strain curve.

2.5.2 Ductility at intermediate temperatures ($25^{\circ}\text{C} < T < 540^{\circ}\text{C}$)

Ductilities increase after $\sim 200^{\circ}\text{C}$, this is coincident with a change in deformation behavior at $\sim 175^{\circ}\text{C}$, ie. slip activity, as observed in Ti-24-11. This implies more slip systems available in the α_2 phase. At temperatures $\sim 425^{\circ}\text{C}$ failure in the stronger microstructures along grain boundary α_2 leaving ductile dimples is reminiscent of conventional Ti alloys. Also, the fracture toughness of the material is increasing with temperature implying a greater capacity for plastic work. Fracture strains and stresses are too poorly characterized at these temperatures to draw any conclusions as to details on failure process.

Issues: (1) Is failure still dominated by crack nucleation? Or is propagation becoming more important with temperature? (2) Is the α_2 phase failing by cleavage or is plasticity playing a greater role? (3) Are cracks propagating in a similar fashion as at room temperature?

Approach: (1) Use pre-polished flat tensile specimens to observe changes in deformation character as a function of temperature and strain. (2) Employ acoustic emission techniques in detecting crack nucleation. (3) Use round tensile bars to gain fracture strain and stress data, information also to be used later in the analysis stage to confirm observations and trends.

2.5.3 Ductility Loss and Failure at elevated temperature, $\geq 540^{\circ}\text{C}$

At 540°C and above, failure within $\alpha_2 + \beta$ processed microstructures changes from nucleation of cracks within or at the interfaces of primary α_2 to void nucleation at the

primary α_2 /matrix interface. At 650°C there is a significant drop in uniform elongation while reduction in area continues to increase. The strength of the material has not significantly changed over this temperature range. Initial indications are that the strain rate sensitivity of the work hardening rate at 650°C is zero or below, thus leading to rapid strain localization. The decrease in uniform elongation is consistent with a zero strain rate sensitivity of the work hardening rate. Also, in this temperature range, the strength of the β phase is falling at a much faster rate than the α_2 phase and may be undergoing strain softening.

Issues: (1) What is the strain rate sensitivity of the work hardening rate at elevated temperatures? (2) Is the strain rate sensitivity a function of microstructure? (3) Where is void nucleation occurring in various microstructures? (4) At what local true strain is void nucleation occurring?

Approach: (1) Elevated temperature tensile tests on round tensile bars with varying strain rate and temperature. Section to study void nucleation. (2) Prepolished flat tensile bars at elevated temperature to study slip band formation and void nucleation. Grid applied to selected samples to look for evidence of creep mechanisms.

2.5.4 Fracture Toughness Testing

Very little work has been performed on studying toughening behavior at room temperature, let alone at elevated temperature. The relationship between crack path and tortuosity and microstructure has not been studied in these materials. Toughness appears to be strongly controlled by crack propagation.

Issues: (1) What are the macroscopic effects of microstructure on toughness, e.g. relation of crack path to microstructure? (2) What are the temperature effects on toughness? Does crack path change with temperature or is local increase in plasticity more important?

(3) Are there local events which affect crack front/microstructure interactions? (4) Is the increase in α_2 plasticity adding to the measured fracture toughness of the alloy?

Approach: (1) Room temperature fracture toughness testing of all the microstructures to establish a data base from which to start. (2) Elevated temperature testing for a few microstructures around the temperature at which toughness apparently falls (if this is indeed the case).

3. EXPERIMENTAL PROCEDURE

3.1 Material Processing

Six different microstructures were produced in the Ti-25-10-3-1 alloy using hot-die forging and post-forging heat treatments. Processing was selected so as to provide microstructural variation in primary α_2 volume fraction and secondary α_2 lath size. The starting billets for hot-die forging were cylindrical with 10 cm diameter x 11 cm height. The heat of material studied was found to have a β transus of approximately 1075°C, as determined by metallography and DTA. Forging was carried out with a stroke rate of 1.25 cm/min to a final height of 3.3 cm for a total reduction in height of 70%. The die temperature was maintained at 982°C by induction heating. Post-forge heat treatment consisted of a direct salt-bath age at 815°C for 30 minutes followed by air cooling to room temperature. The variable forging parameters are listed in Table 3.1.

Table 3.1 Work piece forging temperatures.

<u>Microstructure</u>	<u>Pre-forge soak, 2 hours (°C)</u>	<u>Processing field</u>
25/C	1021	$\alpha_2 + \beta$
25/F	1021	$\alpha_2 + \beta$
10/C	1049	$\alpha_2 + \beta$
10/F	1049	$\alpha_2 + \beta$
0/C	1104	β
0/F	1104	β

The designations used for the microstructures represent an abbreviated description of the final microstructures. The number prefacing the designation is the volume percent primary α_2 and the letter following the number is the size of the secondary α_2 laths. For example, microstructure 10/F is comprised of 10 volume percent primary α_2 in a matrix

containing fine Widmanstätten secondary α_2 laths. These microstructures will be fully described in section 3.

At this point, the microstructures in Microstructures 25/C & 25/F, 10/C & 10/F and 0/C & 0/F were identical. Microstructures 25/C, 10/C and 0/C were then annealed and furnace aged to promote a coarser secondary α_2 lath size while retaining the same primary α_2 volume fractions as microstructures 25/F, 10/F and 0/F, respectively; the heat treatments used are shown in Table 3.2. Final chemical analysis is listed in Table 3.3, note the lower level of aluminum (23.69 vs. 25 a/o) and the unusually low oxygen content (630 wppm vs. 800 wppm).

Table 3.2 Anneal and age treatments for microstructures 25/C, 10/C and 0/C.

<u>Microstructure</u>	<u>Anneal for 1 hour (°C)</u>	<u>Age for 2 hours (°C)</u>
25/C	1021	815
10/C	1049	815
0/C	1104	815

Table 3.3 Chemical analysis of the heat under study.

	<u>Ti</u>	<u>Al</u>	<u>Nb</u>	<u>V</u>	<u>Mo</u>	<u>Fe</u>	<u>O</u>	<u>N</u>	<u>H</u>	<u>C</u>
a/o	bal.	23.69	10.19	3.19	1.16	0.051	0.189	0.032	0.141	0.112
w/o	bal.	13.30	19.70	3.38	2.31	0.060	0.063	0.009	0.003	0.028

3.2 Mechanical Testing

A general overview of where the various mechanical test specimens were machined from the forged pancakes can be found in Figure 3.1. The round specimen configuration used for room temperature tensile testing is shown in Figure 3.2. Specimens were machined from within the plane of the forged pancake and normal to its radius, a C-R

orientation. Crush grinding was used to achieve the final specimen shape, no additional treatment was given to the specimen surface. Testing was performed in accordance with ASTM E 8-89 using a screw driven Instron machine.¹⁰² An MTS extensometer with a nominal gage length of 12.7 mm was used to measure strain, the extensometer was left in place to failure. A crosshead speed of 0.0021 mm/s was used, giving an initial strain rate of $1.67 \times 10^{-4} \text{ s}^{-1}$. Load and displacement data were recorded on an X-Y recorder. A Physical Acoustics Locan AT system was used to collect acoustic emissions (AE) during tensile testing. A transducer with a 250 MHz peak frequency response was coupled to the specimen with high vacuum grease. A specially constructed stainless steel cage was used in the load train to allow attachment of the acoustic emission transducer to the top of the tensile bar. Teflon tape was wrapped around the threaded ends of the tensile samples to minimize extraneous noise production and transfer.

Elevated temperature tensile testing used the same specimen geometry as in room temperature tensile testing. Testing was performed on a servo-hydraulic MTS machine equipped with a Perkin-Elmer vacuum system, the vacuum during testing was maintained at approximately $1 \times 10^{-7} \text{ Pa}$. Induction heating was used with an acoustic frequency power supply. A susceptor made of 6.4 mm thick stainless steel pipe was needed to obtain a uniform temperature gradient along the gage length of the specimen. Slots were machined into the susceptor to allow for the extensometer rods and thermocouple leads. Thermocouples spot welded to both ends of the gage length of the tensile specimen were used to monitor the temperature profile during the test. Specimens were soaked at the test temperature for approximately 15 minutes. An MTS high temperature extensometer, with nominal gage length of 14 mm, was used to measure extension to failure. Computer controlled displacement rate was used during testing, with load and extension data being acquired digitally. Microstructures 10/F and 0/C were tested from 450°C to 750°C in 50°C intervals. Microstructure 0/F was also tested between 450°C and 750°C, but at 100°C intervals. Two samples were tested at each temperature, one at a crosshead speed of 0.14

mm/s and the other at 0.0014 mm/s, giving initial strain rates of 10^{-2} and 10^{-4} s^{-1} , respectively. A personal computer was used to help analyze the digitally acquired data to obtain modulus, yield strength, ultimate tensile strength, elongation and work hardening exponent values.

Flat tensile bars were machined from the forged pancake in the R-C orientation, Figure 3.3. The broad faces of these specimens were mechanically polished to 6 microns, and then polished with Buehler Mastermet. A 12 μm , center to center, square grid was applied using photo-lithography. The grid was then etched into the specimen surface using reactive argon etching. Testing of the specimens was carried out using a servo-hydraulic test frame with an MTS controller. The specimens were tested in an environmental chamber in a temperature range between 450°C and 700°C. Heating of the specimens was by water cooled quartz lamps placed approximately 5 mm from the specimen surface. Four thermocouples were tack welded to the surface of the specimen to provide independent zone control of the temperature. Temperature was generally maintained to within 10°C. Initial tests were performed using a Ti gettered helium atmosphere; however, this atmosphere was not suitable to prevent surface cracking in specimens at 450°C. Remaining tests were performed in a vacuum of approximately $1 \times 10^{-6} \text{ Pa}$. An MTS high temperature extensometer with a nominal extensometer gage length of 14 mm was used to specimen failure. A crosshead speed of 0.021 mm/s was used, giving an initial strain rate of $1.5 \times 10^{-3} \text{ s}^{-1}$. Data was collected using a personal computer.

Elevated temperature tensile tests in a lab air environment were conducted using the round tensile specimen geometry in Figure 3.2. The same servo-hydraulic test machine and heating method was used as in the testing of the flat tensile bars. The tensile specimens were soaked at temperature for 20 minutes prior to testing. An MTS elevated temperature extensometer was used to measure strain during the test. A nominal gage length of 10 mm was used. Crosshead speeds of 0.002, 0.02, 0.2 and 1 mm/s were used to achieve initial

strain rates of 2×10^{-4} , 2×10^{-3} , 2×10^{-2} and $1 \times 10^{-1} \text{ s}^{-1}$, respectively. Data were recorded with an X-Y recorder in addition to digital recording with a personal computer.

A compact tension specimen was used for room temperature fracture toughness testing, Figure 3.5. Specimens were machined from the forged pancake in a C-R orientation. Testing was done following the procedures in ASTM E399-83.¹⁰³ Initially, a blunt-notched specimen geometry was used; however, fatigue pre-cracking was extremely difficult to control after initiation due to the high stress intensity values required for initiation. Therefore, a chevron-notched specimen was used with excellent results in both initiating and controlling fatigue crack growth. Pre-cracking was initiated at $10 \text{ MPa}\sqrt{\text{m}}$, 10 Hz and $R = 0.1$. Crack length was measured during pre-cracking using front face compliance, the applied load was automatically controlled by computer. Heat tinting at 500°C for 20 minutes was used to mark the fatigue pre-crack front. Specimens were loaded to failure at a rate of 17 N/s or $0.25 \text{ MPa}\sqrt{\text{m/s}}$.

Elevated temperature toughness testing was conducted using the multi-specimen J_{Ic} approach outlined in ASTM E813-88.¹⁰⁴ Specimens were machined from the forged pancake in the C-R orientation. A chevron-notched bend bar, Figure 3.4, was used for these tests. Testing was performed on screw-driven Zwick machine, with data recorded on an X-Y recorder. A lab air, resistance heated convection furnace was used to heat the specimen. A thermocouple was placed approximately 20 mm from the specimen. The specimen was brought to temperature slowly, typically requiring 2 hours, and stabilized at the test temperature for 15 minutes. Temperature control was maintained to within $\pm 2^\circ\text{C}$. A nickel superalloy was used to construct the three point bend fixture; 10 mm diameter alumina rods were used as the rollers. The bottom rollers had a span of 40 mm. A steel rod to measure load line displacement was placed at the specimen notch and brought through the lower load train to a transducer attached to the lower crosshead. Specimens were tested at 450°C , 550°C and 650°C with a crosshead speed of 0.0083 mm/s. An unnotched bend bar was elastically bent at each temperature to obtain a combined specimen

and machine modulus. Bending theory was used to calculate the compliance of the specimen, from which the compliance of the machine was derived. Calculation showed that a maximum correction to the data would be approximately 1%, as this made little contribution to the overall J values it was ignored. Pre-cracking of the specimens was accomplished in three point bending on a resonant frequency fatigue machine at room temperature. The specimens were broken after elevated temperature crack growth using the same room temperature fatigue technique. Due to the natural heat tinting of the specimen while tested at temperature, the fatigued pre-crack and elevated temperature crack growth fronts were macroscopically obvious. The crack fronts were magnified 20x and transferred to paper using a light microscope electronically coupled to an X-Y recorder through a moveable X-Y stage and transducers. The area of crack growth at elevated temperature was then measured from the resulting plot with a polar planimeter and divided by the measured specimen thickness, B, to obtain an average crack length. The area under the load-displacement curves was also measured with a polar planimeter to obtain the plastic energy expended during the test.

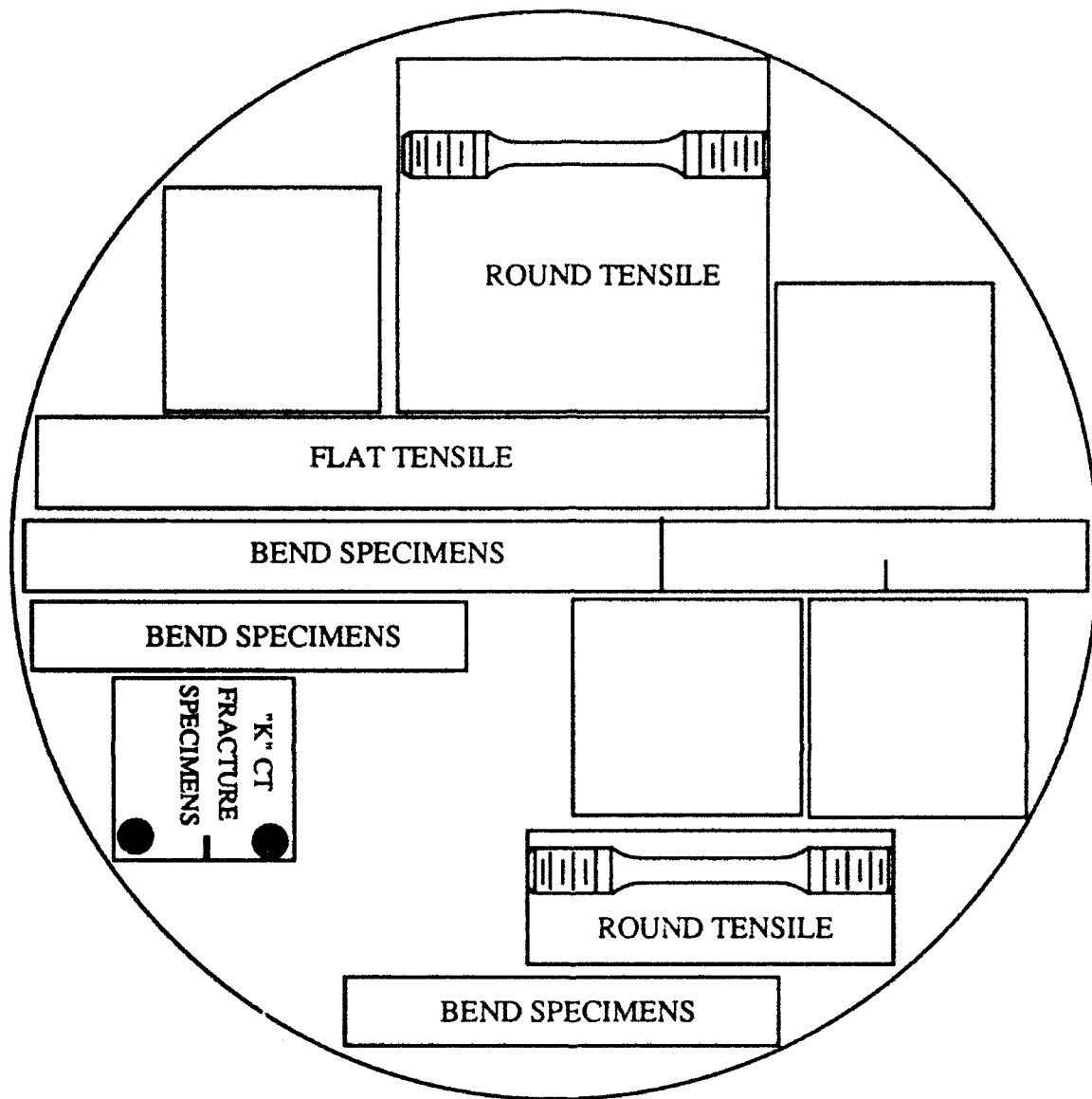


Figure 3.1 Locations where specimens were machined from the forgings.

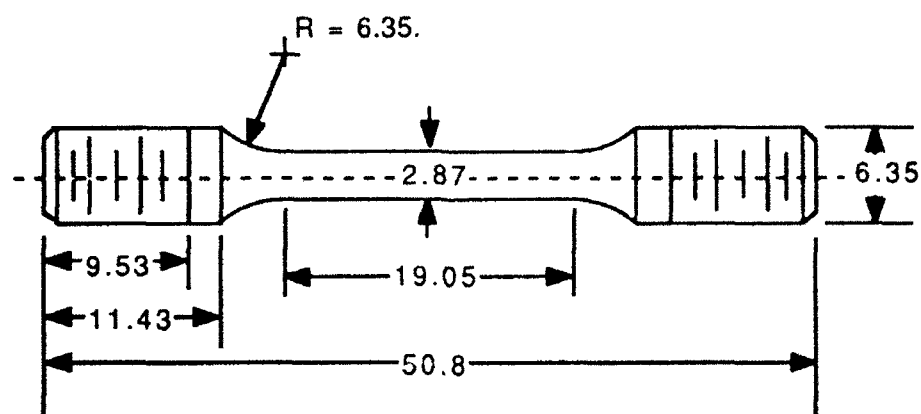


Figure 3.2 Axisymmetric round tensile bar. All dimensions are in millimeters.

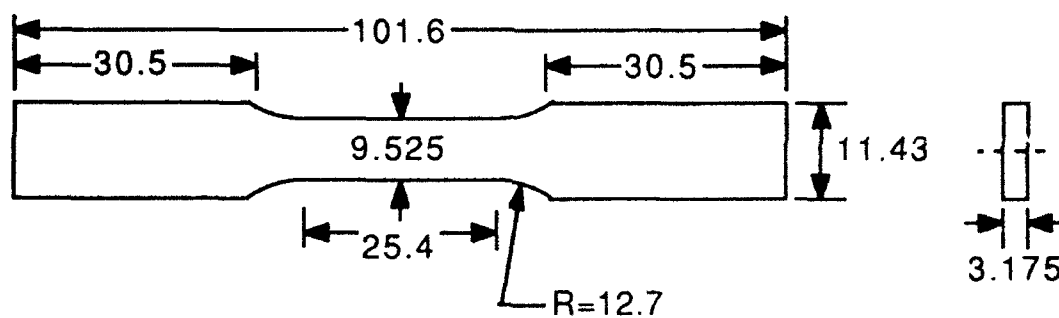


Figure 3.3 Flat tensile bar. All dimensions are listed in millimeters.

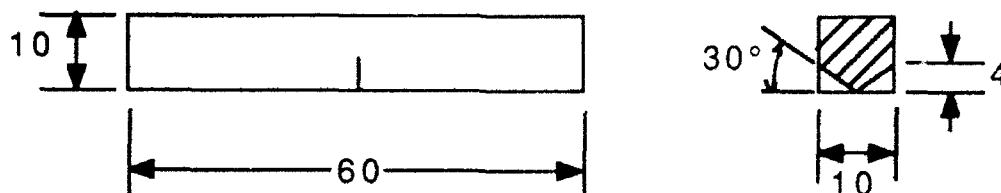
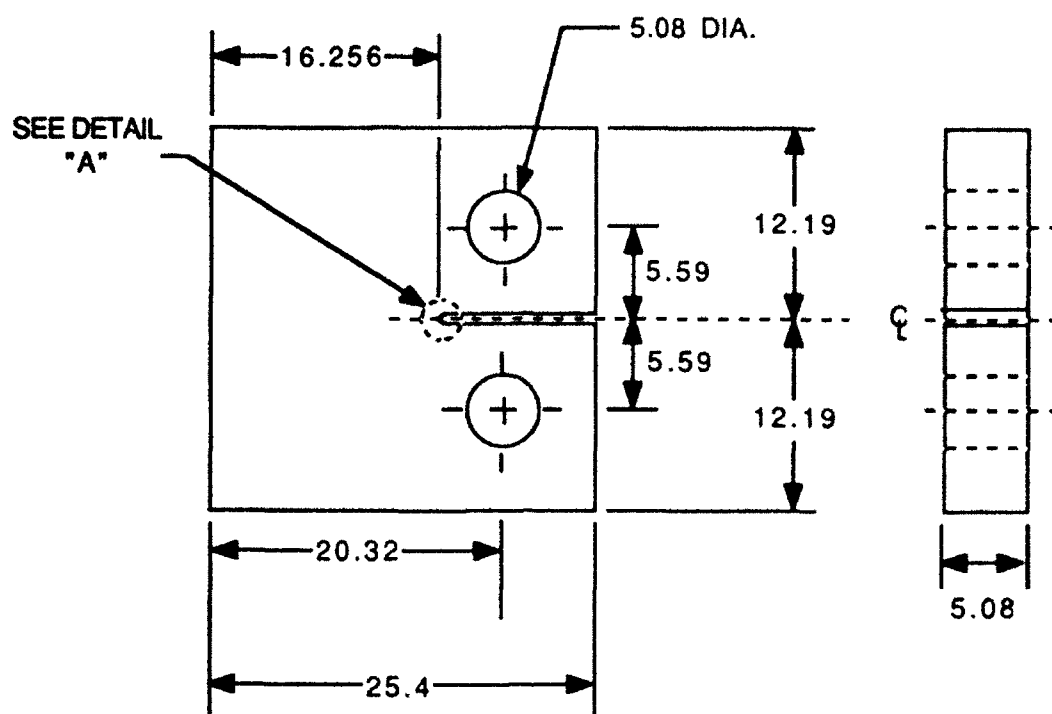


Figure 3.4 Three-point bend bar used for elevated temperature J-testing. All dimensions are listed in millimeters.



DETAIL "A"
CHEVRON NOTCH

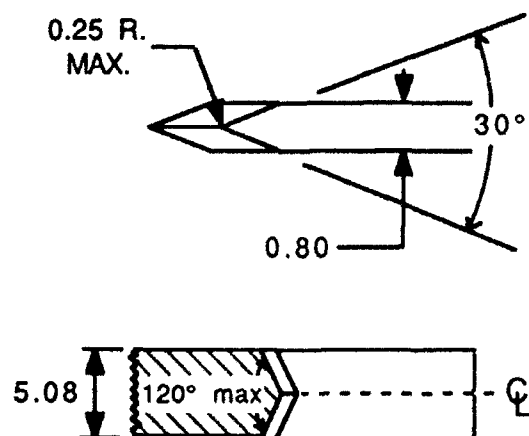


Figure 3.5 Compact tension specimen used for room temperature fracture toughness. All dimensions are listed in millimeters.

3.3 Microscopy

Specimens for light and scanning electron microscopy were prepared by mechanical polishing down to 800 grit SiC with water. Afterwards, the specimens were polished with 6 μm diamond paste and then given a final polish with Buehler Mastermet colloidal silicate solution. Specimens for light microscopy, and some for SEM observation, were etched with Kroll's reagent 90 ml H_2O , 10 ml HCl and 1 ml HF . Either a Nikon Epiphot or Reichart-Jung microscope was used for light microscopy. Either a JEOL 840 or Philips 525M was used for scanning electron microscopy.

Specimens for transmission electron microscopy were prepared by cutting a thin slice and mechanically polishing it to 0.75 mm. A 3 mm disc was punched out and electropolished using a Fischione twin jet polisher at -40°C with a solution of 17 ml HClO_4 . Foils were examined using a JEOL 2000FX at 200kV.

3.4 X-ray Diffraction

Specimens for X-ray Diffraction (XRD) were prepared by mechanical polishing slices of approximately 10 mm square to 800 grit, no electropolishing or etchants were used. This procedure was used so as to avoid false orthorhombic peaks caused by hydrogen artifacts, as seen by other researchers.⁴⁸ A Rigaku rotating anode diffractometer was used to generate and collect diffraction data. A Cu target was used with an accelerating voltage of 40 kV and 150 mA. Data was collected at $0.12^\circ/\text{min}$ at steps of 0.020° .

4. RESULTS

4.1 Microstructural Characterization

Micrographs of the final microstructures are found in Figures 4.1 through 4.6. The prior β grains in the $\alpha_2+\beta$ processed microstructures (25/C, 25/F, 10/C & 10/F) were equiaxed, though with irregular boundaries, in the plane of the forging and had an average diameter of approximately 1.05 mm. The through-thickness height of the prior β grains was about 0.30 mm. The prior β grain size of microstructure 0/F was measured to be 1.09 mm in the plane of the forging and 0.34 mm in the through-thickness direction. Microstructure 0/C, on the other hand, obviously underwent recrystallization of the β during the post forging β solution treatment. The β grains were equiaxed in all directions and had an average diameter of approximately 0.59 mm. Primary α_2 morphology was analyzed using the linear intercept method, the results of which are listed in Table 4.1.¹⁰⁵ The secondary α_2 lath size was measured to be 0.5 μm in microstructures 25/F, 10/F and 0/F and 1 μm in microstructures 25/C, 10/C and 0/C. While the secondary α_2 laths in microstructures 25/F, 10/F and 0/F had a finely distributed Widmanstätten morphology, they were sometimes found in aligned packets in microstructure 0/F, particularly at the prior β grain boundaries. Microstructures 25/C, 10/C and 0/C commonly exhibited regions of aligned Widmanstätten laths within the prior β grains and continuous grain boundary α_2 along the prior β grain boundaries.

Analysis with AEM has shown that a bcc derivative phase was present in all of the microstructures and had the ordered B2 structure, Figure 4.7. X-ray diffraction was used to determine the phases present in the microstructures, Figures 4.8, 4.9 and 4.10. Peaks corresponding to the α_2 and B2 phases were found in all microstructural conditions. Peaks consistent with the ordered orthorhombic phase, α_2'' , were identified in the $\alpha_2+\beta$ processed conditions as well as in microstructure 0/F. Microstructure 0/C did not show

any evidence of the ordered orthorhombic phase. This phase could be present with too small volume fraction, $< \sim 5\%$, to be detected. The location of the orthorhombic phase was assumed to be associated with the secondary α_2 laths, but was not specifically determined in this study.¹⁴

The area fraction of the B2 phase within the microstructures was analyzed using a computerized image analyzer. The calculation of the amount present was based on contrast analysis from SEM micrographs from three separate locations for each microstructure. The area fraction of B2 phase present was in the range 30-36% for microstructures 10/F, 0/C and 0/F. There is an amount of subjectivity involved in this analysis, resulting in a confidence level of $\pm 2\%$.

To check the stability of these microstructures, a specimen from microstructure 10/F was exposed in a furnace in an air environment at 650°C for 3 hours and water quenched. The sample was then sectioned, polished and the center of the specimen was examined with a SEM. The resulting photographs were analyzed with an image analyzer to determine the B2 volume percent. No appreciable difference was noticed between the values obtained in the exposed specimen and the volume percentages quoted in the previous paragraph. Therefore, there did not appear to be any significant change in the amount of B2 at the test times and temperatures used in this study.

Table 4.1 Analysis of final microstructures.

<u>Microstructure</u>	<u>N_L (mm⁻¹)</u>	<u>N_A (mm⁻²)</u>	<u>r (μm)</u>	<u>V_V</u>	<u>λ (μm)</u>
25/C	34.4	4,333	5.1	0.23	22.4
25/F	31.7	3,574	5.6	0.24	24.0
10/C	15.7	2,247	4.5	0.09	57.8
10/F	17.6	2,563	4.4	0.10	51.0

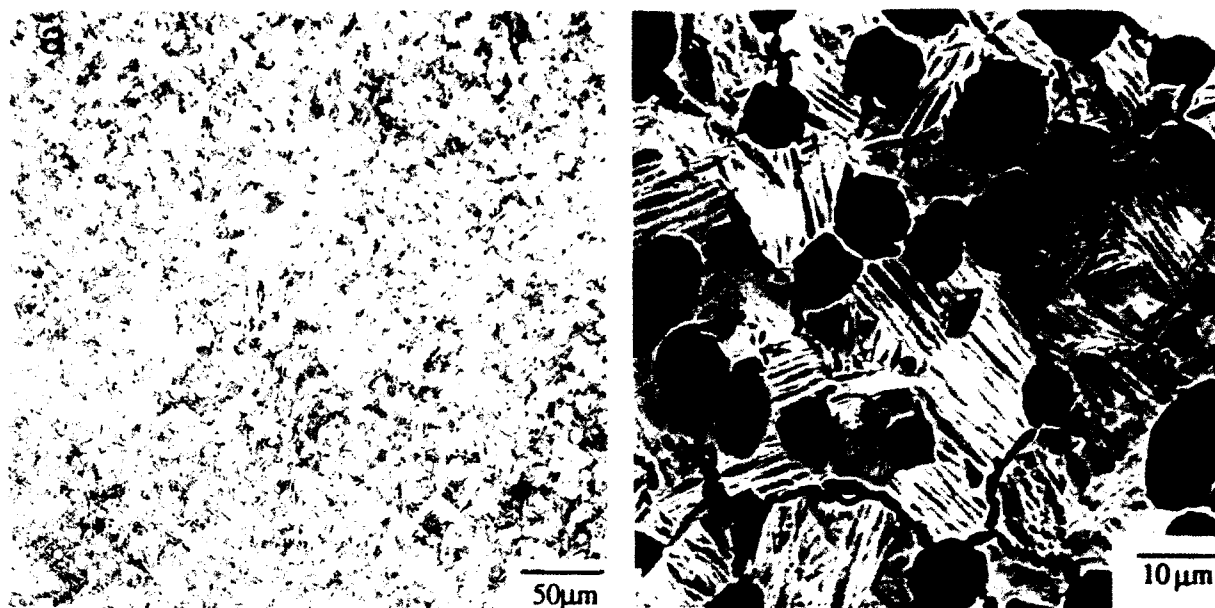


Figure 4.1 Microstructure 25/C. (a) Light micrograph (b) SEM micrograph.

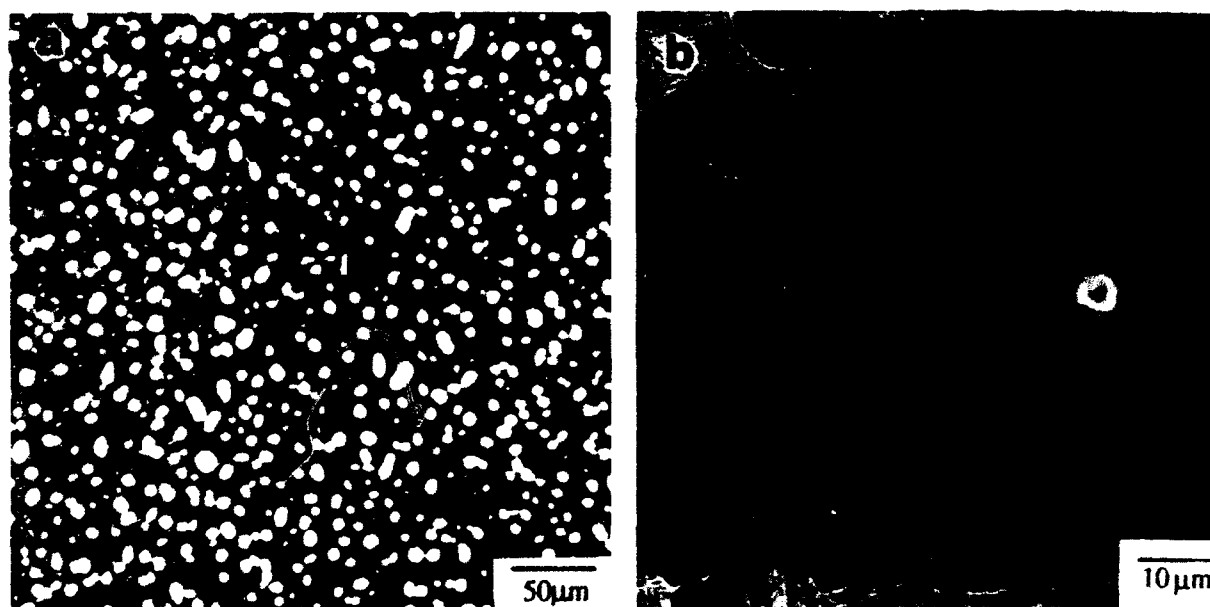


Figure 4.2 Microstructure 25/F. (a) Light micrograph (b) SEM micrograph.

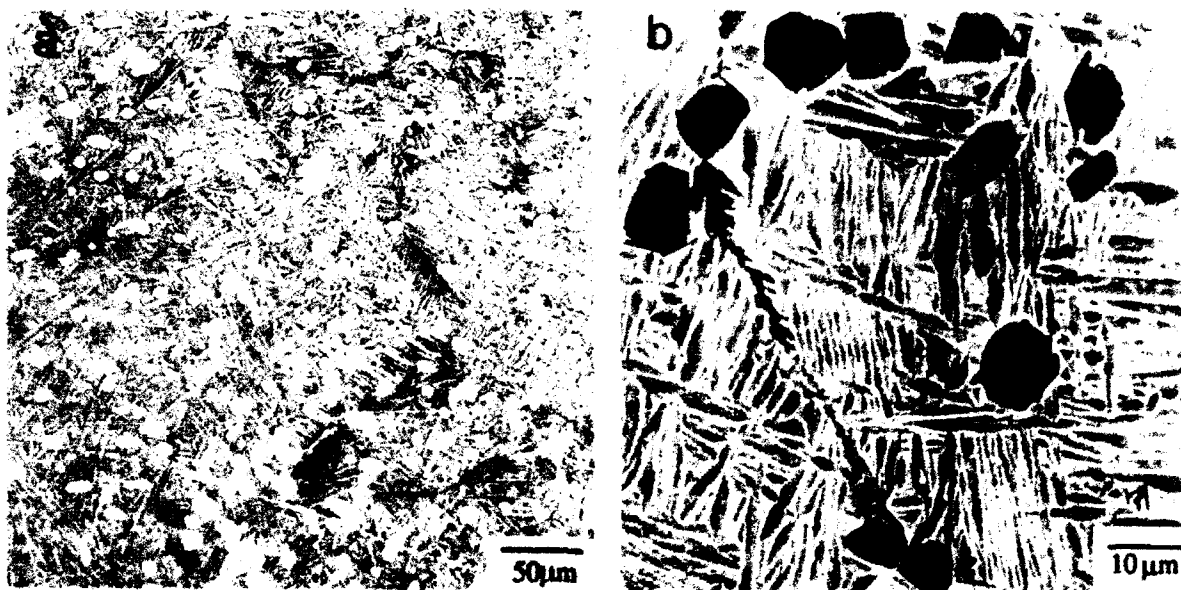


Figure 4.3 Microstructure 10/C. (a) Light micrograph (b) SEM micrograph.

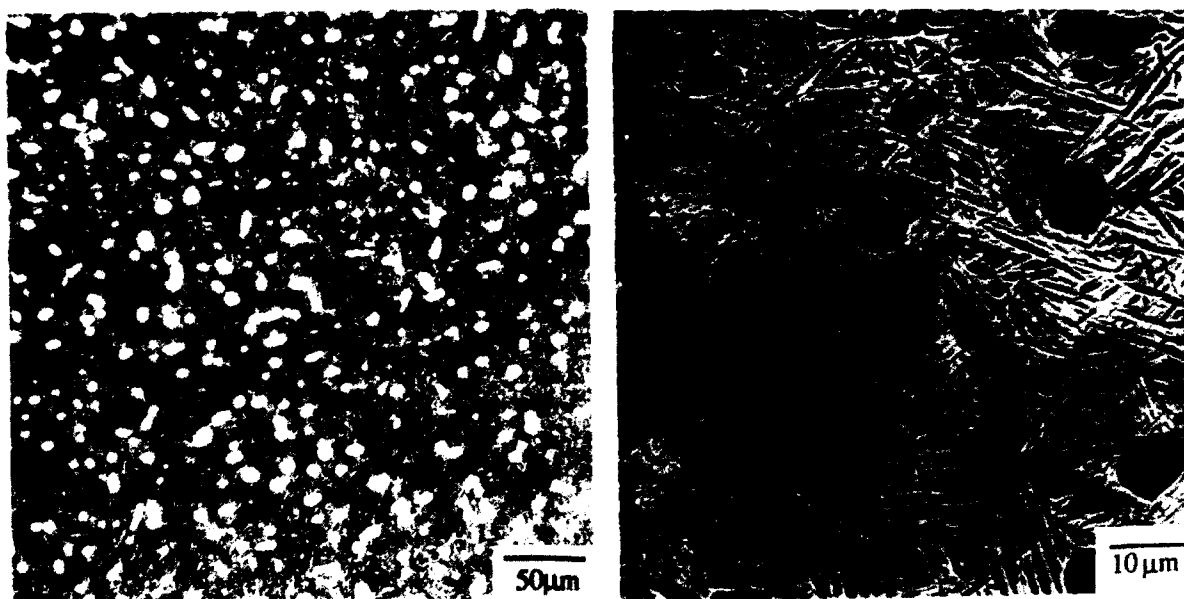


Figure 4.4 Microstructure 10/F. (a) Light micrograph (b) SEM micrograph.

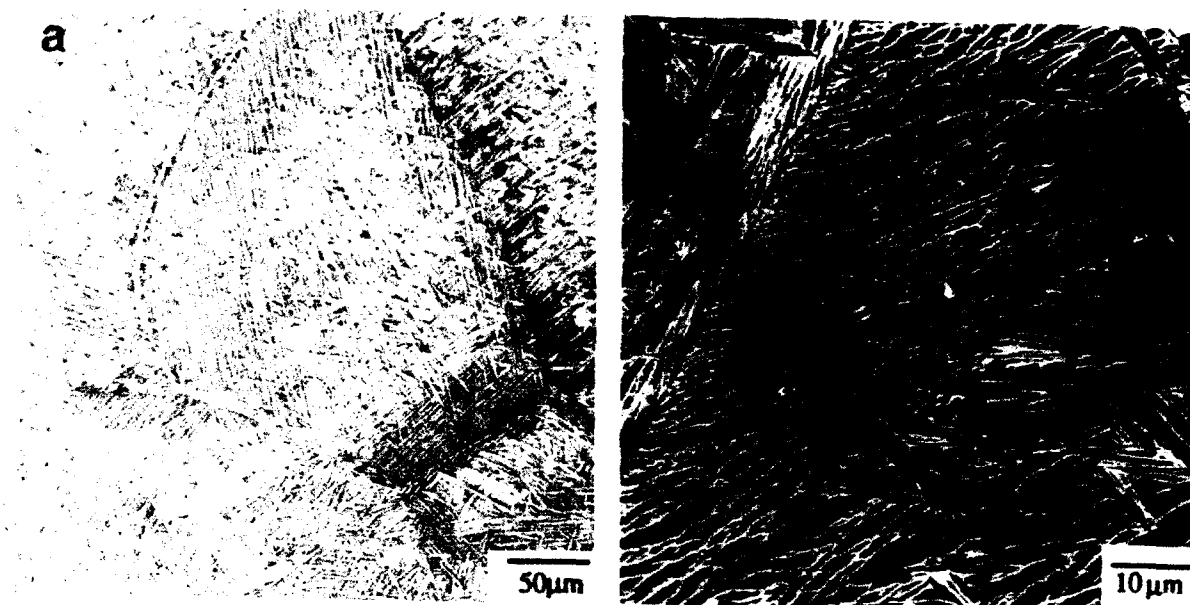


Figure 4.5 Microstructure 0/C. (a) Light micrograph (b) SEM micrograph.

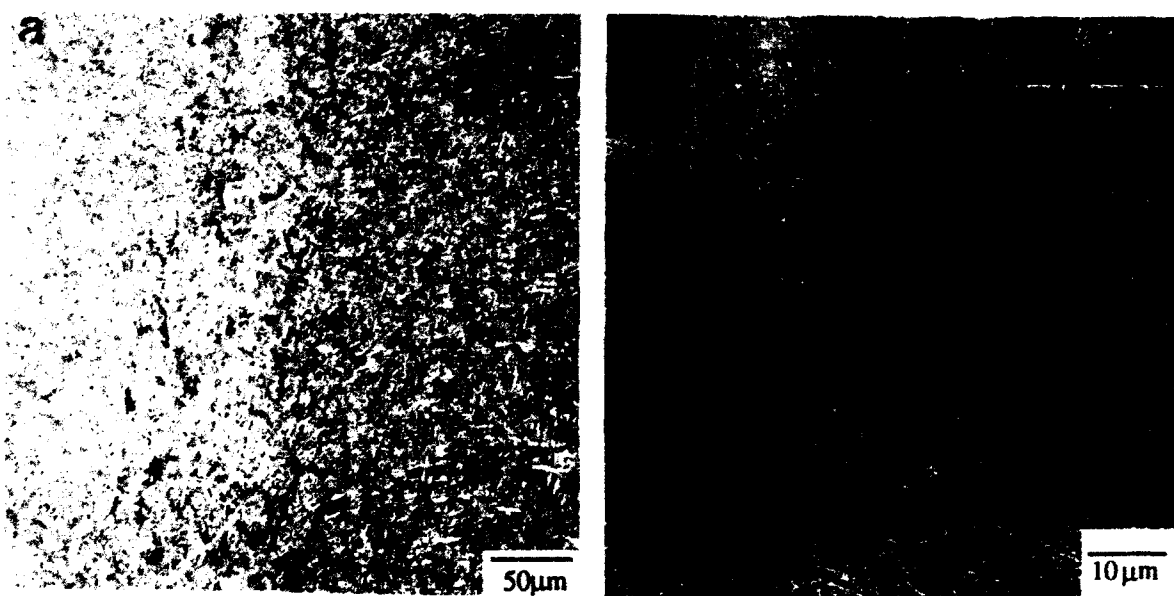


Figure 4.6 Microstructure 0/F. (a) Light micrograph (b) SEM micrograph.

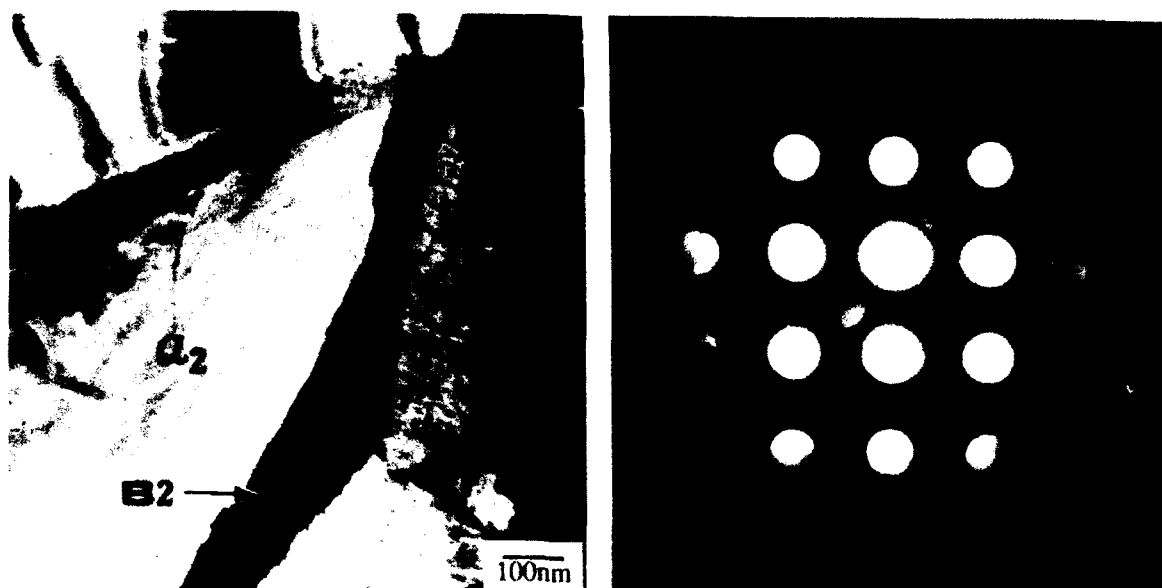


Figure 4.7 (a) AEM micrograph of microstructure in microstructure 0/F. (b) Microdiffraction pattern showing the [001]_{B2} zone.

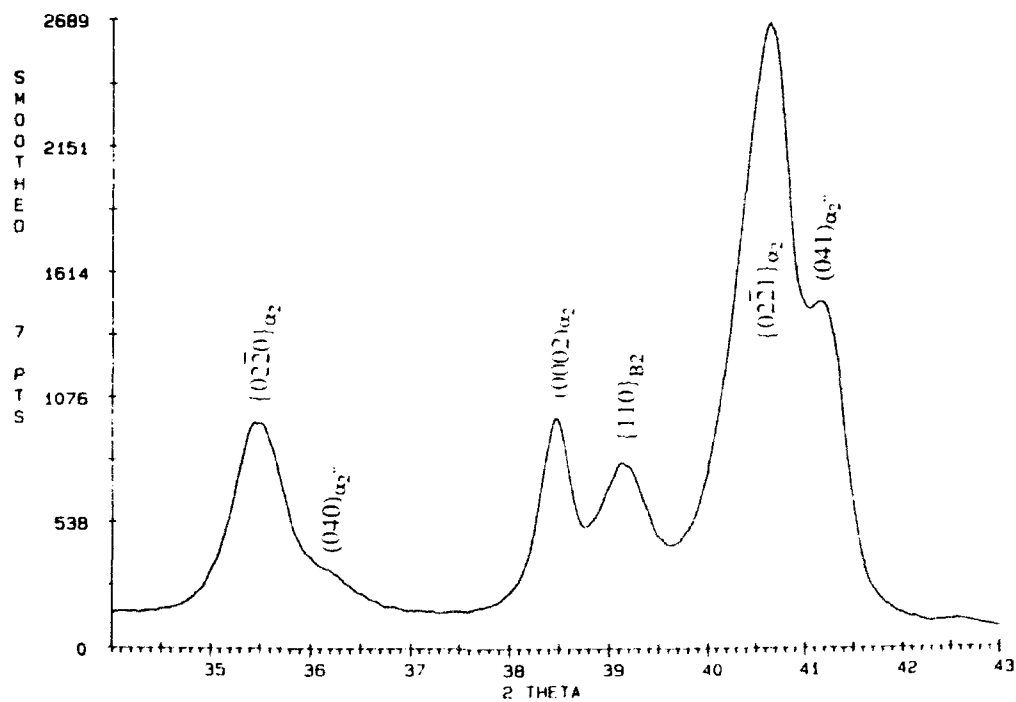


Figure 4.8 X-ray plot of microstructure 10/F. Peaks corresponding to the α_2 , B2 and ordered orthorhombic phases are evident.

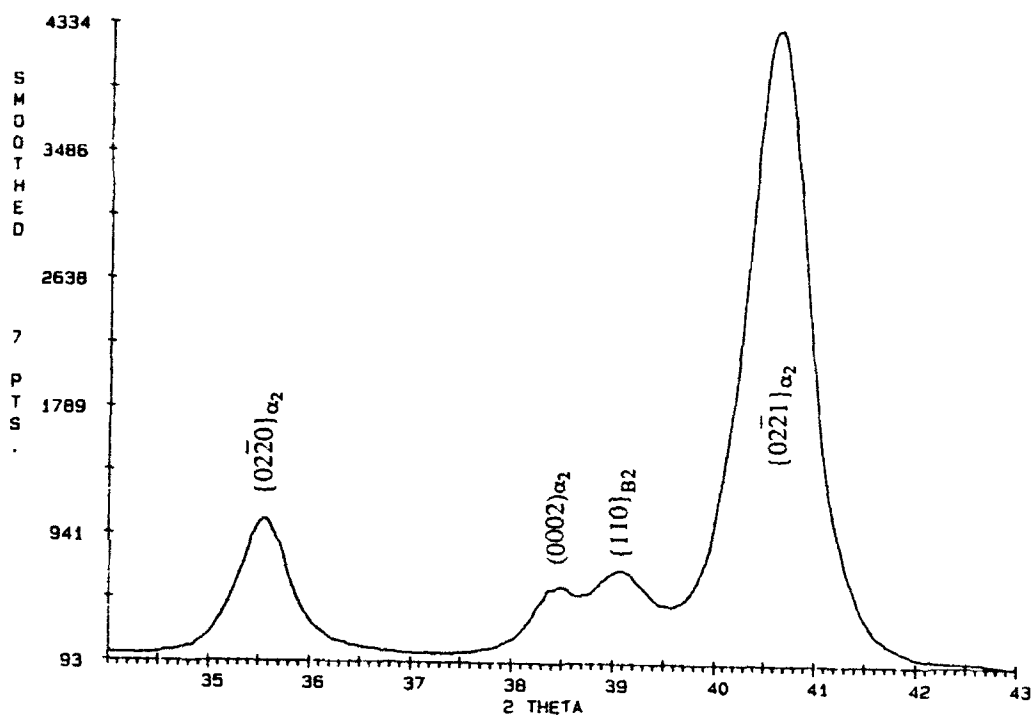


Figure 4.9 X-ray plot of microstructure 0/C. Peaks corresponding to the α_2 , and the B2 phases are evident.

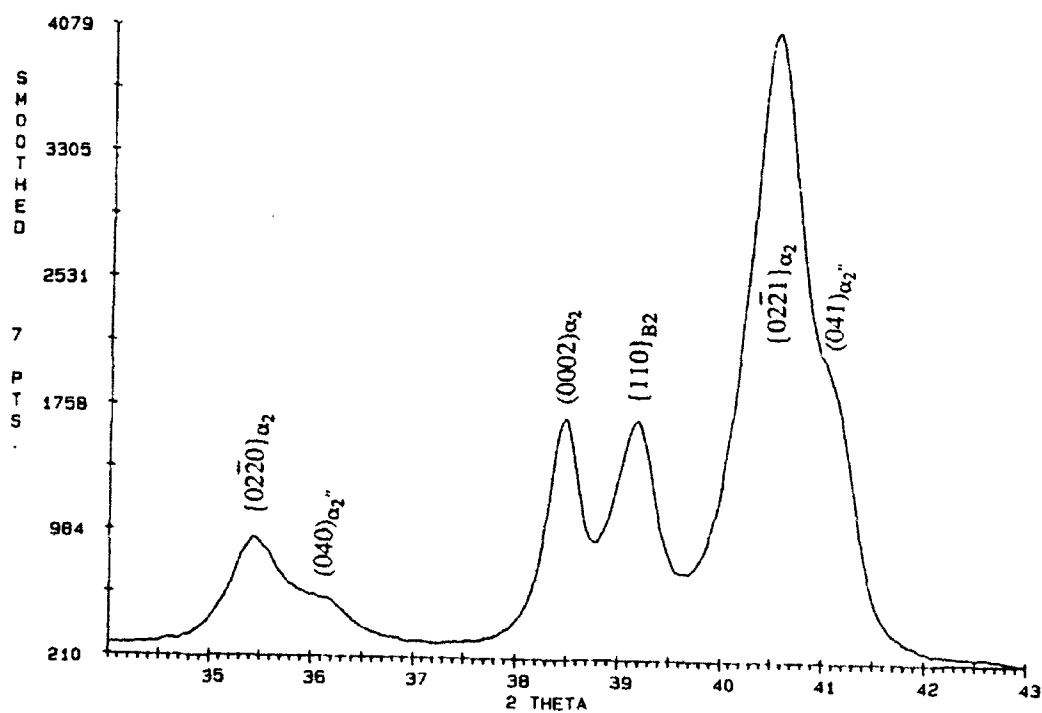


Figure 4.10 X-ray plot of microstructure 0/F. Peaks corresponding to the α_2 , B2 and ordered orthorhombic phases are evident.

4.2 Mechanical Testing

4.2.1 Room Temperature Tensile Testing

The results of the room temperature tensile tests for both round and flat geometries are listed in Table 4.2. Microstructures having similar secondary α_2 lath spacing exhibited similar yield strengths. The fracture stress was also dependent on microstructure, with the finer secondary α_2 lath structure giving a higher σ_F . Fracture stress was determined from tensile tests by dividing the load at fracture by the final area of the tensile specimen. Note that microstructure 0/C had a significantly lower fracture stress, ~ 100 MPa, than that of the other two coarse microstructures, 25/C and 10/C. The tensile elongations, values from extensometer measurements, were reasonably close for all of the $\alpha_2 + \beta$ processed microstructure. Microstructure 10/F, however, showed a true fracture strain that was nearly 30% lower than the other $\alpha_2 + \beta$ processed microstructures. The β processed microstructures exhibited elongations that were almost 50% lower than the $\alpha_2 + \beta$ processed microstructures, while their true fracture strains were the same as that in microstructure 10/F. The UTS, ϵ_f (except for microstructures 25/F and 10/C) and σ_F were all lower in the flat tensile specimens. Failure appeared to initiate near the corners of the flat specimens. In at least one of the specimens, microstructure 0/C, failure was caused by a large, apparently machining induced, defect at the surface. Thus, it is concluded that the lower properties in the flat tensile bars are related to the specimen geometry and/or the machining practice.

The tensile results for the flat bars are approximate, the displacement data was recorded on a time based scale. The data were normalized to the known properties obtained from the round tensile bars for microstructure 10/C. The load data obtained were correct, but variations in the displacement data are to be expected. Therefore, values such as the ultimate tensile strength and true fracture strength are correct, whereas the values dependent on displacement such as yield strength, modulus and elongation cannot be assumed to be

accurate. Small strains to failure in flat tensile bars, measurements such as reduction of area show scatter in their values.

Table 4.2 Room temperature tensile test results.

<u>Micro- structure</u>	<u>Type</u>	<u>E</u> (GPa)	<u>YS</u> (MPa)	<u>UTS</u> (MPa)	<u>% EL</u>	<u>% ROA</u>	<u>ϵ_f</u>	<u>σ_F</u> (MPa)
25/C	Round	94.4	563	806	7.0	9.9	0.104	895
	Flat	100.2	672	NA	NA	6.8	0.073	NA
25/F	Round	115.1	726	958	6.2	9.4	0.098	1058
	Flat	113.7	745	896	1.6	10.7	0.115	1005
10/C	Round	104.8	581	821	6.5	8.7	0.091	900
	Flat	104.5	632	725	0.8	9.2	0.098	799
10/F	Round	105.9	753	967	5.9	6.7	0.070	1037
	Flat	106.1	711	904	2.1	4.0	0.043	943
0/C	Round	90.2	556	745	3.5	6.7	0.069	799
	Flat	88.6	618	656	0.3	1.1	0.012	664
0/F	Round	104.0	809	996	3.6	7.6	0.079	1078
	Flat	101.6	727	812	0.6	4.5	0.045	849

The load-displacement curves obtained from the round specimen room temperature tensile tests were converted to true stress-true strain curves. Strain hardening exponents were determined from these curves by fitting the data to a Hollomon equation (4.1) describing power law hardening, where $\epsilon = \epsilon_e + \epsilon_p$.¹⁰⁶

$$\sigma = K\epsilon^n \quad (4.1)$$

The data was also fit to a Ludwik equation.¹⁰⁷ The values from both equations are tabulated in Table 4.3.

$$\sigma - \sigma_0 = K\epsilon_p^n \quad (4.2)$$

Table 4.3 Work hardening exponents at room temperature.

<u>Microstructure</u>	Hollomon: $0.01 < \epsilon < 0.05$		Ludwik: $\epsilon_p < 0.05$	
	<u>K (MPa)</u>	<u>n</u>	<u>K (MPa)</u>	<u>n</u>
25/C	1311	0.17	1138	0.49
25/F	1480	0.14	1560	0.55
10/C	1309	0.16	1411	0.54
10/F	1492	0.13	1312	0.53
0/C*	1387	0.18	1870	0.60
0/F*	1642	0.14	1377	0.52

* True plastic strains of only 0.037 and 0.036 achieved in microstructures 0/C and 0/F, respectively.

Following the Hollomon equation, the microstructures were again grouped in similar behavior as their work hardening response was dependent on the scale of the secondary α_2 lath size. Microstructures with coarse secondary α_2 , microstructures 25/C, 10/C and 0/C, while having appreciably lower yield strengths, have higher work hardening exponents. The Ludwik equation gives no apparent microstructural trends in its K or n values.

Acoustic emission (AE) results appear to indicate when crack nucleation occurs in the tensile stress-strain curve. The output of the acoustic emission transducer during room temperature tensile testing expressed as root mean square (RMS) voltage is presented in Figure 4.11 for each microstructure. The results presented were identical in behavior between the duplicate tests performed for each microstructure.

The output of the transducer was generally quiet from the start of the tensile test, excepting microstructures 25/C and 10/C, until very near final failure of the test specimen. Increased bursts of acoustic activity was generally observed at strains only within approximately 0.5% of catastrophic failure. This increase in activity is believed to be associated with the nucleation of microcracks in the specimen.

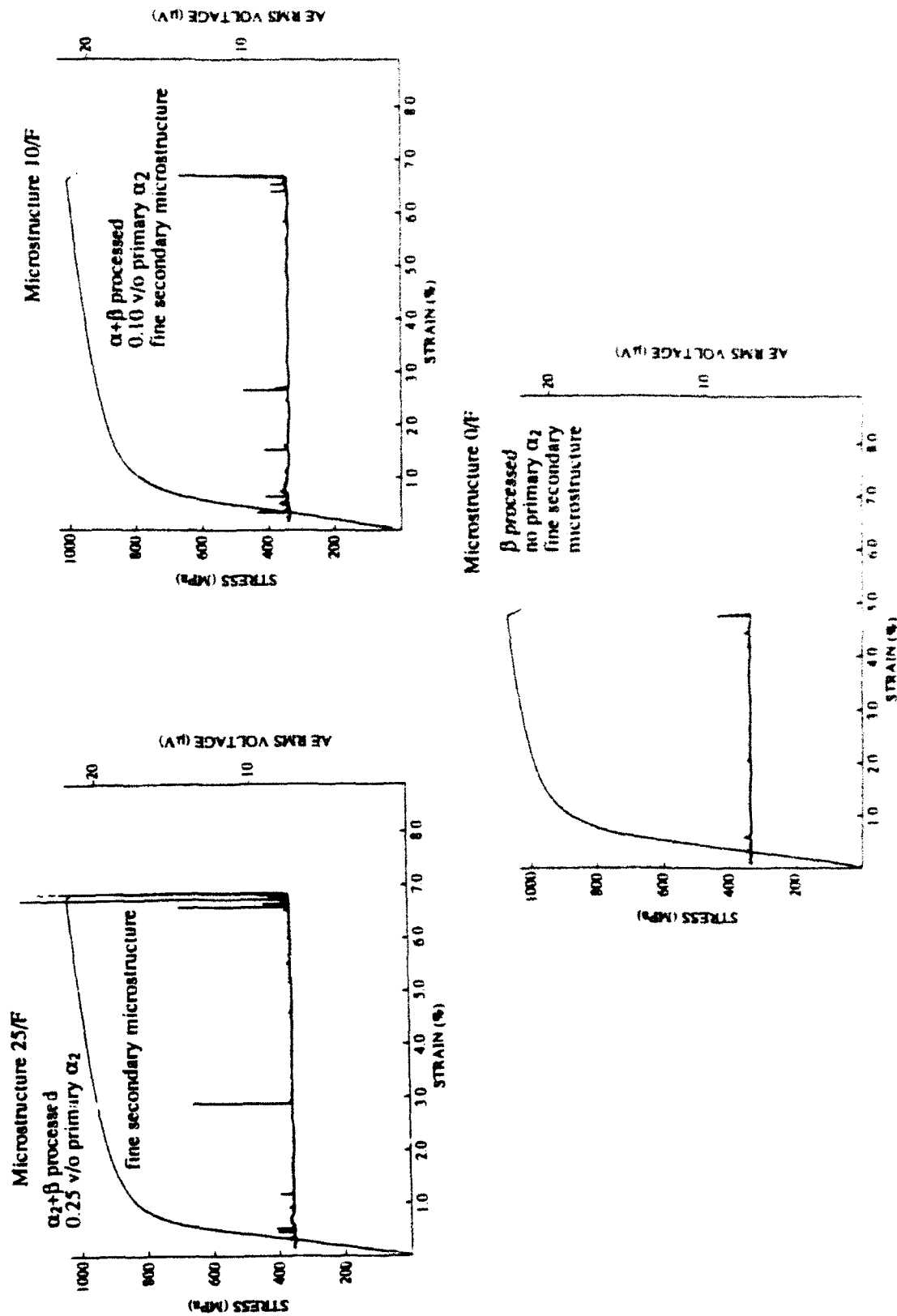


Figure 4.11 Engineering stress-strain and AE RMS voltage-strain curves for room temperature tensile tests of the fine Widmanstätten microstructures 25/F, 10/F and 0/F.

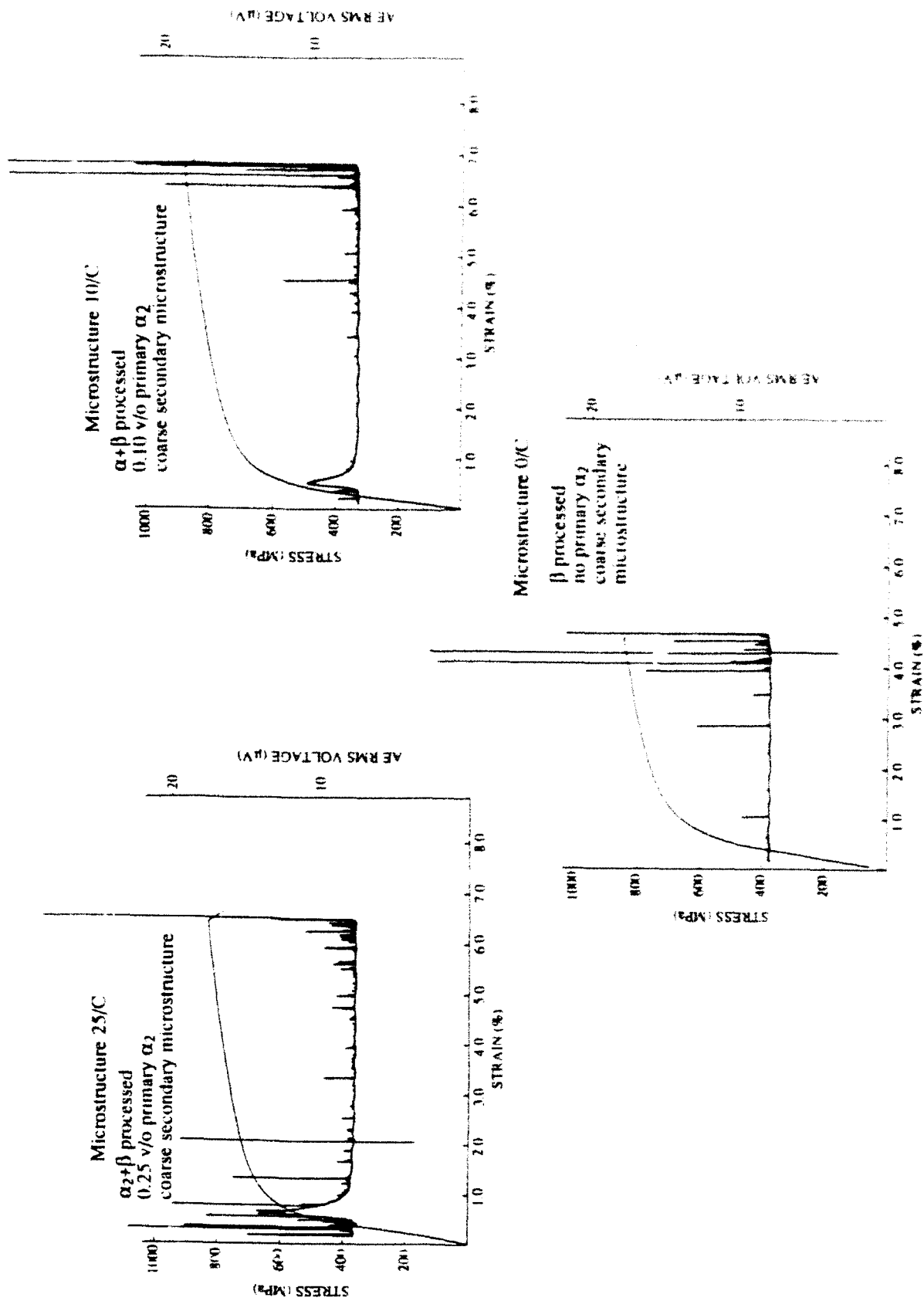


Figure 4.11 Engineering stress-strain and AE RMS voltage-strain curves for room temperature tensile tests of the coarse Widmanstätten microstructures 25/C, 10/C and 0/C.

4.2.2 Elevated Temperature Tensile Testing in Vacuum

The results of these tests are listed in tabular form in Tables 4.4 and 4.5, and in graphic form in Figures 4.12 - 4.14. Examples of the engineering and true stress-strain plots obtained are shown in Figures 4.15 - 4.17.

Yield strengths dropped by approximately 30% from room temperature to 450°C where they remained relatively constant to 650°C, after which they began to fall again. The relative yield strength differences between the microstructures observed during room temperature testing persisted at elevated temperature. Ultimate tensile strengths fell continuously with temperature. Plastic elongation to failure for microstructure 10/F remained approximately constant at values around 30% in the temperature range 450°C-750°C, Figure 4.12a. In this same temperature range the reduction of area increased from ~45 to ~75%. A similar trend was observed in microstructure 0/F where the plastic elongations also remained near 30%, Figure 4.14a. However, the reduction of area values were generally higher as compared to microstructure 10/F, ranging from ~35% to 87%. Microstructure 0/C demonstrated increasing elongation to >30% at 600°C, after which the elongation fell discontinuously to a value of ~20% at 650°C, Figure 4.13a. Reductions of area for microstructure 0/C paralleled the trend in elongation and were significantly lower than those observed in microstructures 10/F and 0/F.

The true fracture stress and strain for each microstructure as a function of temperature are plotted in Figures 4.18 - 4.20. The true fracture stress was calculated by dividing the load at fracture by the final cross sectional area of the tensile specimen. The true strain was calculated from the final cross sectional area of the tensile specimens. Each microstructure exhibited a true fracture stress which was approximately 50% higher at 450°C than at room temperature. These values remain approximately constant up to 600°C and then drop precipitously after this temperature. Additionally, there appeared to be a dependence of the true fracture stress on strain rate above 600°C in microstructure 10/F. The fracture stress at the slower strain rate, 10^{-4} s^{-1} , was approximately 600 MPa lower

than at 10^{-2} s^{-1} in this temperature range. The true fracture strain increased with temperature for microstructures 10/F and 0/F, Figures 4.18 and 4.20. This increase was nearly linear for microstructure 10/F, but appeared parabolic for microstructure 0/F. The true fracture strain increased for microstructure 0/C to 600°C , after which it dropped by nearly 40% at 650°C , Figure 4.19.

Examination of Table 4.5 reveals that testing the flat tensile bars in a gettered helium environment had a significant effect on the true fracture stresses and strains as compared to testing in the same specimen geometry in vacuum. In microstructure 10/F the fracture stresses were reduced by approximately 40% and the fracture strains by as much as 60% when compared to the values obtained from round tensile bars. Only a slight debit in the fracture stress and strain was noticed in the specimens from microstructure 0/C tested in helium. Additionally, the fracture stresses and strains obtained from microstructure 10/F tested in helium were nearly the same as those of microstructure 0/C. In contrast, flat tensile bars from microstructure 0/F, tested in vacuum, had similar fracture stresses and strains as compared to their round counterparts. This result suggests that the problems associated with specimen geometry and/or machining practice are not as critical in the flat specimens at elevated temperatures. Microstructure 10/C, tested in vacuum, exhibits similar fracture stress levels to microstructure 0/C.

Table 4.4 Elevated temperature tensile properties from round specimens tested in vacuum.

Temp (°C)	Initial $\dot{\epsilon}$ (s ⁻¹)	YS (MPa)	UTS (MPa)	E (GPa)	%EL	%ROA	ϵ_f	σ_F (MPa)
<u>Microstructure 10/F</u>								
450	10 ⁻⁴	530	890	101.2	32.3	49.2	0.678	1635
	10 ⁻²	525	860	91.6	34.5	47.0	0.635	1472
500	10 ⁻²	500	850	85.7	31.5	58.1	0.869	1742
550	10 ⁻⁴	540	820	86.8	28.5	61.5	0.955	1625
	10 ⁻²	550	825	93.5	25.0	60.3	0.925	1513
600	10 ⁻⁴	500	840	93.3	(a)	(b)	--	--
	10 ⁻²	465	730	91.8	30.0	64.6	1.04	1581
650	10 ⁻⁴	500	540	79.3	26.0	68.7	1.16	608
	10 ⁻²	470	690	89.1	36.0	63.2	0.999	1209
700	10 ⁻⁴	480	630	80.9	23.0	67.9	1.14	327
	10 ⁻²	480	640	81.9	27.5	70.9	1.24	1085
750	10 ⁻⁴	400	510	65.9	29.0	73.4	1.33	150
	10 ⁻²	440	560	77.5	32.5	69.5	1.19	590
<u>Microstructure 0/C</u>								
450	10 ⁻⁴	380	780	100.0	(d)	26.5	0.308	1279
	10 ⁻²	390	790	80.3	29.0	37.2	0.465	1257
500	10 ⁻⁴	390	740	80.0	33.5	40.1	0.512	1210
	10 ⁻²	400	760	75.1	29.5	30.9	0.369	1092
550	10 ⁻⁴	(c)	--	--	--	38.8	0.490	--
	10 ⁻²	400	720	81.6	31.5	42.6	0.556	1220
600	10 ⁻⁴	380	740	84.3	35.5	42.4	0.552	1251
	10 ⁻²	380	640	77.7	(d)	37.3	0.467	989
650	10 ⁻⁴	400	690	78.8	32.5	48.5	0.663	1233
	10 ⁻²	370	555	74.0	20.5	29.0	0.343	719
700	10 ⁻⁴	390	635	89.7	19.5	24.3	0.279	753
	10 ⁻²	340	500	65.0	22.0	31.1	0.373	443
750	10 ⁻⁴	360	550	81.8	20.0	(b)	--	--
	10 ⁻²	330	480	74.3	20.0	(b)	--	--
<u>Microstructure 0/F</u>								
450	10 ⁻⁴	340	485	65.4	(d)	32.8	0.397	610
	10 ⁻²	340	485	65.4	(d)	32.8	0.397	610
550	10 ⁻⁴	540	910	92.6	23.5	37.4	0.469	1429
	10 ⁻²	520	910	95.7	(c)	32.6	0.395	1341
650	10 ⁻⁴	490	880	105.5	(c)	48.8	0.670	1583
	10 ⁻²	490	810	96.3	29.5	57.0	0.844	1603
750	10 ⁻⁴	480	680	81.2	24.5	70.9	1.24	1376
	10 ⁻²	500	710	74.3	(c)	67.7	1.13	1270
750	10 ⁻⁴	480	(e)	71.9	--	(e)	--	--
	10 ⁻²	530	680	69.9	30.0	86.7	2.01	765

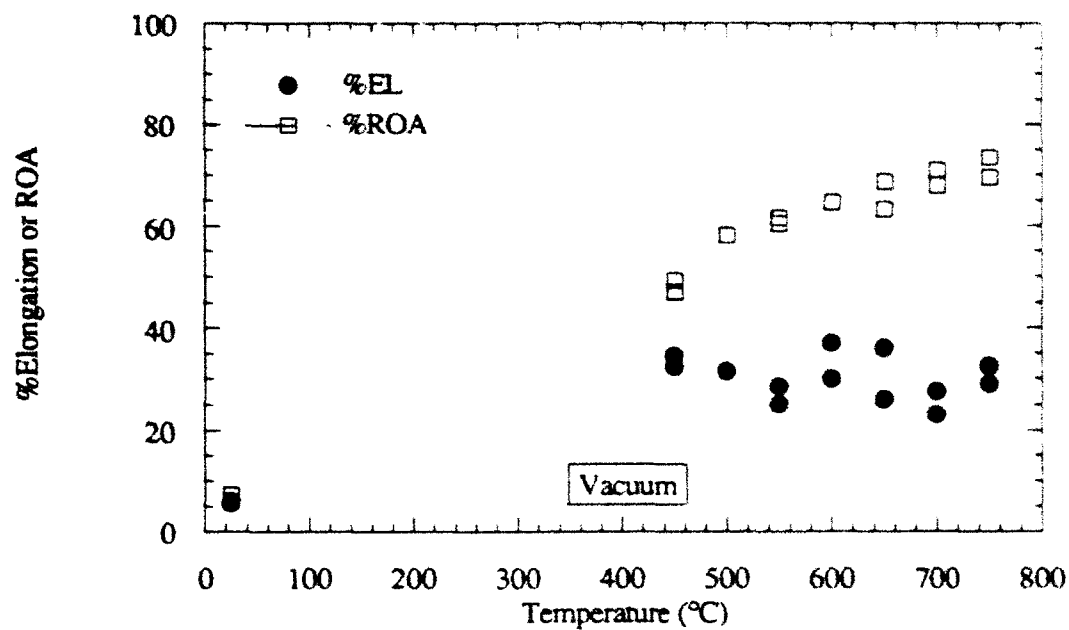
(a) overheated during test. (b) sample put into compression after test. (c) extensometer slipped. (d) failure out of extensometer gage length. (e) sample not pulled to failure.

Table 4.5 Elevated temperature tensile properties for flat specimens.

<u>Temp (°C)</u>	<u>YS (MPa)</u>	<u>UTS (MPa)</u>	<u>E (GPa)</u>	<u>%EL</u>	<u>%ROA</u>	<u>ϵ_f</u>	<u>σ_F (MPa)</u>	<u>Env.</u>
<u>Microstructure 10/C</u>								
450	445	800	105.1	26	35.0	0.431	1231	Vac
500	(a)	--	--	--	--	--	--	--
550	420	676	103.0	25	49.3	0.680	1216	Vac
600	440	707	107.8	25	31.9	0.384	1025	Vac
650	405	564	103.8	34	44.9	0.596	715	Vac
<u>Microstructure 10/F</u>								
450	460	779	92.4	17	20.5	0.239	981	He
500	(b)	780	--	--	27.1	0.317	1053	He
550	459	749	92.1	29	25.5	0.295	977	He
600	380	635	92.1	20	19.2	0.213	702	He
650	(b)	580	89.6	>25(b)	43.4	0.570	707	Vac
700	314	534	(b)	(b)	46.7	0.629	318	Vac
<u>Microstructure 0/C</u>								
450	395	727	86.0	13	22.0	0.248	932	He
500	403	737	95.5	30	35.5	0.439	1142	Vac
550	389	677	92.1	20	29.7	0.353	949	He
600	380	569	89.6	18	34.0	0.416	746	Vac
650	365	532	86.5	21	31.9	0.384	648	Vac
700	314	480	(b)	(b)	34.5	0.423	513	Vac
<u>Microstructure 0/F</u>								
450	530	871	112.7	25	40.2	0.513	1450	Vac
550	496	776	104.0	31	50.7	0.707	1330	Vac
650	452	649	116.25	36	54.4	0.785	739	Vac

(a) computer data acquisition failed. (b) extensometer slipped.

(a)



(b)

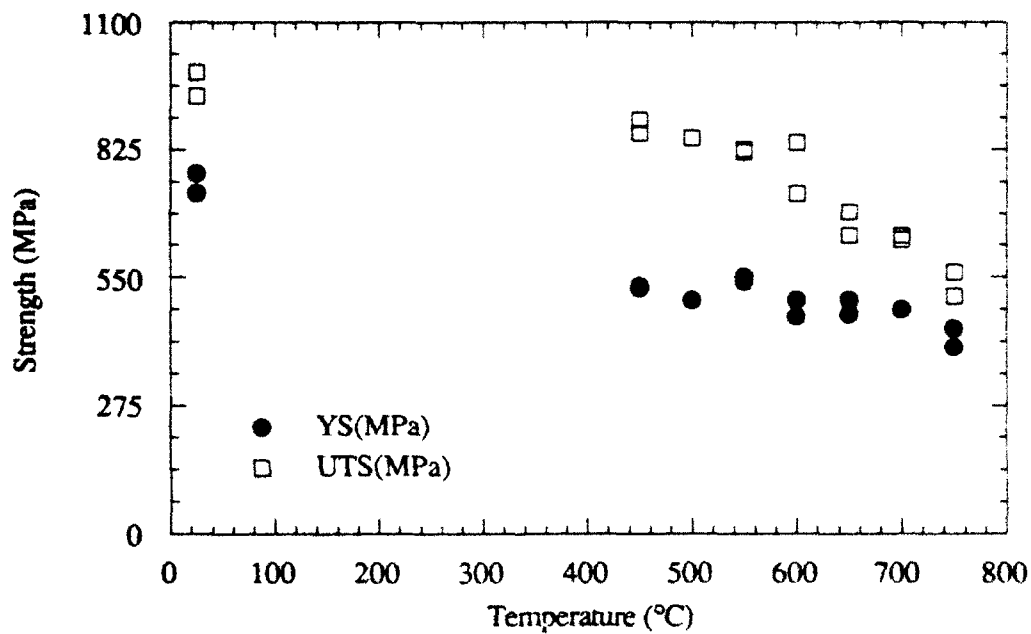
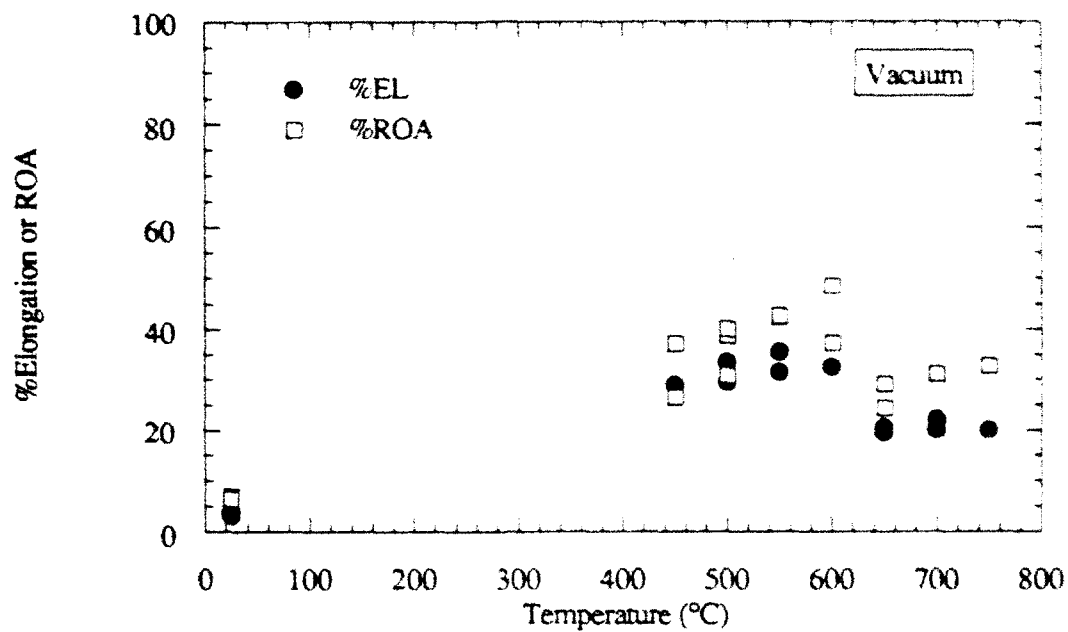


Figure 4.12 Data from round tensile specimens of microstructure 10/F tested in vacuum. (a) Plastic elongation and reduction of area at failure as a function of temperature. (b) Yield strength and ultimate tensile strength as a function of temperature.

(a)



(b)

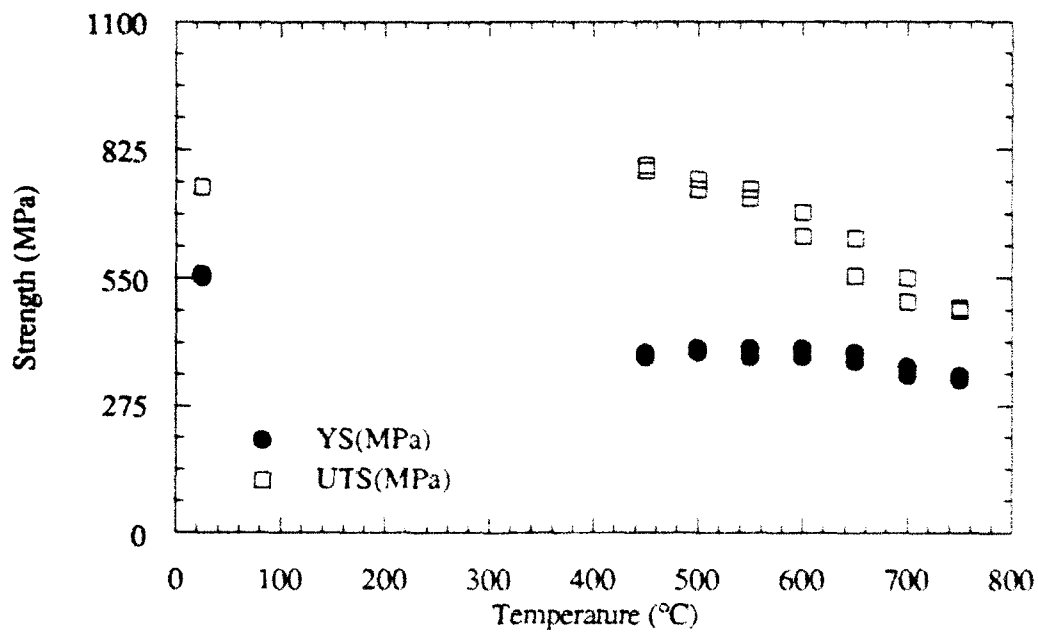
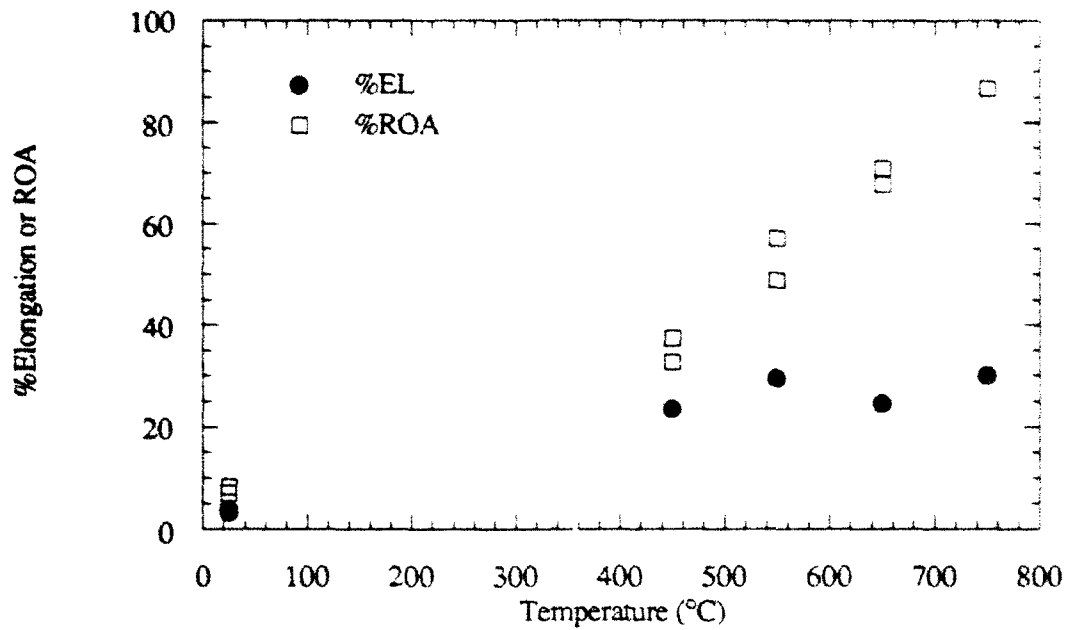


Figure 4.13 Data from round tensile specimens of microstructure 0/C tested in vacuum. (a) Plastic elongation and reduction of area at failure as a function of temperature. (b) Yield strength and ultimate tensile strength as a function of temperature.

(a)



(b)

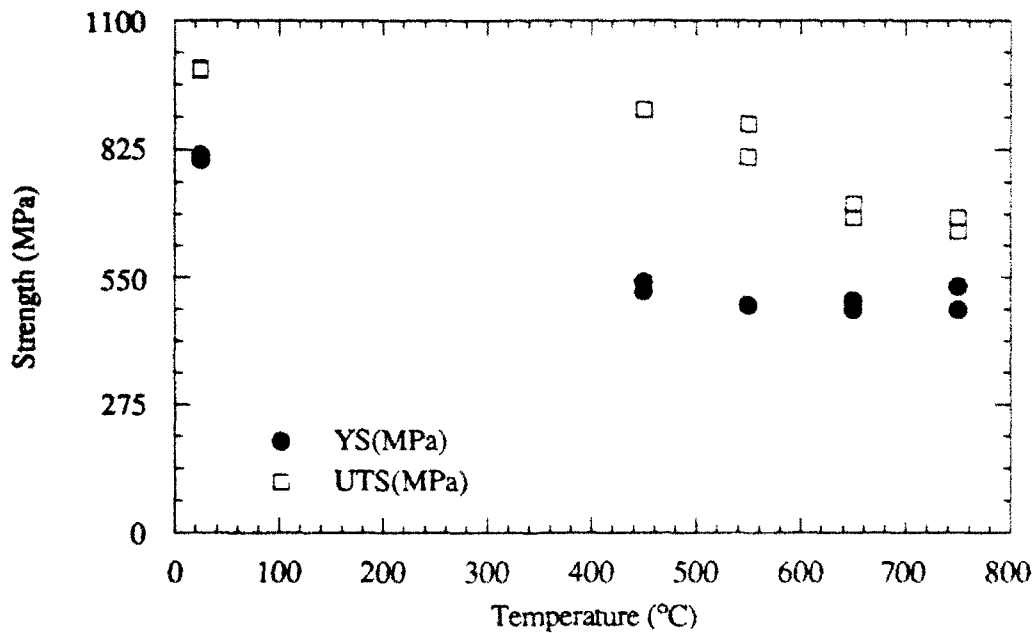


Figure 4.14 Data from round tensile specimens of microstructure 0/F tested in vacuum. (a) Plastic elongation and reduction of area at failure as a function of temperature. (b) Yield strength and ultimate tensile strength as a function of temperature.

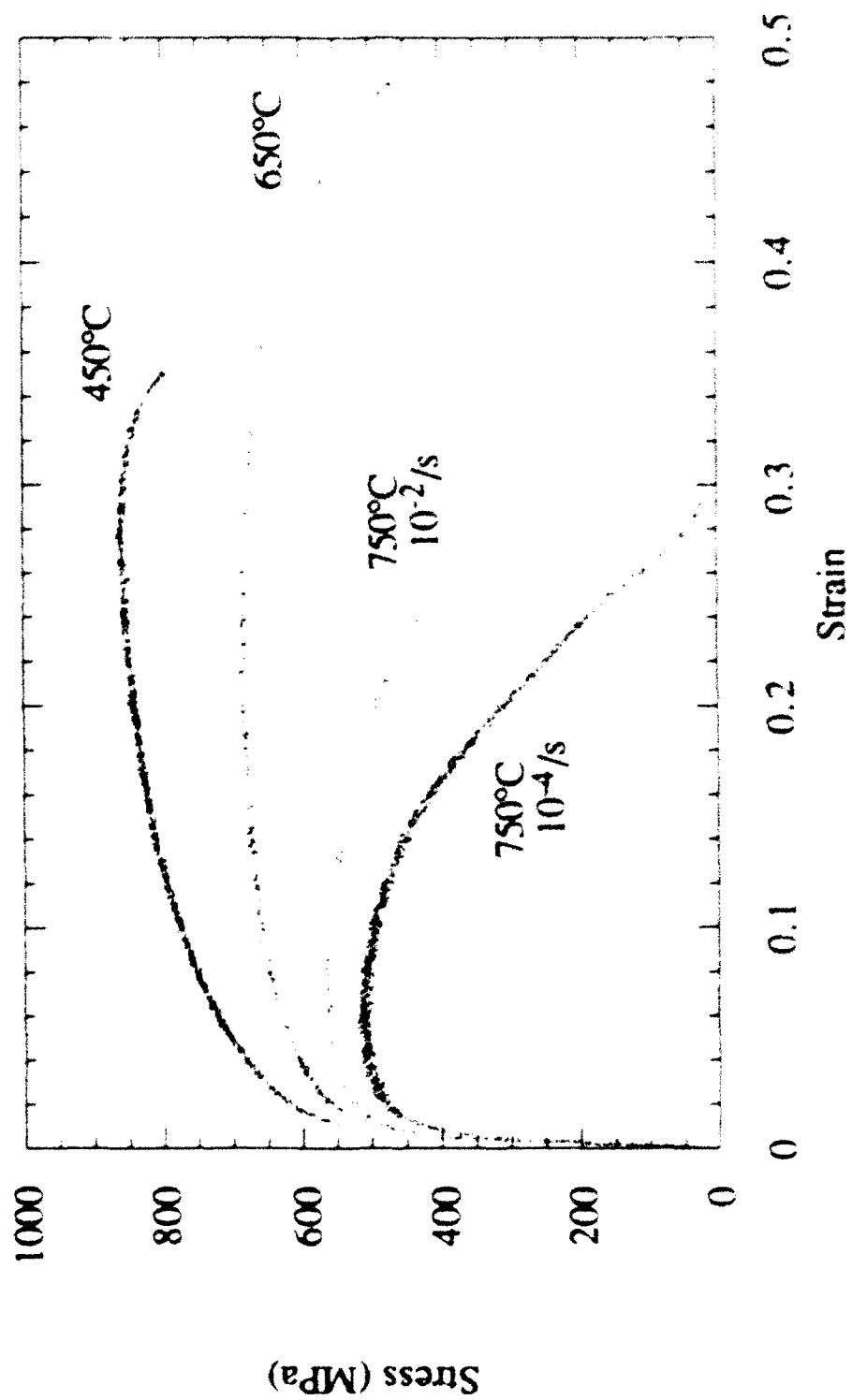


Figure 4.15 (a) Representative engineering stress-strain plots of microstructure 10M tested in vacuum

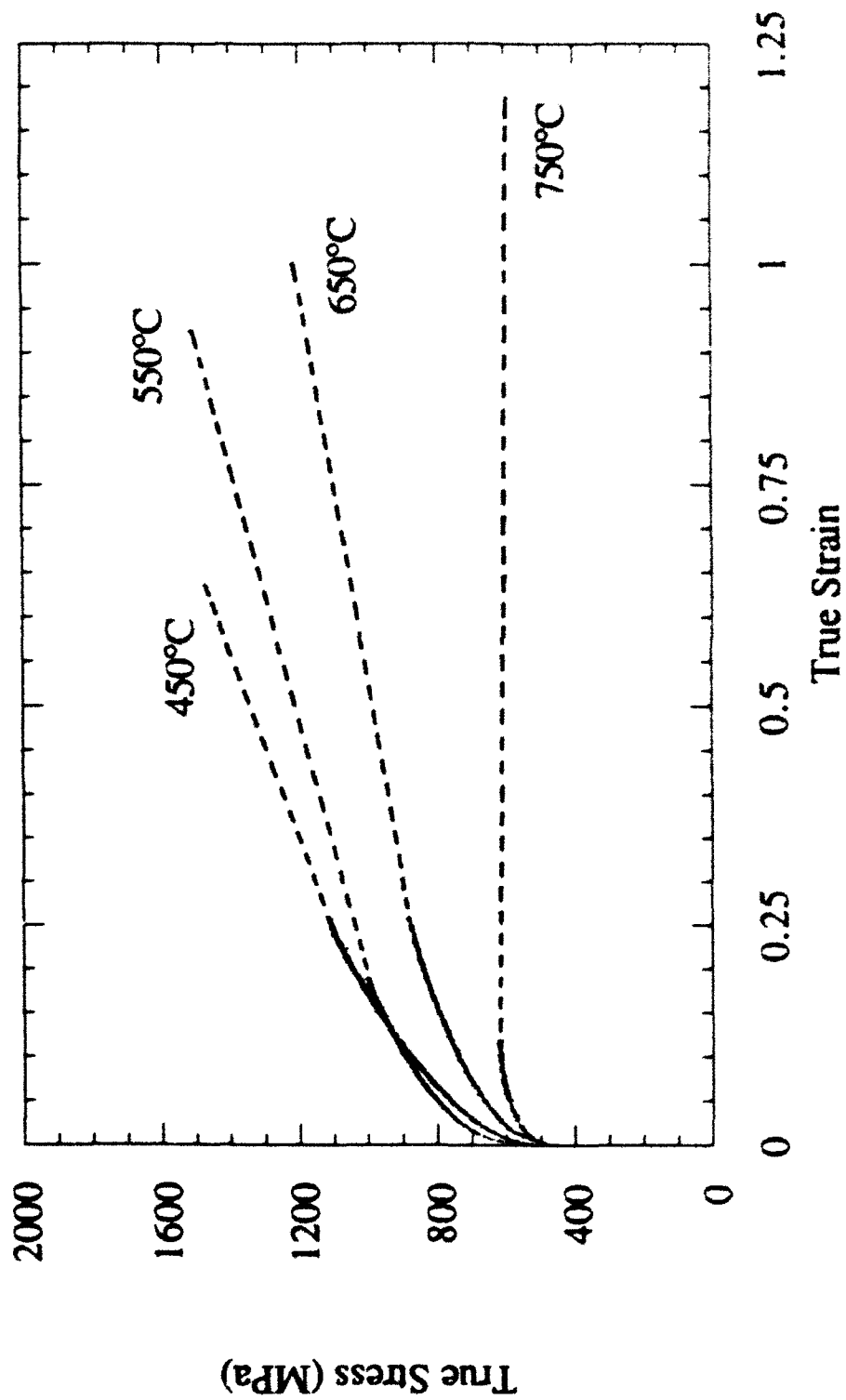


Figure 4.15 (b) Representative true stress-true strain plots of microstructure 10/F in vacuum at a strain rate of 10^{-2} s^{-1} .

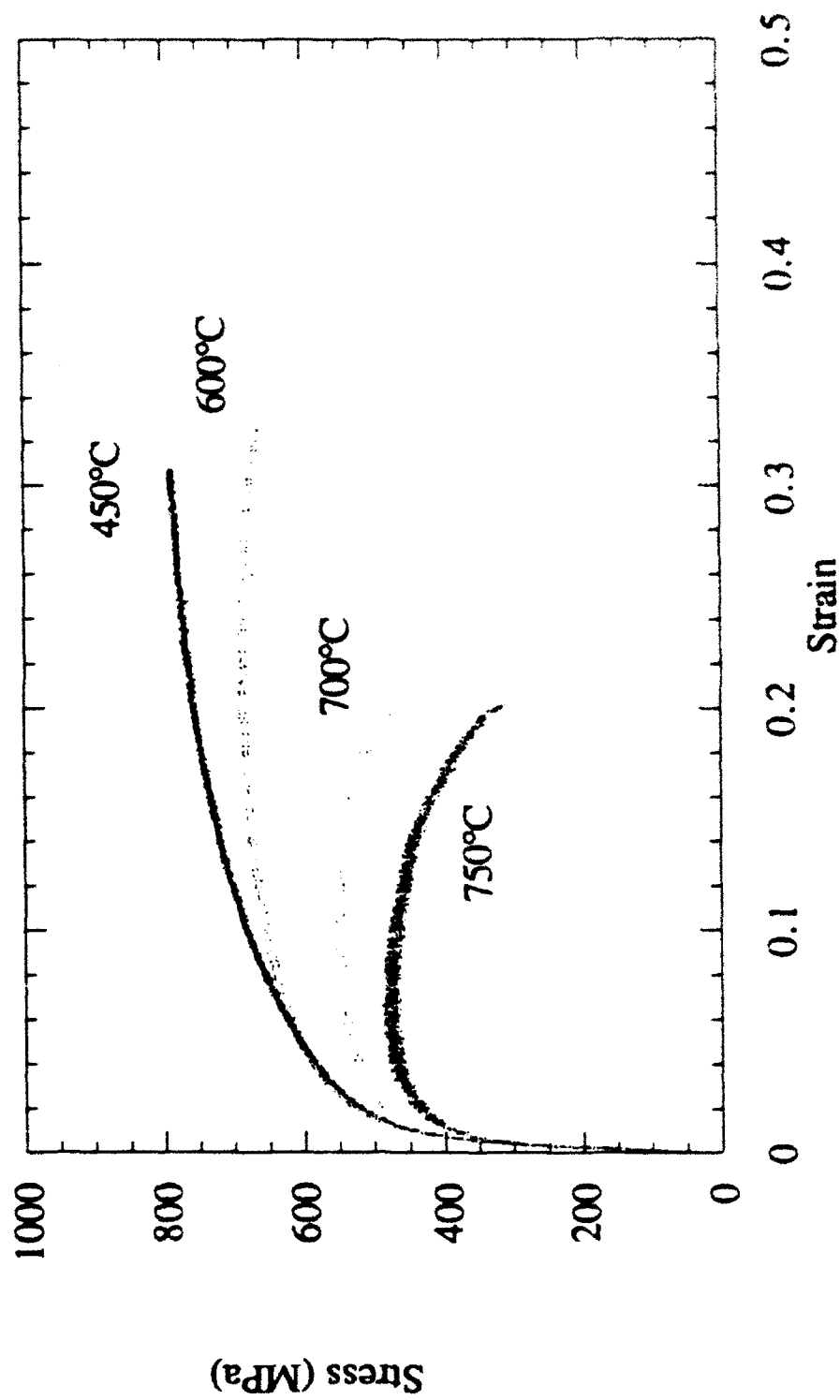


Figure 4.16 (a) Representative engineering stress-strain plots of microstructure O/C tested in vacuum.

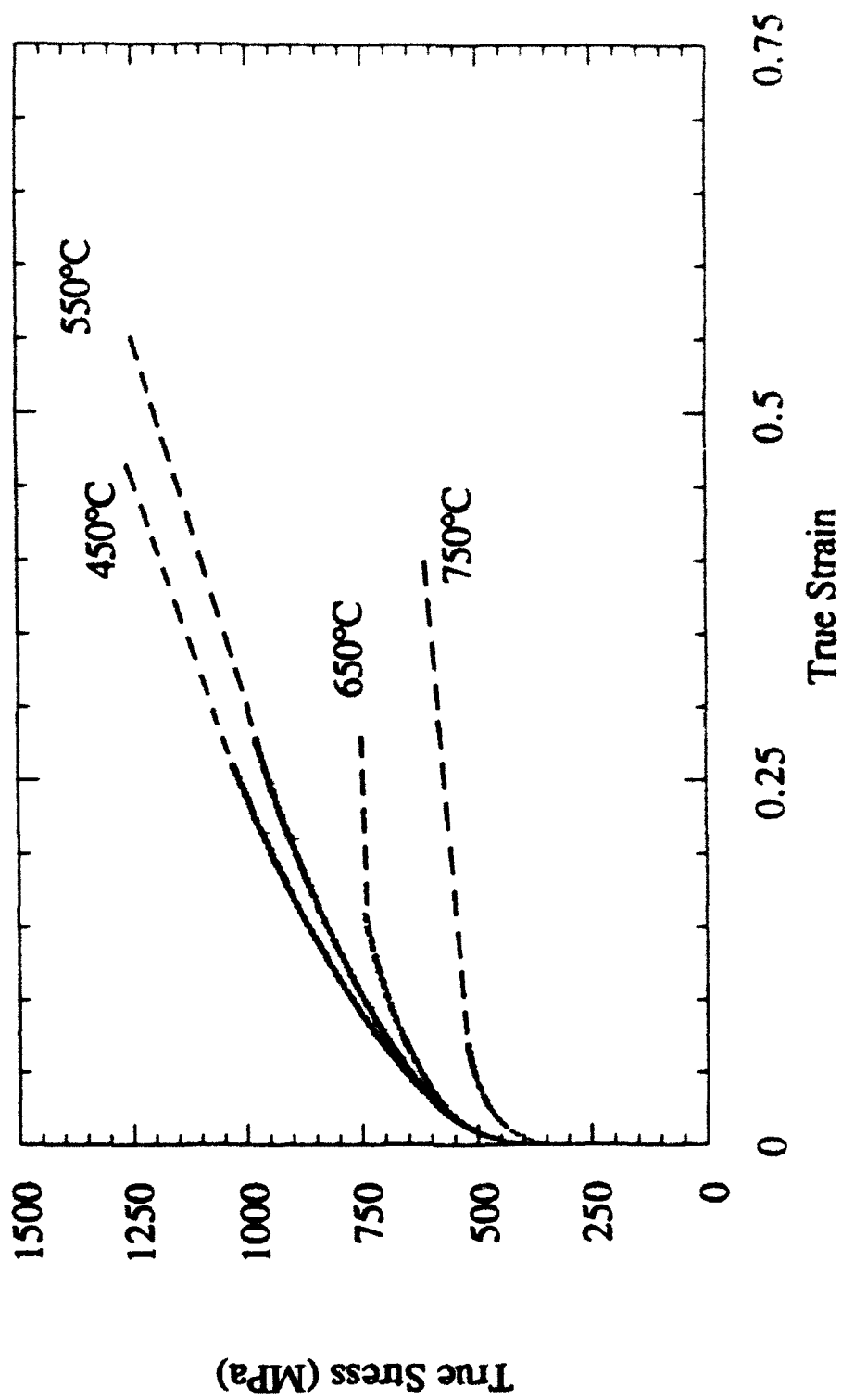


Figure 4.16 (b) Representative true stress-true strain plots of microstructure 0/C in vacuum at a strain rate of 10^{-2} s^{-1} .

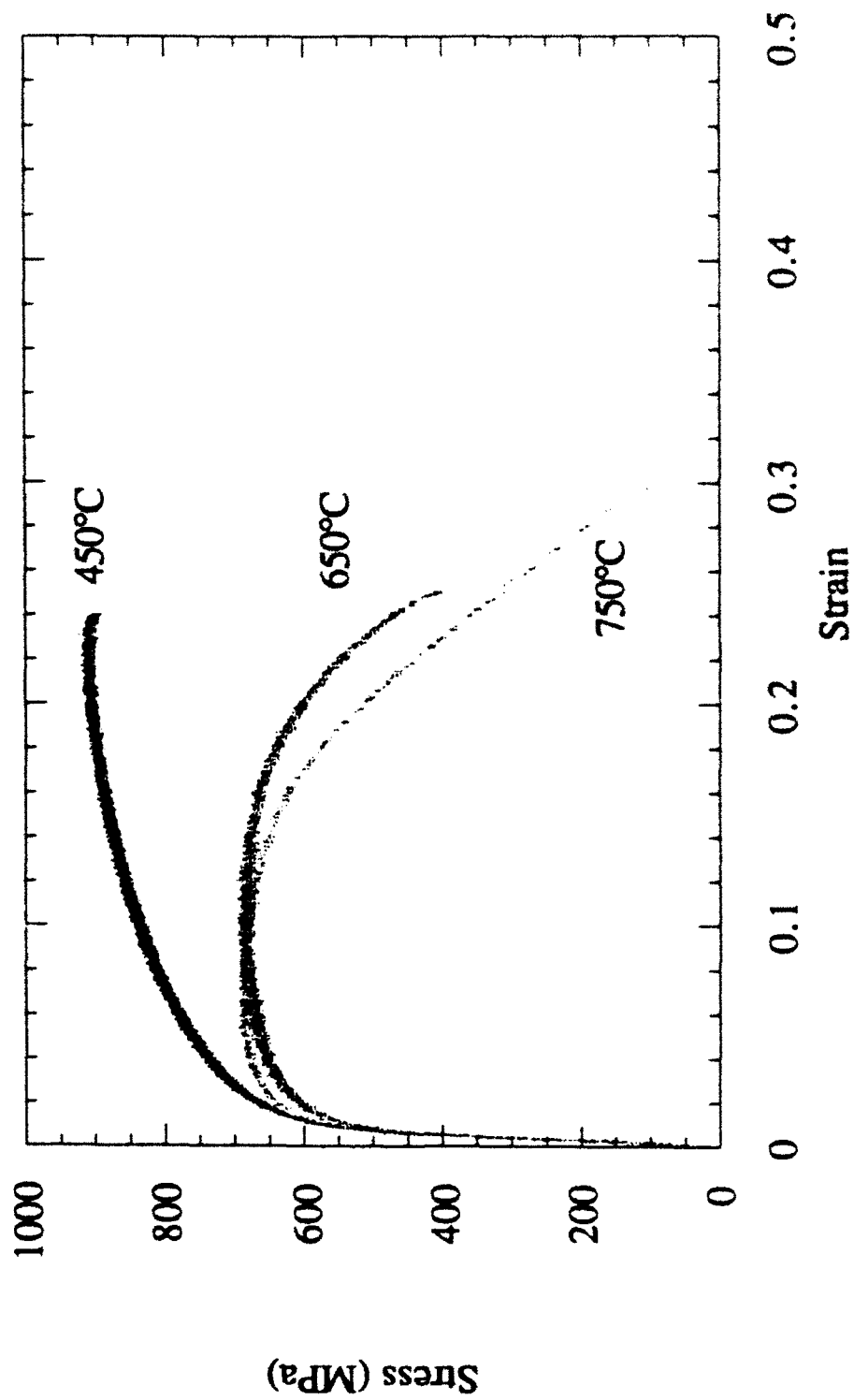


Figure 4.17 (a) Representative engineering stress-strain plots of microstructure Q/F tested in vacuum.

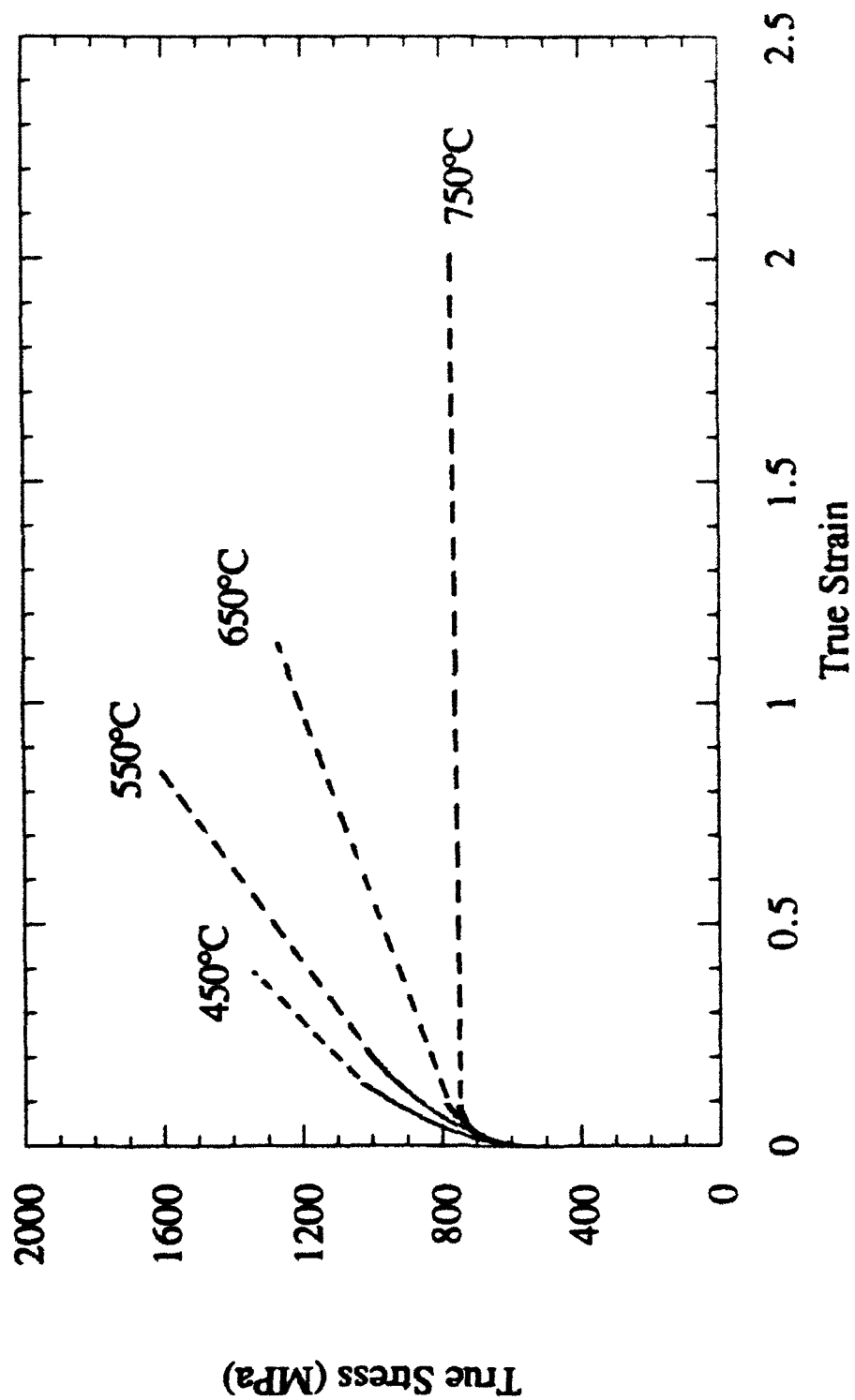


Figure 4.17 (b) Representative true stress-true strain plots of microstructure 0/F in vacuum at a strain rate of 10^{-2} s^{-1}

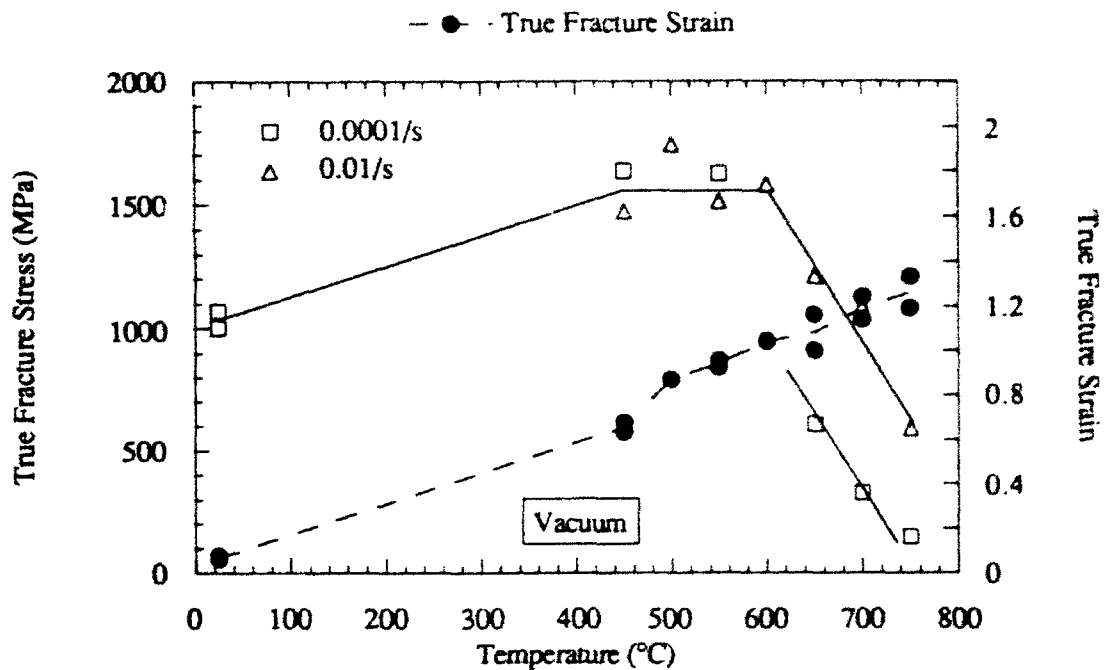


Figure 4.18 True fracture stress and strain for microstructure 10/F plotted as a function of temperature.

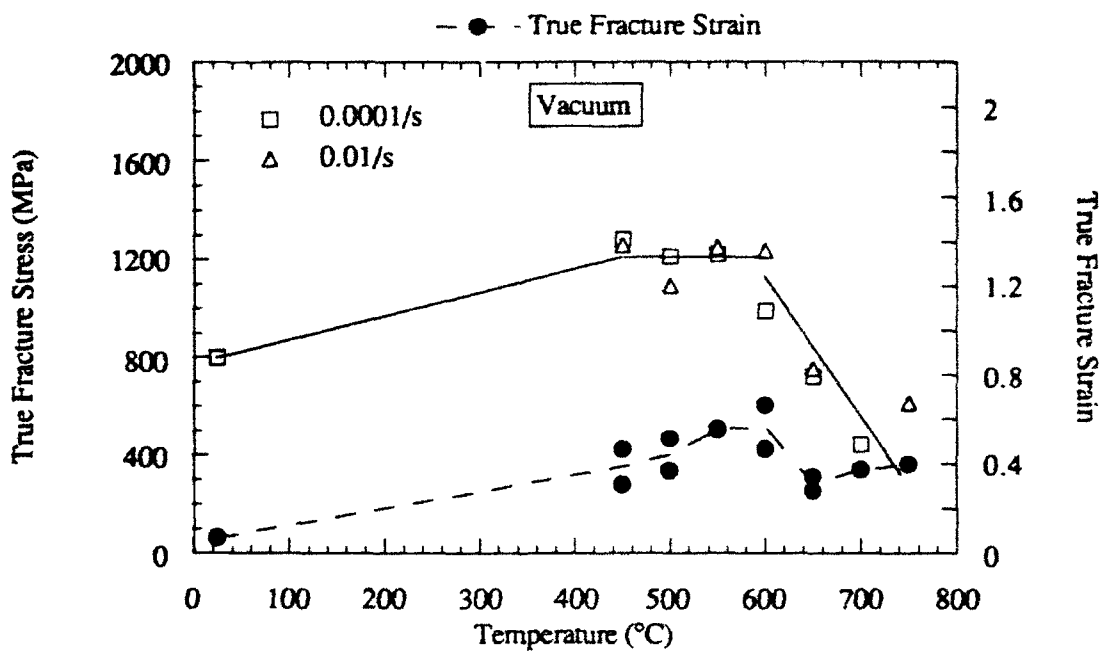


Figure 4.19 True fracture stress and strain for microstructure 0/C plotted as a function of temperature.

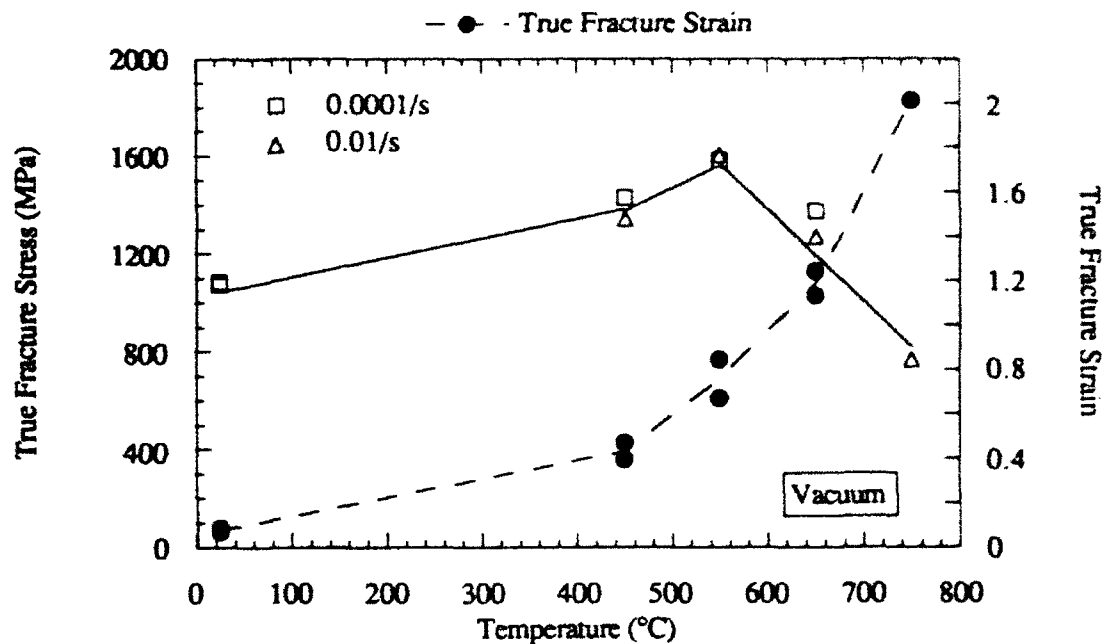


Figure 4.20 True fracture stress and strain for microstructure 0/F plotted as a function of temperature.

The engineering stress-strain curves were converted to true stress-true strain curves and analyzed for strain hardening exponents. The Hollomon expression for power law strain hardening, equation (4.1), was used to determine the strain hardening exponent, n . The curves were analyzed in two regions of strain hardening: $0.01 < \epsilon < 0.10$ and $\epsilon > \epsilon_u$. The results are tabulated in Table 4.6 and graphed in Figures 4.21, 4.22 and 4.23.

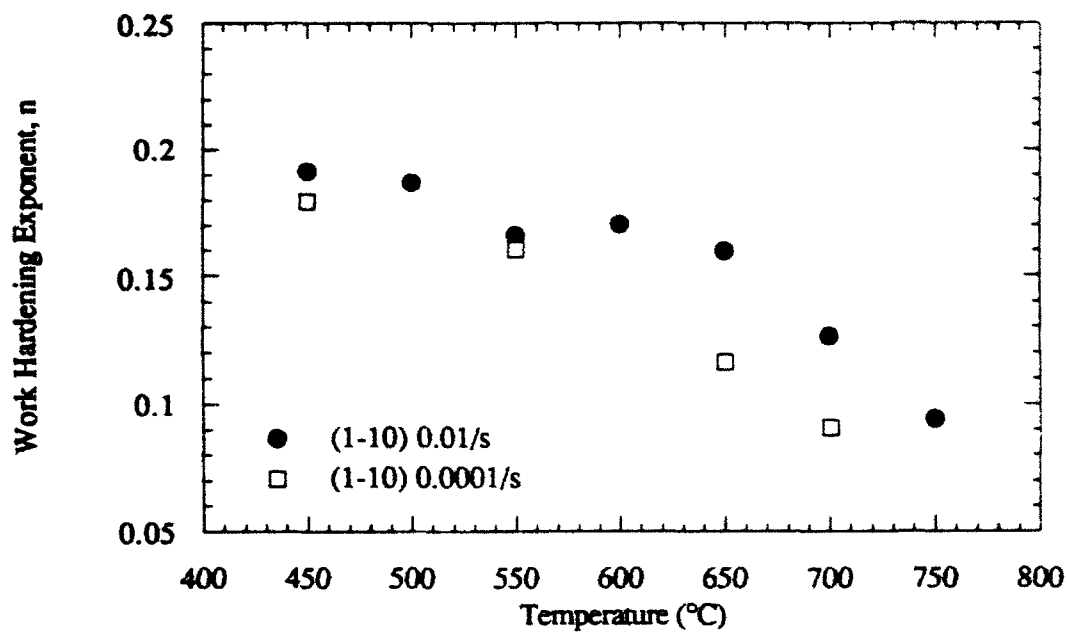
Within each microstructure there did not appear to be a large variation in n with strain rate below 650°C. In general, the n value for the higher crosshead speed was slightly higher than, or equal to, the n value for the lower crosshead speed. However, the n values measured above 600°C for microstructure 10/F were greater at the higher strain rate than that at the lower strain rate, Figure 4.21.

Table 4.6 Strain rate hardening exponents for round tensile specimens.

Micro- structure	Temp (°C)	Initial $\dot{\epsilon}$ (s ⁻¹)	Hollomon				Ludwik	
			0.01 < ϵ < 0.10		$\epsilon > \epsilon_u$		$\epsilon_p < 0.10$	
			K (MPa)	n	K (MPa)	n	K (MPa)	n
10/F	450	10 ⁻⁴	1342	0.18	2000	0.37	1146	0.49
		10 ⁻²	1327	0.19	1800	0.33	2103	0.74
	500	10 ⁻⁴	--	--	--	--	--	--
		10 ⁻²	1294	0.19	1875	0.38	965	0.46
	550	10 ⁻⁴	1274	0.16	1560	0.30	979	0.45
		10 ⁻²	1293	0.17	1675	0.32	1156	0.51
	600	10 ⁻⁴	--	--	--	--	--	--
		10 ⁻²	1142	0.17	1875	0.46	1676	0.66
	650	10 ⁻⁴	958	0.12	575	-0.13	671	0.43
		10 ⁻²	1054	0.16	1375	0.30	1225	0.62
	700	10 ⁻⁴	NA	NA	230	-0.64	553	0.38
		10 ⁻²	949	0.13	1125	0.25	NA	NA
	750	10 ⁻⁴	NA	NA	120	-0.89	NA	NA
		10 ⁻²	NA	NA	580	-0.03	NA	NA
0/C	450	10 ⁻⁴	1273	0.22	NA	NA	1198	0.46
		10 ⁻²	1246	0.22	1850	0.41	1247	0.51
	500	10 ⁻⁴	1182	0.21	1685	0.39	1160	0.50
		10 ⁻²	1203	0.21	1710	0.39	1562	0.61
	550	10 ⁻⁴	1074	0.19	1650	0.40	1115	0.53
		10 ⁻²	1174	0.20	1700	0.40	1480	0.57
	600	10 ⁻⁴	1003	0.17	1400	0.37	771	0.41
		10 ⁻²	1118	0.19	1515	0.37	1065	0.48
	650	10 ⁻⁴	874	0.16	950	0.18	839	0.50
		10 ⁻²	1012	0.17	800	0.04	887	0.44
	700	10 ⁻⁴	770	0.14	100	-1.04	608	0.42
		10 ⁻²	837	0.14	NA	NA	586	0.35
	750	10 ⁻⁴	709	0.12	NA	NA	520	0.38
		10 ⁻²	NA	NA	750	0.19	NA	NA
0/F	450	10 ⁻⁴	1435	0.19	2050	0.38	1676	0.59
		10 ⁻²	1435	0.19	2050	0.38	1534	0.54
	550	10 ⁻⁴	1312	0.18	1745	0.35	1267	0.49
		10 ⁻²	1285	0.18	1975	0.41	1011	0.44
	650	10 ⁻⁴	1036	0.13	1250	0.28	840	0.44
		10 ⁻²	1078	0.14	1200	0.24	1084	0.52
	750	10 ⁻⁴	NA	NA	NA	NA	NA	NA
		10 ⁻²	985	0.11	750	0	748	0.45

NA: values of n that were invalid.

(a)



(b)

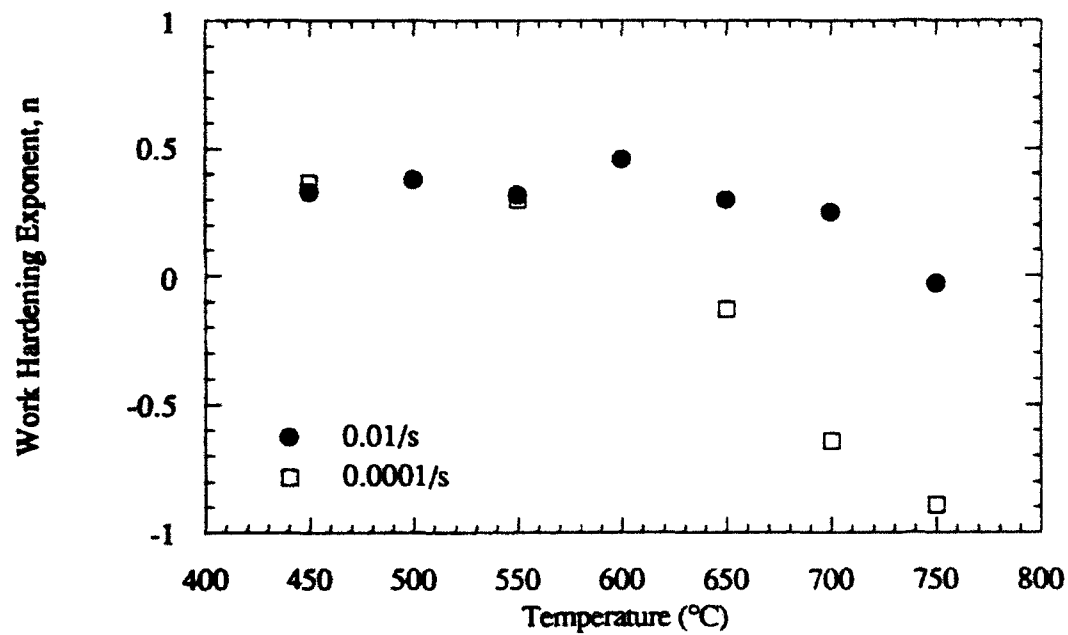
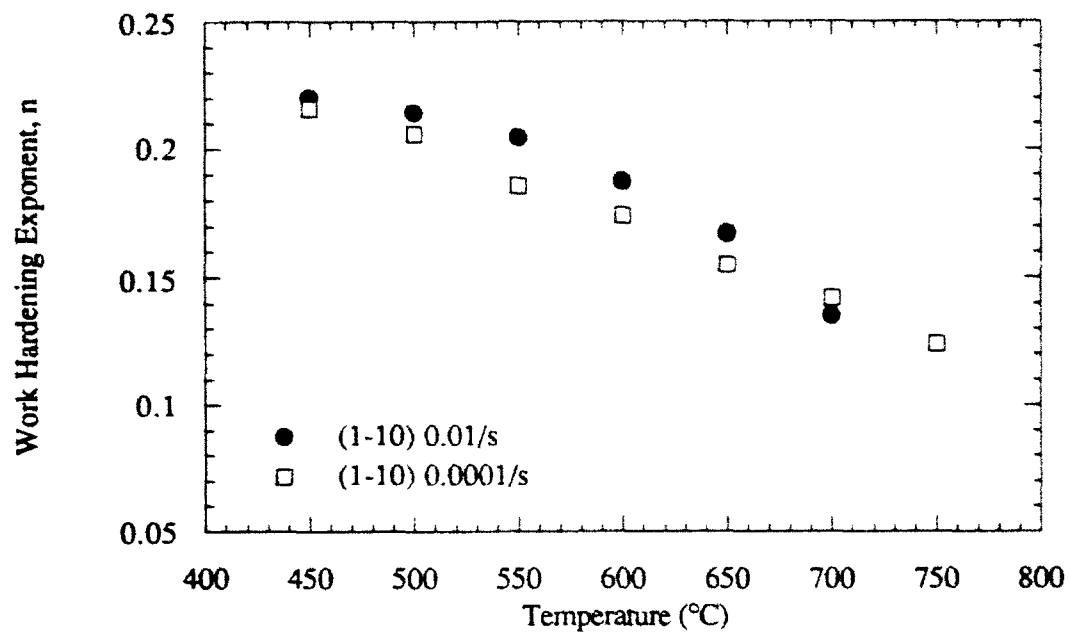


Figure 4.21 Strain hardening exponent, n , plotted as a function of temperature for (a) $0.01 < \epsilon < 0.10$ (b) $\epsilon > \epsilon_u$ for microstructure 10/F.

(a)



(b)

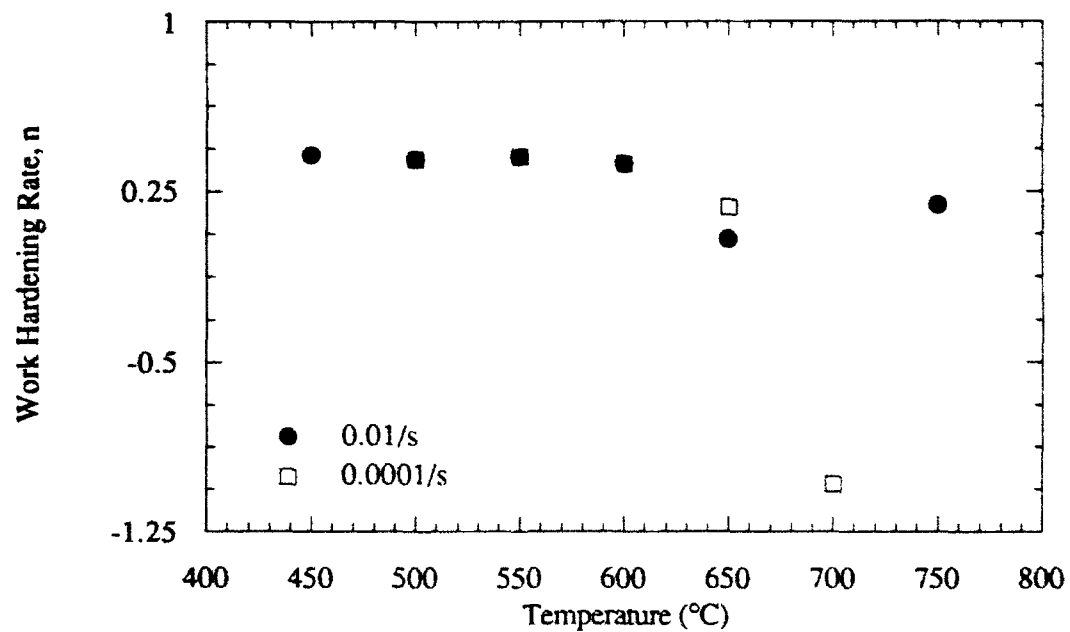
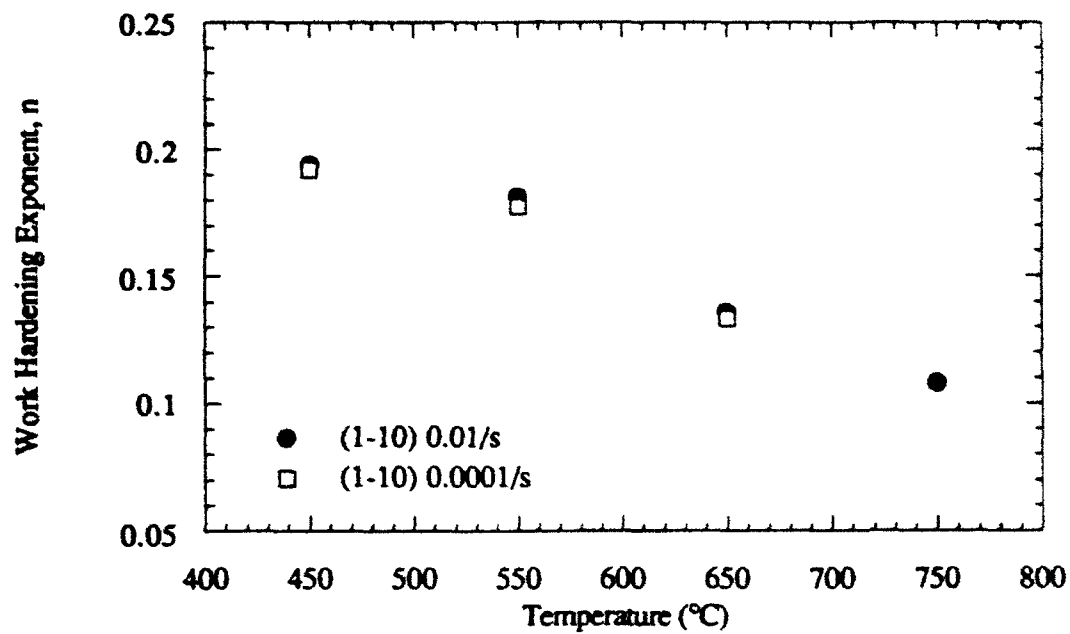


Figure 4.22 Strain hardening exponent, n , plotted as a function of temperature for (a) $0.01 < \epsilon < 0.10$ (b) $\epsilon > \epsilon_u$ for microstructure 0/C.

(a)



(b)

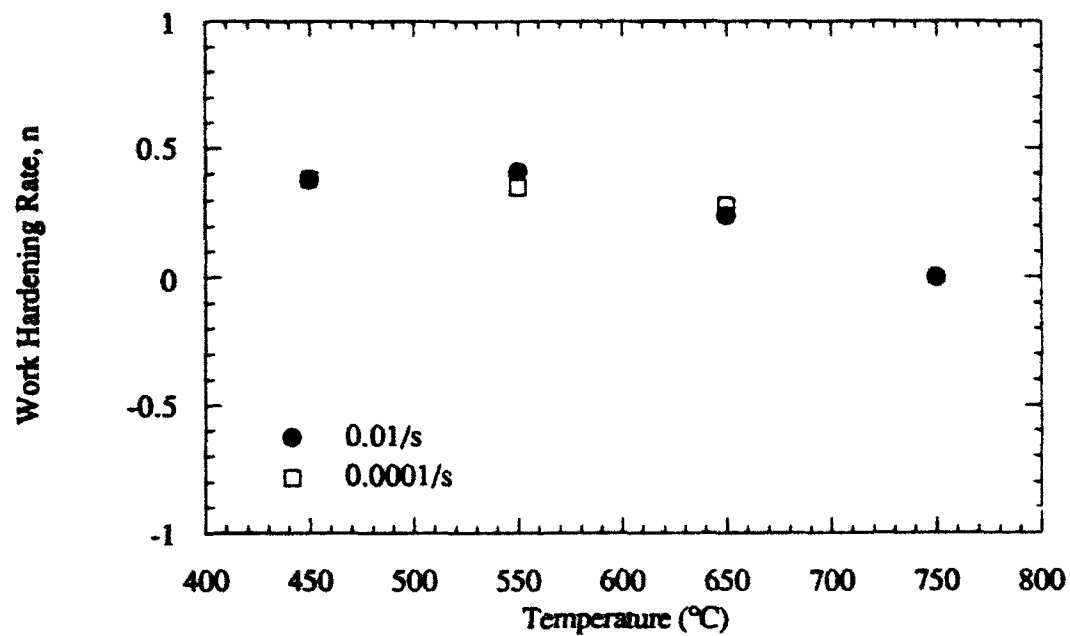


Figure 4.23 Strain hardening exponent, n , plotted as a function of temperature for (a) $0.01 < \epsilon < 0.10$ (b) $\epsilon > \epsilon_u$ for microstructure 0/F.

4.2.3 Elevated Temperature Tensile Testing in Air

Elevated temperature tensile testing in air was undertaken to study the effect of environment on tensile properties. In particular, environmentally assisted surface crack growth into the tensile specimen was of interest. The mechanical property results are listed in Table 4.7 along with the corresponding properties obtained in vacuum.

Table 4.7 Elevated temperature tensile properties of microstructure O/F tested in air.

Temp (°C)	Initial $\dot{\epsilon}$ (s^{-1})	YS (MPa)	UTS (MPa)	E (GPa)	%EL	%ROA	ϵ_f	σ_F (MPa)
<u>550°C</u>	2×10^{-4}	463	698	61.3	11.3	16.4	0.18	446
	2×10^{-3}	518	810	72.8	17.2	24.8	0.28	1013
	2×10^{-2}	472	802	79.1	35.8	56.3	0.83	1350
	Vacuum	490	810	96.3	29.5	57.0	0.84	1603
<u>650°C</u>	2×10^{-3}	476	667	76.9	14.8	16.2	0.18	201
	2×10^{-2}	508	734	75.5	25.4	46.2	0.62	774
	1×10^{-1}	476	724	74.3	29.1	60.9	0.94	1179
	Vacuum	480	680	81.2	24.5	70.9	1.24	1376

The data show that there was a significant effect of environment on the tensile properties. As the strain rate was increased, all mechanical properties expected to be affected by environmental exposure increased. At 550°C, a strain rate of $2 \times 10^{-2} s^{-1}$ resulted in properties which were similar to those achieved in vacuum testing. Observations along the gage length of the tensile specimens indicated environmentally induced circumferential cracking at all temperatures and strain rates, Figure 4.24. However, these cracks only grew significant distances into the specimen at lower strain rates. At 550°C and the highest strain rate, the fracture surface indicated no growth of cracks into the specimen.

While the properties of specimens tested at 650°C were also increasing with strain rate, only those obtained at $1 \times 10^{-1} \text{ s}^{-1}$ are close to the values seen in vacuum testing. This mechanical property trend indicates that the dynamic environmental degradation appears to be nearly one order of magnitude quicker at 650°C as compared to 550°C.

Crack growth rates were determined by measuring crack extension into the gage section and dividing by the time spent during plastic deformation. The fastest crack growth rates were determined to be 0.005 mm/s at 550°C and 0.025 mm/s at 650°C. In both instances these rates were constant between the two highest strain rates used and therefore can be considered to be the strain rate independent crack growth rates.

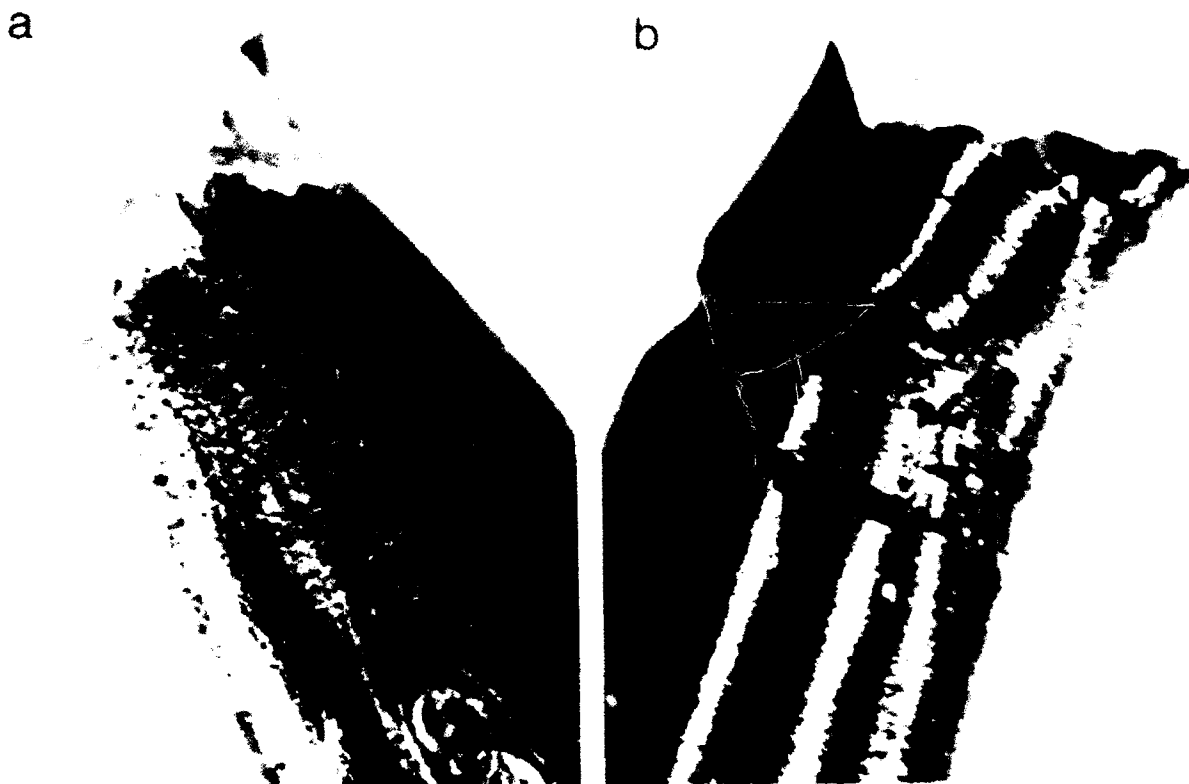


Figure 4.24 Light macrograph of tensile specimens of microstructure 0/F tested in air at 650°C. (a) Strain rate of $1 \times 10^{-1} \text{ s}^{-1}$. (b) Strain rate of $2 \times 10^{-3} \text{ s}^{-1}$.

4.2.4 Room Temperature Fracture Toughness Testing

The results of room temperature fracture toughness testing are summarized in Table 4.8.

Table 4.8 Room temperature fracture toughness values.

Microstructure	K _{IC} - Sample 1		K _{IC} - Sample 2	
	(MPa√m)	P _{max} /P _Q	(MPa√m)	P _{max} /P _Q
25/C	19.1	1.08	21.1	1.06
25/F	19.7*	1.13	18.9	1.08
10/C	20.8	1.06	20.7	1.06
10/F	18.3*	1.16	20.1	1.00
0/C	18.0*	1.15	20.5	1.10

* Due to a high P_{max}/P_Q ratio, these values can only be regarded as a K_Q.

These are amongst the highest fracture toughness values reported for Ti-25-10-3-1, which are typically closer to 15 MPa√m. Also, no trends with respect to microstructure were apparent in the fracture toughness results.

4.2.5 Elevated Temperature Fracture Toughness Testing

The raw data gathered from the multi-specimen J testing is presented in Table 4.9. The data were fit to a power law equation for J versus Δa, equation 4.3,¹⁰⁴ and are plotted in Figures 4.25 through 4.33:

$$J = C_1 \exp(\Delta a)^{C_2} \quad (4.3)$$

J_Q was determined by the intersection of this plotted line with the 0.2 mm offset line. The tearing modulus, T_R, was taken as the linear slope of the J vs. Δa curve between Δa values of 0.25 and 1.3 mm. ASTM E813 requirements for providing a valid J_{IC} value

were not met in all instances, in some cases the (a/W) ratio was just below that required. In other cases, there was not a point in the last valid data region, between the 1.0 mm offset and 1.5 mm exclusion lines (conditions with high T_R), or the point acquired was slightly beyond the 1.5 mm exclusion line (conditions with low T_R and J_{Ic}). K_{Ic} was determined from the J_{Ic} values based on the linear elastic relation below, equation (4.4), and the results are presented in Table 4.10. A Poisson's ratio of 0.29 was used in the calculations.¹⁰⁸

$$K_{Ic} = \sqrt{\frac{E \cdot J_{Ic}}{(1-\nu^2)}} \quad (4.4)$$

The three microstructures exhibited a similar toughening response with temperature; these are plotted in Figure 34. The initiation toughness for microstructures 10/F and 0/F increased from 450°C to 550°C, and fell dramatically at 650°C. The tearing modulus was likewise increased at 550°C and returned at 650°C to a value similar to that at 450°C. Microstructure 0/C, on the other hand, showed toughness decreasing with temperature. This may have been due, in part, to the very high tearing modulus of microstructure 0/C. The high slope of T_R made accurate determination of a J_Q value at 550°C difficult.

The crack propagation rates during elevated temperature bending are listed in Table 4.11. These values were estimated from the load-displacement curves by using the crosshead displacement rate and load line displacement data. Only the region past the linear elastic loading portion of the curve was used in determining crack growth time. At 450°C microstructures 10/F and 0/F exhibited similar crack growth rates, while the rate in microstructure 0/C was nearly half their value. At 550°C the crack growth rates for all three microstructures were nearly identical and were half the rates observed at 450°C. At 650°C the crack growth rates were increased to values near those of 450°C for microstructures 10/F and 0/C, while microstructure 0/F had a crack growth rate that was nearly double the rates of the other two microstructures.

Table 4.9 Raw data from elevated temperature J testing.

(J_E = elastic component, J_P = plastic component, $J_T = J_E + J_P$)

Temp (°C)	a/W	Δa (mm)	J_E (kJ/m ²)	J_P (kJ/m ²)	J_T (kJ/m ²)
<u>Microstructure 10/F</u>					
450	0.500	0.27	27.3	32.4	59.7
	0.477	0.59	25.0	62.1	87.1
	0.451	1.04	17.8	87.2	105.0
	0.474	1.66	10.8	119.4	130.2
550	0.497	0.23	28.6	37.8	66.4
	0.513	0.32	30.6	86.4	117.0
	0.499	0.68	26.8	109.1	135.9
	0.521	0.93	21.9	165.2	187.1
650	0.553	0.50	12.5	17.9	30.4
	0.545	0.56	13.7	35.2	48.9
	0.550	0.96	8.2	49.8	58.0
	0.536	1.55	6.2	78.7	84.9
<u>Microstructure 0/C</u>					
450	0.496	0.26	30.4	52.4	82.8
	0.527	0.55	22.2	29.9	102.1
	0.524	0.72	21.6	84.4	106.0
	0.524	1.11	13.2	98.1	111.3
	0.506	1.12	16.0	122.5	138.5
	0.522	1.44	9.0	120.0	129.0
550	0.513	0.28	26.1	38.3	64.4
	0.523	0.44	29.2	92.3	121.5
	0.485	0.70	21.1	122.3	143.4
	0.472	1.05	21.7	197.2	218.9
650	0.514	0.39	12.4	13.8	26.2
	0.514	0.58	13.0	31.6	44.6
	0.519	1.14	8.7	43.2	51.9
	0.510	1.83	5.2	64.6	69.8
<u>Microstructure 0/F</u>					
450	0.502	0.25	30.6	25.7	56.3
	0.595	0.58	25.1	36.7	61.8
	0.506	0.72	32.6	52.2	84.8
	0.544	1.13	17.2	71.1	88.3
550	0.413	0.16	28.8	40.3	69.1
	0.527	0.34	28.6	59.7	88.3
	0.497	0.39	30.5	88.7	119.2
	0.589	0.75	22.1	164.2	186.3
650	0.529	0.40	15.6	9.5	25.1
	0.489	0.50	13.7	12.5	26.2
	0.479	0.79	15.8	23.3	39.1
	0.539	1.66	8.0	59.0	67.0

Table 4.10 Elevated temperature J_{Ic} data

Temp (°C)	C_1	C_2	σ_y (MPa)	$25 J_Q/\sigma_y$ (mm)	T_R	J_{Ic} (kJ/m ²)	K_{Ic} (MPa√m)
<u>Microstructure 10/F</u>							
450	105.2	0.424	701	2.03	19.8	57	77.7
550	190.7	0.615	684	3.05	41.2	83.5	91.0
650	61.3	0.759	575	0.82	18.2	18.75	41.7
<u>Microstructure 0/C</u>							
450	118.7	0.267	577	3.64	25.9	84	90.6
550	210.0	0.859	535	3.09	107.2	66.2	79.1
650	50.6	0.962	475	0.60	28.0	11.4	32.0
<u>Microstructure 0/F</u>							
450	84.5	0.313	720	1.85	11.1	53.9	71.5
550	211.3	0.648	668	3.36	66.6	89.7	100.3
650	46.1	0.721	579	0.65	12.0	15	35.8

Table 4.11 Estimates of three point bend bar crack propagation rate at elevated temperatures.

<u>Microstructure</u>	<u>450°C</u>	<u>550°C</u>	<u>650°C</u>
10/F	0.021 mm/s	0.010 mm/s	0.023 mm/s
0/C	0.014	0.009	0.029
0/F	0.029	0.009	0.049

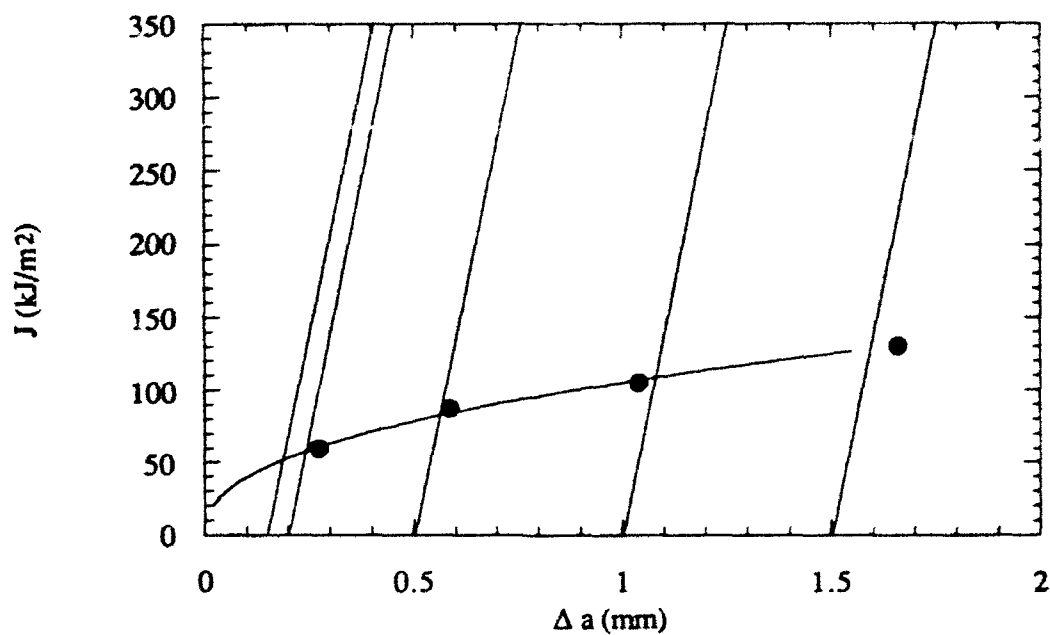


Figure 4.25 J vs. Δa plot for microstructure 10/F, 450°C.

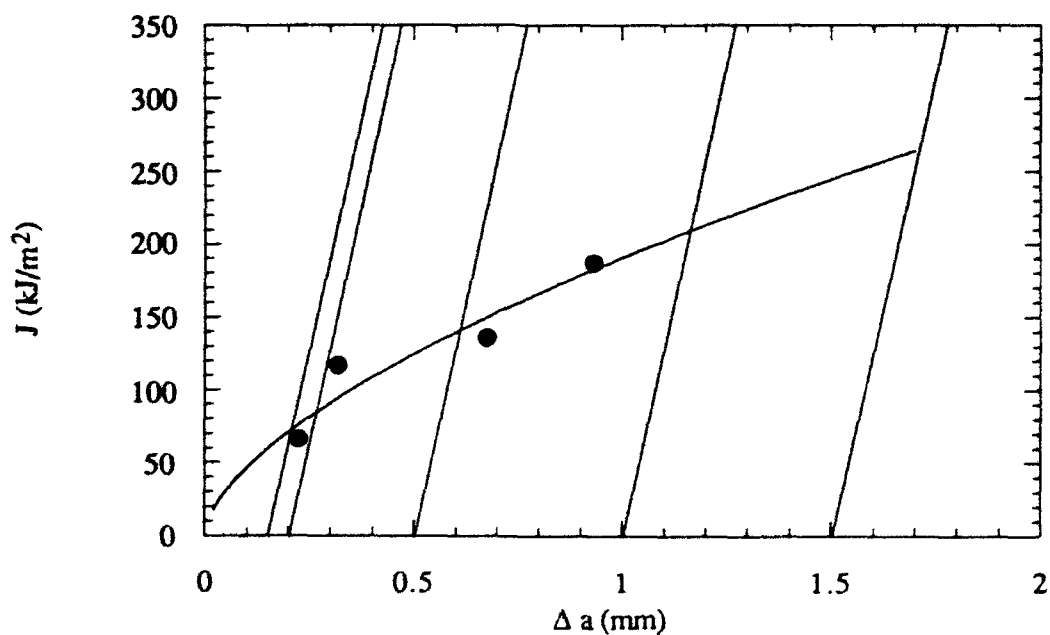


Figure 4.26 J vs. Δa plot for microstructure 10/F, 550°C.

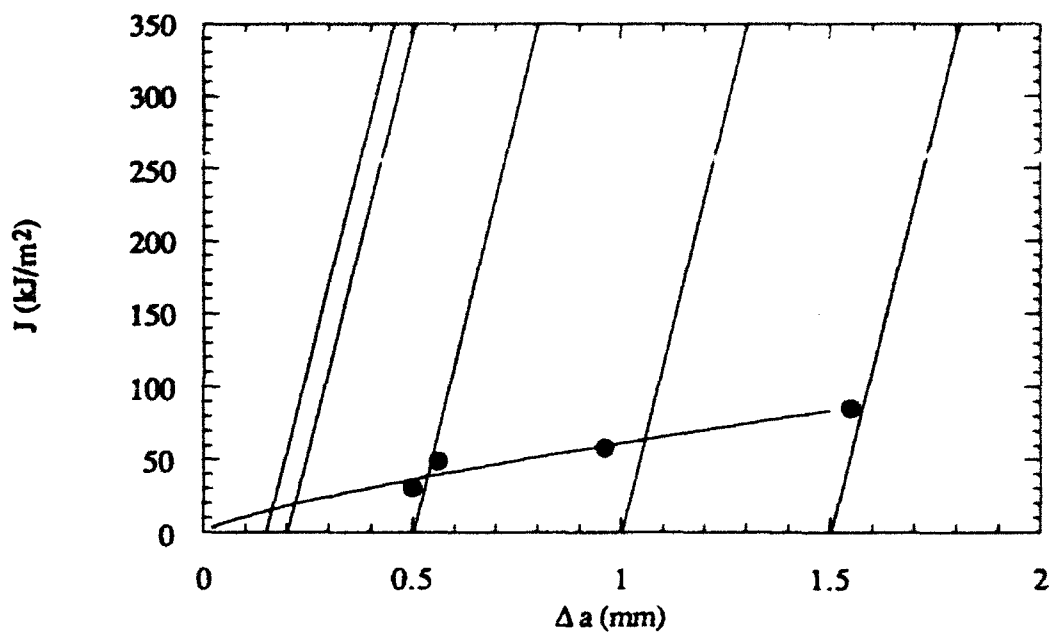


Figure 4.27 J vs. Δa plot for microstructure 10/F, 650°C.

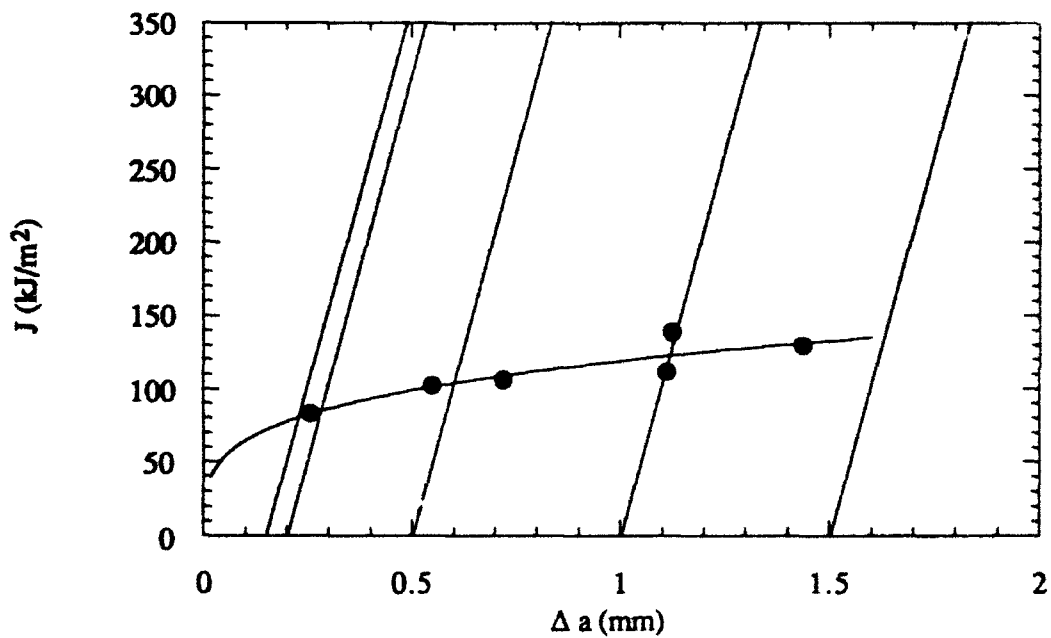


Figure 4.28 J vs. Δa plot for microstructure 0/C, 450°C.

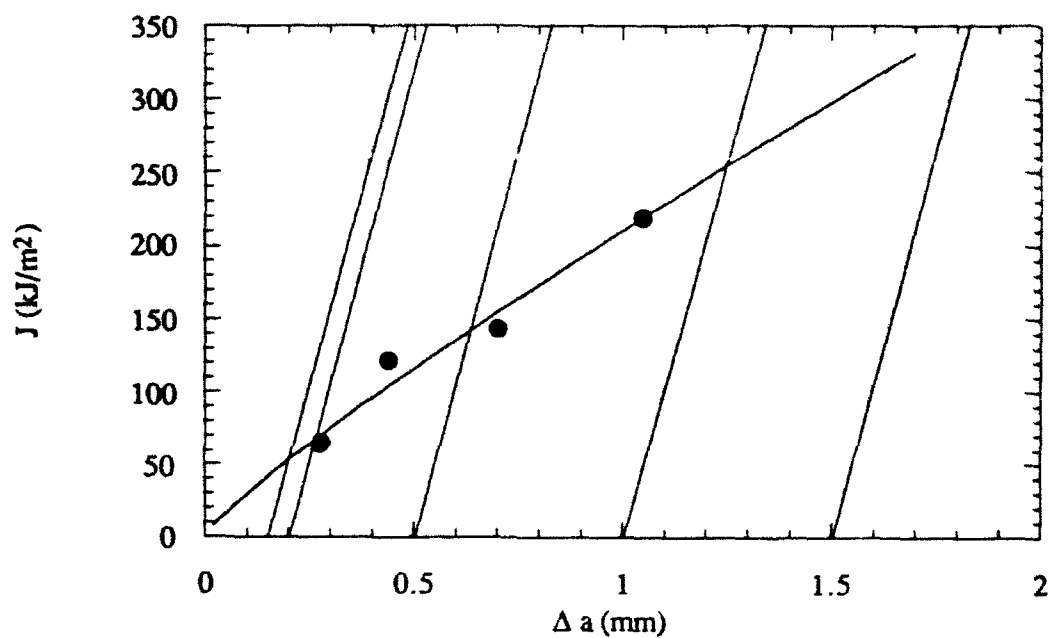


Figure 4.29 J vs. Δa plot for microstructure 0/C, 550°C

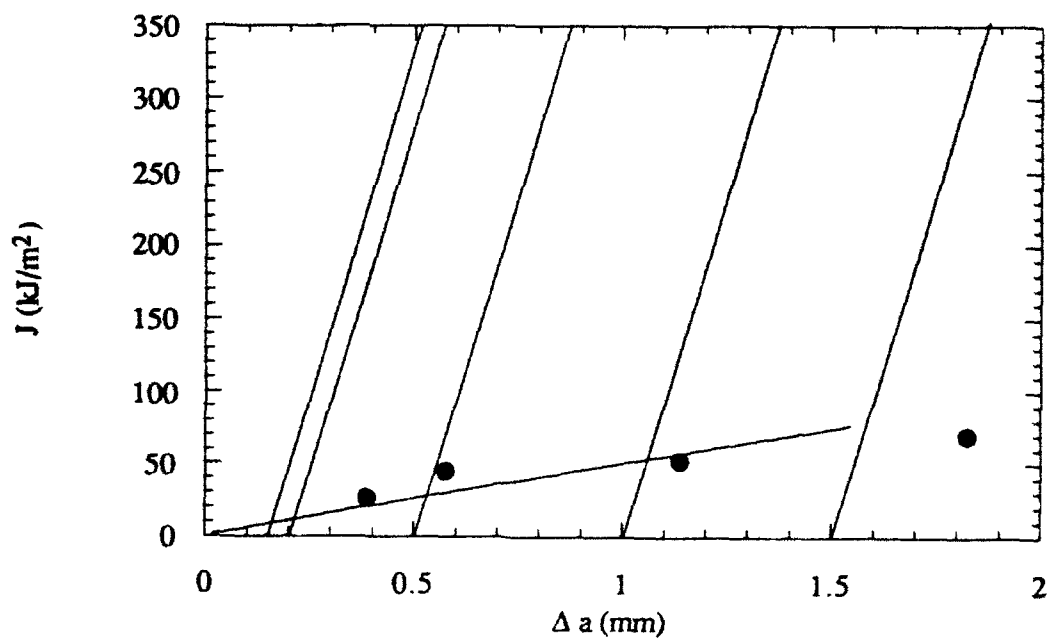


Figure 4.30 J vs. Δa plot for microstructure 0/C, 650°C.

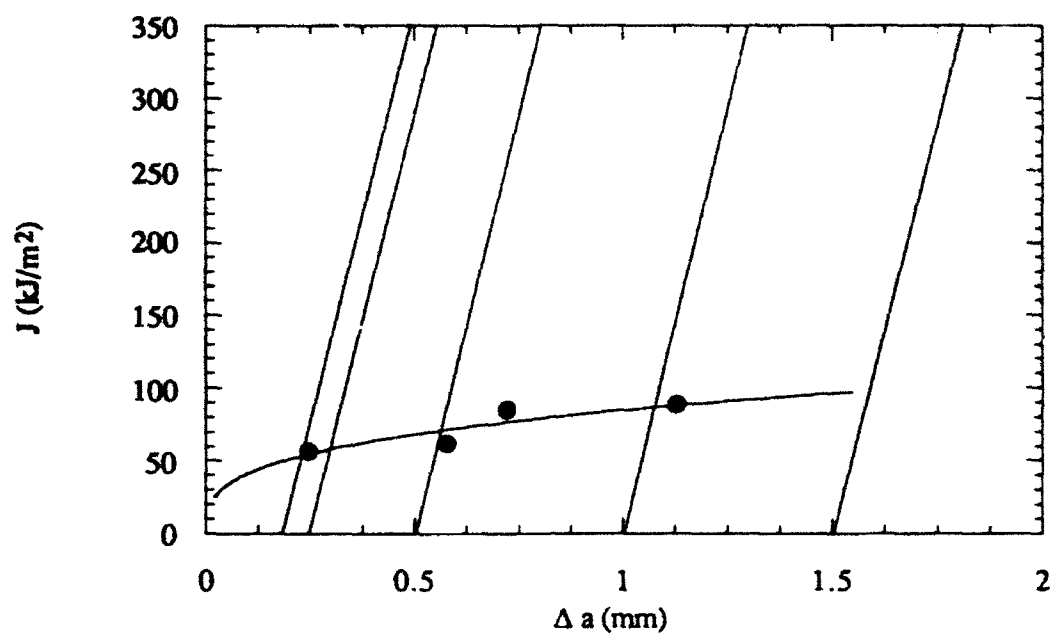


Figure 4.31 J vs. Δa plot for microstructure 0/F, 450°C

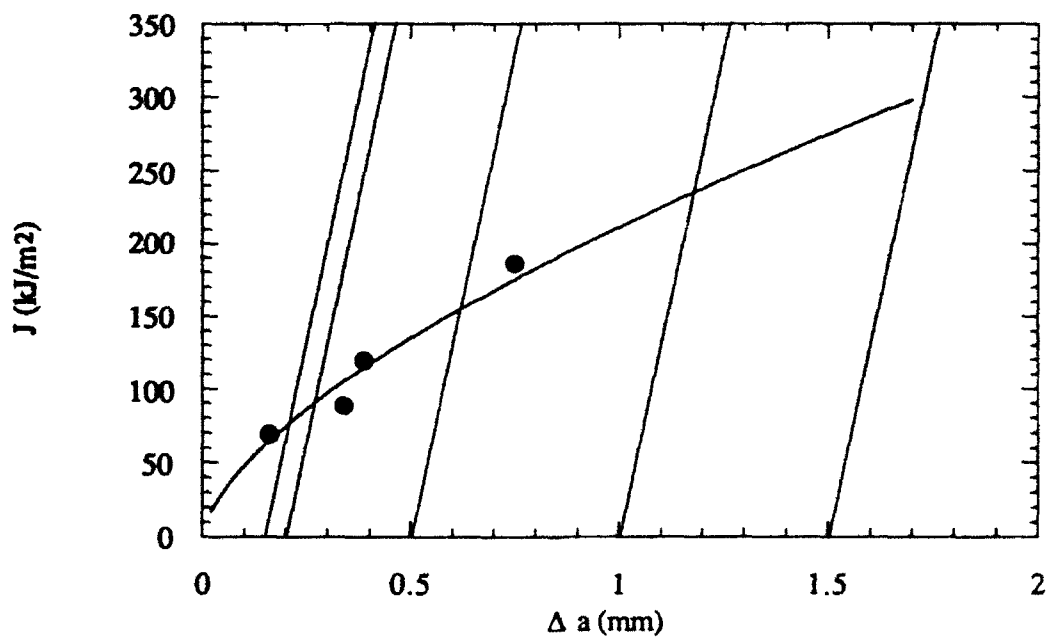


Figure 4.32 J vs. Δa plot for microstructure 0/F, 550°C.

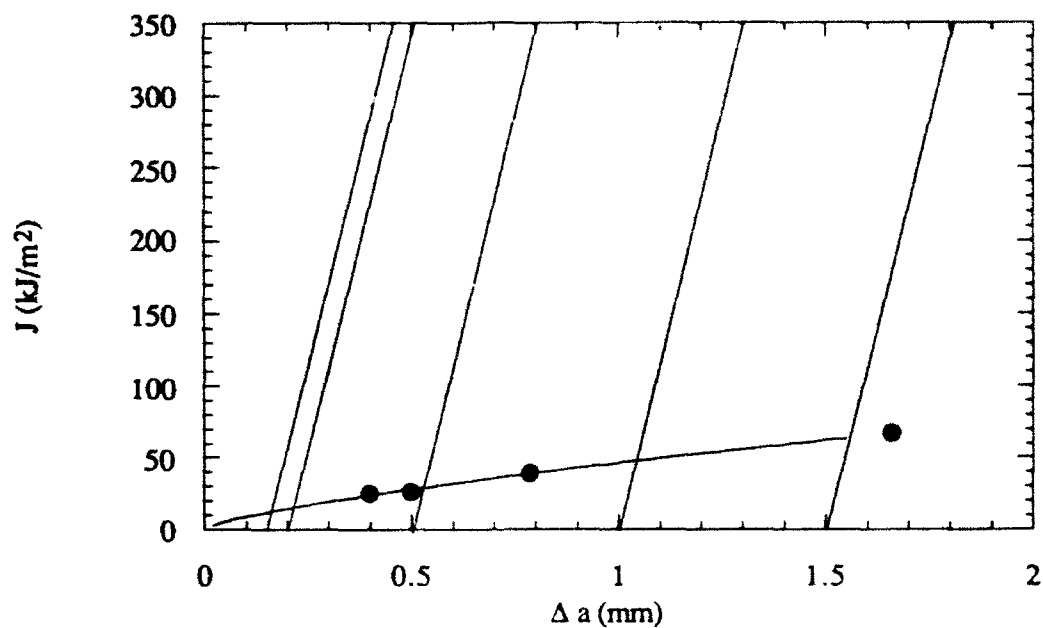


Figure 4.33 J vs. Δa plot for microstructure 0/F, 650°C.

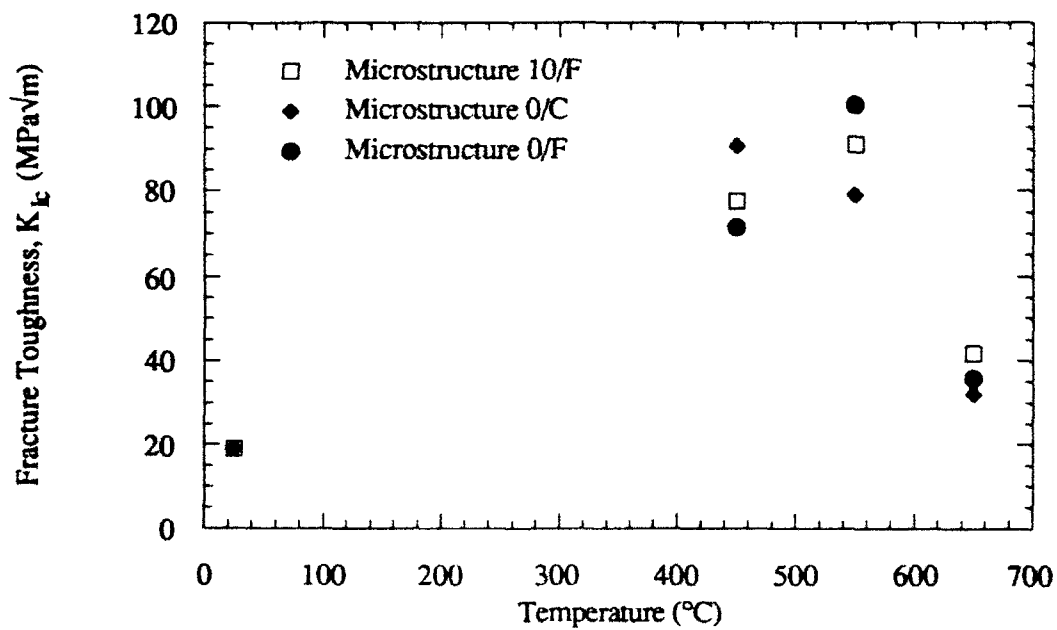


Figure 4.34 Combined fracture toughness data for all three microstructures.

4.3 Fractography

4.3.1 Room Temperature Tensile Specimens

SEM fractography of the room temperature tensile specimens showed in all cases that failure occurred in a brittle mode. By following the river markings on the fracture surface, the point where initiation occurred was located. Not all microstructures exhibited a clear initiation site. However, such was the case in microstructure 10/C, where Figure 4.35 gives a macroscopic view of the fracture surface. Closer examination in the region of convergence of the river markings showed a flat region which extended over an approximately 200 μm diameter area, Figure 4.36. Sectioning of these samples, to be discussed shortly, showed that the fracture features observed in this region were associated with many similarly oriented secondary α_2 laths with primary α_2 particles mixed throughout. Magnification of the fracture features revealed sharp tear ridges, associated with the B2 phase, between the α_2 laths, and river markings on the secondary and primary α_2 particles, Figure 4.37. Examination of the other microstructures showed similar microstructural correlation to fracture features, with microstructures having a fine secondary α_2 lath structure exhibiting a finer appearance, Figure 4.38.

Application of the 12 μm grid on the flat tensile bars was successful enough to provide useful results. Although the coverage of the gage length was variable. When problems arose they were because the tensile bars were not completely flat. In such cases, the glass mask did not make good contact with the surface of the specimen and the pattern was not completely transferred. SEM revealed interesting results from the flat tensile bars after room temperature tensile testing, most due just to the fact that the surface of the specimen was pre-polished. Distortions in the grid indicated the scale of deformation on the surface and the spatial distribution of strain. These local deformation observations can be described in two ways: (1) dislocation slip bands interacting with the grid pattern; (2) the

macroscopic effect of slip on causing larger distortions to the pattern. Local tensile strains measured for one sample, microstructure 25/F, ranged up to $\epsilon = 0.5$ in one 12 μm box, with no indication of failure, Figure 4.39. A box adjacent to this, however, contained a crack at a primary α_2 particle/matrix interface which apparently occurred at a much lower local strain.

SEM observation of the flat tensile bars revealed differences in crack initiation sites amongst the various microstructures. Starting with the coarse secondary α_2 lath structure in a β processed material, microstructure 0/C, slip bands and slip band intersections on the specimen's surface were profuse with some of these intersections resulting in crack nucleation, Figure 4.40. These slip bands were approximately 60 μm long in the coarse secondary α_2 microstructures. Additionally, there was also occasional evidence of shear crack nucleation. Cracks were also observed to occur at prior β grain boundaries within the grain boundary α_2 , Figure 4.41.

With a small addition of primary α_2 , 0.10 volume fraction, in a coarse secondary α_2 matrix (microstructure 10/C) some of the surface cracking observed was associated with the primary α_2 grains. Slip bands in the matrix were often times seen to have intersected with a failed primary α_2 particle, Figure 4.42. However, a large proportion of cracks observed on the surface were still caused by slip line intersections. Increasing the volume fraction of primary α_2 to 0.25 while maintaining a coarse secondary α_2 size, as in microstructure 25/C, still resulted in long slip lines being a prominent feature on the specimen's surface. However, a greater proportion of cracks were observed to be nucleating at or within primary α_2 grains than at slip band intersections. The slip bands in microstructures 25/C and 10/C were shorter than in microstructure 0/C, measuring approximately 40 μm in length.

In the fine Widmanstätten microstructure containing 0.25 volume fraction primary α_2 (microstructure 25/F) the initiation sites were almost exclusively associated with primary α_2 grains. Crack initiation was observed to occur within the individual grains, as

in Figure 4.43, or at the primary α_2 /matrix interfaces, as in Figure 4.44. The failed interface at the primary α_2 particle had a dimpled appearance in Figure 4.44, consistent with the localized plastic strains observed. Primary α_2 particles associated with interfacial failure typically displayed slip band intersections with the perimeter of the particle at the point of failure, Figure 4.45. In some cases, as in Figure 4.45, small steps at the interface, presumably caused by slip band intersection with the particle surface, were evident. Cracks within the primary α_2 grains appeared to be nucleated by two mechanisms. First, some cracks were observed to lie along the operating slip planes and were not necessarily oriented perpendicular to the stress axis, as in Figure 4.43. The second case found cracks nucleating normal to the stress axis, Figure 4.46. This particular instance could be evidence of a crack in a slip plane oriented at a 45° angle to the surface of the specimen, or in a plane normal to the tensile axis upon which no slip would have been expected to occur. The steps observed on the free surfaces of these failed primary α_2 particles appear to be a cross section of the river markings seen on the fracture surface.

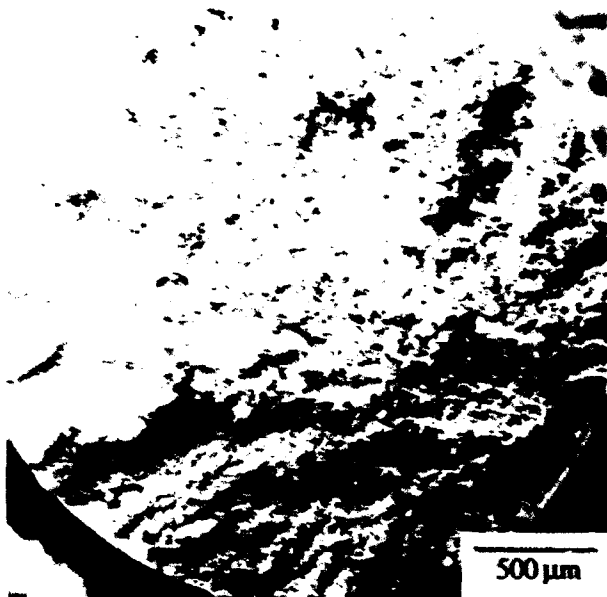


Figure 4.35 Room tensile fracture surface of microstructure 10/C.

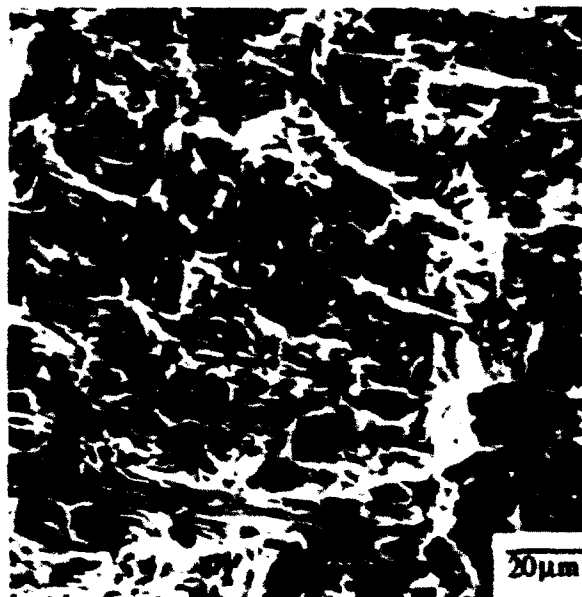


Figure 4.36 Initiation region in sample shown in Figure 4.35.



Figure 4.37 Magnification of Figure 4.36.

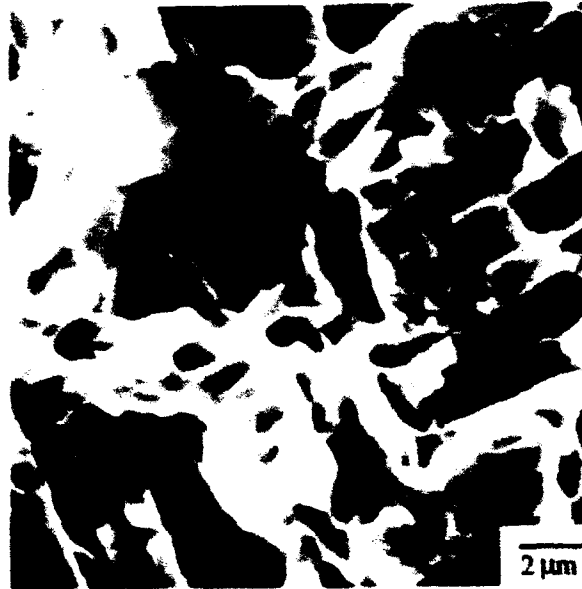


Figure 4.38 Fracture surface of a room temperature tensile specimen from microstructure 10/F.

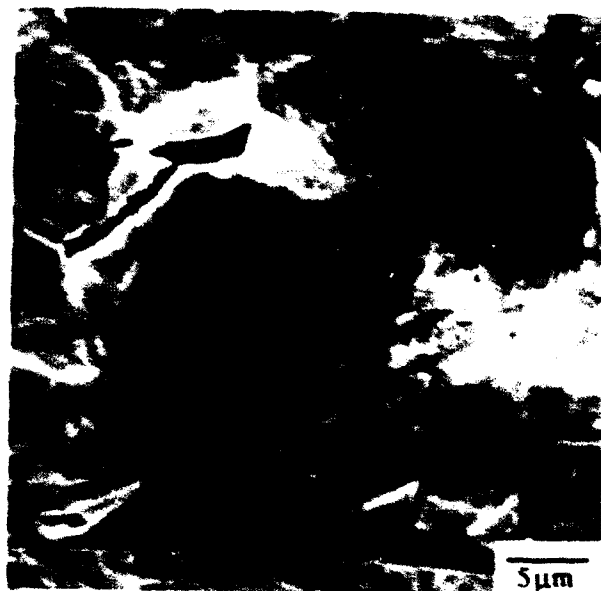


Figure 4.39 Surface of the strained flat tensile specimen from microstructure 25/F.



Figure 4.40 Flat tensile specimen surface from microstructure 0/C. Crack nucleation occurring at slip band intersections.

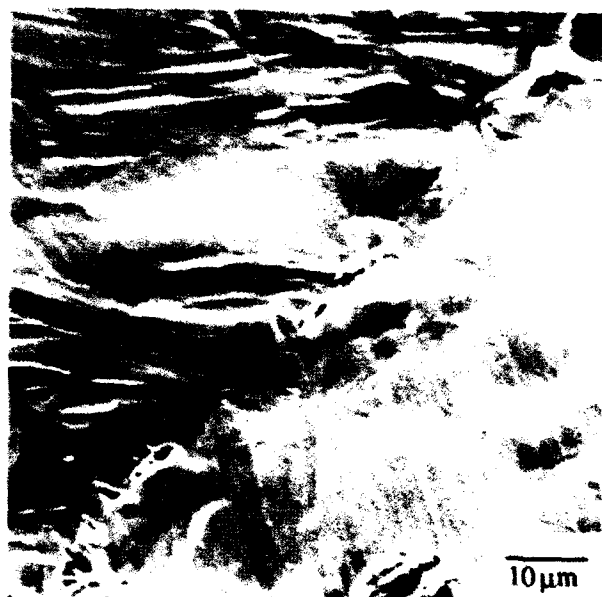


Figure 4.41 Flat tensile specimen surface from microstructure 0/C. Cracking across adjoining prior β grain boundaries.

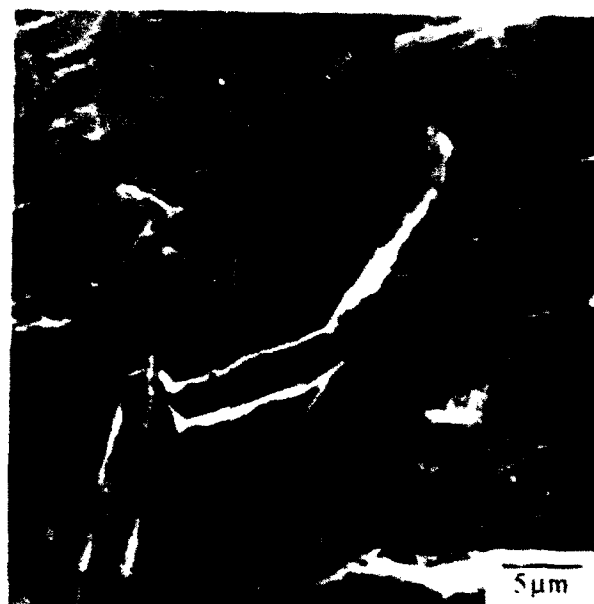


Figure 4.42 Flat tensile specimen surface from microstructure 10/C. Matrix slip band intersection with a failed primary α_2 grain.



Figure 4.43 Flat tensile specimen surface from microstructure 25/F. Crack nucleation along slip bands in primary α_2 grain



Figure 4.44 Flat tensile specimen surface from microstructure 25/F. Crack nucleation at interface of primary α_2 grain and matrix.



Figure 4.45 Flat tensile specimen surface from microstructure 10/F. Slip band intersections with the α_2 /matrix interface.

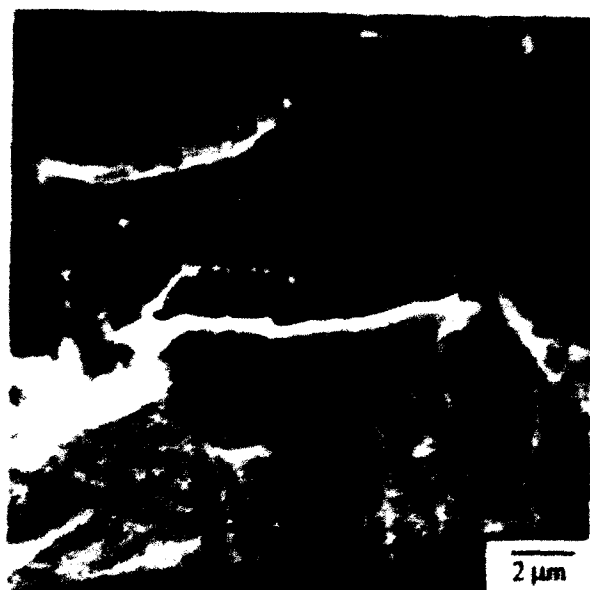


Figure 4.46 Flat tensile specimen surface from microstructure 25/F. Crack nucleation normal to tensile axis within a primary α_2 grain.

Metallographic sectioning of the tensile bars longitudinal to their gage length helped to correlate features observed on the fracture surfaces with the underlying microstructure. Four fracture features were of particular interest. First was the brittle failure of the secondary α_2 laths. The appearance of these features on the fracture surface directly correlated with their metallographic appearance in the underlying microstructure, Figure 4.47. Similarly, a one to one correspondence between the B2 phase and the ductile tear ridges pulling up around the secondary α_2 laths can be seen in this same figure. The intersections of failed primary α_2 particles were likewise easily seen in cross section, leaving a nearly circular and flat feature on the fracture surface. The final feature was ductile dimpling observed at room temperature. In Figure 4.48 it can be seen that this feature occurred in the failure of a prior β grain boundary. This gave a similar appearance to that seen in the interfacial failure between a primary α_2 grain and the matrix, Figure 4.44.

Sectioning of the failed tensile specimens also revealed similar crack nucleation sites to those observed on the surface of the pre-polished tensile bars. This result helps validate and generalize the surface observations noted previously. Figure 4.49 shows crack nucleation at the primary α_2 /matrix interfaces as well as within the primary α_2 particles in microstructure 10/C. A particularly interesting crack, which was initiated at a primary α_2 /matrix interface, is shown in Figure 4.50. The length of this crack was measured to be approximately 70 μm long. The crack appeared to propagate by following an apparent sub-boundary at the base of an aligned region of secondary α_2 laths. The "boundary" was described by the secondary α_2 /B2 interfaces at the tips of the α_2 laths. The crack became deflected at one point where it was forced to go through secondary α_2 laths by cleaving the laths along a plane very near the orientation of the basal plane. The crack became re-oriented near its tip and was finally arrested at a region of B2 phase backed by a secondary α_2 lath lying perpendicular to the crack path, Figure 4.51. Note what appears to be a plastic zone surrounding the crack tip.

Figures 4.52 and 4.53 show crack nucleation associated with grain boundary α_2 and the aligned α_2 laths at prior β grain boundaries in microstructure O/C. The crack in Figure 4.52 is approximately 60 μm in length. An enlargement of the crack tip region in Figure 4.52 reveals the process by which the crack must be propagating, Figure 4.53. As above, the α_2 laths failed along a plane very close to the basal plane. Furthermore, the B2 phase was observed to be pulled up around the α_2 laths as if it had behaved as a plastic bridge or ligament during crack extension.

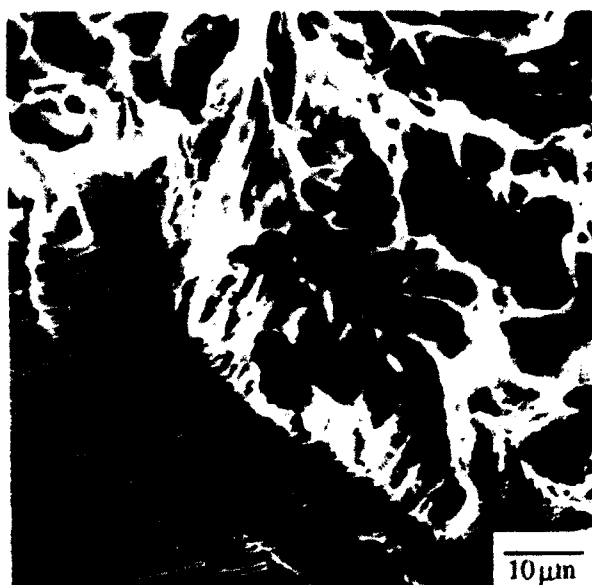


Figure 4.47 Sectioned tensile specimen from microstructure 10/C.

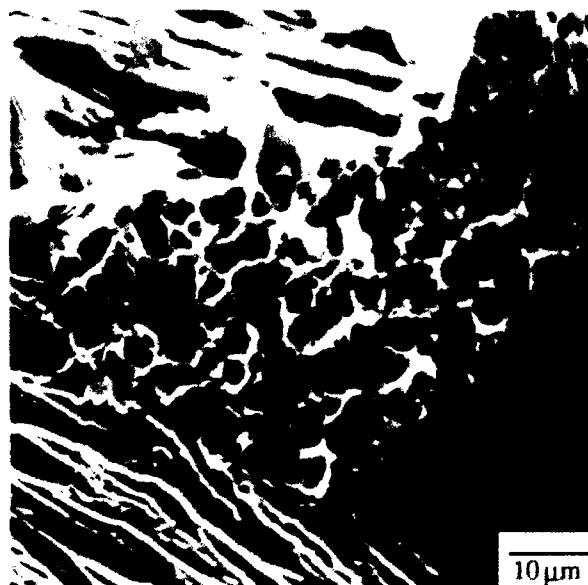


Figure 4.48 Sectioned tensile specimen from microstructure 0/C.

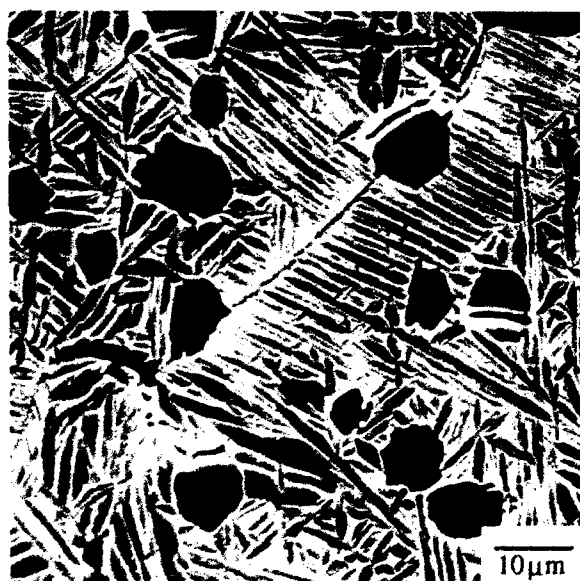


Figure 4.49 Sectioned tensile specimen from microstructure 10/C. Crack nucleation within primary α_2 grains and at primary α_2 /matrix interfaces.



Figure 4.50 Sectioned tensile specimen from microstructure 10/C. Crack nucleation at primary α_2 /matrix interfaces and extension into the matrix.



Figure 4.51 Sectioned tensile specimen from microstructure 10/C. Enlargement of crack tip from Figure 4.50; note the apparent plastic region at the crack tip.



Figure 4.52 Sectioned tensile specimen from microstructure 0/C. Crack nucleation associated with the prior β grain boundary.



Figure 4.53 Sectioned tensile specimen from microstructure 0/C. Enlargement of crack tip region in Figure 4.52.

4.3.2 Elevated Temperature Tensile Specimens Tested in Vacuum

Examination of the round elevated temperature tensile specimens using SEM revealed that all of the microstructures exhibited a gage length that was free from circumferential cracking. Flat tensile bars exhibited surface cracking only when the bar had been tested in a helium atmosphere. Additionally, shear lips were present on all of the specimens throughout the temperature range studied.

Macroscopic examination of the failed tensile bars from microstructure 10/F shows that failure propagation in the center of the specimens occurred transgranularly in a relatively smooth manner in the temperature range 450-600°C, Figure 4.54. Additionally, failure appeared to have initiated at the prior β grain boundaries at 450, 500 and 550°C, Figure 4.55. The fracture surface at these grain boundaries exhibited a dimpled structure, Figure 4.56. Closer examination in the fast fracture region at the center of the specimens showed a bimodal distribution of features. Large, 7-10 μm diameter, flat regions were surrounded by much finer dimples, averaging 1 μm , Figure 4.57. No significant change in these features was observed in the temperature range 450-600°C. As temperature was increased to 650°C, however, the fracture surfaces at the center of the specimens deviated from a flat surface, becoming more ductile in appearance, Figure 4.58. Additionally, a single failure initiation site was not evident. Both the large flat regions and fine dimples seen below 650°C were no longer present. Now, large and relatively uniformly spaced dimples were the primary feature on the fracture surface, Figure 4.59. These dimples grew more well defined and uniformly spaced as the temperature approached 750°C, Figure 4.60. The sides of the dimples also became less smooth and took on a more textured appearance at 750°C, Figure 4.61.

SEM examination of microstructure 0/F showed that it behaved quite similarly to microstructure 10/F, exhibiting failure initiation associated with prior β grain boundaries at 450 and 550°C. A very fine dimple structure was also present at these initiation sites. The center of the specimen was also similar in appearance to microstructure 10/F. However,

there was an absence of the 7-10 μm flat features, resulting in a more uniformly distributed fine dimple structure. Again following the trend observed in microstructure 10/F at 650°C, the fracture surface in microstructure 0/F became less flat and more ductile in appearance than at the lower temperatures. Initiation appeared to be associated with an inclined prior β grain boundary at this temperature, Figure 4.62. The center of the specimen exhibited larger voids mixed with the fine dimples, Figure 4.63. The large voids, $\sim 5 \mu\text{m}$ diameter, became more prominent at 750°C with no evidence of finer voids. Some voids much larger in size, $\sim 20 \mu\text{m}$, were also observed on the fracture surface. The size of the more numerous voids at 750°C was approximately half the void size observed in microstructure 10/F, Figure 4.64.

Microstructure 0/C consistently showed failure initiation associated with prior β grain boundaries for all temperatures examined. However, the source of initiation changed with temperature. In the range 450-600°C, brittle failure was observed across prior β grain boundaries, Figure 4.65. At 650°C and above, a dimpled intergranular failure occurred along the prior β grain boundaries, Figure 4.66.

Metallographic sectioning of tensile specimens from microstructure 10/F revealed that the primary α_2 grains had undergone significant deformation in the necked region as evidenced by their elongated appearance in the direction of the tensile axis, Figures 4.67 and 4.68. Limited instances of void nucleation at the primary $\alpha_2/\text{B2}$ interfaces at the tops of the deformed particles were found a short distance, up to 200 μm , below the fracture surface, Figure 4.67. Primary α_2 particles were also observed to fail by cracking, generally at an inclined angle to the tensile axis, Figure 4.68. While relatively rare at 450°C, the occurrence of both of these failure modes increased slightly with increasing temperature up to 600°C. At 650°C, however, the volume fraction of voids nucleating at the primary $\alpha_2/\text{B2}$ interfaces increased dramatically, Figure 4.69. A number of the voids had also started to coalesce, Figure 4.70. The volume fraction of voids, depth below the fracture surface, and extent of coalescence were all increased at 750°C, Figure 4.71. Little evidence of primary α_2 cracking could be found at this temperature.

Microstructure 0/F again gave similar results in examination of tensile sectioning to microstructure 10/F. At both 450 and 550°C no voids were observed below the fracture surface. Only very limited amounts of cracking were observed and were located within several microns below the fracture surface. However, voids were present at 650°C in relatively large numbers, Figure 4.72. These voids were found to nucleate primarily along the prior β grain boundaries, the boundaries in this microstructure were oriented parallel to the tensile axis. Void nucleation was also observed between dissimilarly oriented packets of aligned secondary α_2 laths. The specimen at 750°C exhibited a far larger volume fraction of voids that had begun to coalesce, Figure 4.73.

Microstructure 0/C exhibited very little cracking below the fracture surface at 450°C. At 500, 550 and 600°C, larger numbers of cracks were observed below the fracture surfaces. These were associated with dissimilarly oriented packets of aligned secondary α_2 laths or with prior β grain boundaries, to which they were oriented perpendicularly and approximately normal to the tensile axis, Figure 4.74. In both cases the cracks appeared to form along the α_2/β_2 interfaces, Figure 4.75. No instances of cracked α_2 laths below the fracture surface were observed between 500 and 600°C. At 650°C a few cracks were found below the fracture surface. Those seen were generally formed along prior β grain boundaries lying approximately normal to the tensile axis, Figure 4.76. Nucleation of these cracks appeared to have been initiated at prior β grain triple points. These were again created by the separation of α_2/β_2 interfaces, and appeared to be associated with the secondary α_2 laths, Figure 4.77. Examination of the specimens at 700°C and 750°C shows that large cracks are formed at the prior β grain boundaries, Figure 4.78, as well as at packets of aligned α_2 lying roughly normal to the tensile axis.

Observation of the pre-polished flat tensile bar surfaces confirmed the observations made in sectioning of the round tensile bars regarding nucleation sites for failure. Slip on the specimen surface was generally finely dispersed in the $\alpha_2+\beta$ processed microstructures, and finer still in the fine secondary α_2 microstructures. In the $\alpha_2+\beta$ processed microstructures, slip bands in the matrix intersecting with primary α_2 particles

appeared to provide the nucleus for void formation at the interface, Figure 4.79. Microstructure 0/F showed intense slip bands intersecting with the prior β grain boundaries, Figure 4.80. The intersections of these slip bands with the boundaries resulted in crack nucleation. Slip bands also intersected the prior β grain boundaries in microstructure 0/C, Figure 4.81. Since the prior β grains are more equiaxed than in microstructure 0/F, they present more grain boundary area oriented normal to the tensile axis. After crack nucleation in microstructure 0/C, the cracks were seen to spread along the prior β grain boundaries.

The grid pattern was very difficult to distinguish on the surface of the specimens tested at elevated temperature. This appears to be due to the effects of elevated temperature exposure. Whether this results in a thin oxide layer which acts to mask the grid, sublimation from the surface in vacuum, or inward diffusion has sufficiently blurred the grid lines is uncertain.

Measurements of deformation in the primary α_2 particles near the fracture surface were made using the sectioned tensile bars. An example of strained primary α_2 particles is shown in Figure 4.68. The average particle height dimensions after deformation were translated to true strain values using the original spherical diameter of the primary α_2 particles. The results are presented in Figure 4.82. The error bars on the plot represent a 95% confidence level. The true strain of the primary α_2 particles increased with temperature to 550-600°C. After this, the strain in the primary α_2 particles decreased with increasing temperature, even though the true fracture strain continued to increase.

The locations of void nucleation were also measured below the fracture surface. The cross-sectional area corresponding to the location of the void furthest from the fracture surface was then used to calculate a true strain for void nucleation. The void nucleation strain, ϵ_{nuc} , is compared to the true strain to failure, ϵ_f , in Figures 4.83-4.85. At temperatures where only one point is shown, no voids were observed to lie at significant distances below the fracture surface, i.e. $\epsilon_{\text{nuc}} = \epsilon_f$. Microstructures 10/F and 0/F both display a ϵ_{nuc} value of approximately 0.6, which is nearly independent of temperature. The

exception is at 750°C in microstructure 10/F where one point is observed to lie at a much lower ϵ_{nuc} , this is associated with a specimen tested at the low strain rate. The ϵ_{nuc} value in microstructure 0/C was not constant and followed the same trend as that of ϵ_f .

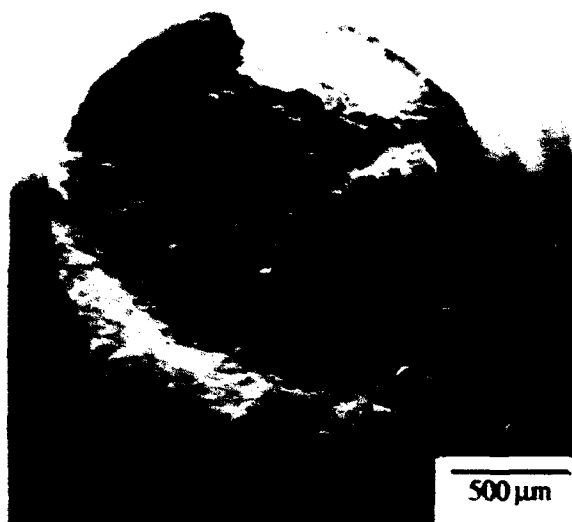


Figure 4.54 Round tensile specimen from microstructure 10/F tested at 450°C.



Figure 4.55 Tensile specimen from microstructure 10/F tested at 450°C. Near apparent initiation site at prior β grain boundary.

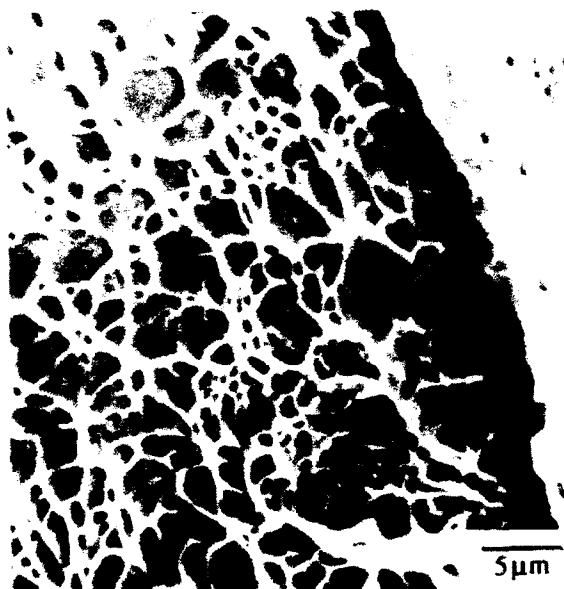


Figure 4.56 Enlargement of the prior β grain boundary area in Figure 4.55 showing fine dimples associated with the initiation site.

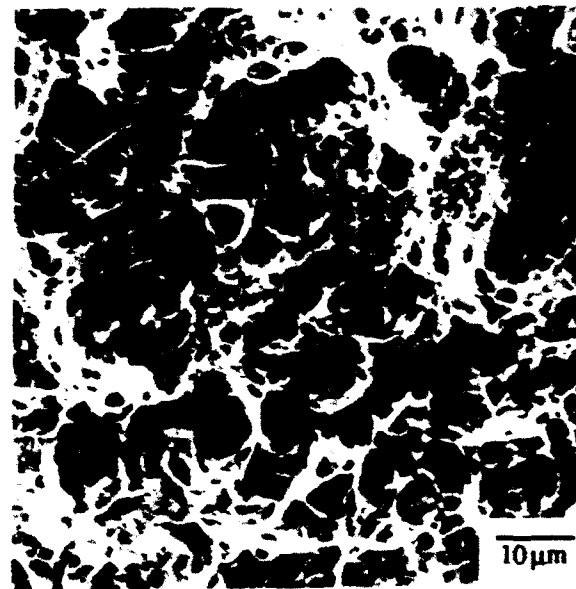


Figure 4.57 Center of a round tensile specimen from microstructure 10/F tested at 450°C with a duplex distribution of fracture features.



Figure 4.58 Tensile specimen from microstructure 10/F tested at 650°C showing a more ductile appearing fracture surface.

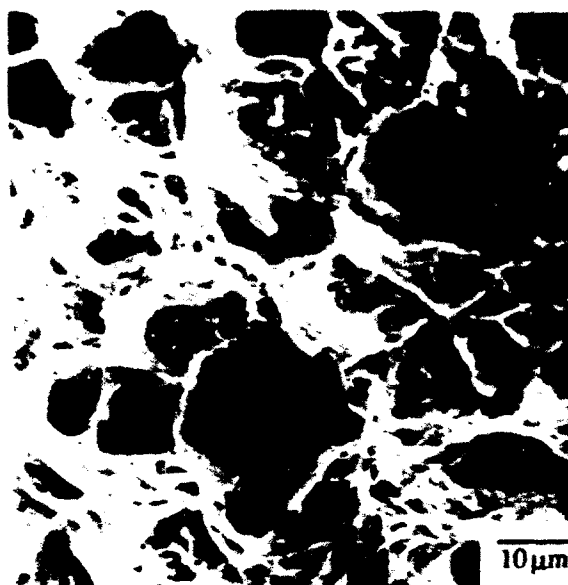


Figure 4.59 Tensile specimen from microstructure 10/F tested at 650°C with larger dimples.

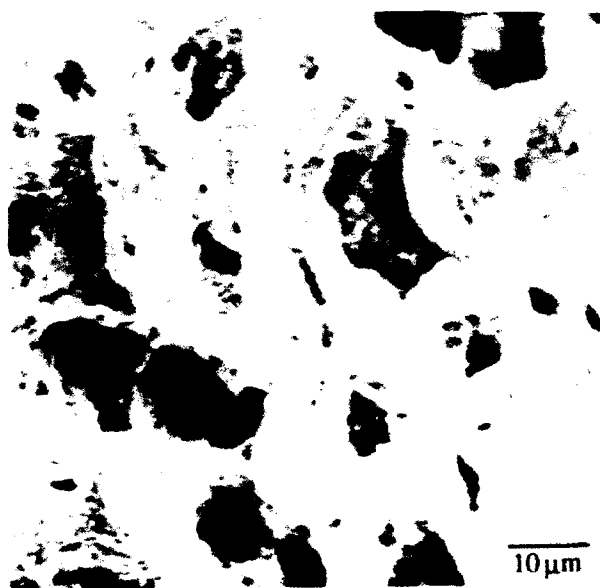


Figure 4.60 Tensile specimen from microstructure 10/F tested at 750°C. Fracture surface has even larger and more uniformly spaced dimples.

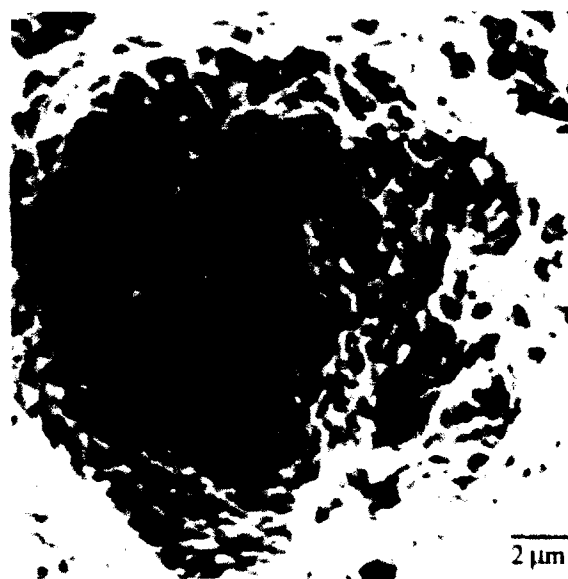


Figure 4.61 Enlargement of the dimple structure in Figure 4.60. Dimples exhibit a textured appearance along their walls.

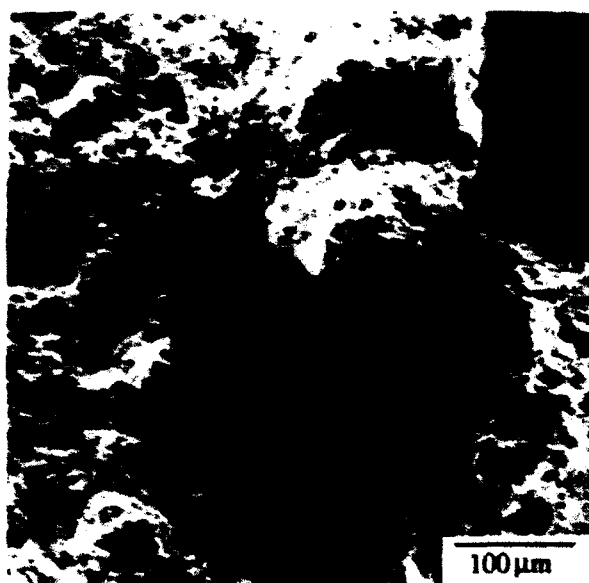


Figure 4.62 Tensile specimen from microstructure O/F tested at 650°C. Region on fracture surface exhibiting failure along an inclined prior β grain boundary.

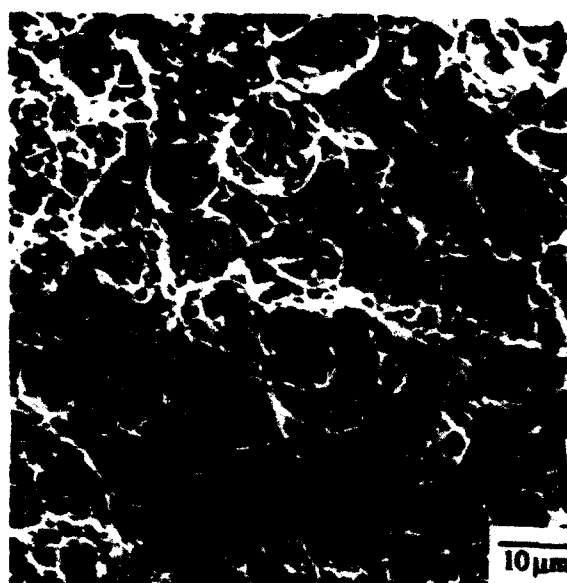


Figure 4.63 Tensile specimen from microstructure O/F tested at 650°C. Fracture surface now exhibits larger dimples mixed with the finer ones seen at lower temperature.

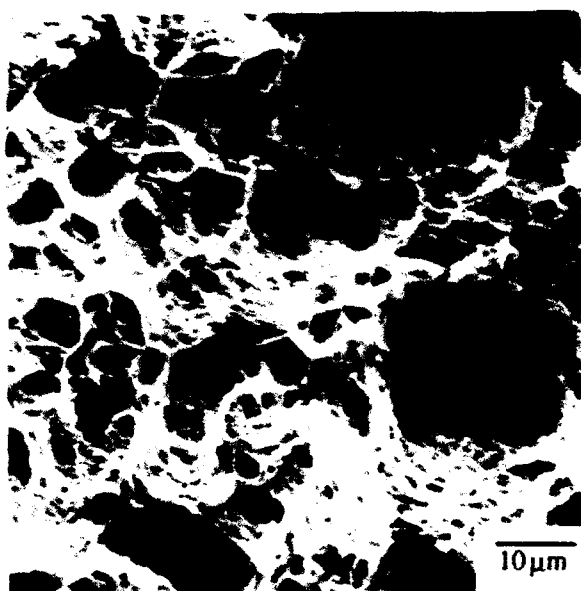


Figure 4.64 Tensile specimen from microstructure O/F tested at 750°C. Dimple size was about half that in microstructure 10/F at the same temperature.

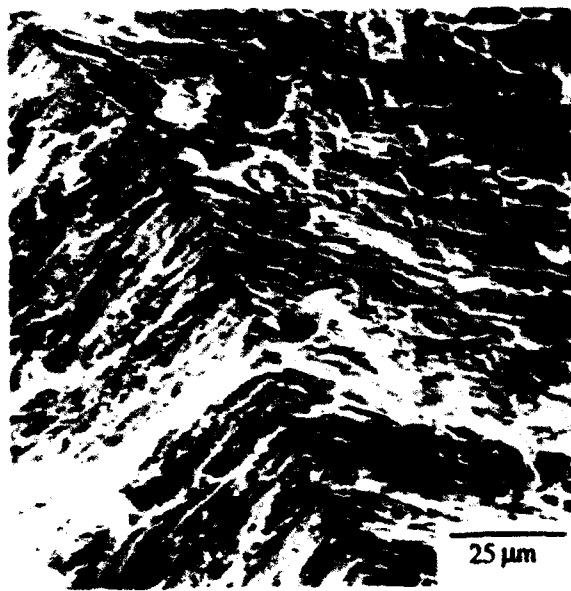


Figure 4.65 Tensile bar from microstructure O/C tested at 450°C. Near the failure initiation site on fracture surface, showing aligned secondary α_2 structure.



Figure 4.66 Tensile bar from microstructure 0/C tested at 700°C. Fracture surface reveals primarily intergranular failure along the prior β grain boundaries.



Figure 4.67 Tensile bar from microstructure 10/F tested at 450°C. Primary α_2 was elongated in direction of the tensile axis, with voids nucleating at ends.

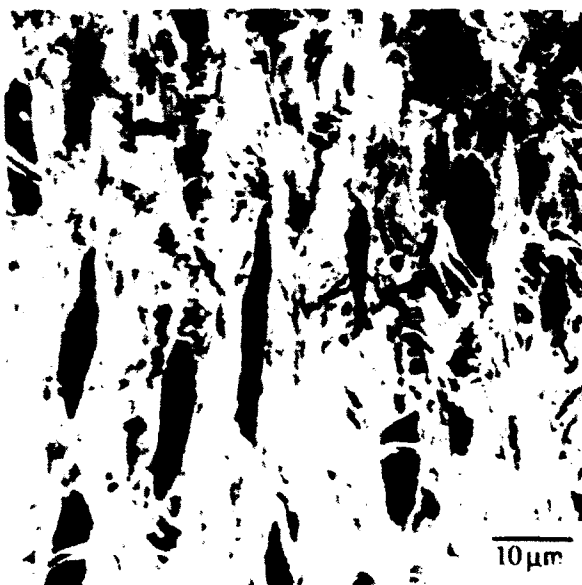


Figure 4.68 Tensile bar from microstructure 10/F tested at 500°C. Primary α_2 grains are observed to fail by cracking along a plane inclined to the tensile stress.

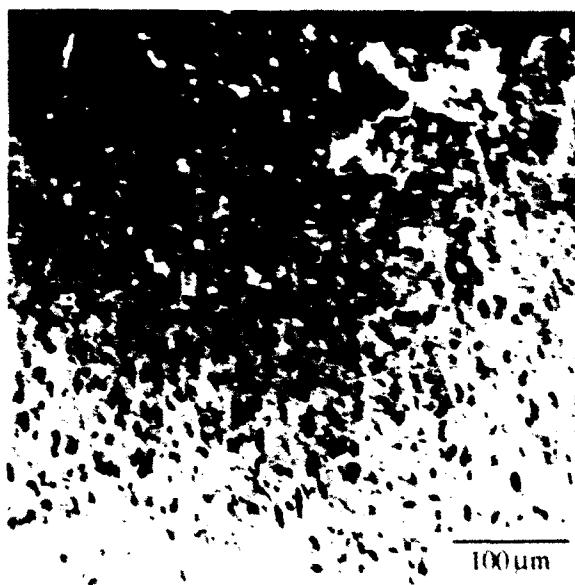


Figure 4.69 Tensile bar from microstructure 10/F tested at 650°C. The fraction of voids has increased dramatically compared to lower test temperatures.

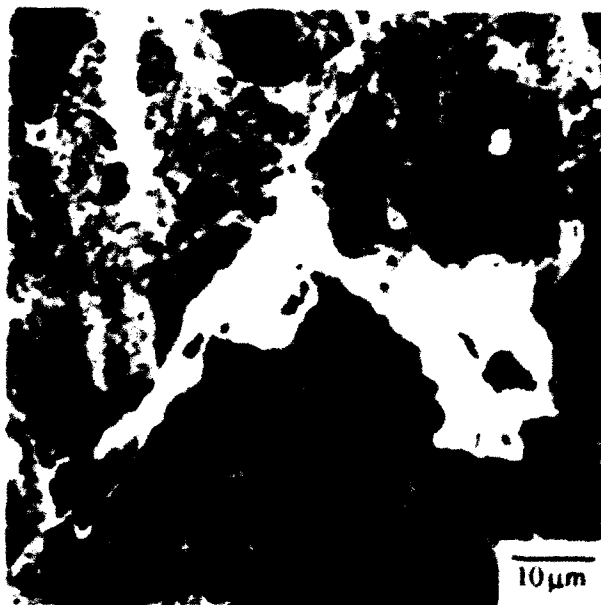


Figure 4.70 Tensile bar from microstructure 10/F tested at 650°C. A number of voids are observed to have coalesced below the fracture surface.

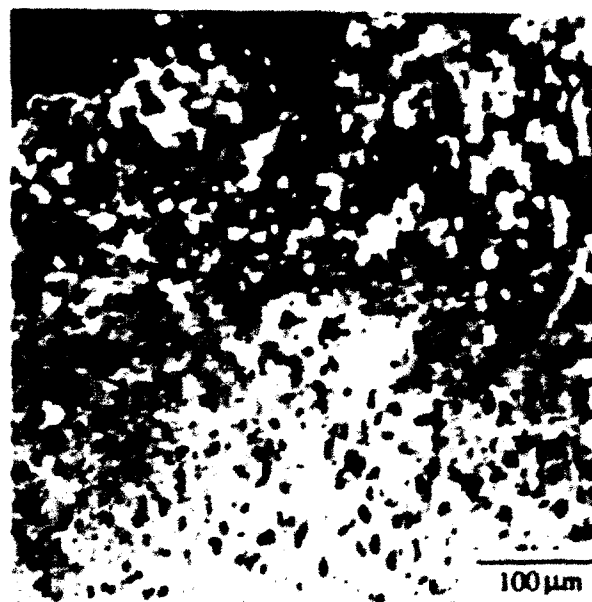


Figure 4.71 Tensile bar from microstructure 10/F tested at 750°C. The volume fraction of voids has continued to rise from 650°C.

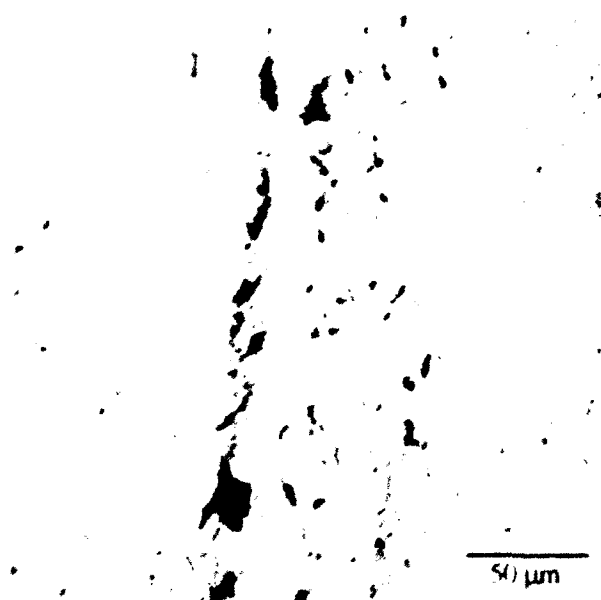


Figure 4.72 Tensile bar from microstructure 0/F tested at 650°C. A large number of voids has nucleated below the fracture surface.

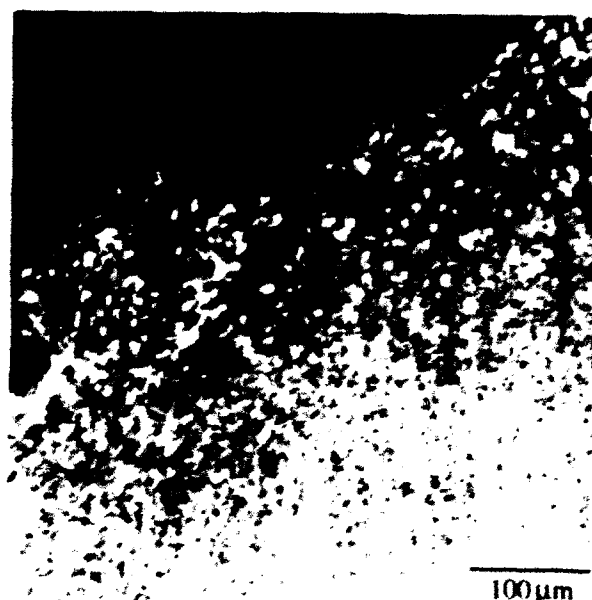


Figure 4.73 Tensile bar from microstructure 0/F tested at 750°C. A much larger volume fraction of voids was present as compared to 650°C.

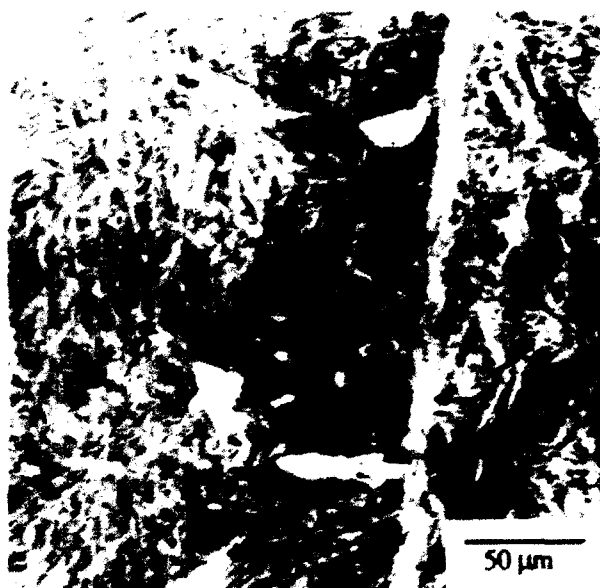


Figure 4.74 Tensile bar from microstructure 0/C tested at 550°C. Cracks nucleated at a prior β grain boundary.

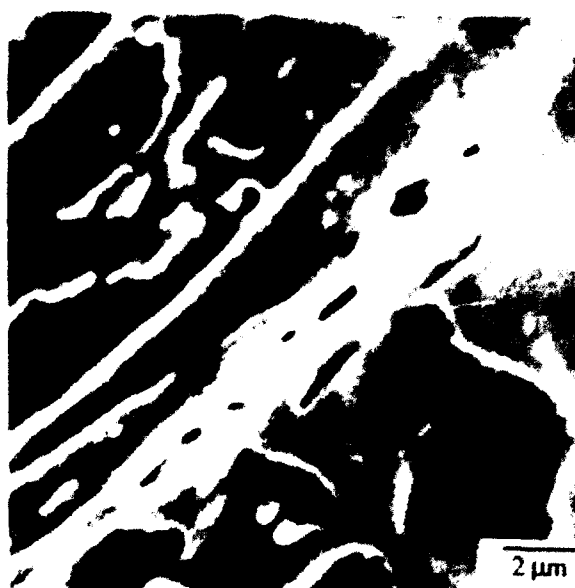


Figure 4.75 Enlargement of cracks in microstructure 0/C tested at 550°C showing that they appear to nucleate at the $\alpha_2/\text{B2}$ interfaces.

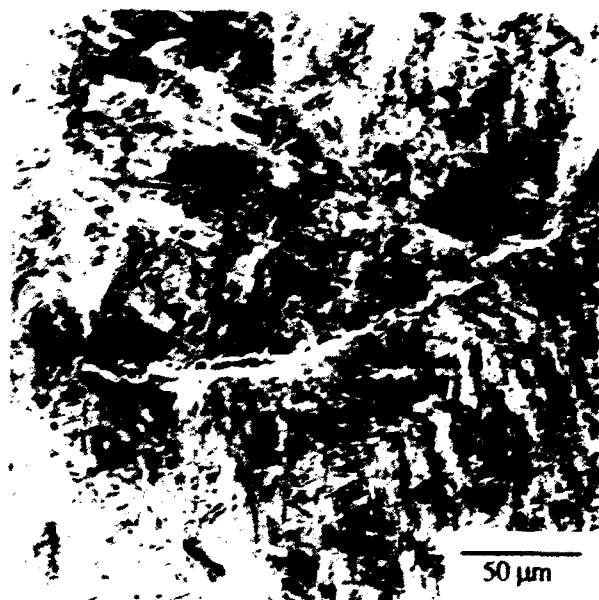


Figure 4.76 Tensile bar from microstructure 0/C tested at 650°C. Cracks nucleate at prior β grain boundaries which are normal to the tensile axis.

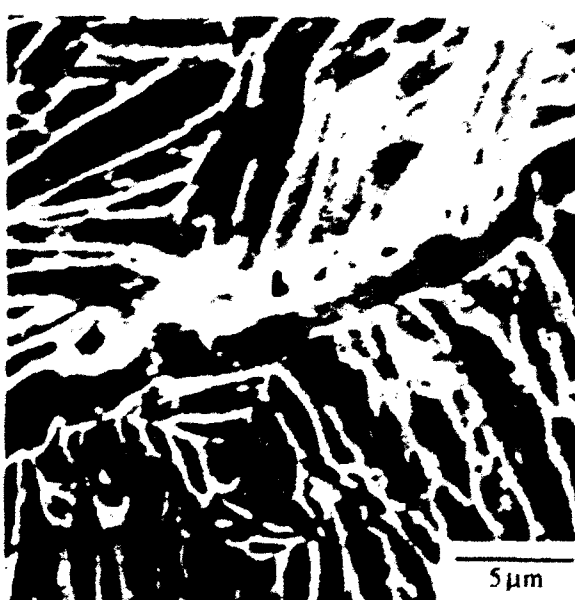


Figure 4.77 Enlargement of cracked region in microstructure 0/C tested at 650°C showing separation of the grain boundary α_2 and B2 interface.

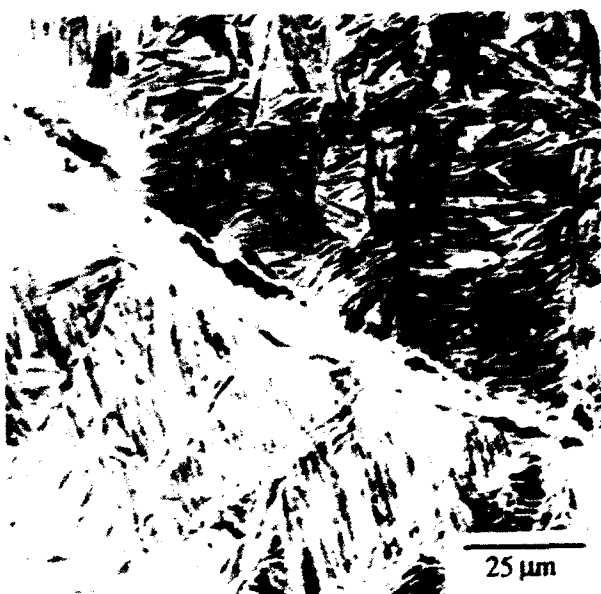


Figure 4.78 Tensile bar from microstructure 0/C tested at 700°C showing separation of the prior β grain boundaries.

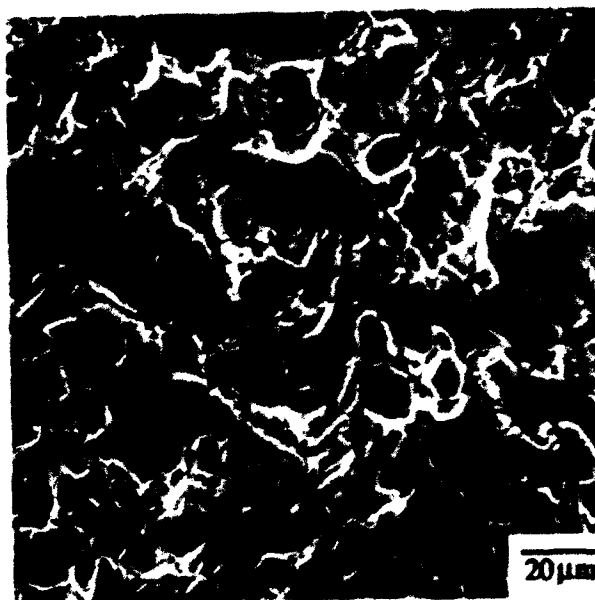


Figure 4.79 Surface of a flat tensile bar from microstructure 10/F at 650°C. Fine slip bands intersect with primary α_2 grains.

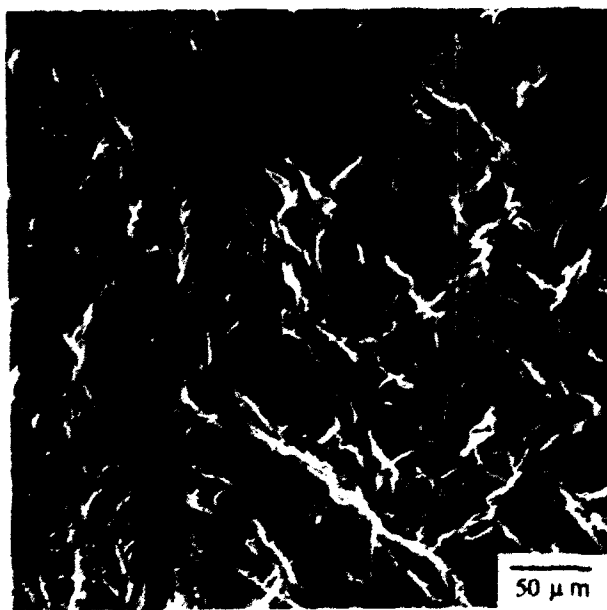


Figure 4.80 Surface of flat tensile bar from microstructure 0/F. Slip band intersections at a prior β grain boundary.



Figure 4.81 Surface of flat tensile bar from microstructure 0/C. Slip band intersections at a prior β grain boundary.

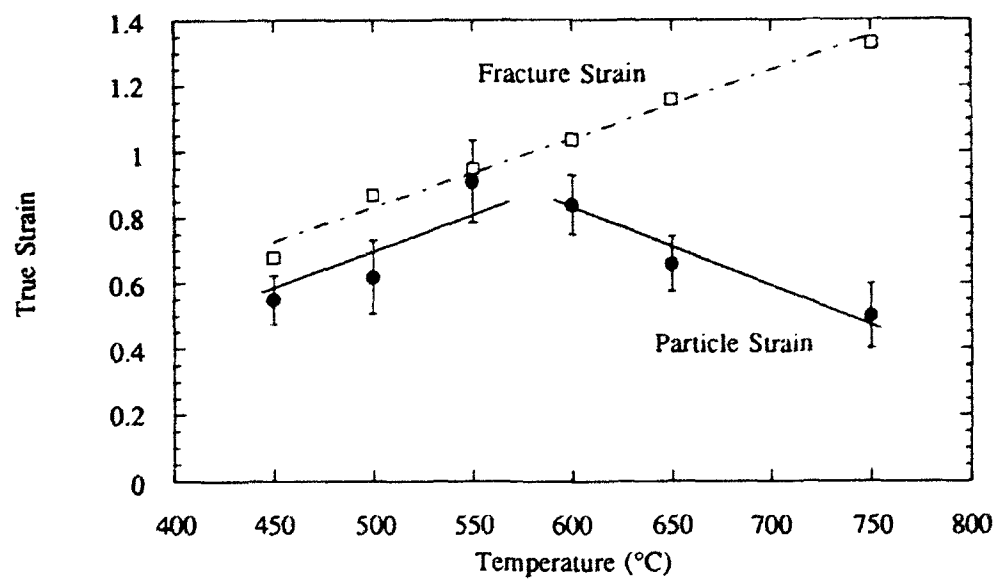
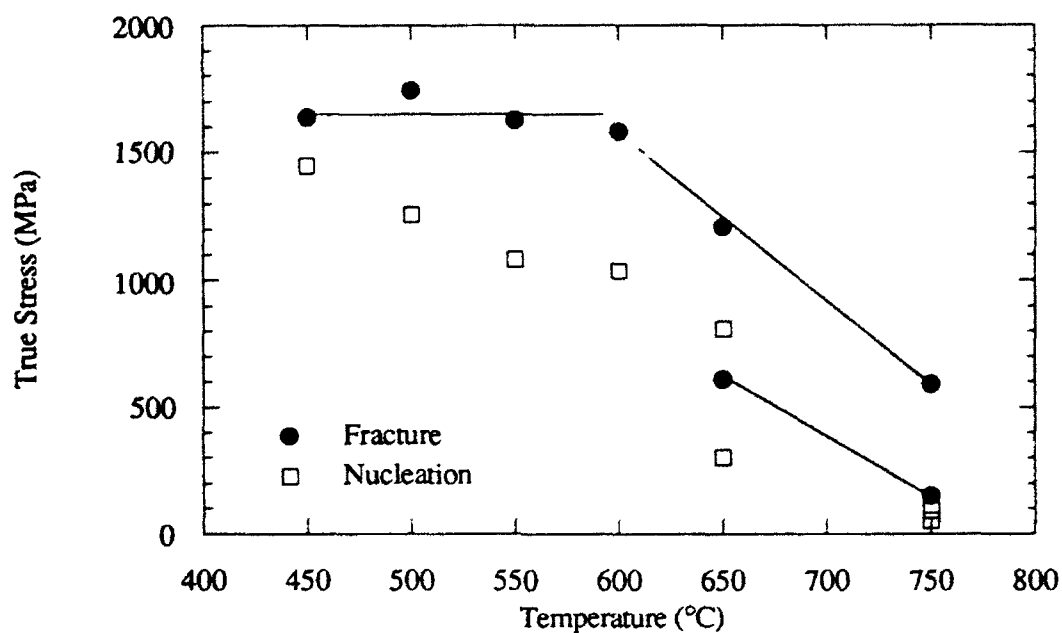


Figure 4.82 True strain to tensile failure and true strain measured in the primary α_2 particles in microstructure 10/F as a function of temperature.

(a)



(b)

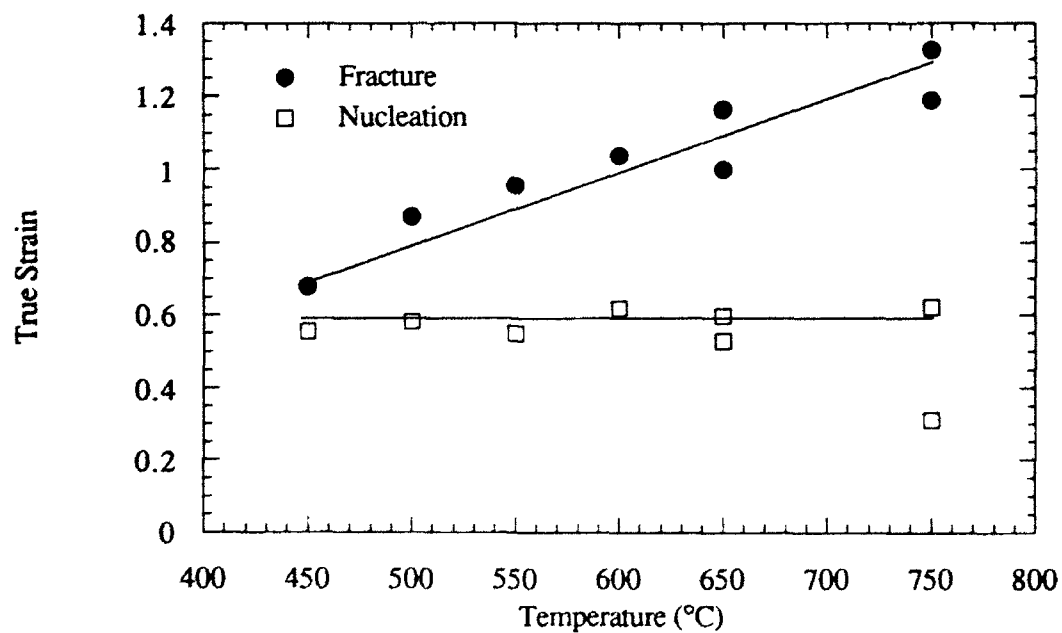
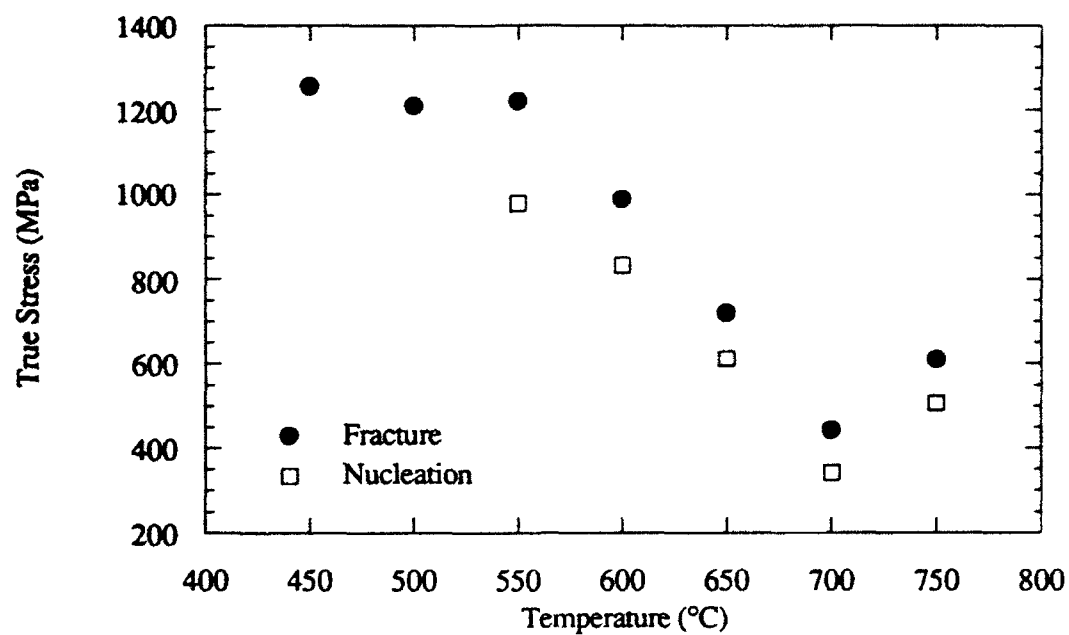


Figure 4.83 (a) True fracture stress and void nucleation stress, and (b) True fracture strain and void nucleation strain plotted as a function of temperature for microstructure 10/F.

(a)



(b)

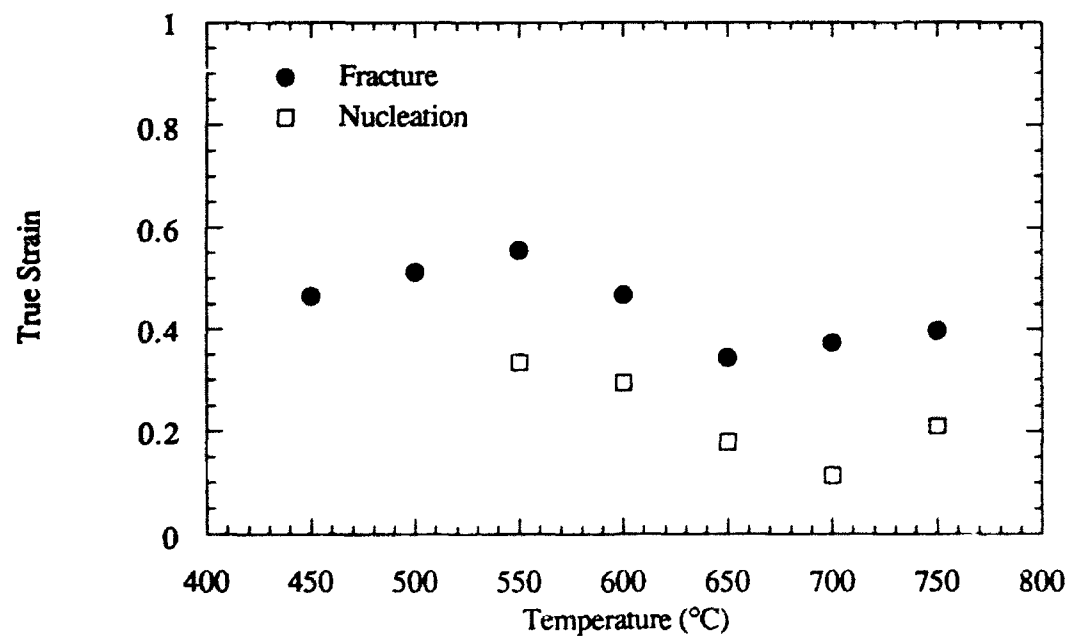
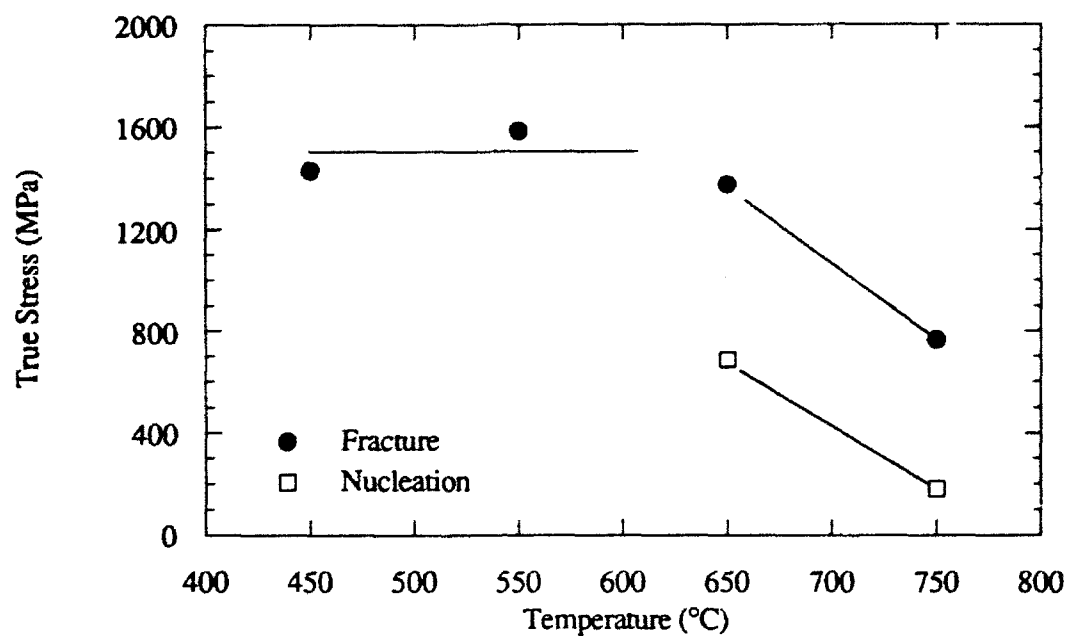


Figure 4.84 (a) True fracture stress and void nucleation stress, and (b) True fracture strain and void nucleation strain plotted as a function of temperature for microstructure 0/C.

(a)



(b)

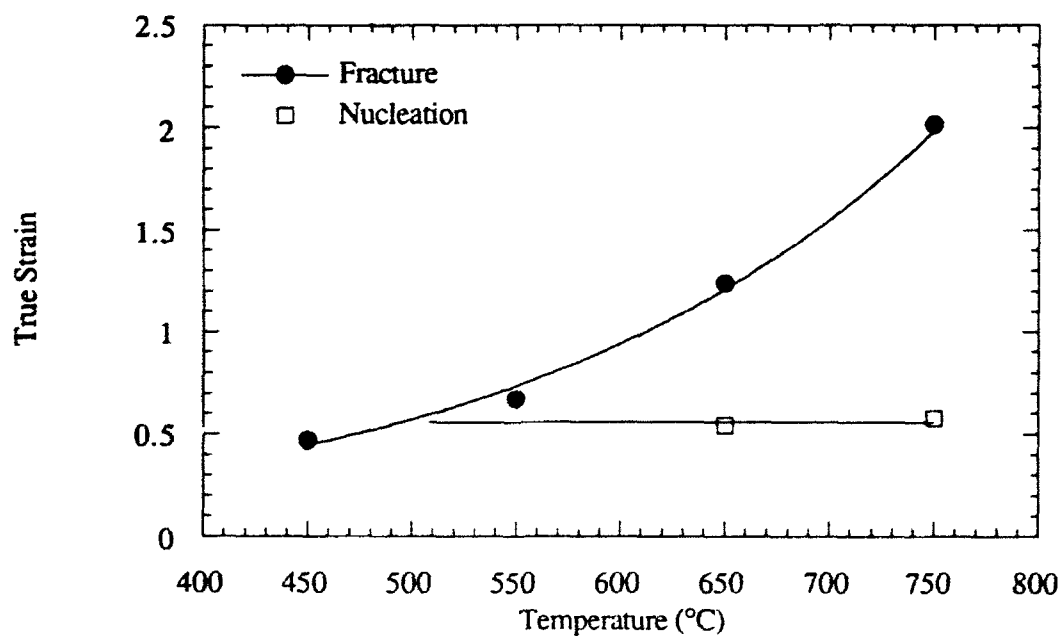


Figure 4.85 (a) True fracture stress and void nucleation stress, and (b) True fracture strain and void nucleation strain plotted as a function of temperature for microstructure 0/F.

4.3.3 Room Temperature Fracture Toughness Specimens

Cross sectioning the fractured compact tension specimens revealed that the macroscopic appearance of the fracture path was relatively flat in all of the $\alpha_2 + \beta$ processed microstructures, Figure 4.86. The fracture path was only slightly more tortuous in the β processed microstructure 0/C, Figure 4.87. Microscopically, crack extension occurs by an apparently low energy mechanism, following a direction which was perpendicular to the long axis of secondary α_2 laths, through primary α_2 particles, and along the interfaces of the $\alpha_2/\text{B2}$ phases. While there were limited instances of secondary cracks, Figure 4.88, in general there were few cracks observed below the fracture surface.

4.3.4 Elevated Temperature Fracture Toughness Specimens

Light macroscopic examination of the fractured specimens reveals that at 450°C the crack front behaved similarly between the three microstructures and propagated smoothly and perpendicular to the stress axis, Figure 4.89. At 550°C the crack front appeared slightly more ragged and inclined to the stress axis, Figure 4.90. At 650°C the crack front had become quite rough, with large protrusions of growth extending from the main crack front, Figure 4.91. The fracture surface of a bend bar of microstructure 0/C tested at 650°C clearly showed failure along the prior β grain boundaries and was reminiscent of the vacuum tensile fracture surface at the same temperature, Figure 4.92.

SEM observation of the fracture surface of microstructure 10/F tested at 450°C did not reveal any more information macroscopically. The fracture surface at low magnification was similar to the fast fracture region in tensile bars from microstructure 10/F tested in vacuum at 450°C. At higher magnification the failed primary α_2 particles were observed to have river markings on their surfaces, Figure 4.93. However, the fracture

surface clearly displayed less of the small ductile dimples seen on tensile fracture surfaces. Similar observations were made for microstructures 0/C and 0/F at this temperature.

At 550°C all of the microstructures exhibited a distinct line across the fracture surface normal to the crack growth direction which appeared to extend as a plane down into the specimen, Figure 4.94. This line was quite obvious at the onset of crack growth and was a distinct feature in the remaining portion of the fracture surface as well. Higher magnifications showed a similar appearance in the fracture surfaces to those at 450°C, although there appeared to be evidence of more ductile tearing at 550°C, Figure 4.95. This line, as was seen in cross sectioning, was associated with crack branching.

Observation of the fracture surface of microstructure 10/F tested at 650°C revealed a rough fracture surface with large numbers of secondary cracks running down into the fracture surface, Figure 4.96. Higher magnification showed that the microstructure appeared to be failing in a brittle mode during elevated temperature crack growth, Figure 4.97. In fact, there seemed to be little difference in the microscopic appearance of the fracture surface to that of a fracture surface from a specimen tested at room temperature. Enlarging a region assumed to be associated with a primary α_2 particle revealed a flat surface exhibiting river markings, Figure 4.98.

Microstructure 0/F also showed a rough fracture surface with numerous secondary cracks at 650°C. The crack appeared to grow transgranularly but revealed the underlying prior β grain structure, Figure 4.99. Microscopic examination again revealed a fracture surface that was similar in appearance to the brittle fracture found in room temperature specimens.

The fracture surface of microstructure 0/C at 650°C clearly showed intergranular crack growth that was dependent on the prior β grain structure, Figure 4.100. Secondary cracking in this instance appeared to be associated with the prior β grain boundaries. Microscopic evaluation showed that failure was also occurring in a brittle manner.

Sectioning of bent, but unbroken, bars also showed a similarity in crack propagation behavior of the three microstructures. On a macroscopic scale, the crack tips appeared to have been blunted before the crack extended perpendicularly to the stress axis at 450°C, Figures 4.101. A few, relatively small cracks, 1 - 10 μm , were observed to nucleate at a distance of 5 - 30 μm ahead of the main crack tip and in the plane of crack growth. These cracks were associated with failure of the primary and secondary α_2 phase. Only rare occurrences of cracks lying out of the main crack growth plane were observed.

Crack growth deviated from a straight path at 550°C and showed significant bifurcation of the crack tip in all three microstructures; sometimes resulting in multiple crack fronts, Figure 4.102. The crack tips appeared to have been blunted prior to extension and bifurcation, particularly in microstructure O/C, Figure 4.103. The direction of the branches followed the microstructural texture of the secondary α_2 laths, propagating by the failure of the laths in a direction generally perpendicular to their long axis, Figure 4.104. As at 450°C, cracks were observed to nucleate ahead of the crack tip by 10 - 50 μm . These cracks were again associated with the α_2 phase, but appeared to have a larger crack tip opening displacement (CTOD) as compared to those at 450°C.

At 650°C the crack tips no longer exhibited large scale bifurcation. Also, the crack tips were sharper, with the CTOD visibly smaller than at 450 and 550°C, Figure 4.105. The main crack appeared to be growing by linking with large cracks nucleated ahead of the crack tip, Figure 4.106. These cracks appeared to be associated with the failure of α_2 and the separation of the $\alpha_2/\text{B2}$ interfaces, Figure 4.107. In microstructure O/C these cracks were usually associated with prior β grain boundaries, Figure 4.108.

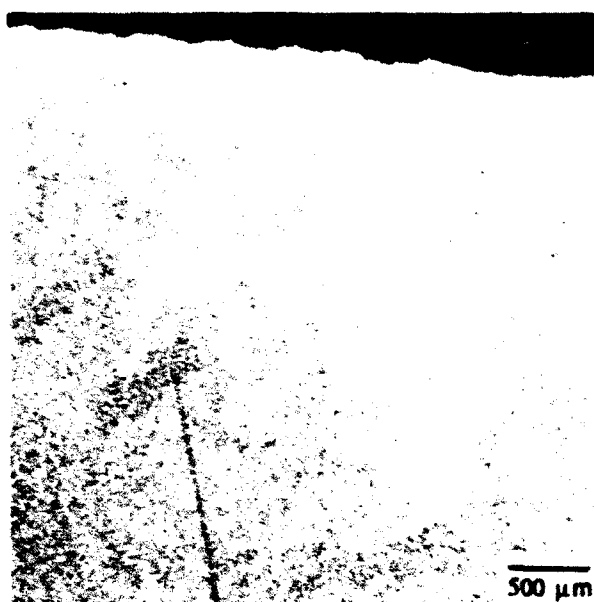


Figure 4.86 Metallographic section of K_{IC} specimen from microstructure 10/F tested at room temperature. Fracture path was flat.



Figure 4.87 Metallographic section of K_{IC} specimen from microstructure 0/C tested at room temperature. Fracture path was still relatively flat.



Figure 4.88 Enlargement of sectioned crack path from microstructure 10/C showing limited secondary cracking.

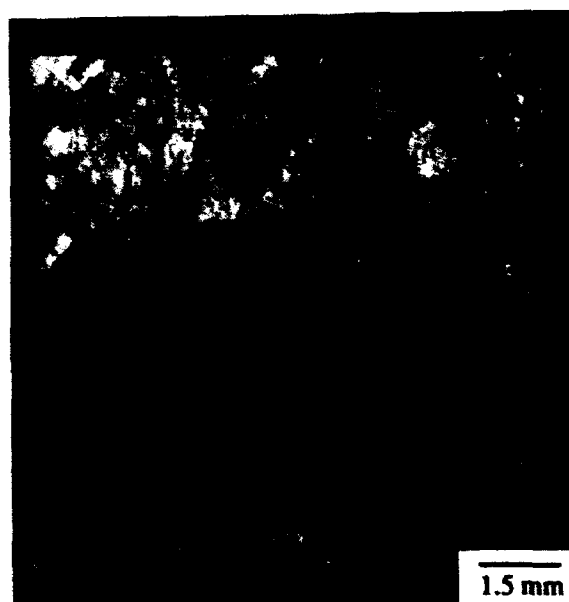


Figure 4.89 Light macrograph of broken J bend bar from microstructure 10/F tested at 450°C.

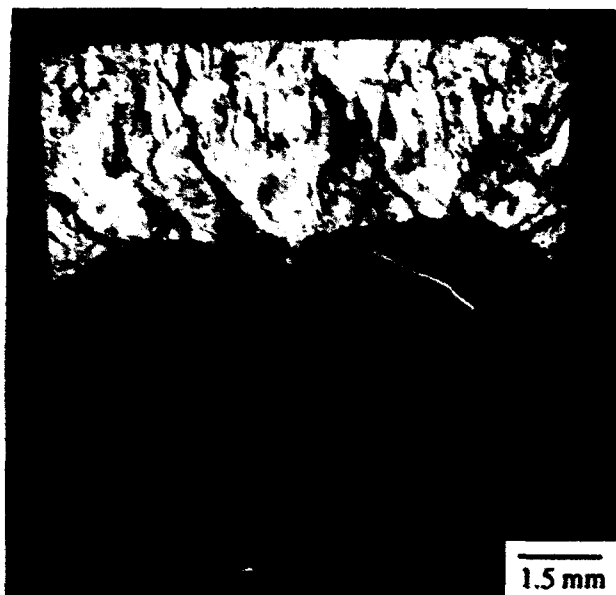


Figure 4.90 Light macrograph of broken J bend bar from microstructure 10/F tested at 550°C.

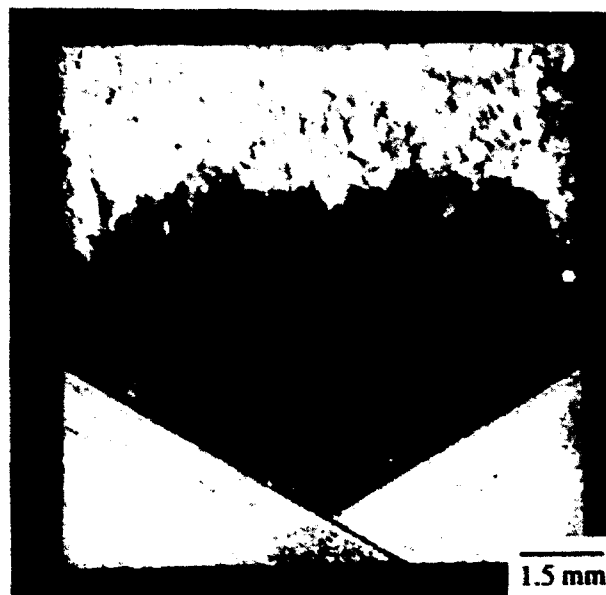


Figure 4.91 Light macrograph of broken J bend bar from microstructure 10/F tested at 650°C.

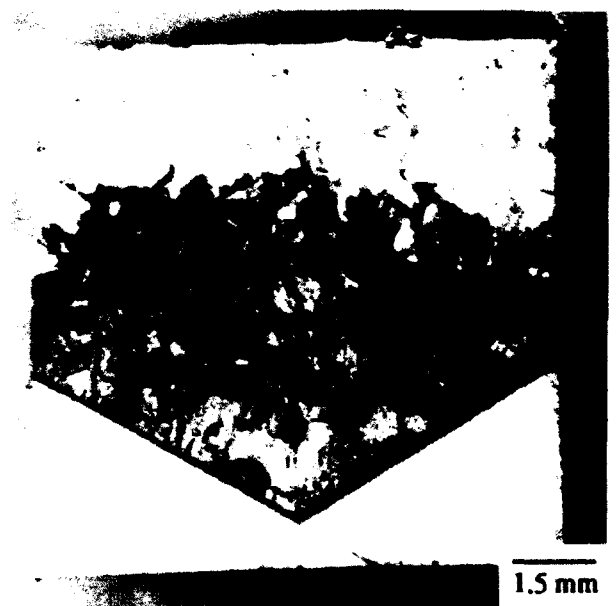


Figure 4.92 Light macrograph of broken J bend bar from microstructure 0/C tested at 650°C.



Figure 4.93 Fracture surface of J bend bar from microstructure 10/F tested at 450°C.



Figure 4.94 Fracture surface of J bend bar from microstructure 0/F tested at 550°C.

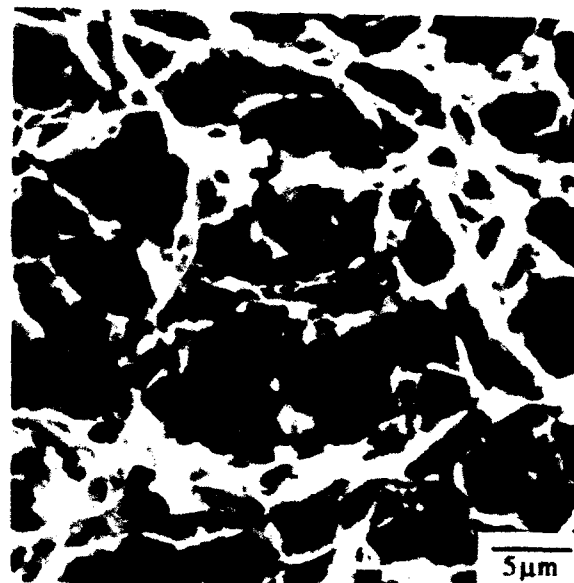


Figure 4.95 Enlargement of fracture surface in Figure 4.94.

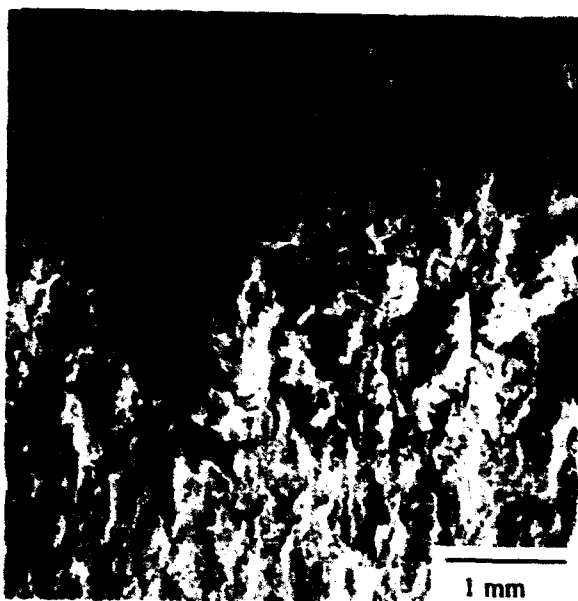


Figure 4.96 SEM macrograph of broken J bend bar from microstructure 10/F tested at 650°C.

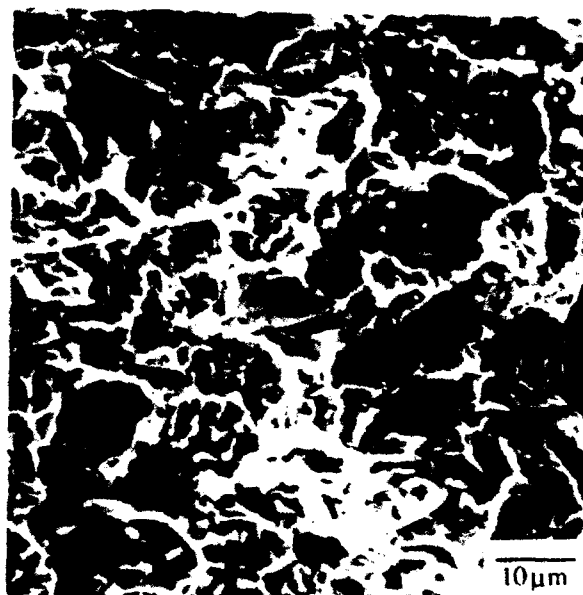


Figure 4.97 Enlarged view of Figure 4.96 showing fracture by a brittle mode.

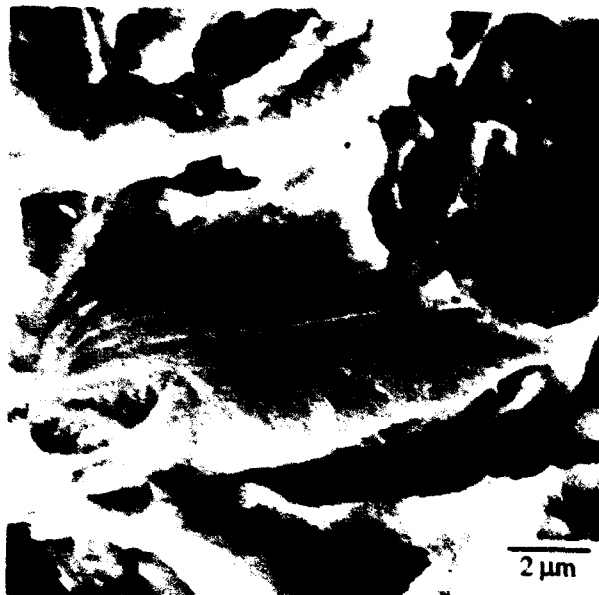


Figure 4.98 Enlarged view of Figure 4.97 showing primary α_2 with river markings.

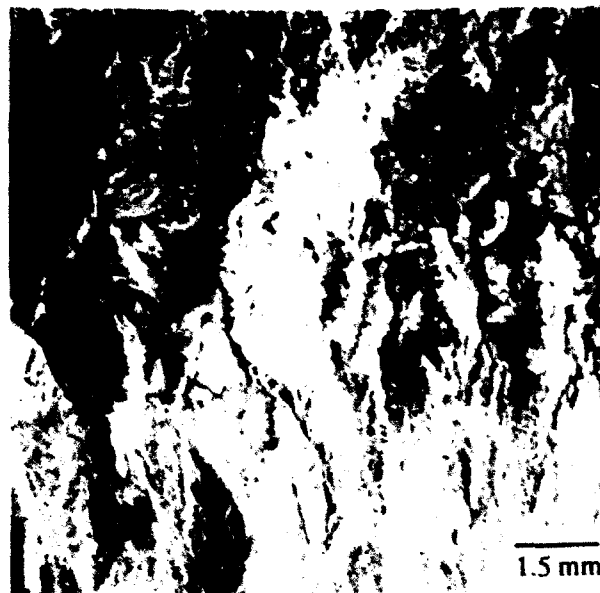


Figure 4.99 SEM macrograph of broken J bend bar from microstructure 0/F tested at 650°C.

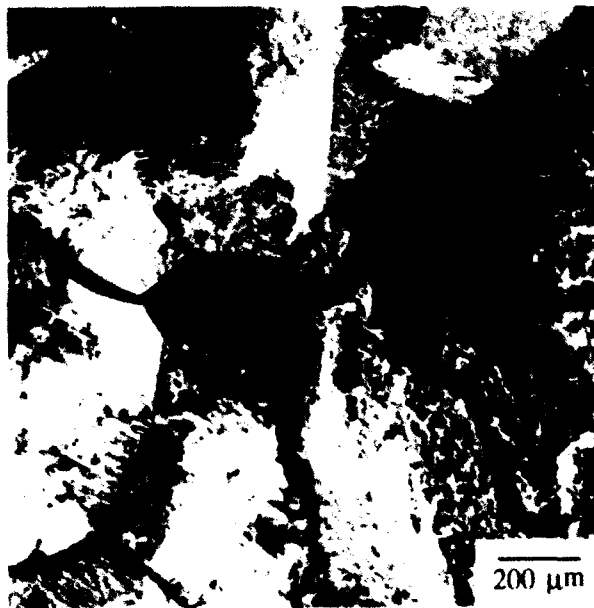


Figure 4.100 SEM macrograph of broken J bend bar from microstructure 0/C tested at 650°C.

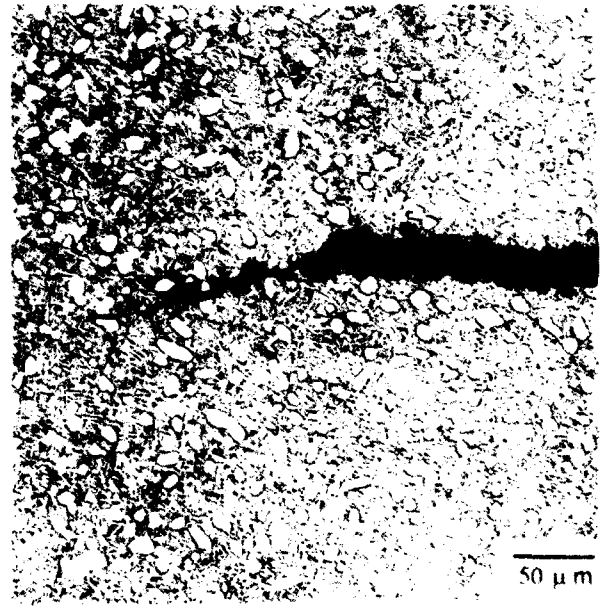


Figure 4.101 Metallographic section of J bend bar from microstructure 10/F tested at 450°C.

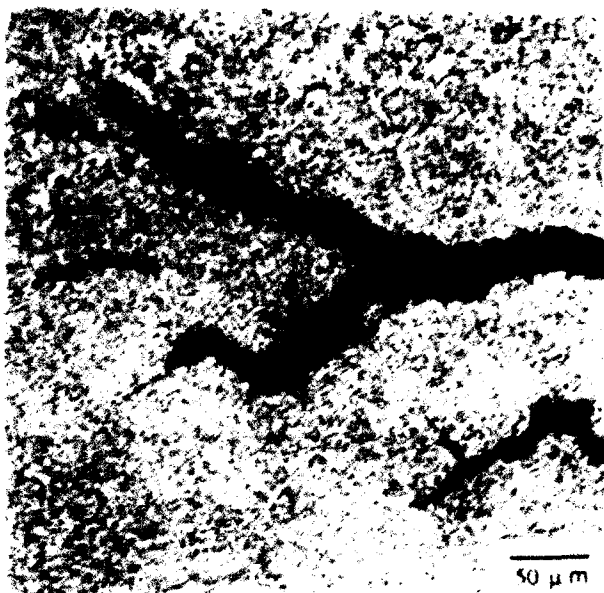


Figure 4.102 Metallographic section of J bend bar from microstructure O/F tested at 550°C.

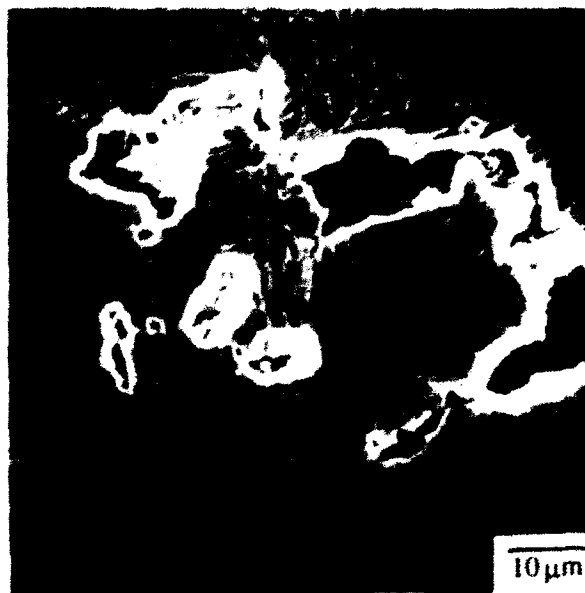


Figure 4.103 Metallographic section of J bend bar from microstructure O/C tested at 550°C.



Figure 4.104 Enlargement of bifurcating crack front in Figure 4.102.

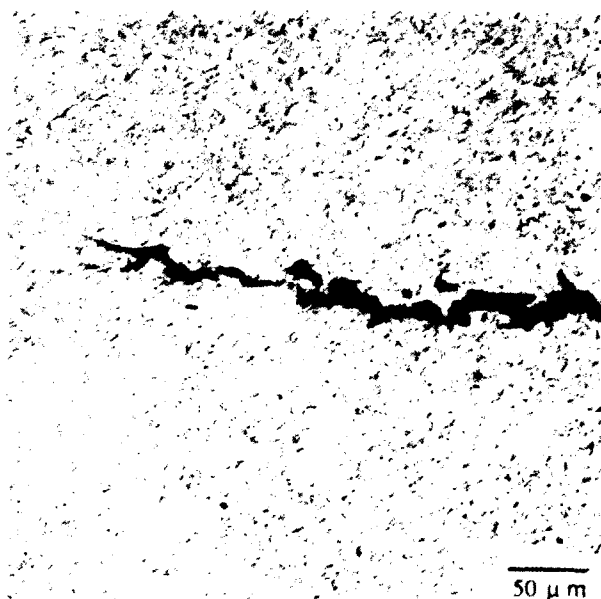


Figure 4.105 Metallographic section of J bend bar from microstructure 10/F tested at 650°C.



Figure 4.106 Enlargement of crack tip region in Figure 4.105.

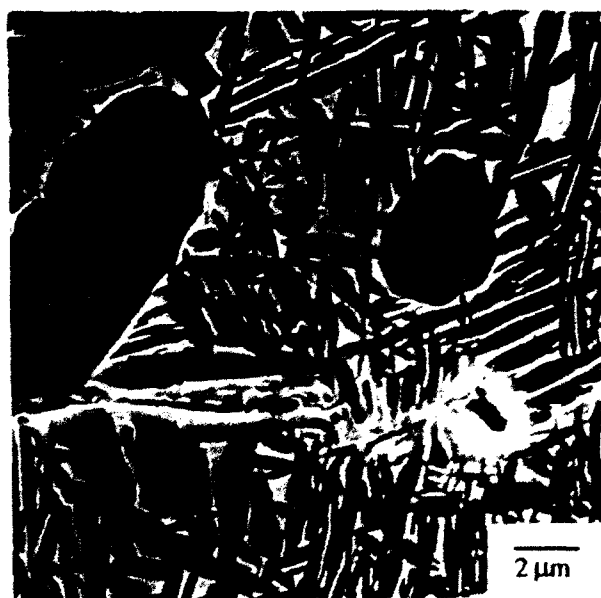


Figure 4.107 Metallographic section of J bend bar from microstructure 10/F tested at 650°C.



Figure 4.108 Metallographic section of J bend bar from microstructure 0/C tested at 650°C.

5. DISCUSSION

5.1 Room Temperature Deformation and Fracture

5.1.1 Tensile Behavior

Numerous studies have shown that microstructure has a profound effect on the tensile properties of $\alpha_2+\beta$ /B2 alloys.^{28,82,89} The results of this study, likewise, confirm these previous observations of a strength and ductility dependence on microstructure. The intent of this study was to show where sources of fracture initiation were occurring and how they relate to the macroscopically measured properties.

The fine secondary α_2 matrix was found to have an approximately 45% higher yield strength as compared to the coarse matrix in microstructures containing similar volume fractions of primary α_2 . As reviewed previously, boundary strengthening mechanisms in titanium alloys appear to obey a relationship where yield strength is proportional to the inverse of the secondary α_2 size, λ^{-1} (where λ is in meters).^{83,84} Substituting the tensile properties into an equation to relate yield stress to secondary α_2 size gives:

$$\sigma_y = 303 \times 10^6 + 253 \lambda^{-1} \text{ Pa} \quad (5.1)$$

In fact, if the data are fit to the conventional Hall-Petch dependency of yield strength on $\lambda^{-1/2}$, the value for σ_f is found to be -54.8×10^6 , a physically meaningless number. The break down in the conventional Hall-Petch description may be due to the fine scale of the boundary strengthening microstructural constituents (1 μm and 0.5 μm in the present study). These are very near, or smaller than, the typical 1 μm dislocation cell size formed during deformation in most metals.

The strengths measured in this study are approximately 15-20% lower as compared to similar microstructures from a previous study.²⁸ This difference is most likely attributable to the lower oxygen and aluminum contents in the material used in this study. Blackburn and Smith have shown oxygen to be a particularly potent strengthener.³

The Hollomon work hardening exponent, from Equation (4.1), at room temperature for the fine secondary α_2 microstructure is 0.14, lower as compared to the value of 0.17 for the coarse microstructure. This could be related to the effect that differing yield strengths can have on the work hardening exponent as determined from the Hollomon equation. The Ludwik relation, Equation (4.2), avoids this problem and gives a work hardening exponent that is independent of yield strength. As can be seen in Table 4.3, the work hardening rates determined with the Ludwik equation are microstructurally independent.

The surface observations of deformation showed that all of the microstructures are prone to localized, intense slip band formation. However, the fine secondary α_2 microstructures displayed shorter and more homogeneously distributed slip bands in the matrix. The coarse secondary α_2 microstructures showed rather coarse slip bands that were approximately 40-60 μm in length as compared to 10-20 μm for the fine secondary α_2 matrix. The slip bands were observed to intersect with other slip bands within the matrix and with primary α_2 particles. The slip bands appeared to traverse secondary α_2 laths across their short dimension; this observation is consistent with slip on the (0001) planes, as has been previously observed by others.^{76,109} As the coarser secondary α_2 microstructures have α_2 laths which are wider and aligned, it is not surprising that they have a longer slip band length.

When considering failure by a brittle mechanism, the process should be divided into three stages: (1) slip band formation, (2) crack nucleation, and (3) crack propagation. Acoustic emission monitoring of tensile tests at room temperature suggests that plastic deformation extends some increment of strain before crack nucleation occurs. However,

once nucleated, cracks propagate quickly promoting catastrophic failure. The low number density of cracked α_2 particles observed below the fracture surface helps support this postulate. The crack nucleation events occur at the same relative locations in the tensile stress-strain curves among microstructures with similar volume fractions of primary α_2 . This typically occurs within the final 0.5% strain preceding failure. Having similar elongations to failure, the coarser grained microstructures nucleate cracks at a lower uniaxial tensile stress.

In $\alpha_2+\beta$ processed microstructures, tensile failure initiates at the primary α_2 particles. These particles provide initiation sites through their failure by three mechanisms. The first is by a cleavage-like fracture of the particles themselves, characterized by the presence of river markings on the fractured surfaces of the particles. These particles are likely positioned in hard orientations for slip. In the coarse secondary α_2 matrices of microstructures 25/C and 10/C, these cracks are observed to nucleate at the intersections of matrix slip bands with the primary α_2 . Other cracks within the primary α_2 particles were observed to lie along the operating slip planes within the particles and were inclined with respect to the stress axis. The intersections of these slip planes with the interface between the primary α_2 particle and the matrix leads to ledges which are stress risers. These stress risers act as nucleation sites for crack propagation.

The third nucleation site associated with primary α_2 particles is by decohesion of the interface between the particles and the surrounding matrix. Sometimes this decohesion is associated with the boundary between two neighboring primary α_2 particles. In either case, these cracks also appear to be nucleated by the intersection of slip bands in either the primary α_2 or the matrix with the interface between the primary α_2 particle and the surrounding matrix or a neighboring primary α_2 particle. As this appears to occur near the same stress level as the other two mechanisms of failure, and the slip band lengths are comparable, the effective energy for interphase interfacial fracture must be similar.

The coarse secondary $\alpha_2 + \beta$ -processed microstructures also exhibit "V-crack" nucleation associated with the intersection of two slip bands within the matrix. While slip bands are observed in the fine secondary α_2 microstructures, no cracks are observed at their intersections.

β -processed material with the coarse secondary α_2 microstructure also exhibits "V-crack" nucleation within the matrix at the intersection of slip bands, and cracking of the grain boundary α_2 due to apparent strain incompatibilities across the prior- β grain boundaries. This behavior in β -processed microstructures has been previously observed and described by Lukasak and Koss in Ti-24-11.⁸⁹

Low, Stroh, and others have shown that brittle fracture can be directly related to the grain size of a material.^{110,111} The basic relationships used to describe brittle failure can be derived in a similar fashion to the Hall-Petch expression describing yield strength; the stress at the end of a slip band being dependent on the grain size of a single phase material. The grain size limits the number of dislocations attainable in a pile-up within a grain. In this study, grain size can be interpreted as the slip band length for a particular microstructure. Stroh's theory only allows for nucleation controlled fracture, i.e. once the fracture stress is reached, catastrophic failure occurs. On the other hand, Smith's theory for brittle failure describes a situation where a dislocation slip band intersection with a brittle particle causes the particle to fail, allowing for growth controlled mechanisms.¹¹² This is the most appropriate model for this material where brittle failure has been shown to initiate in the α_2 particles. The schematic representations of where brittle failure is initiated in each of the microstructures are drawn in Figures 5.1-5.3. Figures 5.1 and 5.2 apply to primary α_2 failure in the $\alpha_2 + \beta$ processed microstructures while Figure 5.3 depicts initiation in the β processed microstructures. The acoustic emission results suggest that nucleation of cracks within the α_2 occurs very close to failure, and as such, failure can be considered to be nucleation controlled. As recently reviewed by Thompson,¹¹³ Smith's

model to predict the critical fracture stress for initiation-controlled brittle failure can be written:

$$\tau_F = \tau_f + \left[\frac{2 \mu \gamma_{eff}}{\pi (1 - \nu) L} \right]^{\frac{1}{2}} \quad (5.2)$$

and,

$$\sigma_F = \sigma_f + 2 \left[\frac{2 \mu \gamma_{eff}}{\pi (1 - \nu) L} \right]^{\frac{1}{2}} \quad (5.3)$$

Where L is a measure of dislocation pile-up length, γ_{eff} is the effective energy for fracture in the matrix, σ_f is the friction stress from the Hall-Petch relationship and μ is the shear modulus. A dependence of the fracture stress on $L^{-1/2}$ is not in contradiction with the λ^{-1} dependence of the yield strength. The values of L are on the order of 10-60 μm , much larger than the 0.5-1 μm slip length size which determines the yield stress. Equation (5.3) can be rewritten to determine the effective fracture energy from known values:

$$\gamma_{eff} = \left[\frac{\pi (1 - \nu) L}{2 \mu} \right] \cdot \left[\frac{\sigma_F - \sigma_f}{2} \right]^2 \quad (5.4)$$

γ_{eff} is taken as the effective energy for fracture for an α_2 particle, and L the slip length involved in promoting failure. As nucleation occurred at a strain level nearly equivalent to that for catastrophic failure, the mechanical properties at fracture were used in all calculations. In microstructure 10/F failure was associated with the primary α_2 particles, which showed failure by slip band decohesion. Therefore, the situation depicted in Figure 5.1 is applicable and a value for L of 9 μm corresponding to the primary α_2 particle diameter was used. The other values used were $\sigma_F = 1037$ MPa (Table 4.2), $\sigma_f = 303$ MPa (equation 5.1), and $\mu = E/2(1+\nu) = 41.1$ GPa, where $\nu = 0.29$.¹⁰⁸ This yields a

value for γ_{eff} of approximately 33 J/m², in fairly good agreement with the value determined by Chu and Thompson for Ti-24-11 of 27 J/m².⁹⁴ This value is now taken as the effective fracture energy to fail an α_2 particle and should be similar for the coarse microstructures.

Using the values for microstructure 10/C of $\sigma_F = 900$ MPa a value for L of 13.6 μm is obtained. Although this is smaller than the observed slip band lengths of this microstructure ~ 40 μm , it at least qualitatively shows that a longer slip band is required to cause failure of the primary α_2 particles. Applying the same value for γ_{eff} to the β -processed microstructures, values for slip band length required to initiate failure were determined to be 8.1 μm for microstructure 0/F ($\sigma_F = 1078$ MPa) and 19.8 μm for microstructure 0/C ($\sigma_F = 799$ MPa). Again, these lengths are in relatively reasonable agreement with the relative slip band length measurements on the pre-polished tensile bars (10-20 μm for microstructure 0/F and 40-60 μm for microstructure 0/C). One source of error that must be considered is the σ_f term used in equations (5.3) and (5.4) as this is derived from equation (5.1), which is dependent on a λ^{-1} relation of yield stress.

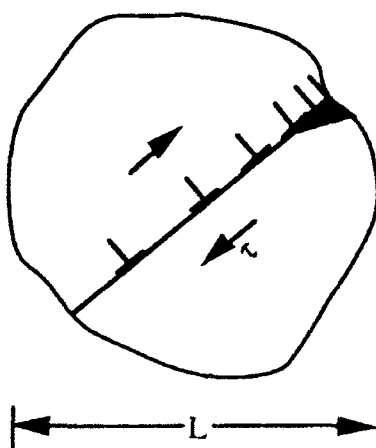


Figure 5.1 Depiction of failure in a primary α_2 particle by slip band decohesion. Slip band length corresponds to particle size.

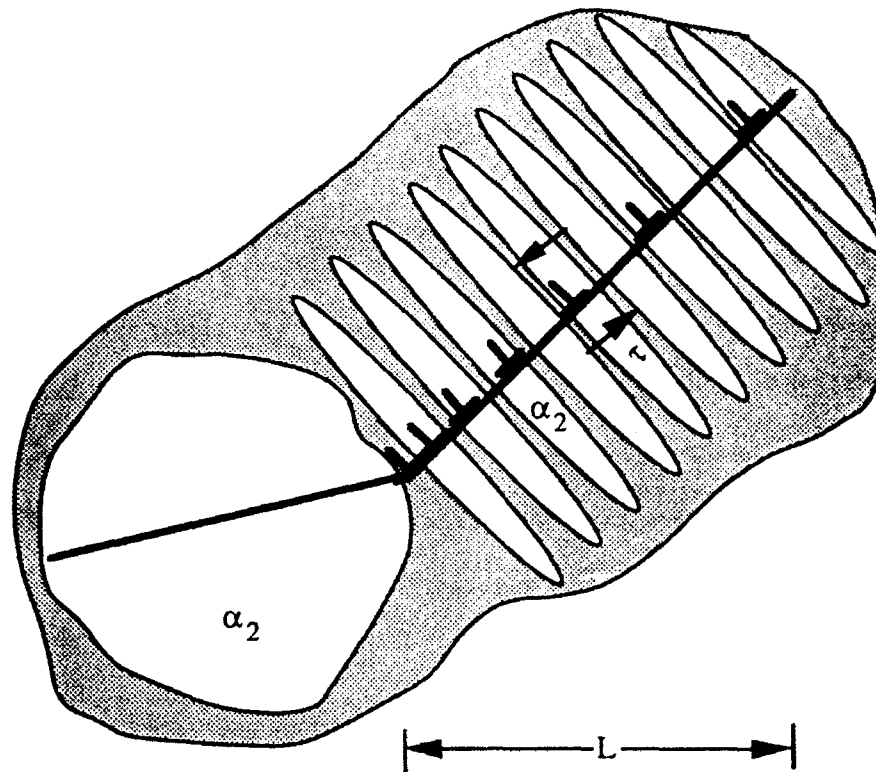


Figure 5.2 Schematic of matrix slip band intersecting with a primary α_2 particle. Slip band length corresponds to secondary α_2 packet size.

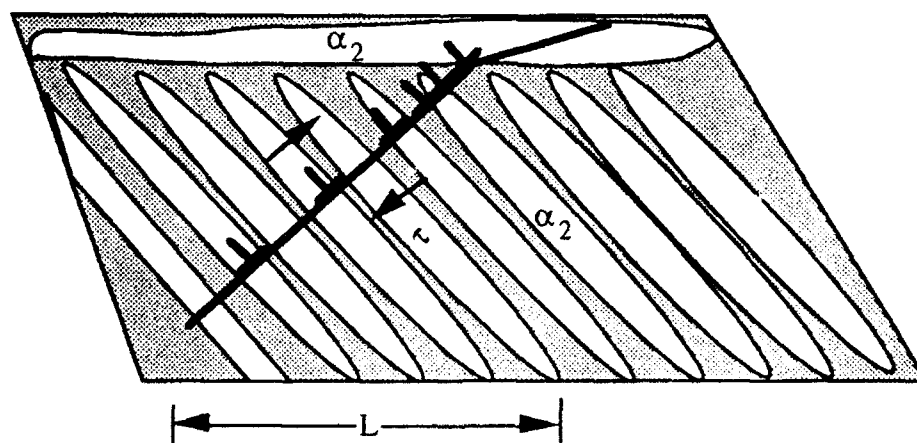


Figure 5.3 Schematic of matrix slip band intersecting with grain boundary α_2 . Slip band length corresponds to secondary α_2 packet size.

Now attention is turned to crack propagation. Crack propagation from the initiation site proceeds rapidly through the matrix by the brittle fracture of secondary α_2 laths ahead of the crack tip, or by following the α_2 /B2 interfaces. These cracks are oriented perpendicularly to the long axis of the secondary α_2 laths, indicating a fracture plane that is near (0001). The B2 phase surrounding the cracked secondary α_2 laths forms a ligament which bridges the crack and fails in a ductile mode, leaving a knife edge ridge between the α_2 laths. The B2 phase is also observed to act as a crack arrester when present in sufficient thickness. The coarse secondary α_2 microstructures can contain large regions of similarly aligned α_2 laths which provide an easy crack propagation path after nucleation. A schematic drawing of this process is presented in Figure 5.4.

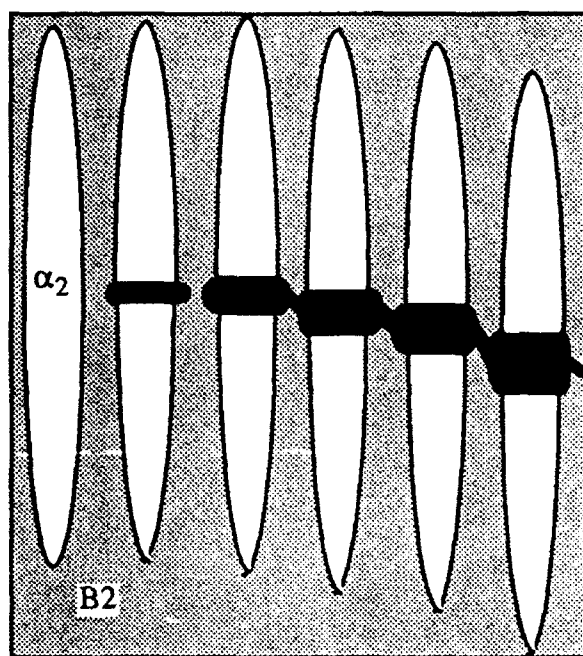


Figure 5.4 Crack propagation process through secondary α_2 laths.

In the β processed microstructure O/C, easy crack propagation can occur along well defined prior β grain boundaries which are approximately normal to the tensile axis. This

can leave a dimpled appearance on the fracture surface. These dimples are associated with the B2 phase which is present at the interface of grain boundary α_2 . The dimples appear to be the result of the separation of the sometimes aligned secondary α_2 laths from the grain boundary α_2 . This process was observed to occur at elevated temperatures. It is proposed that at room temperature, as seen in brittle cracking of secondary α_2 laths, the B2 phase pulls up around the tips of the aligned secondary α_2 laths, leaving a dimpled appearance. This process is drawn schematically in Figure 5.5.

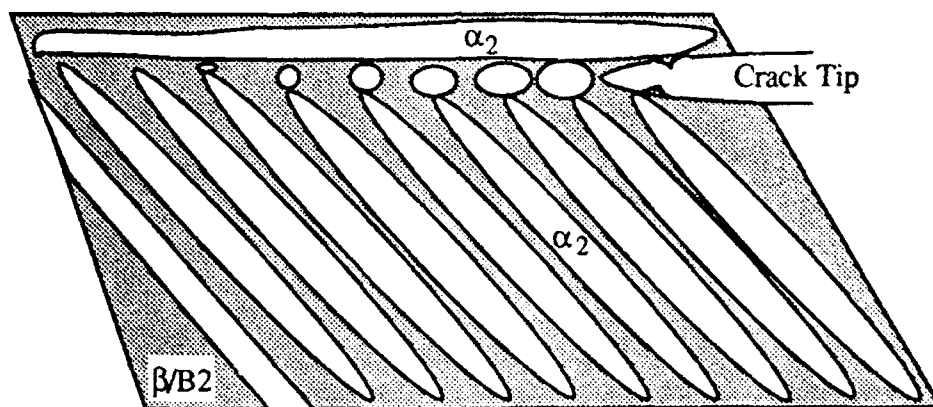


Figure 5.5 Schematic of crack propagation along a prior β grain boundary depicting the origin of dimples seen on the fracture surface. The dark features represent the β /B2 phase.

It is clear that in the six microstructures studied, failure is dominated by crack initiation. The strain at which each individual microstructure fails is based on achieving a critical normal fracture stress. This, in part, is determined by the dislocation pile-up length, L . In materials of similar yield strength, shorter dislocation pile-up lengths result in higher applied fracture stresses. Unfortunately, a shorter dislocation pile-up length generally corresponds to finer microstructural scale in these materials and therefore a higher yield stress. The significance of a higher yield strength is that less plastic deformation is required before the fracture stress is reached. Within this view, a constant nucleation stress is maintained at the pile-up tip; however, the macroscopic stress must increase since the

intensification factor varies with pile-up length. In terms of evaluating tensile elongation, the fracture stress in relation to strain is described as a trade off between yield strength and stress concentration at the end of dislocation pile-ups. The relation between these two competing values can perhaps be best visualized in terms of elongation to failure by combining the Hollomon equation relating tensile stress to strain behavior, equation (4.1), with Smith's equation describing fracture stress, equation (5.3). When these two equations are combined, an expression predicting the failure strain in initiation-controlled failure is obtained:

$$\epsilon_F = \left[\frac{1}{K} \left(\sigma_f + 2 \left[\frac{2 \mu \gamma_{eff}}{\pi (1 - \nu) L} \right]^{\frac{1}{2}} \right) \right]^{\frac{1}{n}} \quad (5.5)$$

It is now evident in this expression how the slip length, L , and yield stress, as represented through K , effect the tensile elongation. In the particular microstructures of the present study, the two considerations are balanced, perhaps fortuitously, to yield similar tensile ductilities.

5.1.2 Fracture Toughness

Testing has shown that there was no measured influence of microstructure on fracture toughness at room temperature in this study. On a microscopic scale there appears to be little difference in the propagation path of the advancing crack. The crack proceeds by the brittle fracture of secondary α_2 laths, with relatively little deviation from the plane normal to the stress axis. Studies by Chan and Soboyejo have shown that the β (B2) phase is the largest contributor to increasing room temperature fracture toughness through crack blunting and bridging mechanisms.^{88,99} The amount and distribution (thickness) of the B2 phase was fairly uniform among the microstructures tested in this study. The B2 phase was continuous in all of the microstructures and had a measured area fraction of between

30 and 36% B2 phase, slightly higher than the ~25% value found in the studies by Chan and Soboyejo. Thus, it is expected that the fracture toughness is similar for all of the microstructures.

Based on the models by Chan and Soboyejo, it is not surprising that there is not a large difference in these values, even when judging the macroscopic appearance of the fractured specimens. In particular, the fracture surface of microstructure 0/C has a visually more tortuous appearance as compared to that of the other microstructures. The coarse and aligned microstructure, 0/C, might have been expected to have a higher fracture toughness value than the other microstructures based on results obtained by Marquardt.⁹⁷ However, while the coarse secondary α_2 laths are aligned in regions, microstructure 0/C cannot be termed 'colony', as was the case in Marquardt's study. Additionally, the prior β grain size in this microstructure was found to be smaller than for all other microstructures. This is due to the one hour β anneal after final forging; evidently the time allowed for annealing was insufficient to permit substantial β grain growth after recrystallization. Again, Chan and Soboyejo have modeled the contributions of crack deflection to measured fracture toughness.^{88,99} They both found that without significant deflection of the crack tip, $>45^\circ$, there would be no substantial increase in fracture toughness. Therefore, it must be concluded that macroscopic crack deflection caused by the coarser microstructure, even in this case, was insufficient to result in a noticeable increase in the measured fracture toughness.

5.2 Elevated Temperature Deformation and Fracture

5.2.1 Work Hardening and Strengthening

The yield stress behavior is presented below as being dependent on the inverse of secondary α_2 lath size at elevated temperatures:

$$450^{\circ}\text{C:} \quad \sigma_y = 220 \times 10^6 + 160 \lambda^{-1} \text{ Pa} \quad (5.6)$$

$$550^{\circ}\text{C:} \quad \sigma_y = 290 \times 10^6 + 100 \lambda^{-1} \text{ Pa} \quad (5.7)$$

$$650^{\circ}\text{C} \quad \sigma_y = 260 \times 10^6 + 110 \lambda^{-1} \text{ Pa} \quad (5.8)$$

$$750^{\circ}\text{C:} \quad \sigma_y = 180 \times 10^6 + 150 \lambda^{-1} \text{ Pa} \quad (5.9)$$

It is evident that the constant, k' (k' is used to distinguish it from the k in a Hall-Petch equation), in front of the size dependent variable, λ , has fallen significantly from the value of 253 Pa·m at room temperature to an average value of approximately 130 Pa·m above 450°C. Although the dependence of the yield stress is described here as a function of the inverse of secondary α_2 lath size, the significance of k' in this instance is expected to have similar physical significance to the k term in the $d^{-1/2}$ dependent Hall-Petch relation. The value of the k constant has been shown to indicate the relative ease of dislocation processes in a Hall-Petch relationship.¹¹⁴ A decreasing value of k indicates that the ease of dislocation motion in one or more slip systems has increased. This increase is derived from a lowering of the critical resolved shear stress on particular slip systems, increased cross slip and a reduction of dislocation locking. The value of k' at elevated temperature approaches that of 69.5 Pa·m determined for conventional $\alpha+\beta$ titanium alloys.⁸³ This suggests that deformation in this intermetallic alloy at elevated temperature behaves similarly to conventional titanium alloys at room temperature. Though no studies have focused on determining a specific temperature at which the dislocation behavior changes,

the preponderance of mechanical property data that are presented throughout this and following sections tends to support an argument that there are significant changes in the fundamental deformation model(s) in this material as the deformation temperature increases.

The Hollomon strain hardening exponents at 450°C were found to be slightly higher for each of the three microstructures as compared to their room temperature values. This is consistent with the lower yield stresses at elevated temperatures which tend to increase the n values. The values of n fell with temperature. This decrease in strain hardening rate with temperature is consistent with Gittis's results for single phase α_2 , but are contrary to Chan's work on Ti-24-11 tested at similar temperatures.^{81,98,115} The decrease in strain hardening rate with temperature is generally expected in most metallic materials.

There did not appear to be a significant strain rate effect on n in the three microstructures below 650°C. However, microstructure 10/F did show a substantial decrease in work hardening rate above 650°C when tested at a slower strain rate. This effect was observed in both regions of strain examined $0.01 < \epsilon < 0.10$ and $\epsilon > \epsilon_u$. Care must be taken in interpreting these results as significant void volume fractions were present in the necked region. However, the decrease in the work hardening rate in the strain range $0.01 < \epsilon < 0.10$, where no voiding should be present, can be considered to be a realistic indicator of work hardening trends.

Gittis and Koss have shown that the strain rate sensitivity of n is very low for a single phase α_2 alloy up to 650°C.^{81,115} On the other hand, they found that the β alloy studied was very strain rate sensitive at 650°C, and also exhibited flow softening behavior at this temperature. The β alloy in their work, based on the β phase found in Ti-24-11, cannot be considered to be truly single phase as evidence was seen in AEM analysis of an ω -type precipitate. However, the results presented here are from an overaged condition where the amount and size of ω phase present in the alloy would not be expected to contribute significantly to the strengthening mechanisms in the β phase. All three microstructures in the present study appeared to demonstrate a trend towards flow

softening behavior above 600°C that is consistent with the β phase alloy in Gittis's work. Again the influence of void fraction in the necked region must be taken into consideration. Additionally, a Bridgman correction to the fracture stress is appropriate. However, measurements of the necked regions on the failed tensile bars indicated that they are relatively diffuse, with a maximum correction in fracture stress of 10% being calculated.

If a simple rule of mixtures approach for the work hardening exponent is conceptually applied to the α_2 +B2 alloy, then:

$$n_{avg} = f_{\alpha_2} n_{\alpha_2} + f_{B2} n_{B2} \quad (5.10)$$

Where f_{α_2} and f_{B2} are the volume fractions of α_2 and B2 respectively. The volume fraction of each phase remains constant throughout the temperature range under consideration here. As the n_{α_2} term has been shown to remain relatively constant with temperature,^{81,115} then the n_{B2} term must be decreasing, perhaps substantially, and becomes more dominant as temperature increases to compensate for the decreasing n value for the two phase mixture. In this situation the rule of mixtures approach is no longer valid. Though it cannot be stated conclusively from the data presented here that the B2 phase in the alloy under current consideration is undergoing flow softening behavior, it is clear that the influence of the B2 phase on the work hardening behavior of the two phase alloy is significant at 650°C and above.

5.2.2 Tensile Failure

Increasing the test temperature to 450°C led to a decrease in the yield strength and an increase in elongation, true fracture strain and true fracture stress for all of the microstructures. The severe drop in elongation observed near 600°C for similar microstructures in a previous study⁸⁷ was not readily apparent in this study. Even though elongation remained approximately constant in the temperature range 450-750°C for

microstructures 10/F and 0/F, the reduction of area continued to increase with temperature. This behavior still indicates a trend towards earlier onset of strain localization as the temperature increases; i.e., the uniform elongation decreases, which is consistent with the decrease of n with temperature.

5.2.2.1 Behavior in the Range 450°C - 600°C

Failure at temperatures below 650°C will be discussed first. Examination of the tensile specimen fracture surfaces showed that failure in microstructures 10/F, 0/C and 0/F up to 600°C appeared to be associated with the prior β grain boundaries. Additionally, the true fracture stress increased by approximately 50% in all of the microstructures at the higher test temperatures as compared to room temperature. The role of primary α_2 in failure will be discussed first as it is the largest individual microstructural unit.

If a cleavage-like mechanism were still operating as the source of initiation, evidence of numerous failed primary α_2 particles would be expected to lie below the fracture surface in microstructure 10/F. This would be the case if an assumed temperature independent normal tensile stress were controlling brittle fracture. As the fracture stress at elevated temperatures is 50% higher than at room temperature, many cracks should be nucleated once a stress equivalent to the fracture stress at room temperature is reached. Thus, crack nucleation should occur at a low strain relative to the high failure strains actually measured at elevated temperatures. Chan's model implies that the high toughness matrix would arrest these cracks until a stress sufficient for propagation through the matrix could be obtained.⁹¹ In fact, few failed primary α_2 particles were observed below the fracture surface between 450 and 600°C. Those particles that had failed often showed cracks lying at an inclined angle to the tensile axis indicating failure more likely associated with slip band decohesion.

The primary α_2 particles were observed to be quite elongated in the direction of the tensile axis, indicating the ease of large scale deformation at elevated temperature. Indeed, measurements of the aspect ratios of primary α_2 particles near the fracture surface in this temperature range showed that strains within the primary α_2 particles were near the macroscopically measured failure strains, Figure 4.82. It can be concluded, then, that the brittle fracture stress for crack nucleation in the α_2 phase lies above the fracture stress obtained in these elevated temperature tensile tests. This again lends support for an increase in the ease of activating slip systems above 300°C. This results in an increased plastic accommodation of stress and strain concentrations at the boundaries, thus avoiding the brittle cracking of the α_2 phase. Although by a different mechanism, this conclusion is similar to that of Jolley where he observed that the transition temperature for cleavage in iron was lowered by the addition of nickel.¹¹⁶ He found that nickel resulted in promoting more wavy slip within the alloy as opposed to planar slip in unalloyed iron.

The only signs of brittle or cleavage failure in the 450 - 600°C temperature range were seen on the fracture surfaces in the final fracture region of the tensile specimens and were associated with the primary α_2 grains. The remainder of the fracture surface was covered with uniformly spaced dimples, apparently associated with either individual secondary α_2 laths or packets of laths. Since the primary α_2 particles are observed to fail by a brittle mechanism in the final fracture region of the fracture surface, it may be concluded that the very high strain rate experienced by the microstructure during final fracture raises the brittle to ductile transition temperature.

Now attention is turned to failure initiation at elevated temperature. The most likely site from observation of the fracture surfaces is at the interface between the grain boundary α_2 and B2 phases present at the prior β grain boundaries. In a manner similar to that proposed for conventional titanium alloys, strain might be expected to accumulate more rapidly at the prior β grain boundaries due to the larger dimensions of the microstructural components there as well as the difference in strain gradients across the boundary

region.¹¹⁷ Thus, at large stresses and strains cracks are nucleated at the prior β grain boundaries apparently between the grain boundary α_2 and the B2 phase.

Sectioning of the failed tensile bars revealed some primary α_2 /B2 interfacial decohesion, demonstrating that this interfacial cohesive strength was very nearly reached at the measured fracture stress. Additionally, decohesion of slip bands in the primary α_2 particles was also apparent. However, these few cracks that do occur within the prior β grain interior do not appear to propagate. This may be attributed to their relatively small size as compared to that needed to overcome the fracture toughness of the α_2 +B2 matrix. Measurements of true strain to void or crack nucleation show that the values obtained are relatively temperature insensitive in microstructures 10/F and 0/F, Figures 4.83 and 4.85. At the same time the true stresses for void nucleation are observed to decrease with increasing temperature. This suggests that the nucleation event is a strain controlled process. Thus, at a given level of deformation, the strain accumulation within, presumably, the B2 phase is sufficient to cause incompatibility at a stress concentrator, resulting in void nucleation. Therefore, a requirement for cracking within the α_2 phase to initiate failure appears to be unnecessary to initiate failure. At 450°C, the lack of voids below the fracture surface indicates that when a void is nucleated, the stress at the interface is sufficient to immediately propagate a crack along the grain boundary α_2 and B2. The matrix toughening mechanisms which pertain to a propagating crack under these conditions, such as blunting, deflection, and perhaps bridging, would not be relevant for a crack propagating along such interfaces. The crack propagates in a fashion similar to that depicted in Figure 5.4. As temperature is increased from 450°C to 600°C, it is evident that necking occurs at lower strains. Void nucleation still occurs at a constant true strain level, but voids do not appear to coalesce and form a propagating crack until a nearly temperature insensitive fracture stress is reached.

In microstructures 0/C and 0/F deformation was observed to be less homogeneous than in microstructure 10/F, with macroscopic deformation occurring on the scale of the

prior β grains, as evidenced by the large offsets at the prior β grain boundaries on the flat pre-polished tensile samples. Crack nucleation sites in these two microstructures were observed to be associated with the intersections of slip bands and the prior β grain boundaries. If such an intersection results in a crack at a prior β grain boundary that is oriented perpendicular to the tensile axis, then rapid crack growth appears to occur. Cracks nucleated at prior β grain boundaries oriented parallel to the tensile axis did not propagate. Again, this was probably due to an insufficient driving force to propagate these small cracks through the tough matrix.

When a crack propagating along the prior β grain boundary reaches a critical size, rapid transgranular fracture occurs across the rest of the specimen. In microstructure 10/F rapid fracture proceeds by cracking primary α_2 particles ahead of the crack, leaving ductile dimples in the ligaments between the primary α_2 particles. In microstructures 0/C and 0/F the appearance of the fracture surface is ductile with ductile tear ridges associated with the B2 phase.

The effect that matrix toughness has on crack propagation and hence final failure, is examined through the use of Chan's model for propagation of a crack.⁹¹ Chan's model predicts tensile failure in a brittle material based on a critical J-integral criterion. This is based on the work of Dowling which describes the J-integral expressions for various crack geometries in infinite bodies.¹¹⁸ The model assumes that a crack is already present in the material when load is applied, and no allowance is made for nucleation or growth of the flaw during testing. The physical description of the situation appears to be appropriate for the present case where a single flaw along a prior β grain boundary is dominant and transitions to transgranular failure. This was not the case at room temperature where many small flaws were nucleated in a narrow interval of strain. Failure is predicted to occur when the critical normal stress, or viewed as a critical J_{Ic} , is met for unstable crack propagation. The model assumes an internal circular crack of half length 'a' in a round bar

tensile specimen. The expression for the J-integral under a remote stress of σ_∞ is described by:¹¹⁸

$$J = J_e(1 + J_z/J_e + J_p/J_e) \quad (5.11)$$

Where J_e is defined as the elastic loading contribution, J_p the plastic loading contribution and J_z a plastic zone contribution due to Irwin. For materials exhibiting plastic deformation following power-law hardening, the contributing terms can be described by:¹¹⁸

$$J_e = \frac{0.405(1-\nu^2)\sigma_\infty^2 \pi a}{E} \quad (5.12)$$

$$\frac{J_z}{J_e} = 0.0675 \left(\frac{N-1}{N+1} \right) \left(\frac{\sigma_\infty}{\sigma_y} \right)^2 \left[1 + \left(\frac{\sigma_\infty}{\sigma_y} \right)^2 \right]^{-1} \quad (5.13)$$

$$\frac{J_p}{J_e} = \frac{3\alpha'}{2(1-\nu^2)\sqrt{1+3/N}} \left(\frac{\sigma_\infty}{\sigma_y} \right)^{N+1} \quad (5.14)$$

where 'a' is the crack half-length, E is the Young's modulus, ν is Poisson's ratio, N is the inverse of the strain hardening exponent ($N = 1/n = \frac{\partial \ln \epsilon_p}{\partial \ln \sigma}$), σ_y is the yield stress and α' is a constant from the Ramberg-Osgood equation describing the tensile stress-strain curve:

$$\epsilon = \frac{\sigma}{E} + \alpha' \epsilon_y \left(\frac{\sigma}{\sigma_y} \right)^N \quad (5.15)$$

α' is determined by the modulus, strain offset used to determine yield point, ϵ_{py} , and the yield stress:

$$\alpha' = \frac{\epsilon_{py} E / \sigma_y}{1 + \epsilon_{py} E / \sigma_y} \quad (5.16)$$

Microstructures 10/F and 0/F were used to determine how well the model predicted failure. The physical values used in fitting the model were taken from tensile testing results and are listed in Table 5.1.

Table 5.1 Physical values for fine secondary α_2 microstructures.

<u>E (GPa)</u>	<u>n</u>	<u>N</u>	<u>σ_y</u>	<u>α'</u>
95.3	0.39	2.6	530	5.66

The relation between the J-integral value as a function of stress ratio for two different flaw sizes is shown in Figure 5.6. The experimentally determined σ_F/σ_y ratios for microstructures 10/F and 0/F are shown on the plot as a box. Figure 5.6 shows that the model predicts a 1-1.5 mm flaw before unstable crack growth should proceed. The failure initiating flaws associated with the prior β grain boundaries were observed to be within a range closer to 200-400 μm . Therefore, the model appears to over estimate the flaw size at which failure will occur. This may be due to the relatively small gage diameter of the tensile specimen in relation to the flaw size. This situation leads to a much higher actual true stress across the plane in which the flaw lies. Additionally, the model is limited by an inability to predict flaw initiation and handle numerous nucleation sites, as encountered at room temperature.

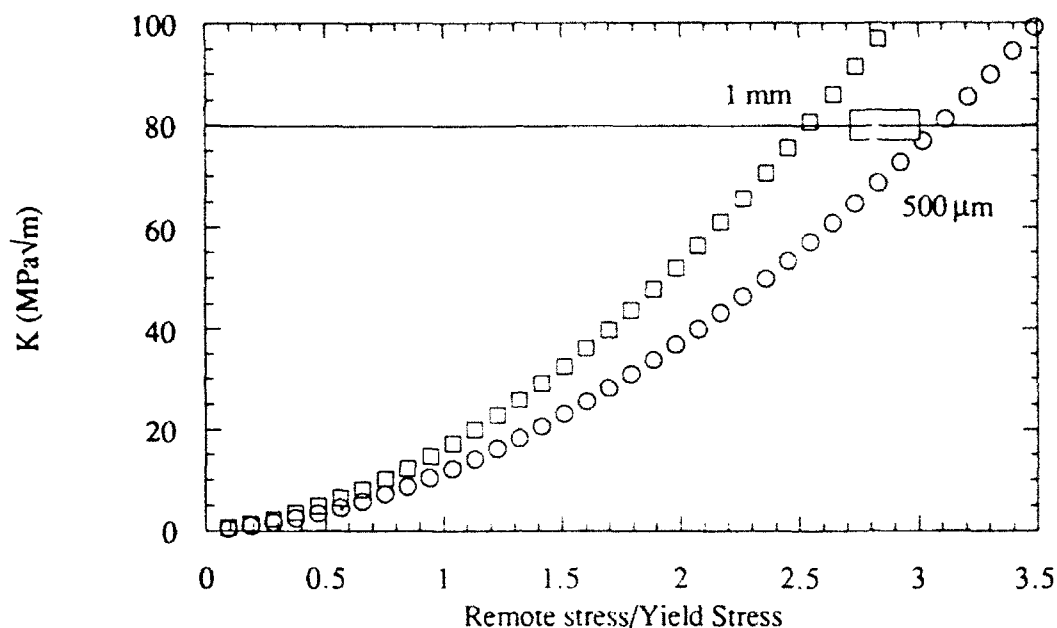


Figure 5.6 Stress intensity factor, K , plotted against the ratio of applied true stress over yield strength at 450°C . The horizontal line indicates the measured fracture toughness, and the box denotes the experimentally measured values at failure. Plotted from the values of the fine secondary α_2 microstructures 10/F and 0/F.

5.2.2.2 Behavior in the Range 650°C - 750°C

At temperatures higher than 600°C it was clear that there was a significant change in the failure mechanism in all of the microstructures. For microstructures 10/F and 0/F this was characterized by a rapid drop in fracture stress, a large increase in the number of voids observed below the fracture surface, and by the visible differences in the dimple structure on the fracture surface. No features on the fracture surface were consistent with brittle fracture in this temperature range. Microstructure 0/C exhibited the same dramatic drop in fracture stress, as well as a concurrent and discontinuous drop in both elongation and reduction of area.

The fracture surface of the tensile specimens from microstructure 0/C showed intergranular failure reminiscent of a failed creep specimen. Failure initiation sites were clearly associated with the prior β grain boundaries. Here cracks were nucleated at the prior grain boundary triple points. These cracks propagated along the grain boundary α_2/β_2 interface until they reached a critical size sufficient to cause failure. Crack nucleation at grain boundary triple points can sometimes be indicative of a grain boundary sliding process. To examine grain boundary sliding as a possible deformation mechanism, the bulk, D_v , boundary, D_b and effective, D_{eff} , diffusion rates for Ti self-diffusion in β titanium were first calculated. β titanium was selected as the appropriate phase as there is a significant amount of β/β_2 phase within Ti-25-10-3-1 and it is considered to be the faster path for diffusion, as compared to α (or α_2), due to its higher diffusion rates. The values used in the analysis are those of the β phase in conventional titanium alloys. These were used due to the lack of similar information in the intermetallic alloy under study here. They are considered to be an upper limit in predicting a diffusional process and, therefore, a conservative estimate.

$$D_v = 4.54 \times 10^{-4} \exp\left(-\frac{31,300 \text{ cal/mol}}{RT}\right) \text{ cm}^2/\text{s} \quad [\text{ref. 119}] \quad (5.17)$$

taking half the bulk activation energy as an estimate of boundary activation energy:¹²⁰

$$L_b = 4.54 \times 10^{-4} \exp\left(-\frac{15,650 \text{ cal/mol}}{RT}\right) \text{ cm}^2/\text{s} \quad (5.18)$$

$$D_{eff} = D_v \left[1 + \frac{\pi \delta}{d} \frac{D_b}{D_v} \right] \text{ cm}^2/\text{s} \quad (5.19)$$

where δ is the effective grain boundary thickness and d is the prior β grain size. Substituting $\delta = 5 \text{ \AA}$ ¹²¹ and $d = 0.7 \text{ mm}$ into equation (5.19), a D_{eff} of $1.78 \times 10^{-11} \text{ cm}^2/\text{s}$ is obtained at 650°C.

The maximum strain rate at which grain boundary sliding is a potential mechanism for deformation can be described by the equation:¹²¹

$$\dot{\gamma} = \frac{42 \tau \Omega}{k T d^2} D_{\text{eff}} \quad (5.20)$$

where τ is the shear stress, Ω is the atomic volume and k is Boltzmann's constant. Substituting $\tau = \sigma/\sqrt{3} = 317.5$ MPa, $\Omega = (3.3 \text{ \AA})^3/2$ (for β -Ti) = $1.8 \times 10^{-29} \text{ m}^3$ into equation (5.20), a value for the maximum strain rate for grain boundary sliding is found to be $6.8 \times 10^{-8} \text{ s}^{-1}$, or approximately 4 orders of magnitude slower than the strain rates imposed during tensile testing. From this analysis, grain boundary sliding does not appear to play a significant role in the failure of microstructure O/C.

The uniform change in failure mechanism among the microstructures points to an underlying change in deformation mechanism. The common failure mechanism which all of these microstructures share is failure initiation at the α_2/β_2 interface. As in the temperature range of 450-600°C, surface observations of flat tensile bars revealed that the deformation in microstructures O/C and O/F was inhomogeneous amongst the prior β grains, leading to large strain gradients across the grain boundaries. In this regard a model proposed by Fuji and Suzuki seems to be an appropriate starting point.¹²² Their model was proposed to explain the hot ductility loss observed in $\alpha+\beta$ titanium alloys stressed near the β transus temperature. The model is based on the knowledge that the β phase in these alloys is softer than the α phase in this temperature regime. In this case, the β phase in the region of the prior β grain boundaries accumulates a disproportionate amount of strain which leads to premature void formation and failure at the grain boundaries.

Ankem and Margolin have demonstrated the concept of strain partitioning through a finite element model of an $\alpha+\beta$ Ti-Mn alloy at room temperature. They were able to show that during deformation, strain is preferentially partitioned to the weaker phase.¹²³ In their

situation the weaker phase was taken to be α , which in this alloy has a composition very near pure titanium. Mn goes exclusively into the β phase and leads to solid solution hardening of the β . Their conclusions, however, can be equally applied to the reverse situation where β is weaker.

There are several pieces of evidence to support an argument that the β /B2 phase dominates the deformation behavior in the two phase alloy of the present study at temperatures above 600°C. First is the amount of strain accumulation in the primary α_2 phase in microstructure 10/F tested past 550-600°C. Figure 4.82 clearly shows that even while the true fracture strain continues to increase beyond this temperature, the true strain in the primary α_2 particles is decreasing. Thus, at some point after initial macroscopic yielding the primary α_2 particles cease to participate substantially in the straining process. The continued decline in strain with temperature in the primary α_2 particles is consistent with a decreasing uniform elongation. Another indication of the extent in which β controls deformation lies in the mechanical property data. The decreasing work hardening behavior and high strain rate sensitivity in Ti-25-10-3-1 observed above 600°C are more characteristic of the β phase than that of the α_2 phase. The single phase β (or B2) phase based on the composition analyzed from an α_2 + β /B2 alloy has been shown by Goto and Koss, and Gittis and Koss, to undergo a transition from work hardening to strain softening in the temperature range 600-650°C.^{81,115,124} The β phase was also shown to have a very strain rate sensitive work hardening rate and a rapidly decreasing yield strength with increasing temperature. Additionally, a single phase α_2 alloy deformed in the 350-650°C temperature region shows little decrease in its work hardening rate and maintained a relatively constant yield strength.^{81,115} Thus, a picture is formed where at temperatures above 600°C the β /B2 phase is largely controlling the deformation of these microstructures at large strains.

At temperatures above 600°C a situation now exists where the α_2 and B2 phases are assumed to have similar yield strengths. As straining of the tensile specimen begins, both

phases yield and begin to undergo work hardening. At this stage each is taking on near equi-proportional strain. However, a short time after work hardening begins the lower work hardening B2 phase begins to affect strain partitioning. At this point, the flow stress of the α_2 phase is increasing relative to that of B2. More strain is partitioned to the B2 phase due to its lower flow stress. This obviously becomes a self-perpetuating mechanism leading to continuous partitioning of strain from the α_2 phase to the B2. At some point the α_2 phase no longer participates substantially in the deformation and the B2 phase is left to account for additional increases in strain. This process of strain accumulation in the B2 phase continues until the B2 phase reaches its plastic limit, ϵ_f , due to local constraint of the microstructure around it.

A low work hardening rate within the B2 phase appears to lead to two important observations in the deformation and failure behavior of this alloy. First, as described above, the self-perpetuating nature of strain partitioning to the B2 phase once strain softening has begun, may result in the observed strain localization. At the onset of necking, the region affected experiences greater true strain than in the rest of the gage length and consequently promotes more rapid strain partitioning to the B2 phase. However, opposing this localization is the positive strain rate sensitivity of the flow stress of the B2. Preferential strain partitioning to the B2 phase will also rapidly lead to reduced strain compatibility at interphase interfaces of the large nondeforming α_2 phase. Void nucleation at these interfaces would be expected to occur relatively shortly after the primary α_2 particles stop deforming. This is indeed what was observed in microstructure 10/F.

In microstructure 10/F, the same inhomogeneity of deformation observed in microstructures 0/C and 0/F between the prior β grains was not observed. Additionally, due to the orientation of the prior β grain boundaries, little boundary area is oriented perpendicular to the tensile axis. Therefore, initiation events associated with the prior β grain boundaries are minimized by the grain morphology. However, the primary α_2 particles in this instance are envisaged to act as largely nondeforming particles and,

therefore, sites for strain incompatibility. Voids should, and are observed to, nucleate at the tops and bottoms of the primary α_2 particles where the largest incompatibility coincides with the maximum positive tensile strain. The true strain to void nucleation is observed to be relatively constant with increasing temperature, Figure 4.83. After nucleation, voids are observed to be rather cylindrical in shape. The slow lateral growth of the voids may not only be due to the work hardening rate, which is difficult to quantify in this region of the stress-strain curve, but may also be influenced by the orientation of the surrounding secondary α_2 laths. These have been rearranged through deformation so that their long axes lie approximately parallel to the tensile axis. This orientation is not favorable for slip along the plane of maximum shear stress, making shear band formation across the secondary α_2 laths and between voids difficult. This difficulty in void coalescence combined with a low void nucleation strain compared to strain at failure leads to the large number of voids seen below the fracture surface.

On the other hand, voids nucleate in microstructure 0/F primarily at the prior β grain boundaries at the point where slip bands intersect the boundaries; although, later in deformation, voids are observed to nucleate at small packets of dissimilarly oriented secondary α_2 laths. As the grain boundaries, such as in microstructure 10/F, are oriented mostly parallel to the tensile axis, the voids are not able to propagate rapidly. Failure proceeds by the gradual linking of these voids through the matrix.

In explaining the dramatic decrease in the elongation and reduction of area for microstructure 0/C, as compared to the behavior of microstructures 10/F and 0/F, it is readily apparent that the answer lies largely in the crack propagation path during failure. For microstructure 0/C, once nucleated, a crack has a low energy path of relatively soft B2 phase to follow while propagating along the prior β grain boundaries. A much larger proportion of the energy for plastic deformation of microstructures 10/F and 0/F is expended by void growth and coalescence. Additionally, the strain for void nucleation was found to be half of that for microstructures 10/F and 0/F. The lower strain to failure is

most likely related to the greater strain incompatibility at the prior β grain boundaries due to the coarser microstructure. The combined effects of low strains for void nucleation, and continuous grain boundaries aligned perpendicular to the tensile axis correlates well with the lower observed elongations and reductions of area.

5.2.3 Environmental Effects

Results from elevated tensile testing at 550 and 650°C in air, reported in section 4.2.3, clearly showed a dynamic effect of environment on tensile properties. No significant effects of strain rate on ductility were observed at these temperatures during vacuum testing. However, circumferential surface cracks were observed in all of the specimens tested in air, and crack propagation was temperature and strain rate dependent. Environmentally assisted crack growth into the specimen was effectively stopped at a strain rate of $2 \times 10^{-2} \text{ s}^{-1}$ at 550°C and at $1 \times 10^{-1} \text{ s}^{-1}$ at 650°C. Thus, the environmental attack appears to be on the order of five times faster at 650°C.

The relative speed of oxygen diffusion by bulk processes into the matrix was estimated by using diffusion coefficients available for β phase titanium. The diffusion coefficients for the β phase were used since these are four times faster than for oxygen diffusion in α titanium. The expression for the bulk diffusion coefficient, D_v , used was:¹²⁵

$$D_v = 1.6 \exp\left(-\frac{48,200}{RT}\right) \text{ cm}^2/\text{sec} \quad (5.21)$$

This equation gives a diffusion coefficient of $3.2 \times 10^{-13} \text{ cm}^2/\text{sec}$ at 550°C and $7.7 \times 10^{-12} \text{ cm}^2/\text{sec}$ at 650°C. The diffusion coefficient at 650°C is 24 times larger than that at 550°C. An approximation as to how far bulk diffusion could take place ahead of the crack tip was made by using the shortest test time in which crack growth was observed. For the

test at 550°C this corresponded to 80 seconds, and at 650°C the time was reduced to only 12 seconds. The expression used for estimating the furthest extent of one dimensional mass transfer was:

$$x = \sqrt{Dt} \quad (5.22)$$

The results indicate that oxygen will only penetrate to a depth of 50 nm at 550°C and to 96 nm at 650°C during these test times. These depths do not appear to be sufficient to cause embrittlement at the crack tip. This suggests that other diffusional mechanisms including dislocation pipe diffusion, boundary diffusion and perhaps stress-assisted diffusion are certainly playing a large role in oxygen transport at these temperatures. In making an estimate as to the diffusion rate for boundary diffusion, the activation energy for boundary diffusion was assumed to be half that for volume diffusion, i.e. 24,100 cal/mol. Substituting this value into equation (5.21), values for D_b of 6.36×10^{-7} and 3.14×10^{-6} cm²/s at 550 and 650°C, respectively, were obtained. To calculate an approximate diffusion rate of oxygen at the crack tip, an effective diffusion rate can be estimated from equation (5.19). Where the effective grain boundary thickness, δ , is taken to be 5 Å; and the grain size, d , to be 1 µm. Substitution of these values into equation (5.19) gives an effective diffusion coefficient, D_{eff} , of 1.0×10^{-10} and 4.9×10^{-9} cm²/s at 550 and 650°C, respectively. Again equation (5.22) is used to estimate the distance that oxygen will penetrate into the bulk at the crack tip. Depths of 2.8 µm at 550°C and to 2.4 µm at 650°C were calculated. These values are more consistent with the scale of the microstructural units involved in failure.

However, the above calculations were all made assuming a stationary crack front for the duration of the test. In reality, by subtracting the length of the initial surface cracks that popped-in early in straining from those measured at the end of the test, values of crack propagation rates at 550 and 650°C were found to be 5.8 µm/s and 21.7 µm/s, respectively. Clearly, the diffusion estimates and the embrittling mechanisms at the crack

tip are much quicker than have been estimated by traditional models of diffusional processes. Adsorption of oxygen at the crack tip leading to very localized embrittlement could be another possibility in this circumstance.

5.2.4 Elevated Temperature Toughness

The two microstructures, 10/F and 0/F, tested at 450°C by interrupted bend bar experiments exhibited similar crack growth behavior. The crack tip was characterized by a relatively large crack tip opening displacement and apparent blunting prior to extension. Blunting of the crack has two significant implications. First, it implies that the surrounding matrix was very plastic, allowing for significant deformation at the crack tip. Second, blunting decreases the stress intensity at the crack tip in a similar fashion to that described by the Inglis solution for a blunt, elliptical hole:¹²⁶

$$\sigma_{\beta\beta} = \sigma \left(1 + 2 \sqrt{\frac{a}{\rho}} \right) \quad (5.23)$$

Both of these results have the effect of increasing the fracture toughness of the material by increasing the work to failure. As Chan and Soboyejo have shown, the most significant influences on initiation toughness are rendered by intrinsic mechanisms to the material.^{88,99} This was primarily rendered through blunting by the β phase at the crack tip at room temperature. In addition to more macroscopic crack tip blunting at 450°C, the intrinsic toughness of single phase α_2 alloys has been shown to increase with temperature.^{2,101} Other mechanisms which can increase the initiation toughness include crack deflection and microcracking around the crack tip. The results of the present study show that these two mechanisms are not operating at 450°C. The crack tip was not observed to even approach the 45° deflection necessary to impart significant toughening due to deflection. Additionally, the only microcracks observed were in front of the crack tip and in the plane

of crack growth. The location of these cracks puts them in an anti-shielding mode by allowing the stress field associated with the microcrack to overlap that of the main crack.

Propagation appeared to occur by the continual nucleation of cracks in the α_2 phase ahead of the crack tip followed by linking with the main crack. The cracks nucleated in the α_2 phase ahead of the crack tip were observed to be blunted by the surrounding B2 phase. The main crack tip re-blunts after linking and the process begins again. The tearing modulus at 450°C for all three microstructures is far greater than that reported elsewhere for room temperature testing. Again, as pointed out by Chan and Soboyejo, extrinsic contributors to growth toughness can include crack tip deflection, crack bridging and microcrack shielding.^{88,99} In the current instance contributions from deflection and shielding are minimal. Thus, the growth toughness physically appears to be derived from the repeated process of blunting, microcracking, linking, extension, blunting, etc. Some limited evidence of bridging was also observed and is a likely contributor to toughening during growth. The re-blunting process during extension was more pronounced in microstructure 10/F, perhaps resulting in the higher tearing modulus as compared to microstructure 0/F.

At 550°C measures of the initiation toughness, J_{Ic} , and growth toughness, T_R , were both observed to increase. Blunting still appeared to be an important feature at the crack tip prior to extension. Additionally, extensive crack branching was observed in all of the microstructures. Such behavior results in a large dissipation of fracture energy over the larger number of crack tips. This is a possible factor in the observed increase in tearing modulus. Growth at the crack tip again proceeded by linking of microcracks ahead of the crack tip with the main crack. In microstructures 10/F and 0/F the cracking appeared to be the result of a shear process directly in front of the deflected crack tip. The local orientation of the secondary α_2 laths results in the observed microstructural dependence on crack branching as the crack follows the path where shearing is most favorable. However, microstructure 0/C exhibited microcrack initiation further away from the crack tip. These cracks tended to become blunted and more void-like before linking. One may then

conclude that the blunting of the crack tip and the microcracks ahead of it lead to the higher tearing modulus in microstructure 0/C.

Although environmental embrittlement of the crack tip is a potential contributor to the fracture behavior observed in these tests, it is not considered to be significant at 550°C with the loading rate used. This conclusion is based on an examination of environmentally assisted crack growth rates observed in the air tensile tests. The crack growth rates in the J-bend bars were approximately twice as quick as the strain rate insensitive crack growth rate in the tensile bars, 0.01 vs 0.005 mm/s. Therefore, it would seem that there is insufficient time for the crack tip to become embrittled.

At 650°C the initiation toughness and growth toughness both decreased dramatically. The brittle appearance of the fracture surface indicates that these values were strongly affected by environmental embrittlement. As shown in section 5.2.3, the embrittlement of a crack tip at this temperature proceeds at an exceptionally high rate. The crack growth rates during the J-bend testing were measured to be in the range 0.23 - 0.49 mm/s. This is in good agreement with the environmentally assisted crack growth rates in the air tested tensile specimens which were measured at approximately 0.25 mm/s. Therefore, it is evident that environmental embrittlement of the crack tip was dominating the toughness values measured. The low J_{IC} value, as compared to the tearing modulus, resulted in a fairly flat J vs Δa curve. This, combined with the brittle nature of the failure mode and the possible contributions from high-temperature creep mechanisms, indicates that the K_{IC} value derived from J_{IC} is probably not valid. To check this, K_Q values were directly obtained from the J-bend bar load-displacement curves. Two curves were measured for each microstructure. The results indicate that indeed the J_{IC} values over estimate the initiation toughness in all of the microstructures. The K_Q values obtained were 21.9, 22.2 and 28.5 MPa \sqrt{m} for microstructures 10/F, 0/C and 0/F, respectively. These are not quite valid K_{IC} values because the P_{max}/P_Q values were approximately 1.6, above the maximum value of 1.1 required by ASTM E399.¹⁰³

6. SUMMARY AND CONCLUSIONS

The room and elevated temperature deformation and fracture mechanisms have been examined for several different microstructures in an $\alpha_2 + \beta/B2$ alloy. The results of this study have lead to a number of conclusions as to the tensile and toughening behavior of this class of material. The following is a brief summary of the findings of this study:

1. There is ample evidence from mechanical properties to indicate a change in deformation behavior from room temperature to 450°C. This is evidenced by the significant decrease in the k constant in a Hall-Petch type equation, the absence of brittle failure during tensile deformation and the large strains measured in the primary α_2 particles at temperatures at and above 450°C. The observations suggest that this change in deformation behavior is occurring within the α_2 phase.
2. Failure initiation at 450°C and above is a ductile process. For all three microstructures, crack initiation occurs at the B2 and grain boundary α_2 interface up to 600°C. The resulting crack propagates in a ductile fashion along the prior β grain boundary until a critical flaw size is reached. At this point the crack propagates transgranularly. This transgranular failure results in the brittle failure of primary α_2 particles, indicating that the brittle to ductile transition is strain rate sensitive.
3. Failure initiation at temperatures of 450°C and above is associated with the B2 phase. A constant strain to void nucleation is observed in fine secondary α_2 microstructures up to 750°C. In this same temperature range the stress to void nucleation decreases because of the temperature dependence of the flow stress. With the high stresses achieved in the temperature range 450-600°C, failure occurred very shortly after void nucleation.

4. Another change in deformation occurs above 600°C. At these temperatures, plastic deformation occurs predominantly in the B2 phase. At some point, the α_2 ceases to participate substantially in the deformation process and strain is partitioned primarily to the B2 phase. The material also tends towards flow softening behavior and becomes very strain rate sensitive, both trends are characteristics of the B2 phase.
5. The strain localization in the fine secondary α_2 microstructures, as manifested through a constant elongation but increasing reduction of area, is due to the significantly lower work hardening rate of the B2 phase. As necking initiates, more strain is partitioned to the B2 phase, as this prompts a decrease in the flow stress of the material, more strain tends to accumulate there. The positive strain rate dependence of the work hardening rate tends to counteract this mechanism, but appears to become less effective as temperature is increased.
6. A coarse β processed microstructure exhibited intergranular failure at elevated temperatures. The prior β grains tended to behave as a macroscopic units of deformation. Strain localization at the prior β grain boundaries from the intersections of slip bands resulted in the rapid strain accumulation in the B2 phase. Preferential strain accumulation in the B2 phase was responsible for extensive deformation along the grain boundaries.
7. The fracture surface appearance of the vacuum tensile specimens also changed quite dramatically above 600°C. No regions of brittle failure were observed. Sectioning showed that failure initiation was exclusively located at the α_2 /B2 interface. The concentration of voids in the necked region increased substantially, this was caused by

the low work hardening behavior of the microstructure, allowing more plastic deformation to occur before a stress sufficient to cause failure was reached.

8. Voids were noticeably cylindrical in shape. The alignment of the secondary α_2 laths with the tensile axis at high deformation levels appears to inhibit shear band localization between the voids due to the lack of participation of the α_2 phase in deformation. This process makes void coalescence a more difficult process by limiting void sheet formation, and thus prolongs the failure event.
9. There is a very significant effect of dynamic environmental embrittlement at temperatures as low as 550°C. Strain rates of approximately 10^{-2} and 10^{-1} s^{-1} were required at 550°C and 650°C, respectively, to avoid crack tip embrittlement. Calculation of interstitial diffusion rates showed that the process does not appear to be a bulk embrittlement, but rather a localized embrittlement in the region of the propagating crack.
10. Significant blunting occurs before and during crack growth in J-bend tests at 450 and 550°C. This indicates that intrinsic toughening occurs in this alloy, probably because of the increased plastic capacity of the α_2 phase. At 550°C crack branching becomes pronounced during crack growth. This leads to a dramatic increase in the tearing modulus of the microstructures.
11. At 650°C the effect of environmental embrittlement of the crack tip region becomes significant, leading to a decrease in the measured fracture initiation toughness. Due to the brittle nature of the fracture and the very flat tearing modulus, the J-bend test overestimated the initiation toughness by approximately 50%.

12. Four different sites for failure initiation were identified within these microstructures. In $\alpha_2+\beta$ processed microstructures these include matrix slip band intersection with another slip band to form a V-crack, matrix slip band intersection with primary α_2 particles which initiates brittle failure in the particle, slip band decohesion within primary α_2 particles and slip band intersections with the primary α_2 interfaces to cause interfacial failure. In the β processed microstructures, initiation sites included slip band intersections to cause V-cracks intragranularly, and slip band intersections with prior β grain boundaries causing brittle failure in grain boundary α_2 .
13. Room temperature tensile fracture behavior is fairly well described by Smith's model of nucleation controlled failure.¹¹² An effective fracture energy of 33 J/m² was determined, in good agreement with published data.⁹⁴ Slip band length is critical in determining the fracture stress for a particular microstructure. Furthermore, high yield stress curtails plastic elongation because of intervention of fracture. This is related to the comparable values of yield and fracture stress. In $\alpha_2+\beta$ processed microstructures the minimum slip band length to be considered in calculations is the primary α_2 particle size.

The microstructures used in this study are but a subset of those available through thermomechanical processing of this material. Therefore, while these conclusions apply to the microstructures studied here, care should be taken in broad application to vastly different microstructures one can produce in this system.

7. RECOMMENDATIONS FOR FUTURE RESEARCH

The results of this study have determined the need, in several areas, for future research important to further understanding of high temperature behavior of intermetallic materials.

1. A significant change in the deformation behavior of Ti-25-10-3-1, attributed to the α_2 phase, was observed to occur between room temperature and 450°C. Studies to date have only focused on the room temperature and 650°C behavior of single phase α_2 . Further work to determine the transition temperature for a change in deformation behavior would be useful in explaining the underlying causes for the observed increase in plasticity.
2. Analytical electron microscopic analysis is required in determining the deformation behavior of this two phase alloy. In particular, examination of how the strain partitioning process progresses as a function of strain and increasing difference in flow stress between the α_2 and β /B2 phases at temperatures greater than 600°C would be useful.
3. As temperature increased from 450°C to 750°C, it was apparent that the behavior of the multiphase material was becoming dominated by the minor phase. Finite element modeling of multiphase systems has been performed using the relative strengths of the phases for small strains. A useful undertaking would be to expand these models to include differences in work hardening behavior of the phases and to extend the analysis to higher strain levels. Such a study should include the effects of constraint of one phase on the other, and determine at what strain level one phase is likely to stop participating in the deformation process.

4. In addition to the multiphase deformation analysis, an examination of the deformation behavior of a better compositionally defined and truly single phase $\beta/\text{B2}$ phase would be helpful in supporting the above finite element analyses and multiphase deformation study. In particular, the defining the process by which the $\beta/\text{B2}$ phase appears to undergo a flow softening behavior would be useful.
5. Current models of ductile phase toughening, as they apply to initiation toughness, are limited to physically describing the ductile phase in terms of its volume fraction. However, this is not a complete portrayal of all the relevant variables in the morphology of the phase. A more meaningful model, when considering crack tip mechanisms, might include such physically relevant terms as the thickness of the ductile phase and relation of the thickness dimension to the plane of crack growth (i.e. texture). Figure 7.1 depicts two microstructures having equal volume fractions of a ductile phase. However, because of the dimensions of the constituent phases, the two microstructures would be expected to experience different interactions with the crack tip plastic zone. The figure on the right is similar to the situation obtained in a very coarse colony microstructure, in which a high initiation toughness has been measured.

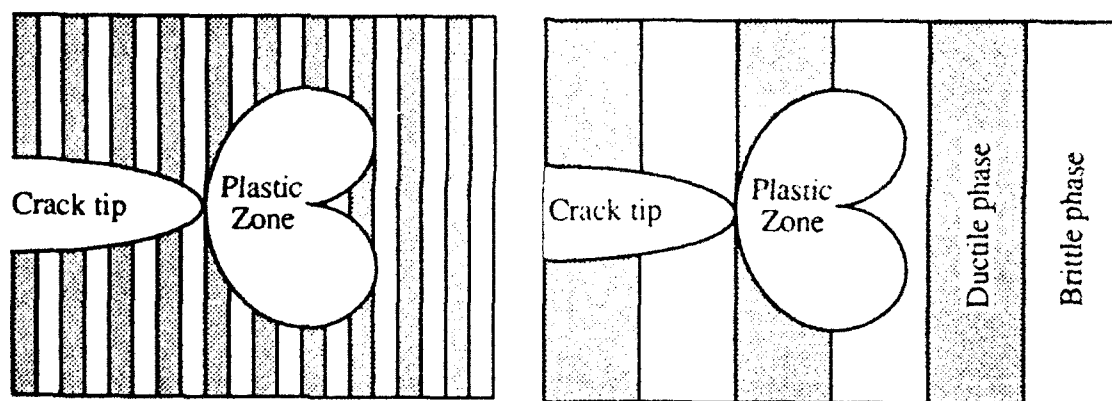


Figure 7.1 Two different microstructures of the same material with the same volume fraction of ductile phase, but differing distributions of the ductile phase.

5. Dynamic environmental embrittlement at a crack tip was shown to have a significant effect on mechanical properties in the short durations encountered in tensile and toughness testing. Available data and bulk diffusional analysis can not adequately explain this rapid embrittlement process. Further studies should be aimed at identifying the surface embrittlement phenomena observed in these intermetallic materials.

8. REFERENCES

1. J.B. McAndrew and C.R. Simcoe: "Investigation of the Ti-Al-Cb System as a Source of Alloys for use at 1200°-1800°F," WADD Technical Report 60-99, Wright-Patterson AFB, 1960.
2. M.J. Blackburn, D.L. Ruckle and C.E. Bevan: "Research to Conduct and Exploratory Experimental and Analytical Investigation of Alloys," AFWAL Technical Report 78-18, Wright-Patterson AFB, 1978.
3. M.J. Blackburn and M.P. Smith: "Research to Conduct and Exploratory Experimental and Analytical Investigation of Alloys," AFWAL Technical Report 80-4175, Wright-Patterson AFB, 1980.
4. M.J. Blackburn and M.P. Smith: "R&D on Composition and Processing of Titanium Aluminide Alloys for Turbine Engines," AFWAL Technical Report 82-4086, Wright-Patterson AFB, 1982.
5. H.A. Lipsitt: in *High-Temperature Ordered Intermetallic Alloys*, MRS Symp., C.C. Koch, C.T. Liu, and N.S. Stoloff, eds., MRS, Pittsburgh, PA, 1985, 351.
6. J.M. Larzen, K.A. Williams, S.J. Balsone and M.A. Stucke: in *High Temperature Aluminides and Intermetallics*, S.H. Whang, C.T. Liu, D.P. Pope, and J.O. Stiegler, eds., TMS-AIME, Warrendale, PA, 1989, 521.
7. R.G. Rowe: in *High Temperature Aluminides and Intermetallics*, S.H. Whang, C.T. Liu, D.P. Pope, and J.O. Stiegler, eds., TMS-AIME, Warrendale, PA, 1989, 375.
8. D.A. Koss, D. Banerjee, D.A. Lukasak, and A.K. Gogia: in *High Temperature Aluminides and Intermetallics*, S.H. Whang, C.T. Liu, D.P. Pope, and J.O. Stiegler, eds., TMS-AIME, Warrendale, PA, 1989, 175.
9. D.M. Dimiduk, D.B. Miracle and C.H. Ward: *Mat. Sci. and Tech.*, 1992, vol. 8, 367.
10. K. Muraleedharan, A.K. Gogia, T.K. Nandy, D. Banerjee and S. Lele: *Metall. Trans. A*, 1992, vol. 23A, 401.
11. D.G. Konitzer, I.P. Jones and H.L. Fraser: *Scripta Metall.*, 1986, vol. 20, 265.
12. H.T. Kestner-Weykamp, D.R. Baker, D.M. Paxton and M.J. Kaufman: *Scripta Metall. Mater.*, 1990, vol. 24, 445.
13. C.H. Ward, B.J. Marquardt and R. Field: manuscript in preparation, 1992.
14. L.A. Bendersky, W.J. Boettinger and A. Roytburd: in *Proc. Conf. 'JIMIS-6'*, Sendai, Japan, 1991.
15. R. Strychor and J.C. Williams: in *Solid→Solid Phase Transformations*, H.I. Aaronson, D.E. Laughlin, R.F. Sekerka and C.M. Wayman, eds., TMS-AIME, Warrendale, PA, 1982, 249.

16. R. Strychor, J.C. Williams and W.A. Soffa: *Metall. Trans. A*, 1988, vol. 19A, 225.
17. L.A. Bendersky, W.J. Boettinger, B.P. Burton, F.S. Biancamello and C.B. Shoemaker: *Acta Metall.*, 1989, vol. 38, 931.
18. M.J. Blackburn: *Trans. AIME*, 1967, vol. 239, 1200.
19. J.L. Murray: in *Binary Alloy Phase Diagrams*, T.B. Massalski, ed., ASM International, Metals Park, OH, 1986, 173.
20. C. McCullough, J.J. Valencia, C.G. Levi and R. Mehrabian: *Acta Metall.*, 1989, vol. 37, 1321.
21. L. Bendersky, W. Boettinger and A. Roytburd: in *ASM Materials Week '90*, Detroit, MI, ASM International, Oct. 1990.
22. H.T. Kestner-Weykamp, C.H. Ward, T.F. Broderick and M.J. Kaufman: *Scripta Metall.*, 1989, vol. 23, 1679.
23. C.H. Ward: Wright Laboratory, unpublished research, 1989.
24. H. Böhm and K. Löhberg: *Z. Metallk.*, 1958, vol. 49, 173.
25. T. Hamajima, G. Lütjering and S. Weisman: *Metall. Trans. A*, 1972, vol. 3, 2805.
26. D. Banerjee, T.K. Nandy and A.K. Gogia: *Scripta Metall.*, 1987, vol. 21, 597.
27. K. Otsuka, C.M. Wayman and H. Kubo: *Metall. Trans. A*, 1978, vol. 9A, 1075.
28. C.H. Ward, J.C. Williams, A.W. Thompson, D.G. Rosenthal and F.H. Froes: in *Sixth World Conference on Titanium*, P. Lacombe, R. Tricot and G. Béranger, eds., Les Éditions de Physique, Paris, 1989, 1103.
29. J. Wittenauer, C. Bassi and B. Walser: *Scripta Metall.*, 1989, vol. 23, 1381.
30. C.H. Ward, J.C. Williams and A.W. Thompson: *Scripta Metall. Mater.*, 1990, vol. 24, 617.
31. T.E. O'Connell and P.A. Flinn: in *Titanium and Titanium Alloys*, J.C. Williams and A.F. Belov, eds., Plenum Press, New York, 1982, 1451.
32. S.M.L. Sastry and H.A. Lipsitt: *Metall. Trans. A*, 1977, vol. 8A, 1543.
33. S. Rozeveld and J.M. Howe: Carnegie Mellon University, unpublished research, 1989.
34. W.A. Baeslack, III, T. Mascarella and T.J. Kelly: *Weld. Res. Supp.*, 1989, vol. 243S, 483.
35. M.J. Cieslack, T.J. Headley, W.A. Baeslack, III: *Metall. Trans. A*, 1990, vol. 21A, 1273.

36. J.C. Williams and M.J. Blackburn: *Trans. AIME*, 1969, vol. 245, 2352.
37. T.W. Duerig, G.T. Terlinde and J.C. Williams: *Metall. Trans. A*, 1980, vol. 11A, 1987.
38. J.C. Williams: in *Titanium and Titanium Alloys*, J.C. Williams and A.F. Belov, eds., Plenum Press, New York, 1982, 1477.
39. P.L. Martin, H.A. Lipsitt, N.T. Nuhfer and J.C. Williams: in *Titanium '80, Science and Technology*, H. Kimura and O. Izumi, eds., TMS-AIME, Warrendale, PA, 1980, 1245.
40. H.I. Aaronson and H.B. Aaron: *Metall. Trans. A*, 1972, vol. 3, 2743.
41. K.N. Tu and D. Turnbull: *Acta Metall.*, 1967, vol. 15, 369.
42. K.N. Tu and D. Turnbull: *Acta Metall.*, 1967, vol. 15, 1317.
43. K.N. Tu: *Metall. Trans. A*, 1972, vol. 3, 2769.
44. W.W. Mullins and R.F. Sekerka: *J. Appl. Phys.*, 1963, vol. 34, 323.
45. W.W. Mullins and R.F. Sekerka: *J. Appl. Phys.*, 1964, vol. 35, 444.
46. D. Banerjee, A.K. Gogia, T.K. Nandy and V.A. Joshi: *Acta Metall.*, 1988, vol. 36, 871.
47. M.J. Kaufman: "Phase Relations in the $Ti_3Al + Nb$ System," AFWAL Technical Report 88-4113, Wright-Patterson AFB, 1988.
48. K. Muraleedharan, S.V. Nagender Naidu and D. Banerjee: *Scripta Metall. Mater.*, 1990, vol. 24, 27.
49. K. Muraleedharan, A.K. Gogia, T.K. Nandy, D. Banerjee and S. Lele: *Metall. Trans. A*, 1992, vol. 23A, 417.
50. J.C. Williams and M.J. Blackburn: Boeing Aerospace Co., unpublished research, 1970.
51. K.S. Jepson, A.R.G. Brown and J.A. Gray: in *The Science, Technology, and Application of Titanium*, R.I. Jaffee and N.E. Promisel, eds., Pergamon Press, Oxford, 1966, 677.
52. T. Mascarella: *M.S. Thesis*, Department of Welding Engineering, The Ohio State University, 1987.
53. W.A. Baeslack III and T.F. Broderick: *Scripta Metall. Mater.*, 1990, vol. 24, 319.
54. D.L. Moffat and D.C. Larbalestier: *Metall. Trans. A*, 1988, vol. 19A, 1677.
55. H. Okamoto and M. Oka: *Metall. Trans. A*, 1986, vol. 17A, 1113.

56. C.H. Ward and J.C. Williams: in 'ASM Materials Week '90', Detroit, MI, ASM International, Oct. 1990.
57. J.A. Peters and C. Bassi: *Scripta Metall. Mater.*, 1990, vol. 24, 915.
58. R. von Mises: *Z. angew. Math. Mech.*, 1928, vol. 8, 161.
59. G.W. Groves and A. Kelly: *Phil. Mag.*, 1963, vol. 8, 877.
60. M.J. Marcinkowski: in *Electron Microscopy and Strength of Crystals*, G. Thomas and J. Washburn, eds., Interscience Publishers, New York, 1963, 333.
61. J.C. Williams and M.J. Blackburn: in *Ordered Alloys*, B.H. Kear *et al.*, eds/, Claitor's Publishing Division, Baton Rouge, 1970, 425.
62. R. Schafrik: *Quarterly Report, Project #70210170*, Air Force Materials Laboratory, Wright-Patterson AFB, 1975.
63. S.M.L. Sastry and H.A. Lipsitt: *Acta Metall.*, 1977, vol. 25, 279.
64. H.A. Lipsitt, D. Shechtman and R.E. Schafrik: *Metall. Trans. A*, 1980, vol. 11A, 1369.
65. W.J.S. Yang: *Metall. Trans. A*, 1982, vol. 13A, 324.
66. R.J. Kerans: *Metall. Trans. A*, 1984, vol. 15A, 1721.
67. S.A. Court, S.A. Skewes, M.H. Loretto and H.L. Fraser: in *Titanium-Rapid Solidification Technology*, F.H. Froes and D. Eylon, eds., TMS-AIME, Warrendale, PA, 1986, 249.
68. M. Thomas, A. Vassel and P. Veyssi re: *Scripta Metall.*, 1987, vol. 21, 501.
69. S.A. Court, M.H. Loretto and H.L. Fraser: *Scripta Metall.*, 1987, vol. 21, 997.
70. S.A. Court, J.P.A. L fvander, M.H. Loretto and H.L. Fraser: *Phil. Mag. A*, 1990, vol. 61, 109.
71. S.A. Court, J.P.A. L fvander, P. Kurath and H.L. Fraser: in *Sixth World Conference on Titanium*, P. Lacombe, R. Tricot and G. B ranger, eds., Les  ditions de Phisique, Paris, 1989, 949.
72. M. Thomas, A. Vassel and P. Veyssi re: *Phil. Mag. A*, 1989, vol. 59, 1013.
73. S.A. Court, J.P.A. L fvander, M.H. Loretto and H.L. Fraser: *Phil. Mag. A*, 1989, vol. 59, 379.
74. A.K. Gogia, D. Banerjee and T.K. Nandy: *Metall. Trans. A*, 1990, vol. 21A, 609.
75. D. Banerjee, A.K. Gogia and T.K. Nandy: *Metall. Trans. A*, 1990, vol. 21A, 627.

76. B.J. Marquardt, G.K. Scarr, J.C. Chesnutt, C.G. Rhodes and H.L. Fraser: in *Sixth World Conference on Titanium*, P. Lacombe, R. Tricot and G. Béranger, eds., Les Éditions de Physique, Paris, 1989, 955.
77. J.P.A. Löfvander, S.A. Court, P. Kurath and H.L. Fraser: *Phil. Mag. Lett.*, 1989, vol. 59, 289.
78. J.C. Williams, A.W. Sommer and P.P. Tung: *Metall. Trans. A*, 1972, vol. 3, 2979.
79. B.F. Greenberg, V.I. Anisimov, Yu.N. Gornostirev and G.G. Taluts: *Scripta Metall.*, 1988, vol. 22, 859.
80. T. Hong, T.J. Waston-Yang, X.-Q. Guo, A.J. Freeman, T. Oguchi and Jian-hua Xu: *Phys. Rev. B*, 1991, vol. 43, 1940.
81. S.J. Gittis and D.A. Koss: in *High-Temperature Ordered Intermetallic Alloys III*, MRS Symp. Proc., Vol 133, C.T. Liu, A.I. Taub, N.S. Stoloff and C.C. Koch, eds., MRS, Pittsburgh, PA, 1989, 323.
82. J. Kumpfert, K.J. Grundhoff, H. Schurmann, Y.T. Lee, C.H. Ward and M. Peters: in *Proc. 2nd European Conf. on Advanced Materials and Processes*; T.W. Clyne and P.J. Withers, eds., The Institute of Materials, London, 1991, 321.
83. J.P. Hirth and F.H. Froes: *Metall. Trans. A*, 1977, vol. 8A, 1165.
84. C.H. Ward and J.C. Williams: Wright Laboratory, unpublished research, 1989.
85. D.G. Rosenthal: Textron/Lycoming, unpublished research, 1986.
86. C.H. Ward and S.J. Balsone: in *Microstructure/Property Relationships in Titanium Aluminides and Alloys*, Y-W. Kim and R.R. Boyer, eds., TMS-AIME, Warrendale, PA, 1991, 373.
87. I. Roman and C.H. Ward: *Scripta Metall. Mater.*, 1992, vol. 27, in press.
88. K.S. Chan: *Metall. Trans. A*, 1992, vol. 23A, 183.
89. D.A. Lukasak and D.A. Koss: *Metall. Trans. A*, 1990, vol. 21A, 135.
90. S.J. Balsone: in *Oxidation of High Temperature Intermetallics*, T. Grobstein and J. Doychak, eds., TMS-AIME, Warrendale, PA, 1988, 219.
91. K.S. Chan: *Scripta Metall. Mater.*, 1990, vol. 24, 1725.
92. J.C. Williams, J.C. Chesnutt and A.W. Thompson: in *Microstructure, Fracture Toughness and Fatigue Crack Growth Rate in Titanium Alloys*, A.K. Chakrabarti and J.C. Chesnutt, eds., TMS-AIME, Warrendale, PA, 1987, 255.
93. A.T. Santhanam and R.E. Reed-Hill: *Metall. Trans. A*, 1971, vol. 2, 2619.
94. W-Y Chu and A.W. Thompson: *Metall. Trans. A*, 1992, vol. 23A, 1299.

95. D.P. DeLuca and B.A. Cowles: "Fatigue and Fracture of Titanium Aluminides," WRDC Technical Report 90-4075, Wright-Patterson AFB, 1990.
96. W.Y. Chu, A.W. Thompson and J.C. Williams: in *Hydrogen Effects on Material Behavior*, N.R. Moody and A.W. Thompson, eds., TMS-AIME, Warrendale, PA, 1990, 543.
97. B.J. Marquardt: in 'AeroMat '90', Long Beach, CA, ASM International, May 1990.
98. K.S. Chan: *Metall. Trans. A*, 1990, vol. 21A, 2687.
99. W.O. Soboyejo: *Metall. Trans. A*, 1992, vol. 23A, 1737.
100. K.S. Chan: *Metall. Trans. A*, 1991, vol. 22A, 2021.
101. M.A. Stucke and H.A. Lipsitt: in *Titanium Rapid Solidification Technology*, F.H. Froes and D. Eylon, eds., TMS-AIME, Warrendale, PA, 1986, 255.
102. ASTM E8-89, "Standard Test Methods of Tension Testing of Metallic Materials," *1989 Annual Book of ASTM Standards, Vol. 03.01*, American Society for Testing and Materials, Philadelphia, PA, 1989, 131-146.
103. ASTM E399-83, "Standard Test Method for Plane-Strain Fracture Toughness of Metallic Materials," *1989 Annual Book of ASTM Standards, Vol. 03.01*, American Society for Testing and Materials, Philadelphia, PA, 1989, 487-511.
104. ASTM E813-88, "Standard Test Method for J_{Ic} , a Measure of Fracture Toughness," *1989 Annual Book of ASTM Standards, Vol. 03.01*, American Society for Testing and Materials, Philadelphia, PA, 1989, 698-712.
105. E.E. Underwood: *Quantitative Stereology*, Addison-Wesley Publishing, Co., Reading, MA, 1970, 4.
106. J.H. Hollomon: *Trans. AIME*, 1945, vol. 162, 268.
107. P. Ludwik: in *Elemente der Technologischen Mechanik*, Springer, Berlin, 1909, 32.
108. R.E. Schafrik: *Metall. Trans. A*, 1977, vol. 8A, 1003.
109. M.A. Morris and D.G. Morris: *Phil. Mag. A*, 1991, vol. 63, 1175.
110. J.R. Low: in *Symp. of Relation of Properties to Microstructure*, American Society for Metals, 1954, 163.
111. A.N. Stroh: *Adv. Phys.*, 1957, vol. 6, 418.
112. E. Smith: *Acta Metall.*, 1966, vol. 14, 985 and 991.
113. A.W. Thompson: in *Proc. 7th World Conference on Titanium*, 1992, in press.
114. R. Armstrong, I. Codd, R.M. Douthwaite and N.J. Petch: *Phil. Mag.*, 1962, vol. 7, 45.

115. S.J. Gittis: *M.S. Thesis*, Metals Science and Engineering Department, The Pennsylvania State University, 1988.
116. W. Jolley; *Trans. AIME*, 1968, vol. 242, 306.
117. J.C. Williams, F.H. Froes, J.C. Chesnutt, C.G. Rhodes, and R.G. Berryman: in *Development of High Fracture Toughness Titanium Alloys*, ASTM STP 651, American Society for Testing and Materials, Philadelphia, PA, 1978, 64.
118. N.E. Dowling; *Eng. Fract. Mech.*, 1987, vol. 26, 333.
119. A.E. Pontau and D. Lazarus: *Phys. Rev. B*, 1979, vol. 19, 4027.
120. P.G. Shewmon: *Diffusion in Solids*, J. Williams Book Co., Jenks, OK, 1983, 164-187.
121. H.J. Frost and M.F. Ashby: *Deformation-Mechanism Maps*, Pergamon Press, Oxford, 1982, 15.
122. H. Fuji and H.G. Suzuki: *Scripta Metall. Mater.*, 1990, vol. 24, 1943.
123. S. Amkem and H. Margolin: *Metall. Trans. A*, 1982, vol. 13A, 603.
124. D. Goto and D.A. Koss: The Pennsylvania State University, unpublished research, 1992.
125. R.J. Wasilewski and G.L. Kehl: *J. Inst. Metals*, 1954, vol. 83, 94.
126. C.E. Inglis: *Trans. Instn Nav. Archit., LV*, 1913, vol. 1, 219.